INVESTIGATION OF STRUCTURAL AND MAGNETIC PROPERTIES OF SPIN-CHAIN OXIDES

By

ANIL JAIN
PHYS01200804021

Bhabha Atomic Research Centre, Mumbai

A thesis submitted to the
Board of Studies in Physical Sciences
In partial fulfillment of requirements
For the Degree of

DOCTOR OF PHILOSOPHY
of

HOMI BHABHA NATIONAL INSTITUTE

June 2012

Homi Bhabha National Institute

Recommendations of the Viva Voce Board

As members of the Viva Voce Board, we certify that we have read the dissertation prepared by Anil Jain entitled "Investigation of Structural and Magnetic Properties of Spin-chain Oxides" and recommend that it may be accepted as fulfilling the dissertation requirement for the Degree of Doctor of Philosophy.

____ **Date:**

Chairman - Prof. S. L. Chaplot

____ **Date:**

Guide/Convener - Prof. S. M. Yusuf

____ **Date:**

Member 1 - Prof. C. V. Tomy

____ **Date:**

Member 2 - Prof. G. Ravikumar

Final approval and acceptance of this dissertation is contingent upon the candidate's submission of the final copies of the dissertation to HBNI.

I hereby certify that I have read this dissertation prepared under my direction and recommend that it may be accepted as fulfilling the dissertation requirement.

Date:

Place:

STATEMENT BY AUTHOR

This dissertation has been submitted in partial fulfillment of requirements for an advanced degree at Homi Bhabha National Institute (HBNI) and is deposited in the Library to be made available to borrowers under rules of the HBNI.

Brief quotations from this dissertation are allowable without special permission, provided that accurate acknowledgement of source is made. Requests for permission for extended quotation from or reproduction of this manuscript in whole or in part may be granted by the Competent Authority of HBNI when in his or her judgment the proposed use of the material is in the interests of scholarship. In all other instances, however, permission must be obtained from the author.

Anil Jain

DECLARATION

I, hereby declare that the investigation presented in the thesis has been carried out by me. The work is original and has not been submitted earlier as a whole or in part for a degree/diploma at this or any other Institution/University.

Anil Jain

Dedicated

to

My Parents

ACKNOWLEDGEMENTS

First and foremost, I would like thank my supervisor Prof. S. M. Yusuf for his guidance and constant support. I am also grateful to him for his careful reading of the draft of this thesis and his valuable suggestions.

I take immense pleasure in thanking Prof. S. L. Chaplot, Head, Solid State Physics Division (SSPD), Bhabha Atomic Research Centre (BARC) and Prof. S. Kailas, Director, Physics Group, BARC for encouragement and never ending support. I would like to thank the members of the doctoral committee; Prof. S. L. Chaplot, Prof. C. V. Tomy, and Prof. G. Ravikumar for their input, valuable discussions, and accessibility.

My special thanks to Prof. J. V. Yakhmi, Dr. I. Nowik, Dr. J. Campo, Dr. L. Keller, Dr. C. Ritter, and Mr. S. S. Meena whose close collaboration has benefited me in this work.

I gratefully acknowledge the help of Dr. R. Chitra, Mr. A. B. Shinde, and Ms. M. B. Gangurde in carrying out various experiments. I thank Dr. A. Das, Mr. P. S. R. Krishna, Dr. A. K. Rajarajan, Dr. D. M. Gaitonde, and Dr. M. D. Mukadam for valuable discussions during the course of this work. I also thank Dr. K. R. Chakraborty, Dr. A. Kumar, Dr. P. Bhatt, Dr. S. K. Mishra, Mr. R. M. Chandak, Ms. M. Halder, Ms. N. Thakur, Mr. A. K. Bera, and Mr. P. K. Manna for their help and company during this thesis work. I thank all my colleagues in SSPD for their support.

Finally, and most importantly, I thank my wife, and friends, especially Dr. V. K. Malik, Mr. A. K. Saxena, and Mr. M. Raj for their love and support.

List of Publications

Papers Published in International Journals

1. *Short-range and long-range incommensurate magnetic ordering in the frustrated antiferromagnets* $Ca_3Co_{2-x}Fe_xO_6$ *: A neutron diffraction study*
   A. Jain and S. M. Yusuf
   Phys. Rev. B **83**, 184425 (2011).

2. *Magnetic ordering in the spin-chain compounds* $Ca_3Co_{2-x}Fe_xO_6$ *(x = 0.2 and 0.4): A neutron diffraction study*
   A. Jain, S. M. Yusuf, J. Campo, and L. Keller
   Phys. Rev. B **79**, 184428 (2009).

3. *Effect of Fe substitution on the magnetic ordering in* $Ca_3(Co_{1-x}Fe_x)_2O_6$
   I. Nowik, **A. Jain**, S. M. Yusuf, and J. V. Yakhmi
   Phys. Rev. B **77**, 054403 (2008).

4. *Neutron diffraction study of quasi-one-dimensional spin-chain compounds* $Ca_3Co_{2-x}Fe_xO_6$
   A. Jain, S. M. Yusuf, and S. Singh
   Pramana - J. Phys. **71**, 923 (2008).

5. *Structural and magnetic properties of the layered compound* $Ca_{2.375}La_{0.125}Sr_{0.5}GaMn_2O_8$
   A. K. Bera, S. M. Yusuf, and **A. Jain**
   Pramana - J. Phys. **71**, 917 (2008).

6. *Structural and magnetic properties of spin-chain compounds* $Ca_3Co_{2-x}Fe_xO_6$
   A. Jain, S. M. Yusuf, and S. Singh
   Phys. Rev. B **74**, 174419 (2006).

7. *Field-induced incommensurate-to-commensurate magnetic phase transition in* $Ca_3Co_{1.8}Fe_{0.2}O_6$ *: A neutron diffraction study*
   S. M. Yusuf, **A. Jain**, and L. Keller
   Phys. Rev. B (under review).

8. *Time dependence of the incommensurate magnetic structure of* $Ca_3Co_2O_6$*: A neutron diffraction study*

A. Jain and S. M. Yusuf
(Manuscript under preparation).

9. *Effect of electron doping on the structural and magnetic properties of* $Ca_3Co_2O_6$
   A. Jain, S. M. Yusuf, and C. Ritter
   (Manuscript under preparation).

Papers Published/Presented in Conferences/Symposia

1. *Coexistence of long-range and short-range magnetic ordering in the frustrated antiferromagnet* $Ca_3Co_2O_6$.
   A. Jain and S. M. Yusuf
   Poster presented in the 56th DAE Solid State Physics Symposium held at SRM University, Kattankulathur, during Dec 19-23, 2011.

2. *Incommensurate magnetic structure of* $Ca_3Co_{1.8}Fe_{0.2}O_6$
   A. Jain and S. M. Yusuf
   AIP Conf. Proceedings **1349**, 1221 (2011).

3. *Magnetism of geometrically frustrated quasi-one-dimensional spin-chain compounds* $Ca_3Co_{2-x}Fe_xO_6$
   A. Jain and S. M. Yusuf
   Proceedings of the Advances in Magnetism: Phenomena and Materials held at Manu Allaya Resort, Manali during June 03-05, 2010
   (Received Best Poster Award).

4. *Magnetism of the spin-chain compound* $Ca_3Co_{1.9}Fe_{0.1}O_6$*: Magnetization and neutron diffraction study*
   A. Jain, S. M. Yusuf, J. Campo, and L. Keller
   J. Phys.: Conf. Ser. **200**, 022021 (2010).

5. *Partially disordered antiferromagnetic structure of frustrated triangular lattice antiferromagnet* $Ca_3Co_{1.9}Fe_{0.1}O_6$
   A. Jain and S. M. Yusuf
   Solid State Physics (India) **54**, 1041 (2009).

6. *Neutron diffraction study of Mn-substituted geometrically frustrated spin-chain compounds* $Ca_3Co_{2-x}Mn_xO_6$
   A. Jain, S. Singh, and S. M. Yusuf
   Proceedings of the Conference on Neutron scattering and Mesoscopic System held at Goa University during Oct 12-14, 2009.

7. *Magnetic Properties of the Low Dimensional Manganite* $Ca_{2.5}Sr_{0.5}AlMn_2O_8$
   A.K. Bera, S. M. Yusuf, and **A. Jain**
   AIP Conf. Proc. **1003**, 160 (2008).

8. *Coexistence of short-range and long-range magnetic order in Fe-doped geometrically frustrated spin-chain compound* $Ca_3Co_2O_6$
   A. Jain, S. M. Yusuf, and L. Keller
   Solid State Physics (India) **53**, 1201 (2008).

9. *Synthesis, crystal structure, and magnetic properties of Fe-doped geometrically frustrated spin-chain oxide* $Ca_3Co_2O_6$
   A. Jain, S. M. Yusuf, and L. Keller
   Proceedings of International Symposium on Materials Chemistry, Dec (2008) 264.

10. *Neutron diffraction and magnetization studies of Fe-doped geometrically frustrated spin-chain compound* $Ca_3Co_2O_6$
    A. Jain and S. M. Yusuf
    Proceedings of International Conference on Magnetic Materials & their Application for 21^{st} Century Oct (2008) 190.

11. *Magnetic properties of the bilayered manganite* $Ca_{2.5-x}La_xSr_{0.5}GaMn_2O_8$
    A. K. Bera, S. M. Yusuf, and **A. Jain**
    Proceedings of International Conference on Advanced Materials (ICAM) held in Bangalore, India during 8-13 Oct, 2007.

12. *Magnetic properties of the spin-chain compound* Ca_3CoFeO_6
    A. Jain, S. Singh, and S. M. Yusuf
    Proceedings of International Conference on Advanced Materials (ICAM) held in Bangalore, India during 8-13 Oct, 2007.

13. *Magnetic properties of mixed Ising and Heisenberg spin-chain compounds*
    A. Jain, S. Singh, and S. M. Yusuf
    Solid State Physics (India) **51**, 931 (2006).

14. *Effect of iron doping on structural and magnetic properties of 1-D Ising ferromagnet* $Ca_3Co_2O_6$
    A. Jain, S. Singh, and S. M. Yusuf
    Proceedings of International Symposium on Materials Chemistry, Dec (2006) 507.

Contents

SYNOPSIS OF THE THESIS SUBMITTED TO THE HOMI BHABHA NATIONAL INSTITUTE FOR THE DEGREE OF DOCTOR OF PHILOSOPHY IN PHYSICS

Name of the Candidate : Anil Jain
Name of the Guide : Prof. S. M. Yusuf
Solid State Physics Division,
Bhabha Atomic Research Centre,
Trombay, Mumbai 400085.
Registration Number : PHYS01200804021
Date of Registration : 01/09/2008
Title of the Thesis : Investigation of structural and magnetic properties of spin-chain oxides
Place of Research Work : Solid State Physics Division,
Bhabha Atomic Research Centre,
Trombay, Mumbai 400085.
Signature of the Candidate :
Signature of the Guide :

SYNOPSIS

Investigation of Structural and Magnetic Properties of Spin-chain Oxides

In the recent years, the low dimensional magnetic materials have attracted a lot of attention due to their unique electronic and magnetic properties. Here, the low dimensional systems refer to the compounds where the arrangements of the magnetic ions are in less than three spatial dimensions e.g. 2D- layers, 1-D or quasi 1-D spin chains, etc. Some of the interesting properties of these compounds are geometrical frustration, multiferrocity, superconductivity, highly anisotropic physical properties, and quantum phase transitions.

Among the low dimensional magnetic materials, quasi-one-dimensional spin-chain compounds of type A_3MXO_6 [A = Ca, Sr, and (M, X) = alkali or transition metal ions] have recently attracted much interest due to their peculiar physical properties. The crystal structure of these compounds consists of chains, made up of alternating face-sharing MO_6 trigonal prisms (TP) and XO_6 octahedra (OCT) running along the crystallographic c axis. These chains, separated by non-magnetic A^{2+} ions, are arranged on a triangular lattice in the ab plane and each chain is surrounded by six chains. One-dimensional character in the magnetic properties of these compounds is expected because the distance between the magnetic ions along the chain is approximately half of the interchain distance. The ferromagnetic intrachain and antiferromagnetic interchain interactions, combined with a triangular arrangement of spin-chains may give rise to a geometrical frustration in these compounds. Since the electronic and magnetic properties are governed by the charge, spin and orbital degrees of freedom, a large number of opportunities exist in these compounds to modify these properties by a suitable substitution of the transition metal ions at the M/X sites.

In this thesis, we concentrate on the structural and magnetic properties of the compounds $Ca_3Co_2O_6$, $Ca_3Co_{2-x}Fe_xO_6$ (x = 0.1, 0.2, 0.4, and 1.0), and $Ca_{2.75}R_{0.25}Co_2O_6$ (R = Lu and Dy). In the compound $Ca_3Co_2O_6$, spin-chains are made up of alternating face sharing CoO_6 octahedra (with Co1) and CoO_6 trigonal prisms (with Co2) with a Co-Co separation of $\sim$ 2.6 Å (along the chain). The different crystalline electric fields at the OCT and TP sites lead to the different spin states of the Co^{3+} ions in this compound; low spin ($S = 0$) and high spin ($S = 2$) states at the OCT($6b$) and TP($6a$) sites, respectively. The Co^{3+} spins at the TP sites have an Ising-like magnetic anisotropy and are aligned along the crystallographic c axis. The choice of the iron substitution at the cobalt site was motivated by the consideration that the Co^{3+} ions at the TP site, in the compound $Ca_3Co_2O_6$, has large orbital moment (1.7 μ_B), while the Fe^{3+} ions have zero orbital momentum (a closed subshell without orbital degrees of freedom). Moreover, the ionic radii of the Co^{3+} and Fe^{3+} with six oxygen coordination are very close (0.61 and 0.645 Å, respectively). No strong lattice effect will, therefore, be introduced, and changes only due to the different magnetic character of the spins of Co^{3+} and Fe^{3+} are expected. The choice of rare earth (R^{3+}) doping at the Ca^{2+} site is motivated by the theoretical prediction from the band structure calculations that magnetic properties for the compound $Ca_3Co_2O_6$ can be tuned by electron doping. The difference in the ionic radii of the rare earth (R^{3+}) and the calcium (Ca^{2+}) may change the distance between magnetic ions. The difference in the oxidation state of the R^{3+} and Ca^{2+} is expected to vary the oxidation state of Co^{3+} in the compound $Ca_3Co_2O_6$. These factors can change the intrachain and interchain magnetic exchange interactions, which can modify the magnetic properties of these spin-chain compounds. The thesis comprises of seven chapters.

Chapter 1 gives a brief overview of some of the most important features of the low dimensional magnetic systems. A brief introduction about the geometrically frustrated magnets, their interesting physical properties, and why one should study them, is given. The crystal structure of the A_3MXO_6 type quasi-one-dimensional spin-chain compounds and how the geometrical frustration arises in these compounds are discussed. An outline of the thesis is given at the end.

In the succeeding chapter, a brief description about the sample preparation techniques used to synthesize the polycrystalline compounds studied in the thesis is given. A brief introduction and working principles of the various experimental techniques (x-ray diffraction, neutron diffraction, dc magnetization, and Mössbauer spectroscopy) employed to investigate the structural and magnetic properties of the compounds are also described. A brief description about the Rietveld method, to refine the crystal structures and to determine the magnetic structures from the powder diffraction data, is also given.

Chapter 3 presents the structural properties of the compounds $\mathrm{Ca_3Co_2O_6}$, $\mathrm{Ca_3Co_{2-x}Fe_xO_6}$ (x = 0.1, 0.2, 0.4, and 1.0), and $\mathrm{Ca_{2.75}}R_{0.25}\mathrm{Co_2O_6}$ (R = Lu and Dy). The Rietveld refinement of x-ray and neutron diffraction patterns confirms that all compounds, except $\mathrm{Ca_3CoFeO_6}$, crystallize in the rhombohedral structure (space group $R\bar{3}c$). For the compounds $\mathrm{Ca_3Co_{2-x}Fe_xO_6}$ (x = 0.1, 0.2, and 0.4), the Rietveld refinement of neutron diffraction patterns and Mössbauer study confirm that the $\mathrm{Fe^{3+}}$ ions are located only at the TP site. For the rare earth substituted compounds $\mathrm{Ca_{2.75}}R_{0.25}\mathrm{Co_2O_6}$ (R = Lu and Dy), the refinement shows that the trivalent rare earth ions R^{3+} are located at the $\mathrm{Ca^{2+}}$ ($18e$) site, and bond lengths Co2-O and Co1-Co2 increase significantly, as compared to the parent compound $\mathrm{Ca_3Co_2O_6}$. The observed increase in the bond lengths Co2-O, with rare earth substitution, suggests that extra electrons are transferred to the Co2 ions at the TP site. The crystal structure of all the compounds, except for $\mathrm{Ca_3CoFeO_6}$, contains one-dimensional chains made up of alternating face-sharing CoO_6 octahedra and $(Co/Fe)O_6$ trigonal prisms, running along the crystallographic c axis. For the compound Ca_3CoFeO_6, the profile matching refinement of the x-ray diffraction pattern confirms a triclinic crystal structure (space group $P\bar{1}$).

Chapter 4 is divided into two parts. The first part of this chapter describes the magnetic structure of the compounds $Ca_3Co_2O_6$ and $Ca_3Co_{2-x}Fe_xO_6$ (x = 0.2 and 0.4). In the first approximation, two different commensurate magnetic structures, (i) amplitude-modulated structure with a propagation vector $\boldsymbol{k} = \{0, 0, 1\}$ and (ii) partially disordered antiferromagnetic (PDA) structure, are able to fit the same neutron diffraction patterns, below their respective Néel temperatures (T_N = 25, 20, and 17 K, for x = 0, 0.2, and 0.4 compounds, respectively). However, a detailed analysis reveals that these compounds order magnetically in an incommensurate spin density wave (SDW) structure, having a modulation and an alignment of the spins along the crystallographic c axis, below T_N. Further, a coexistence of the magnetic long-range and short-range ordering has been observed down to 1.5 K (below T_N). For the parent compound $Ca_3Co_2O_6$, in addition to the magnetic Bragg peaks corresponding to the SDW structure, a second set of magnetic peaks corresponding to the commensurate antiferromagnetic (CAFM) structure with a propagation vector $\boldsymbol{k}_2 = \{0.5, 0.5, 0\}$ appears in the neutron diffraction patterns below ~ 15 K. Moreover, the magnetic Bragg peaks, corresponding to the CAFM and SDW structures, exhibit time dependence at some fixed temperatures below ~ 14 K. Our analysis (for the parent compound $Ca_3Co_2O_6$) shows that the magnetic ground state is a coherent superposition of the magnetic structures belonging to the propagation vectors $\boldsymbol{k}_1 = \{0, 0, 1.009(3)\}$ and $\boldsymbol{k}_2 = \{0.5, 0.5, 0\}$. The second part describes Mössbauer spectroscopy studies of spin-spin relaxation in the compounds $Ca_3Co_{2-x}Fe_xO_6$ (x = 0.2 and 0.4), and nature of magnetic ordering in Ca_3CoFeO_6.

The compounds with $x \leq 0.4$ are paramagnetic above $\sim$ 90 K, and the iron exhibits slow spin relaxation phenomena even at room temperature. However, for the compound Ca_3CoFeO_6,which crystallizes in the triclinic space group $P\bar{1}$, the iron resides almost equally in two different crystallographic sites and exhibits a very high magnetic ordering temperature $T_N \sim$ 500 K. Both iron sites exhibit quadrupole interactions of almost equal size; however, with an opposite sign. These results agree well with the magnetic susceptibility measurements, in which a sharp drop in magnetization is observed above 200 K. The net magnetic interaction is antiferromagnetic, however, with a small ferromagnetic component displaying hysteresis along with a saturation magnetization of about 0.02 μ_B/f.u. at 1.5 K.

Chapter 5 describes the effect of an external perturbation *viz.* magnetic field on the nature of magnetic ordering in the compounds $Ca_3Co_{2-x}Fe_xO_6$ (x = 0, 0.1, 0.2, and 0.4). For all compounds, high temperature magnetic susceptibility obeys the Curie-Weiss law. The value of paramagnetic Curie temperature decreases as the concentration of iron increases ($\theta_p = 27.8$ for $x = 0$ compound) and it becomes negative (-1.6 K for $x = 0.4$) for higher concentration of iron. From the dc-magnetization study, we have derived the value of intrachain and interchain exchange interactions for the compounds $Ca_3Co_{2-x}Fe_xO_6$ (x = 0.0, 0.1, 0.2, and 0.4). A decrease in the intrachain positive exchange constant J' and an increase in the interchain negative exchange constant J have been observed with substitution of iron, which result in deviation from “1D character” in these spin-chain compounds. In the dc magnetization study, we have observed an indication of the presence of a field induced transition from a ferri to a ferromagnetic state. Neutron diffraction study has been carried out to study the spin-spin correlations in the compound $Ca_3Co_{1.8}Fe_{0.2}O_6$, by directly investigating the evolution of the magnetic structures as a function of applied magnetic field (0, 2 and 4 T) and temperature (1.5-100 K). Under an applied field of $\sim$ 2 T, a phase transition from the zero field SDW structure ($T_N \sim 20$ K) to a commensurate amplitude modulated (AM) structure has been observed. With a further increase in the magnetic field ($\sim$ 4 T), the AM structure transforms into a ferrimagnetic structure. In zero applied field, a magnetic short-range ordering (SRO) coexists with the SDW long-range ordering (LRO) at all temperatures below T_N. In the applied magnetic field (2 and 4 T), the SRO is converted into the LRO only over the temperature range 12 - 20 K, however, below $\sim$ 12 K, an increase in the volume fraction of the SRO has been observed. The correlation length for the SRO (below $\sim$ 12 K) also gets affected by the application of field. The magnetic properties of the compounds $\mathrm{Ca_3Co_{1.8}Fe_{0.2}O_6}$ are very much different from the parent compounds $\mathrm{Ca_3Co_2O_6}$. A field induced transition from the zero field modulated PDA structure to a ferrimagnetic structure in the magnetic field of 1.7 T, and then a transition to a ferromagnetic state in the magnetic field of 3.6 T was reported for the parent compound $\mathrm{Ca_3Co_2O_6}$. However, no transition from the modulated PDA structure to the AM structure (before transition to the ferrimagnetic structure) was reported.

Chapter 6 describes the effect of the rare earth substitution at the $\mathrm{Ca^{2+}}$ ($18e$) site on the magnetic properties of the compounds $\mathrm{Ca_{2.75}}R_{0.25}\mathrm{Co_2O_6}$ (R = Lu and Dy). For both compounds, high temperature (in the paramagnetic region) magnetic susceptibility obeys the Curie-Weiss law. The derived values of the paramagnetic Curie temperature (θ_p) are 28.4 and 16.6 K for R = Lu and Dy compounds, respectively. For the parent compound $\mathrm{Ca_3Co_2O_6}$, the value of θ_p is $\sim$ 30 K. The observed decrease in the value of the θ_p indicates a reduction in the dominant intrachain ferromagnetic interaction with rare earth substitution. In the neutron diffraction patterns, additional Bragg peaks appear for both compounds below $\sim$ 16 K, indicating the onset of an antiferromagnetic ordering of cobalt spin-chains on the triangular lattice. The magnetic Bragg peaks at 1.5 K can be indexed using the incommensurate propagation vector $\boldsymbol{k} = \{0, 0, 1.02\}$. The magnetic structure corresponds to the SDW structure, having c axis as direction of the moment and the modulation. For both compounds, refined value of the maximum moment at the $6b$ site is zero. The refined value of the maximum moment at the $6a$ site is same ($\sim 4.2\ \mu_B$) for both compounds. For the parent compound $Ca_3Co_2O_6$, the reported value of the maximum moment at the $6a$ site is $\sim 5.1\ \mu_B$. For the rare earth doped compounds, the refined zero value of the ordered moment at the OCT site confirms that cobalt ions at the OCT sites remain in the 3+ oxidation state. The observed reduction in the value of the maximum moment at the TP site (with rare earth doping), confirms that the oxidation state of a fraction of the cobalt ions at the TP site is reduced from Co^{3+} to Co^{2+}. The qualitative nature of the observed magnetic ground states for the rare-earth substituted compounds is same as that observed for the Fe-substituted compounds $Ca_3Co_{2-x}Fe_xO_6$ ($x = 0.2$ and 0.4), however, different from that observed for the parent compound $Ca_3Co_2O_6$.

The last chapter (Chapter 7) gives a brief summary of the research work carried out in this thesis. The effects of the intrachain and interchain exchange interactions, and external perturbation on the magnetic ground states of the geometrically frustrated compounds are discussed. A novel time dependence in the intensity of the magnetic reflections has been observed for the compound $Ca_3Co_2O_6$. A possibility to study the effect of an external magnetic field on the observed time dependent magnetic behavior (for $Ca_3Co_2O_6$) is also discussed. The magnetic properties of the compounds (A_3MXO_6 family) studied in the present thesis have been compared with other class of frustrated magnetic systems [ABX_3 (A = Cs or Rb, B = Co, X = Cl or Br)], in terms of the nature of the intrachain magnetic exchange interaction. The present thesis also highlights the scope for the future research work, by growing thin films and large size single crystals (necessary to investigate the anisotropic magnetic and transport properties) of these spin-chain oxides. A list of bibliographic references used in this thesis has been given after Chapter 7. A list of publication is also provided.

List of Figures

List of Tables

Chapter 1

Introduction

Dimensionality of a given system, and symmetry of the order parameter of the system are two crucial parameters, which determinate the universality class of a phase transition. The general belief in the universality is that for a given symmetry of the order parameter and range of interaction (short or long-range), the critical properties of a system depend on its dimensionality. In general, dimensionality of a naturally occurring bulk material is determined by its crystal structure, except for a few cases where the effective dimensionality is reduced. Low dimensional systems can be divided into two groups, (i) one dimensional and (ii) two dimensional. The crystal structure of one dimensional compounds contains infinite chains of atoms with strong ionic/covelant, or metallic intrachain, and negligible interchain bondings. On the other hand, the crystal structure of a two dimensional compound contains sheets or slabs of the atoms or polyhedra, which are separated by a weak bonding. Due to the strong directionally of the structure, the physical properties of the low dimensional compounds are highly anisotropic. For example, the one-dimensional nature of transport properties has been observed in some organic semiconductors [11, 12].

The low dimensional magnetic systems refer to the compounds, in which the magnetic (rare-earths, transition-metals, *etc.*) ions are arranged in less then three dimension, such as, 2D layers, quasi-1D chains, *etc.* Low-dimensional magnetic systems have attracted a lot of interest in the recent years not only because of their anisotropic physical prosperities, but also because they exhibit novel quantum effects, such as high temperature superconductivity, spin-density wave, quantum-phase transitions, fractional quantum Hall effect, magnetic frustration, multiferroicity, *etc.* From a theoretical point of view, low dimensional magnetic systems are interesting because the microscopic interactions between spins can be considerably simplified.

This thesis presents an experimental investigations of the structural and magnetic properties of the quasi-1D spin-chain oxides, $Ca_3Co_2O_6$, $Ca_3Co_{2-x}Fe_xO_6$, and $Ca_{2.75}R_{0.25}Co_2O_6$ (R = Lu and Dy), of the A_3MXO_6-family [A = Ca, Sr and (M, X) = alkali or transition metal ions]. As shown in Fig. 1.1, the magnetic ions in these oxides are arranged in chains parallel to the crystallographic c axis. These chains are arranged on a triangular lattice in the ab plane. A quasi-one-dimensional character in the magnetic properties of these oxides arises primarily because the ferromagnetic intrachain exchange interaction between magnetic ions is much stronger than the antiferromagnetic interchain exchange interaction. These spin-chain oxides yield very rich magnetic phase diagrams because competing interactions and low dimensionality both occur naturally in these systems. As the ferromagnetic intrachain exchange interaction is much stronger than antiferromagnetic interchain interaction, in the first approximation, at low temperatures, one can consider each ferromagnetic chain as a giant moment and the resultant magnetic structure as two dimensional structure. Two dimensional Ising-like model has been developed in the literature to understand the magnetic behavior in one of the most interesting compounds ($Ca_3Co_2O_6$) of the A_3MXO_6-family.

To understand the magnetic behavior of these oxides theoretically, it is very important to find out the model Hamiltonian describing the microscopic interaction between atomic spins and to develop the methods to calculate the static and the dynamic spin-spin correlation functions. Now we will discuss some of the exactly

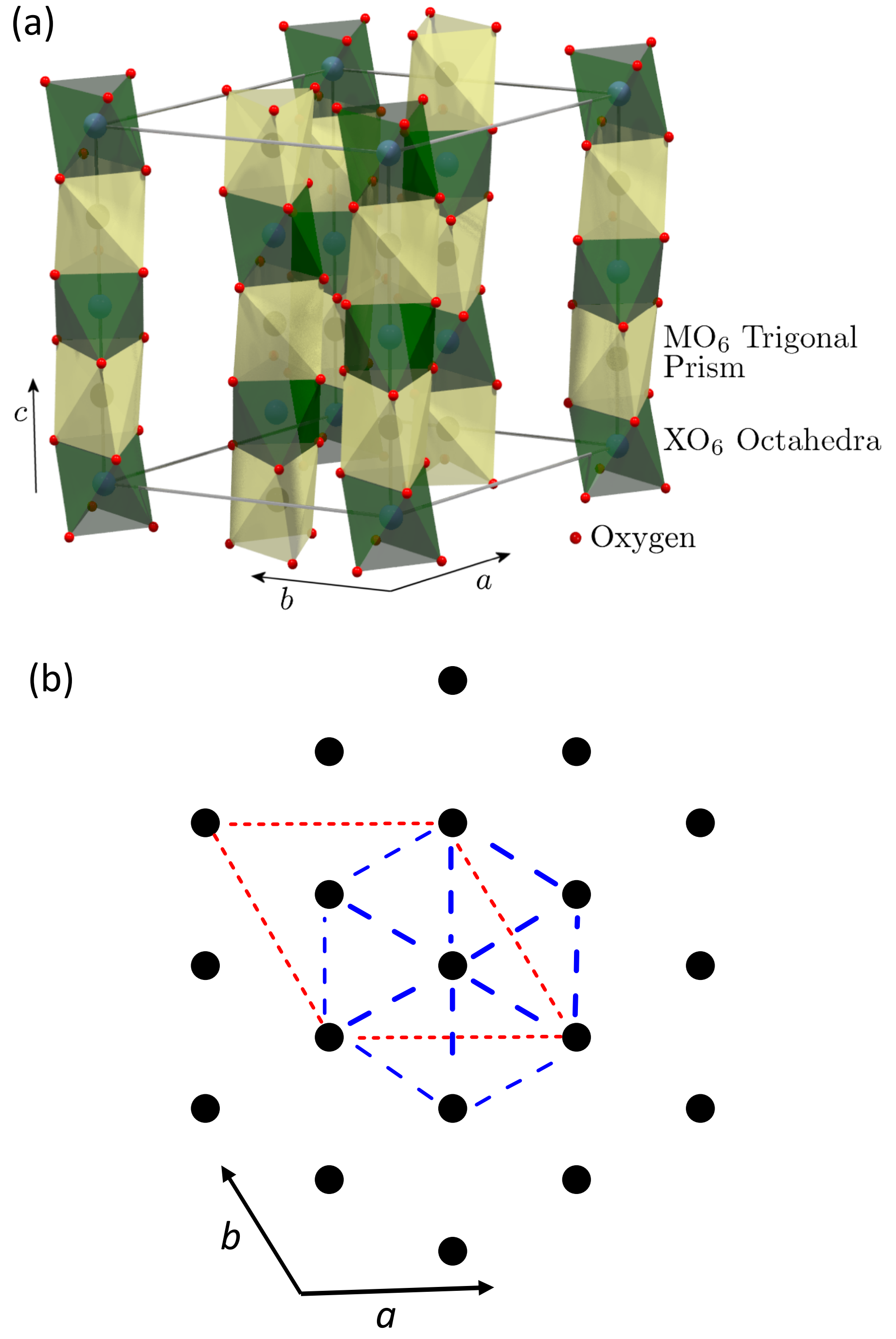

Figure 1.1: (a) Crystal structure of A_3MXO_6-type compounds (for clarity oxygen atoms are shown smaller in size and A atoms are not shown). (b) A projection on the ab plane showing the triangular arrangement of the spin-chains (blue long-dashed lines). The solid (black) circles in Fig. (b) represent the chains and the red short-dashed lines represent the unit cell in the ab plane.

solvable spin models for the low dimensional magnetic systems, which are available in the literature, and are relevant to the types of systems covered in this thesis.

1.1 Spin Models of Magnetism

The model Hamiltonian [13, 14] describing the nearest neighbor spin-spin interactions (due to exchange effects), in the absence of an external magnetic field, is given by,

$$\mathcal{H} = -\sum_{<ij>}[J_x\ S_i^x S_j^x + J_y\ S_i^y S_j^y + J_z\ S_i^z S_j^z)] \ . \tag{1.1}$$

Here J's are the exchange integrals and the summation is over the nearest neighbors. This general Hamiltonian is known as the XYZ model. The values of exchange integrals determine the anisotropy of the exchange interaction. The exchange interactions (i) are isotropic, if $J_x = J_y = J_z$, (ii) have a planar anisotropy if $J_x = J_y$, $J_z = 0$, (iii) have a uniaxial isotropy, if $J_x = J_y = 0$, and $J_z \neq 0$. The cases (i), (ii), and (iii) refer to the Heisenberg, XY, and Ising models, respectively. The summation in Eq. (1.1) can be taken over to a lattice of 1, 2 or 3 dimension. Here it is important to distinguish between magnetic order parameter dimensionality D and the spatial dimensionality (the dimensionality d of the lattice on which the spins reside). The dimensionality of the magnetic order parameters for the Heisenberg, XY, and Ising models are 3, 2, and 1, respectively. However, for each of the models, spins can reside on a lattice of 1, 2, or 3 dimensions, *i.e.*, spatial dimensionality can be 1, 2 or 3.

1.1.1 Ising Model in One Dimension

In the Ising model [13, 15], the spins at every site can have either up or down orientations. The one-dimensional Ising model ($D = 1$, $d = 1$) with nearest neighbor exchange interaction harbors no phase transition (long-range ordering) for $T > 0$. To understand this, we consider a chain of N Ising spins and assume that nearest neighbor interaction is ferromagnetic [$J > 0$]. The Hamiltonian for this system is given by

$$\mathcal{H} = -J \sum_{i=1}^{N-1} S_i^z S_{i+1}^z \quad . \tag{1.2}$$

Here spin $S_i = \pm 1$ and J is exchange constant. The ground state ($T = 0$) of this system corresponds to a state in which all spins are aligned either up or down [Fig. 1.2 (a)]. At $T = 0$, the energy of the system is minimum with $E = -(N-1)J$, and the entropy $S = 0$. The elementary excitation in the one dimensional Ising spin-chain is a domain wall [Fig. 1.2 (b)]. The creation of a domain wall costs an extra energy $E = 2\ J$. Because there are (N-1) sites where the domain wall can

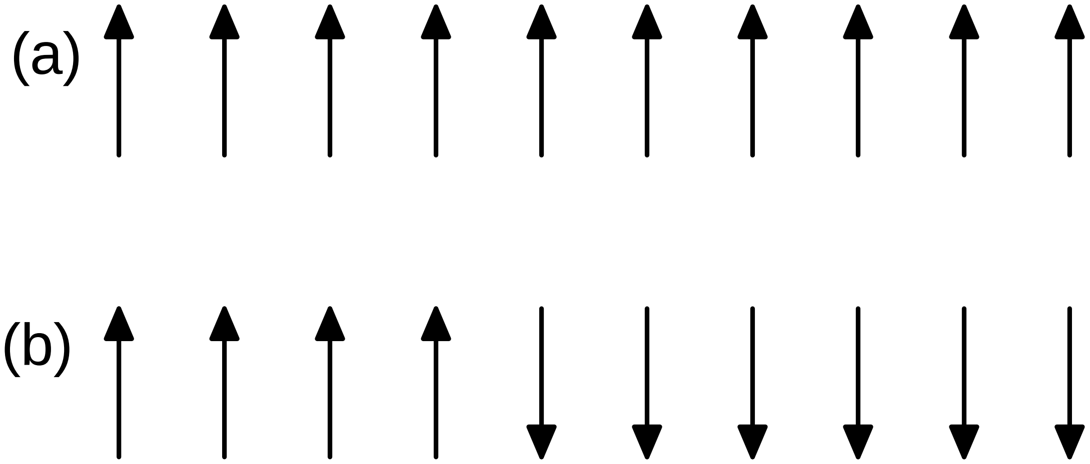

Figure 1.2: The one-dimensional ferromagnetic Ising spin-chain. (a) All spins aligned up. (b) A domain wall for a system of $N = 10$ spins.

move with no cost in energy, the entropy increases by $\triangle S = k_B$ ln(N-1). Hence, the free energy ($F = E$ - T S) cost to create such a domain wall is

$$\triangle\ F = 2J - k_B T\ ln(N-1)\ . \tag{1.3}$$

It is evident from Eq. (1.3) that for $T > 0$, as the size of the system grows ($N \rightarrow \infty$), the creation of a domain wall lowers the free energy. Hence, number of domain walls will increase, resulting in a complete randomization of the spins. The long-range magnetic ordering is therefore not possible at finite temperature in the one-dimensional Ising model.

1.1.2 Ising Model in Two Dimension

In Sec. 1.1.1 we discussed that one-dimensional Ising model does not have phase transition at finite temperature. Now we discuss what happens if the Ising spins are put on the two-dimensional lattice (d = 2), this corresponds to the $2d$-Ising model (for simplicity, we consider square lattice [16]). The defects in this case are domain walls (see Fig. 1.3). As the domain wall can be placed at any of the L columns, the entropy gain by creating such a domain wall is $k_B T$ ln L. The energy cost of creating the domain wall is $2JL$. So the change in the free energy by the creation of such a domain wall is

$$\triangle\ F = 2JL - T\ ln(L)\ . \tag{1.4}$$

It is clear from Eq. (1.4) that $\triangle\ F > 0$ in the limit $L \rightarrow \infty$. Therefore, domain walls cannot be spontaneously created in two dimension and the long-range magnetic ordering is possible below a finite non-zero critical temperature. An Ising model on square lattice was exactly solved by Onsager [17] in 1944. He predicted a long-range magnetic ordering at finite non-zero temperature.

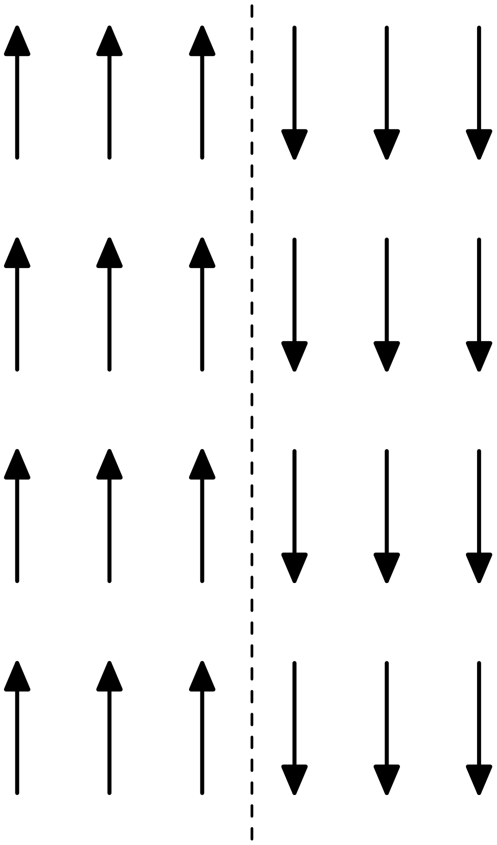

Figure 1.3: Domain wall (dashed line) in the two-dimensional Ising model on the square lattice.

1.1.3 Two-Dimensional Magnetism

An isotropic Heisenberg model in one and two dimensions do not predict a long-range magnetic order at any finite temperature. Destruction of the order at any non-zero temperature can be understood as a consequence of proliferation of spin-waves, which destroys the long-range order. The absence of a long-range order in the two-dimensional systems (with a continuous symmetry) was first proved by Mermin and Wagner [18, 19] in 1966. This predication is often referred as the Mermin-Wagner theorem, which (for the system of localized spins) is quoted as “An infinite d dimensional lattice of localized spins cannot have long-range order at any finite temperature for $d < 3$ if the effective exchange interactions among spins are isotropic in spin space and of finite range". A description of the current theories used to describe the low-dimensional magnetism can be found in Ref.[20].

Now we will discuss the exotic properties of the naturally occurring low dimensional magnetic materials, which have been experimentally observed.

1.2 Exotic Properties of One-dimensional Magnets

The Heisenberg, XY, and Ising models mentioned in Sec. 1.1 do not predict any long-range magnetic order in one-dimension (d = 1) at any finite temperature. This may lead one to think that these one-dimensional magnets are not interesting, but in reality the reverse is true. There exists today an impressive list of quasi-one-dimensional magnets having noncollinear, incommensurate long-range magnetic ordering at low temperatures. Moreover, these magnets have complex magnetic excitations, which are not fully understood.

The one-dimensional spin-chain compounds refer to the systems, in which the spins (Heisenberg, XY, and Ising) are arranged on a line. In a real system, whether spin behaves like Ising, XY, or Heisenberg will depend on the single ion anisotropy due to the crystalline electric field. Despite its relatively simple geometry, one-dimensional spin-chain models are hard to realize experimentally because of the presence of a finite interchain interaction. The weak interchain interaction often couples the spin-chains at very low temperatures, and a three dimensional long-range magnetic ordering develops in the real systems. The most extensively studied Ising and Heisenebrg spin-chain compounds are $CsCoCl_3$ [21, 22] and $KCuF_3$ [23], respectively. In the compound $KCuF_3$, the spin-chains contain magnetic Cu^{2+} (S = 1/2) ions. The values of the antiferromagnetic intrachain and ferromagnetic interchain exchange constants are -394.5 and 18.6 K, respectively [23]. In spite of the very small value of the interchain interaction, 3D magnetic ordering has been observed in the compound $KCuF_3$ below the Néel temperature T_N of 39 K. In the one-dimensional Ising spin-chain system $CsCoCl_3$, the spin-chains contain Co^{2+} ($3d^7$) ions with an effective spin $S = 1/2$ [21, 22]. Because of interchain exchange interactions, the 3D long-range ordering occurs in this compound below 21 K.

Other than the issue that these spin-chain compounds order magnetically or not, a considerable amount of interest was generated over the past three decades, after Haldane's conjecture [24, 25] that the one-dimensional (1D) Heisenberg antiferromagnets have different physical properties for integer and non-integer values of the spins. In the former case, the ground state is separated from the excited state by an energy gap while the latter does not show any energy gap. Before Haldane's conjecture, it was believed that the properties of Bethe ansatz solution [26] for the spin-1/2 Heisenberg chain, which has a gapless excitation spectrum and an infinite correlation length, are valid for an arbitrary spin. Haldane's conjecture has been tested on several compounds [27–29]. We will not discuss in detail the spin-wave excitation of one-dimensional (1D) Heisenberg antiferromagnets because the present thesis deals only with the magnetic structure.

Now we will discuss about the systems in which both competing interactions and low dimensionality occur naturally. The presence of competing (frustrated) interactions in the low dimensional magnets gives rise to a variety of interesting phenomena, ranging from evading the Néel order to the frustration induced long-range magnetic order at finite temperature.

1.3 Frustrated Magnets

A magnet is called frustrated if it has got competing exchange interactions which can't be satisfied simultaneously. If these competing interactions arise due to arrangement of the spins in lattice, not due to the site disorder then the magnet is called a geometrically frustrated magnet. Geometrically frustrated magnets exhibit

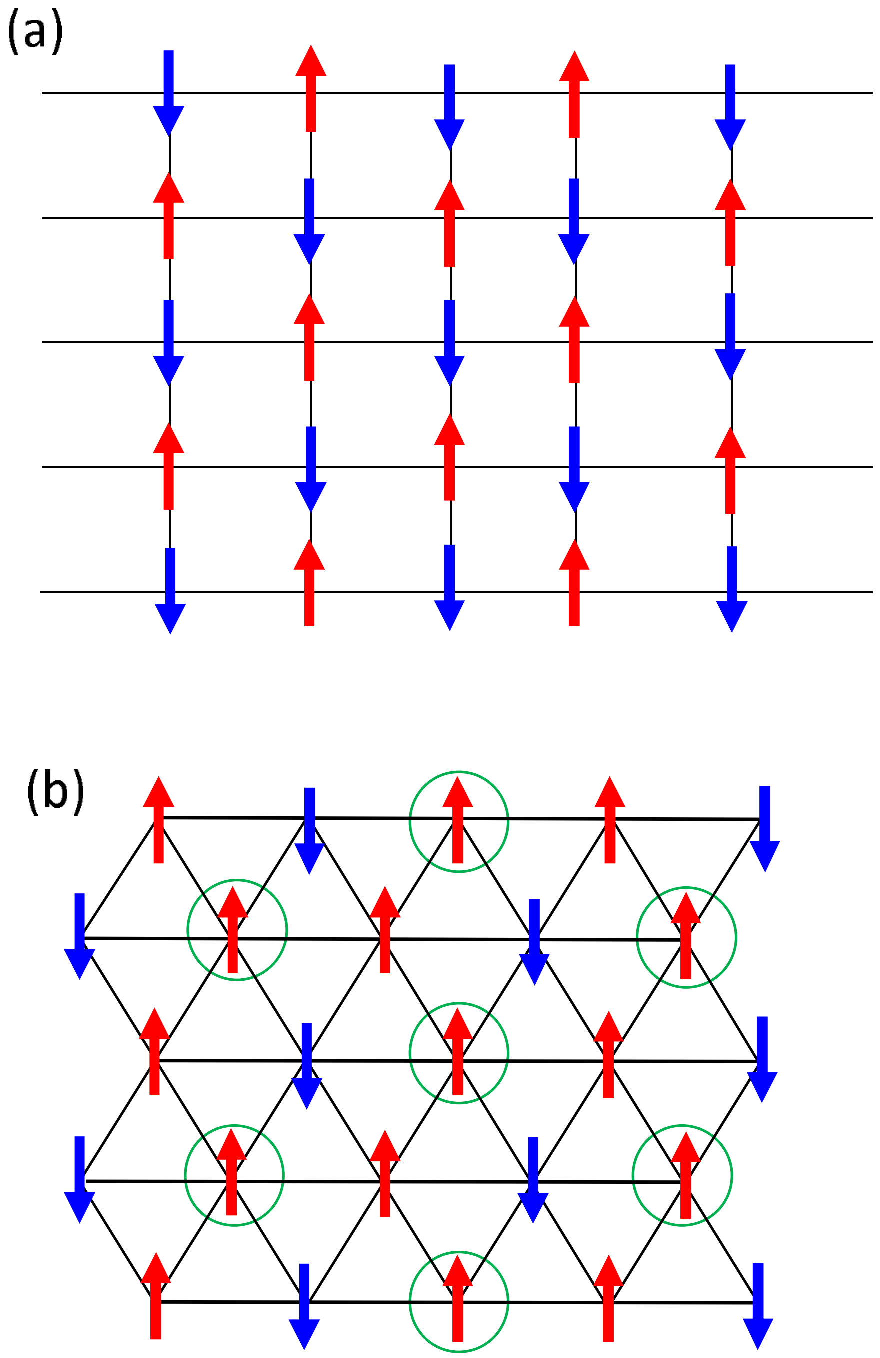

Figure 1.4: A geometrically frustrated antiferromagnet with Ising spins on the two-dimensional (a) square lattice and (b) triangular lattice. The arrows indicate the direction of the spin. The circles in Fig.(b) represent the flippable spins (reproduced from Ref. [1]).

exotic phenomena compared to their unfrustrated counterparts. To have a comparison, let us discuss the behavior of an unfrustrated antiferromagnet. We consider Ising spins on a square lattice with antiferromagnetic nearest neighbor interactions.

Since, the lattice is bipartite, the classical ground state is the two-sublattice Néel state, with all spins up on one sublattice and down on the other sublattice. The ground state is doubly degenerate and minimizes all the interactions simultaneously, as shown in Fig. 1.4 (a). On the other hand, if one considers three Ising spins on a equilateral triangle with nearest-neighbor antiferromagnetic interactions, when two spins are anti-parallel, third spin can have either orientation (up or down), because no exchange field acts on it. As a result, all the interaction bonds cannot be satisfied simultaneously and the system is frustrated. This kind of geometrical frustration on the triangular lattice gives rise to ground state degeneracy. For the triangular lattice with Ising spins, the ground state condition is that one of the three bonds should be frustrated. As a result, instead of ground state being doubly degenerate, which one expects from the discrete symmetry of the Ising spins (up and down), the real ground state is six fold degenerate. If an infinite crystal is made from such a triangular plaquette of the Ising spins, then the ground state has very large degeneracy. This is shown in Fig 1.4 (b), where in some particular configuration 1/3 of spins point up, 1/3 of spins point down, and the remaining 1/3 point either up or down because of net zero exchange field acting on them. The ground state entropy of this antiferromagnet is extensive because at least 1/3 of the spins (which point either up or down) can be chosen in a number of ways. Wannier [30] in 1950 showed that ground-state entropy of two-dimensional triangular lattice antiferromagnet of Ising spins is extensive and approximately 0.323 $\mathrm{k}_B N$, here N is the number of spins and k_B is Boltzmann constant.

The presence of geometrical frustration often leads to a complicated magnetic structure at very low temperatures, wherein the spins and their frustrated interactions reach a compromise with the geometry of the crystal lattice. In some cases, the presence of the frustration can even suppress the long-range magnetic ordering temperature. Due to the large ground state degeneracy, the nature of magnetic ordering in the frustrated magnets is highly sensitive to the perturbation, and a small perturbation (spin-lattice interaction, thermal fluctuation, magnetic field, etc.) can give rise to the exotic magnetic states in these systems.

From the real materials point of view, the non-bipartite geometrically frustrated lattices in the two dimension are triangular and kagomé; and three-dimensional analogues are pyrocholore (built from corner sharing tetrahedra) and face-centered cubic (FCC), as shown in Fig. 1.5.

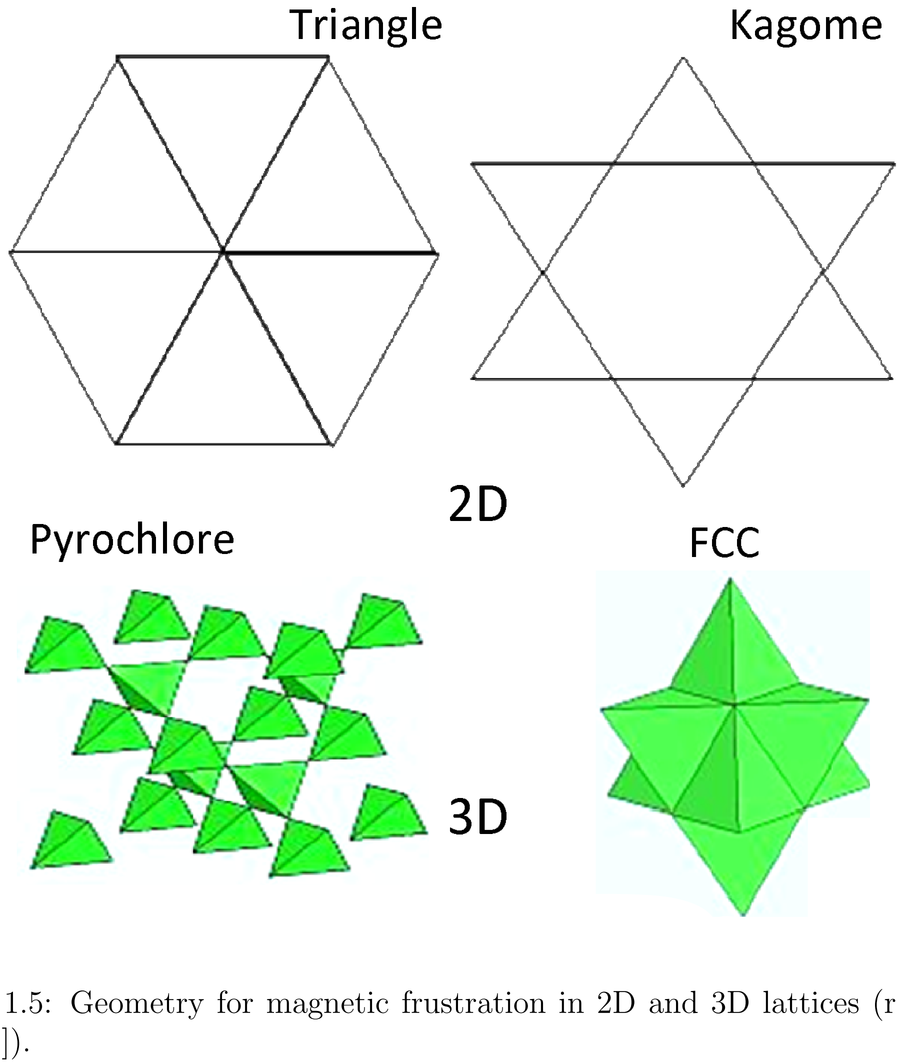

Figure 1.5: Geometry for magnetic frustration in 2D and 3D lattices (reproduced from [2]).

1.4 Motivation

In the present thesis work, we have investigated the compounds, where the 1D Ising spin chains are arranged on a triangular lattice and the exchange interactions between the chains are antiferromagnetic. In literature, there are a few examples where the 1D Ising spin chains are arranged on a triangular lattice. The most of the compounds belong to either $A_3MX\mathrm{O}_6$ family (considered in the present thesis work) or $A'BX_3$ (where A' is an alkali ion, B is a transition metal ion, and X is a halide ion) [31–33] family.

The compound $\mathrm{CsCoCl_3}$ [31, 32] is one of the well studied 1D Ising spin chain compounds in the $A'BX_3$ family. The results of the most of theoretical models [31, 33] for the $A'BX_3$ compounds predict a partially disordered antiferromagnetic (PDA) structure [for this structure 2/3 of Ising spin-chains (with ferromagnetic intrachain coupling) order with antiferromagnetic interchain interaction while the remaining 1/3 are left incoherent (disordered with zero net magnetization)] at higher temperature, and a ferrimagnetic structure at lower temperature (e.g., below 9 K for the compound $\mathrm{CsCoCl_3}$). The crystal structure of the compound $\mathrm{CsCoCl_3}$ consists of chains of $\mathrm{Co^{2+}}$ ions with effective spin $S = 1/2$, arranged on a triangular lattice, running along the crystallographic c axis. Both the intrachain and interchain interactions in this compound are antiferromagnetic. However, the strength of the intrachain exchange interaction is much stronger than that of the interchain exchange interaction. This compound undergoes two successive magnetic phase transitions; one at 21 K and other at 9K. In the temperature range between 9 and 21 K, the PDA state and below 9 K, a ferrimagnetic state have been reported [32].

Among the $A_3MX\mathrm{O}_6$-type spin-chain compounds, the most interesting compound is $\mathrm{Ca_3Co_2O_6}$. The compound $\mathrm{Ca_3Co_2O_6}$ is a model system for the triangular lattice Ising antiferromagnet. The interchain interactions in this compound are antiferromagnetic, however, the intrachain interactions are ferromagnetic, unlike $CsCoCl_3$, where both intrachain and interchain interactions are antiferromagnetic.

Due to the interelation between the spin and orbital degrees of freedom, these cobaltates are very sensitive to the doping levels and external perturbation. Moreover, the cobalt ions in these compounds have one more degree of freedom, a possibility of the spin state transition, other than the common charge, orbital, and spin degrees of freedom. Understanding the behavior of these complex cobaltates requires a detailed experimental investigation of the magnetic structures. The unusual magnetic properties of these frustrated magnets allow them to serve as a model system for many strongly correlated systems.

1.5 Outline of this Thesis

In the present thesis, we have studied the triangular lattice Ising antiferromagnet of A_3MXO_6-family [A = Ca, Sr, and (M, X) = transition metal or alkali ions]. The crystal structure of these compounds consists of chains, made up of alternating face-sharing MO_6 trigonal prisms (TP) and XO_6 octahedra (OCT) running along the crystallographic c axis. These chains, separated by non-magnetic A^{2+} ions, are arranged on a triangular lattice in the ab plane and each chain is surrounded by six chains. The ferromagnetic intrachain and antiferromagnetic interchain interactions, combined with a triangular arrangement of spin-chains give rise to a geometrical frustration in these compounds.

In this thesis, we present the structural and magnetic properties of the compounds $Ca_3Co_2O_6$, $Ca_3Co_{2-x}Fe_xO_6$ (x = 0.1, 0.2, 0.4, and 1.0), and $Ca_{2.75}R_{0.25}Co_2O_6$ (R = Lu and Dy). In the compound $Ca_3Co_2O_6$, spin-chains are made up of alternating face sharing CoO_6 octahedra (with Co1) and CoO_6 trigonal prisms (with Co2) with a Co-Co separation of $\sim$ 2.6 Å (along the chain). The different crystalline electric fields at the OCT and TP sites lead to the different spin states of the Co^{3+} ions in this compound; low spin ($S = 0$) and high spin ($S = 2$) states at the OCT($6b$) and TP($6a$) sites, respectively. The Co^{3+} spins at the TP sites have an Ising-like magnetic anisotropy and are aligned along the crystallographic c axis. The choice of the iron substitution at the cobalt site was motivated by the consideration that the Co^{3+} ions at the TP site, in the compound $Ca_3Co_2O_6$, have large orbital moment (1.7 μ_B), while the Fe^{3+} ions have zero orbital momentum (a closed subshell without orbital degrees of freedom). Moreover, the ionic radii of the Co^{3+} and Fe^{3+} with six oxygen coordination are very close (0.61 and 0.645 Å, respectively). No strong lattice effect will, therefore, be introduced, and changes only due to the different magnetic character of the spins of Co^{3+} and Fe^{3+} are expected. The magnetism of these Fe-substituted compounds is unique in the sense that spin chains are made up of different type of spins: Fe^{3+} (Heisenberg) and Co^{3+} (Ising). The choice of rare earth (R^{3+}) doping at the Ca^{2+} site is motivated by the theoretical prediction from the band structure calculations that magnetic properties for the compound $Ca_3Co_2O_6$ can be tuned by electron doping. The difference in the ionic radii of the rare earth (R^{3+}) and the calcium (Ca^{2+}) may change the distance between magnetic ions. The difference in the oxidation state of the R^{3+} and Ca^{2+} is expected to vary the oxidation state of Co^{3+} in the compound $Ca_3Co_2O_6$. These factors can change the intrachain and interchain magnetic exchange interactions, which can modify the magnetic properties of these spin-chain compounds. The organization of this thesis goes as follows:

After giving an overall introduction in Chapter 1, Chapter 2 gives a brief description about the sample preparation techniques that are employed to synthesize the polycrystalline compounds studied in the thesis. A brief introduction and working principles of the various experimental techniques (x-ray diffraction, neutron diffraction, dc magnetization, and Mössbauer spectroscopy) employed to investigate the structural and magnetic properties of the compounds are also described. A brief description about the Rietveld method, employed to refine the crystal structures and to determine the magnetic structures from the powder diffraction data, is also given.

Chapter 3 presents the structural properties of the compounds $Ca_3Co_2O_6$, $Ca_3Co_{2-x}Fe_xO_6$ (x = 0.1, 0.2, 0.4, and 1.0), and $Ca_{2.75}R_{0.25}Co_2O_6$ (R = Lu and Dy). The Rietveld refinement of x-ray and neutron diffraction patterns confirms that all compounds, except Ca_3CoFeO_6, crystallize in the rhombohedral structure (space group $R\bar{3}c$). For the compounds $Ca_3Co_{2-x}Fe_xO_6$ (x = 0.1, 0.2, and 0.4), the Rietveld refinement of neutron diffraction patterns and Mössbauer study confirm that the Fe^{3+} ions are located only at the TP site. For the rare earth substituted compounds $Ca_{2.75}R_{0.25}Co_2O_6$ (R = Lu and Dy), the refinement shows that the trivalent rare earth ions R^{3+} are located at the Ca^{2+} ($18e$) site, and bond lengths Co2-O and Co1-Co2 increase significantly, as compared to the parent compound $Ca_3Co_2O_6$. The observed increase in the bond lengths Co2-O, with rare earth substitution, suggests that extra electrons are transferred to the Co2 ions at the TP site. The crystal structure of all the compounds, except for Ca_3CoFeO_6, contains one-dimensional chains made up of alternating face-sharing CoO_6 octahedra and $(Co/Fe)O_6$ trigonal prisms, running along the crystallographic c axis. For the compound Ca_3CoFeO_6, the profile matching refinement of the x-ray diffraction pattern confirms a triclinic crystal structure (space group $P\bar{1}$).

Chapter 4 is divided into two parts. The first part of this chapter describes the magnetic structure of the compounds $Ca_3Co_2O_6$ and $Ca_3Co_{2-x}Fe_xO_6$ (x = 0.2 and 0.4). In the first approximation, it is shown in this Chapter that two different commensurate magnetic structures, (i) amplitude-modulated structure with a propagation vector $\boldsymbol{k} = \{0,\ 0,\ 1\}$ and (ii) partially disordered antiferromagnetic (PDA) structure, are able to fit the same neutron diffraction patterns, below their respective Néel temperatures (T_N = 25, 20, and 17 K, for x = 0, 0.2, and 0.4 compounds, respectively). However, our detailed analysis reveals that these compounds order magnetically in an incommensurate spin density wave (SDW) structure, having a modulation and an alignment of the spins along the crystallographic c axis, below T_N. Further, a coexistence of the magnetic long-range and short-range ordering has been observed down to 1.5 K (below T_N). For the parent compound $Ca_3Co_2O_6$, in addition to the magnetic Bragg peaks corresponding to the SDW structure, a second set of magnetic peaks corresponding to the commensurate antiferromagnetic (CAFM) structure with a propagation vector $\boldsymbol{k}_2 = \{0.5,\ 0.5,\ 0\}$ appears in the neutron diffraction patterns below ~ 15 K. Moreover, the magnetic Bragg peaks, corresponding to the CAFM and SDW structures, exhibit time dependence below ~ 14 K. Our analysis (for the parent compound $Ca_3Co_2O_6$) shows that the magnetic ground state is a coherent superposition of the magnetic structures belonging to the propagation vectors $\boldsymbol{k}_1 = \{0,\ 0,\ 1.009(3)\}$ and $\boldsymbol{k}_2 = \{0.5,\ 0.5,\ 0\}$.

The second part of this Chapter describes Mössbauer spectroscopy studies of spin-spin relaxation in the compounds $Ca_3Co_{2-x}Fe_xO_6$ (x = 0.2 and 0.4), and nature of magnetic ordering in Ca_3CoFeO_6. The compounds with $x \leq 0.4$ are paramagnetic above ~ 90 K, and the iron exhibits slow spin relaxation phenomena even at room temperature. However, for the compound Ca_3CoFeO_6,which crystallizes in the triclinic space group $P\bar{1}$, the iron resides almost equally in two different crystallographic sites and exhibits a very high magnetic ordering temperature $T_N \sim$ 500 K. Both iron sites exhibit quadrupole interactions of almost equal magnitude; however, with an opposite sign. These results agree well with the magnetic susceptibility measurements, in which a sharp drop in magnetization is observed above 200 K. The net magnetic interaction is antiferromagnetic, however, with a small ferromagnetic component displaying hysteresis along with a saturation magnetization of about 0.02 μ_B/f.u. at 1.5 K.

Chapter 5 describes the effect of an external perturbation viz. magnetic field on the nature of magnetic ordering in the compounds $Ca_3Co_{2-x}Fe_xO_6$ (x = 0, 0.1, 0.2, and 0.4). For all compounds, high temperature magnetic susceptibility obeys the Curie-Weiss law. The value of paramagnetic Curie temperature decreases as the concentration of iron increases (θ_p = 27.8 for x = 0 compound) and it becomes negative (-1.6 K for x = 0.4) for higher concentration of iron. From the dc-magnetization study, we have derived the value of intrachain and interchain exchange interactions for the compounds $Ca_3Co_{2-x}Fe_xO_6$ (x = 0.0, 0.1, 0.2, and 0.4). A decrease in the intrachain positive exchange constant J' and an increase in the interchain negative exchange constant J have been observed with substitution of iron, which result in deviation from “1D character” in these spin-chain compounds. In the dc magnetization study, we have observed an indication of the presence of a field induced transition from a ferri to a ferromagnetic-like state. Neutron diffraction study has been carried out to study the spin-spin correlations in the compound $Ca_3Co_{1.8}Fe_{0.2}O_6$, by directly investigating the evolution of the magnetic structures as a function of applied magnetic field (0, 2, and 4 T) and temperature (1.5 -100 K). Under an applied field of $\sim$ 2 T, a phase transition from the zero field SDW structure ($T_N \sim$ 20 K) to a commensurate amplitude modulated (AM) structure has been observed. With a further increase in the magnetic field ($\sim$ 4 T), the AM structure transforms into a ferrimagnetic structure. In zero applied field, a magnetic short-range ordering (SRO) coexists with the SDW long-range ordering (LRO) at all temperatures below T_N. In the applied magnetic field (2 and 4 T), the SRO is converted into the LRO only over the temperature range 12 - 20 K, however, below $\sim$ 12 K, an increase in the volume fraction of the SRO has been observed. The correlation length for the SRO (below $\sim$ 12 K) also gets affected by the application of field. The magnetic properties of the compound $Ca_3Co_{1.8}Fe_{0.2}O_6$ are very much different from the parent compound $Ca_3Co_2O_6$. A field induced transition from the zero field modulated PDA structure to a ferrimagnetic structure in the magnetic field of 1.7 T, and then a transition to a ferromagnetic state in the magnetic field of 3.6 T were reported for the parent compound $Ca_3Co_2O_6$. However, no transition from the modulated PDA structure to the AM structure (before transition to the ferrimagnetic structure) was reported.

Chapter 6 describes the effect of the rare earth substitution at the Ca^{2+} ($18e$) site on the magnetic properties of the compounds $Ca_{2.75}R_{0.25}Co_2O_6$ (R = Lu and Dy). For both compounds, high temperature (in the paramagnetic region) magnetic susceptibility obeys the Curie-Weiss law. The derived values of the paramagnetic Curie temperature (θ_p) are 28.4 and 16.6 K for R = Lu and Dy compounds, respectively. For the parent compound $Ca_3Co_2O_6$, the value of θ_p is $\sim$ 30 K. The observed decrease in the value of the θ_p indicates a reduction in the dominant intrachain ferromagnetic interaction with rare earth substitution. In the neutron diffraction patterns, additional Bragg peaks appear for both compounds below $\sim$ 16 K, indicating the onset of an antiferromagnetic ordering of cobalt spin-chains on the triangular lattice. The magnetic Bragg peaks at 1.5 K can be indexed using the incommensurate propagation vector $\boldsymbol{k} = \{0, 0, 1.02\}$. The magnetic structure corresponds to the SDW structure, having c axis as directions of both moment and modulation. For both compounds, refined values of the maximum moment at the $18e$ (the site at which rare-earth ions are located) and $6b$ sites are zero. The refined values of the maximum moment at the $6a$ site are same ($\sim$ 4.2 μ_B) for both compounds. For the parent compound $Ca_3Co_2O_6$, the reported value of the maximum moment at the $6a$ site is $\sim 5.1\ \mu_B$. For the rare earth doped compounds, the refined zero value of the ordered moment at the OCT site confirms that cobalt ions at the OCT sites remain in the 3+ oxidation state. The observed reduction in the value of the maximum moment at the TP site (with rare earth doping), confirms that the oxidation state of a fraction of the cobalt ions at the TP site is reduced from Co^{3+} to Co^{2+}. The qualitative nature of the observed magnetic ground states for the rare-earth substituted compounds is same as that observed for the Fe-substituted compounds $Ca_3Co_{2-x}Fe_xO_6$ ($x = 0.2$ and 0.4), however, different from that observed for the parent compound $Ca_3Co_2O_6$.

The last chapter (Chapter 7) gives a brief summary of the research work carried out in this thesis. The effects of the intrachain and interchain exchange interactions, and external perturbation on the magnetic ground states of the geometrically frustrated compounds are discussed. A novel time dependence in the intensity of the magnetic reflections has been observed for the compound $Ca_3Co_2O_6$. A possibility to study the effect of an external magnetic field on the observed time dependent magnetic behavior (for $Ca_3Co_2O_6$) is also discussed. The magnetic properties of the compounds (A_3MXO_6 family) studied in the present thesis have been compared with other class of frustrated magnetic systems [ABX_3 (A = Cs or Rb, B = Co, X = Cl or Br)], in terms of the nature of the intrachain magnetic exchange interaction. The present thesis also highlights the scope for future research work, by growing thin films and large size single crystals (necessary to investigate the anisotropic magnetic and transport properties) of these spin-chain oxides. A list of bibliographic references used in this thesis has been given after Chapter 7. A list of publication is also provided.

CHAPTER 2

Sample Preparation and Experimental Techniques

This chapter discusses sample preparation method, the principles of the experimental techniques, and computational techniques, employed to investigate the structural and magnetic properties of the spin-chain oxides. After a brief discussion on the sample preparation techniques, x-ray and neutron diffraction techniques are described in more detail, followed by magnetic neutron diffraction technique. Subsequently, a brief description of the dc magnetization and Mössbauer spectroscopy techniques is given. At the end of the chapter, the Rietveld method, to refine the crystal structures and to determine the magnetic structures from the powder diffraction data, is discussed.

2.1 Sample Preparation

All the experiments in the present thesis work have been performed on the polycrystalline samples. The solid state reaction method has been used to synthesize the polycrystalline compounds. The standard solid state reaction method involves mechanically mixing of the constituent metal oxides or carbonates followed by repeated cycles of grinding and heating at high temperatures. The solid state reaction method requires ions to have diffusion across the solid interfaces, which is a very slow process. Therefore, the typical reaction time in a solid state reaction ranges from few days to few weeks, and high temperatures (>800°C) are required to overcome the diffusion barrier. Polycrystalline compounds $Ca_3Co_2O_6$, $Ca_3Co_{2-x}Fe_xO_6$

(x = 0.1, 0.2, 0.4, and 1.0), $\mathrm{Ca}_{2.75}R_{0.25}\mathrm{Co}_2\mathrm{O}_6$($R$ = Lu and Dy)] were made using the following steps. The flow chart is given in Fig. 2.1.

Step 1: The stoichiometric amounts of high purity (>99.9%) reagents [CaO, $\mathrm{Co}_3\mathrm{O}_4$, and $\mathrm{Fe}_2\mathrm{O}_3$, for the compounds $\mathrm{Ca}_3\mathrm{Co}_{2-x}\mathrm{Fe}_x\mathrm{O}_6$; CaCo_3, $\mathrm{Dy}_2\mathrm{O}_3$ or $\mathrm{Lu}_2\mathrm{O}_3$, and CoO for the compounds $\mathrm{Ca}_{2.75}R_{0.25}\mathrm{Co}_2\mathrm{O}_6$] were intimately mixed using an agate mortar and pestle.

Step 2: These powders were calcined at 800 °C for 24 h and then pressed into pellets of diameter $\Phi = 16$ mm using the hydraulic pressure of $\sim$ 2 ton/cm^2.

Step 3: The pellets were placed in a platinum boat, and heated in air up to 1000 °C (at a heating rate of 300 °C/h), and then kept at 1000 °C for 72 h, and then cooled down to room temperature slowly (at a cooling rate of 100 °C/h).

Step 4: The pellets were crushed to fine powder using an agate mortar and pestle, and then pressed into pellets of diameter $\Phi = 16$ mm using the hydraulic pressure of $\sim$ 5 ton/cm^2. Step 5: The pellets were again placed in a platinum boat, and heated in air up to 1000 °C (at a heating rate of 300 °C/h), and then kept at 1000 °C for 72 h, and then cooled down to room temperature slowly (at a cooling rate of 100 °C/h).

Step 6: The phase purity of the sample was checked by x-ray diffraction with a Cu K_α radiation. The scattering angle (2θ) range of 10 °C to 90 °C was scanned (step size = 0.02 °C). For all compounds (except for $\mathrm{Ca}_3\mathrm{CoFeO}_6$), the observed x-ray reflections could be indexed using the space group $R\bar{3}c$. The observed x-ray reflections for the compound $\mathrm{Ca}_3\mathrm{CoFeO}_6$ could be indexed using the space group $P\bar{1}$.

2.2 Scattering Techniques

An integral part of the phase identification of a crystalline material is a scattering experiment. In a typical scattering experiment, as shown in Fig. 2.2, an incident ra-

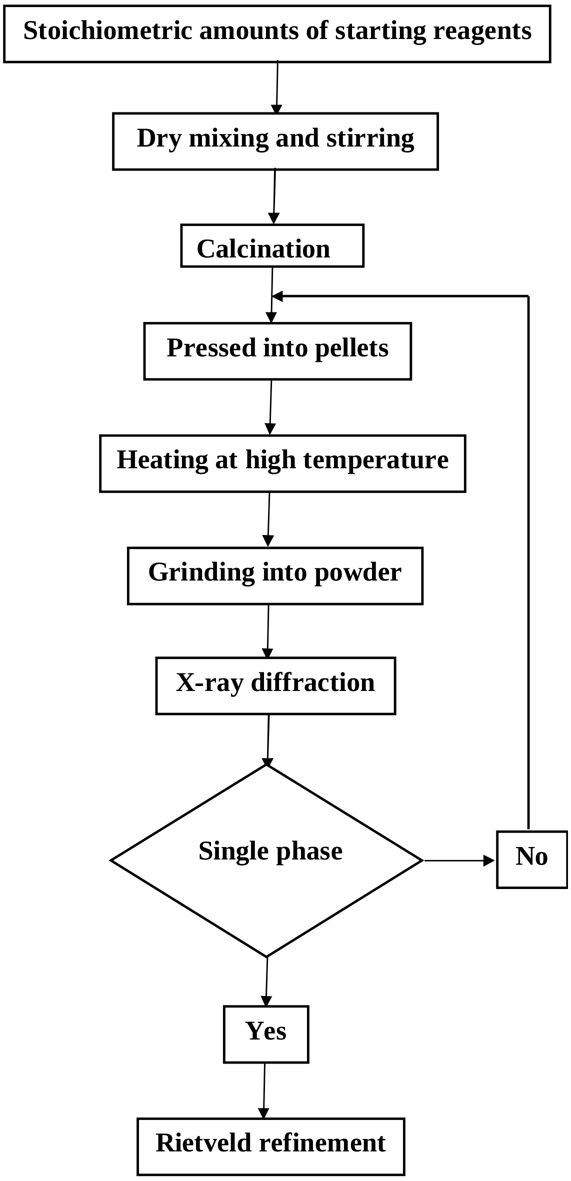

Figure 2.1: Flow chart for the preparation of oxide compounds by the solid-state reaction method.

diation of energy E_i and wave-vector $\boldsymbol{k}_i$ is scattered by the sample into a radiation of energy E_f and wave-vector $\boldsymbol{k}_f$. In the case of elastic scattering $|\boldsymbol{k}_f|$ =$|\boldsymbol{k}_i|$, $E_i = E_f$, and the important parameter to analyze the elastic scattering is momentum transfer or scattering vector $\boldsymbol{Q} = \boldsymbol{k}_f$ -$\boldsymbol{k}_i$, whose magnitude is defined by Q =$(4\pi/\lambda)\sin\theta$.

The simplest scattering experiment, which provides the information about the crystal structure, is Bragg scattering of the incident radiation from the lattice planes. When the wavelength of the incident radiation is comparable to the interatomic spacing, one can find diffracted beams in directions quite different from the incident radiation. By measuring the intensity of the diffracted radiation as a function of the magnitude of the scattering vector ($\boldsymbol{Q}$), one obtains the information about the crystal structure. Now we will discuss Bragg's law, which tells the geometrical conditions for the diffraction from a crystal.

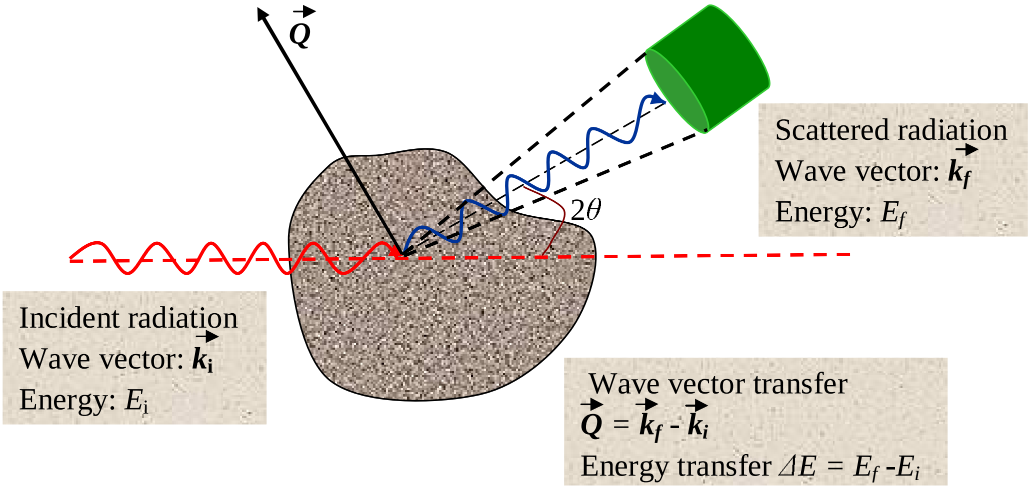

Figure 2.2: Schematic diagram of the scattering geometry (reproduced from Ref. [3]).

2.3 Bragg Formulation for the Diffraction from a Crystal

Bragg considered x-ray diffraction form the crystals as a problem of reflection from the atomic planes. He established that the scattering centres which reflect the x-rays can be represented by a set of parallel planes.The peaks in diffraction pattern appear if the x-rays scattered from the successive planes, are in "phase". In other words, the difference in the path length of the waves scattered from the successive planes must be an integral multiple of the wavelength. For the beams labelled 1 and 2 in Fig. 2.3, the path difference is $2d\ sin\theta$, which should be an integral multiple of the wavelength, *i.e.*

$$2d\ sin\theta = n\lambda\ . \tag{2.1}$$

Eq. (2.1) is Bragg's law, which establishes the relation among the lattice spacing (d), the wavelength of radiation (λ), and the diffraction angle (2θ). The radiations that are usually employed for the diffraction are electron, neutron, and x-ray. Now we will discuss the x-ray and the neutron diffraction in detail, because these radiations have been used for the structural characterization in the present thesis work.

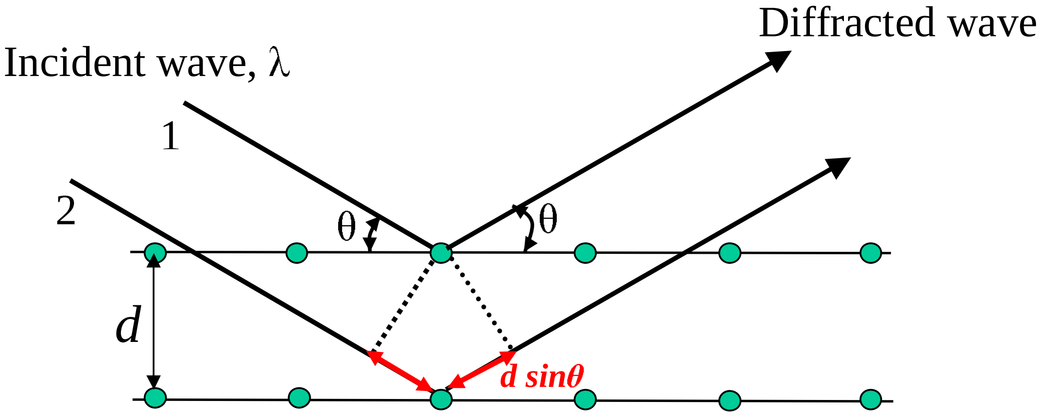

Figure 2.3: Pictorial representration of the Bragg's law.

2.4 X-ray Scattering

When an unpolarized x-ray beam falls on a crystal, it interacts with the electrons of the atoms, primarily through its electric field. In diffraction, we are concerned about a coherent elastic scattering. The differential scattering cross-section (Thomson cross-section) for the scattering of the x-ray (unpolarized) form a single electron is given by

$$\frac{d\sigma}{d\Omega} = \frac{1}{2} r_o^2 (1 + \cos^2 2\theta) \ . \tag{2.2}$$

Here r_o is the classical electron radius and 2θ is the angle between incident and scattered beams. For an atom containing Z electrons, the scattering amplitude is obtained by summing the contribution from all the Z electrons. The scattering cross-section for an atom is given by

$$\frac{d\sigma}{d\Omega} \sim \mid r_o \int \rho(\boldsymbol{r}) e^{i\boldsymbol{Q}.\boldsymbol{r}} d^3\boldsymbol{r} \mid^2 \frac{1}{2}(1 + \cos^2 2\theta) \ . \tag{2.3}$$

The integral in Eq. (2.3) is a Fourier transformation of the electron charge density and is known as atomic form factor $f(Q)$,

$$f\,(Q) = \int \rho(\boldsymbol{r}) e^{i\boldsymbol{Q}.\boldsymbol{r}} d^3\boldsymbol{r} \ . \tag{2.4}$$

The form factor $f(Q) \rightarrow$ Z for $Q \rightarrow 0$, and $f(Q) \rightarrow 0$ for $Q \rightarrow \infty$. The scattering amplitude $F(Q)$ for the crystal lattice is obtained by summing the contribution from all the atoms,

$$F(Q) = \sum_j f_j(Q) e^{i\boldsymbol{Q}.\boldsymbol{R}_j} \ . \tag{2.5}$$

The square of scattering amplitude is the scattering cross-section, that is measured in the scattering experiments. The scattering cross-section for a crystal lattice is given by

$$\frac{d\sigma}{d\Omega} \propto \mid \sum_j f_j(Q) e^{i\boldsymbol{Q}.\boldsymbol{R}_j} \mid^2 \ . \tag{2.6}$$

A more detail discussion on the x-ray diffraction can be found in the Refs. [34, 35].

2.4.1 X-ray Powder Diffractometer

X-ray powder diffraction experiments on the polycrystalline compounds studied in the present thesis were carried on a 12 kW rotating anode x-ray diffractometer (RU 200 Rigaku generator D/max-A) in the Bragg-Brentano geometry, with a Cu K_α radiation.

2.5 Neutron Scattering

2.5.1 Neutron Sources

Neutrons for the scattering experiments can be produced by two methods, (i) nuclear fission and (ii) spallation source. The fission reaction, which occurs inside the uranium fuel rods in the reactor, is given by,

$$^{235}\mathrm{U} + \mathrm{n} \longrightarrow A + B + 2.5\ \mathrm{n}\ .$$

Here A and B are fission products. On the average 2.5 neutrons are produced in one fission reaction. This fission reaction is self-sustaining if on an average 1 out of these 2.5 neutrons produces a further fission. In the spallation source, a high intensity proton beam with an energy of $\sim$ 1 Gev strikes on a heavy metal target (W, Ta). When a high energy proton interacts with a target nucleus, it leaves the target nucleus in a highly excited state. The excited nucleus returns to the ground state with the emission of neutrons, protons, tritons, and alpha particles. These energetic particles interact with the other nuclei of the same target (W, Ta) and excite them in high energy state, and hence produce neutrons in a cascade. The energy spectra of the neutrons produced in the fission and spallation source are quite different (the spallation source produce more high energy neutrons). Neutron spectra for the scattering experiments are tuned by moderator (H_2O, D_2O).

Neutron is an excellent probe to investigate both crystal and magnetic structures. Firstly, because neutron is uncharged particle and therefore don't experience coulomb interaction with the electrons. It interacts directly with the atomic nucleus via strong-force interaction, however, the interaction is very short-range. Neutron can, therefore, penetrate very deep inside most of the materials, and the neutron diffraction acts as a probe where a bulk of sample can be investigated. Secondly, neutron has a magnetic moment, so it interacts with the atomic magnetic moments via a long-range dipole-diploe interaction. The energy of thermal neutrons (few meV) matches with the energy of low energy excitation in the solids, such as phonon and magnon, neutron scattering is, therefore, an excellent probe to study these excitations. In the present thesis, neutron diffraction has been used to study the crystal and magnetic structures of the oxide compounds. The quantity measured in the diffraction experiment is differential scattering cross-section, defined as

$$\frac{d\sigma}{d\Omega} = \frac{\text{total number of neutrons scattered into the solid angle d}\Omega\text{ per unit time}}{(\text{incident flux})d\Omega} \, . \tag{2.7}$$

The differential scattering cross-section has contribution form the nuclear and the magnetic scattering.

2.5.2 Elastic Nuclear Scattering

To describe the elastic scattering of neutrons from a crystalline lattice, we first discuss the scattering of the neutrons with a fix nucleus. Since the wavelength of the thermal neutrons, used in the scattering, is much larger than the range of the nuclear potential, the scattering is isotropic (pure S-wave). The scattering can be described in the first Born approximation, which considers both incoming and outgoing waves as plane waves. The differential scattering cross-section from the Fermi's golden rule, by considering both incoming and outgoing waves as plane waves, is given by

$$\frac{d\sigma}{d\Omega} = (\frac{m_n}{2\pi\hbar^2})^2 \mid \int V(\boldsymbol{r}) e^{-i\boldsymbol{Q}.\boldsymbol{r}} |^2 \, . \tag{2.8}$$

The interaction potential $V(\boldsymbol{r})$ for neutron-nucleus interaction is described by Fermi pseudo potential

$$V(\boldsymbol{r}) = \frac{2\pi\hbar^2}{m_n} \; b \; \delta(\boldsymbol{r} - \boldsymbol{R}) \, . \tag{2.9}$$

Here b is the scattering length and m_n is the mass of the neutron. In general, b can be complex, the imaginary part of b represents an absorption. The value of b for a particular nucleus depends upon the nuclear structure and the spin of neutron-nucleus system. The neutron scattering length b varies quite randomly with atomic number. The scattering lengths for isotopes of the same element can have very different values. The Fermi pseudo potential for the lattice of nuclei at fixed positions R_j is given by

$$V(\mathbf{r}) = \frac{2\pi\hbar^2}{m_n}\sum_j \; b_j \; \delta(\mathbf{r}-\mathbf{R}_j) \; . \tag{2.10}$$

Here b_j is scattering length of the nucleus at site j. Combining Eq. (2.8) with (2.10) yields the cross section

$$\frac{d\sigma}{d\Omega} = |\sum_j b_j \; e^{i\boldsymbol{Q}.\boldsymbol{R}_j}|^2 \; . \tag{2.11}$$

For neutron-nuclear scattering, scattering length b_j for each element depends upon the isotope and spin state of nucleus. If we consider that isotopes and spin states are randomly distributed in a solid, with no correlations among the different lattice positions, then

$$\frac{d\sigma}{d\Omega} = \; <|\sum_j b_j \; e^{i\boldsymbol{Q}.\boldsymbol{R}_j}|^2> \; = \sum_{j,j'} < b_j b_{j'} > e^{i\boldsymbol{Q}.(\mathbf{R}_j-\mathbf{R}_{j'})} \; . \tag{2.12}$$

The average in Eq. (2.12) is over the isotopes and the spin states. Since there are no correlations between the isotopes and the spin states at different lattice positions,

$$< b_j b_{j'} > \;=\; < b_j >< b_{j'} > \;=\; < b^2 >, \; for \; j \neq j'; \tag{2.13a}$$

$$< b_j b_{j'} > \;=\; < b_j >^2 \;=\; < b^2 >, \; for \; j = j'. \tag{2.13b}$$

Combining Eqs. (2.12) and 2.13, we get

$$\frac{d\sigma}{d\Omega} = \sum_{j,j'}^{j\neq j'} < b >^2 e^{i\boldsymbol{Q}.(\boldsymbol{R}_j - \boldsymbol{R}_{j'})} + \sum_j [< b^2 > - < b >^2] \,. \tag{2.14}$$

Using the relation

$$\mid \sum_j e^{i\mathbf{Q}.\boldsymbol{R}_j} \mid^2 = N\frac{(2\pi)^2}{v_o} \sum_{\mathbf{G}} \delta(\boldsymbol{Q} - \mathrm{G}),$$

Eq. (2.14) yields

$$\begin{aligned} \frac{d\sigma}{d\Omega} &= N\frac{(2\pi)^2}{v_o} < b >^2 \sum_{\mathbf{G}} \delta(\boldsymbol{Q} - \boldsymbol{G}) + N[< b^2 > - < b >^2] \\ &= (\frac{d\sigma}{d\Omega})_{coh} + (\frac{d\sigma}{d\Omega})_{inc} \,. \end{aligned} \tag{2.15}$$

Here N is the total number of unit cells and v_o is the volume of the unit cell. From Eq. (2.15) it is clear that incoherent scattering cross-section has no $\boldsymbol{Q}$-dependence and gives a constant background. However, the δ-function in coherent scattering cross-section implies that coherent scattering cross-section is finite when $\boldsymbol{Q} = \boldsymbol{G}$, otherwise it is zero. We know that reciprocal lattice vector $|\mathbf{G}| = 2\pi/d_{hkl}$ and scattering vector $|\mathbf{Q}| = 4\pi \, \sin\theta/\lambda$, then the condition $\boldsymbol{Q} = \boldsymbol{G}$ yields,

$$2d \sin\theta = \lambda,$$

which is Bragg's law. For the crystal structures, having more than one atom per unit cell, the coherent scattering cross-section is given by

$$(\frac{d\sigma}{d\Omega})_{coh} = N\frac{(2\pi)^3}{v_o} < b >^2 \sum_{\mathbf{G}} \delta(\boldsymbol{Q} - \boldsymbol{G})|F_N(\boldsymbol{G})|^2 \,, \tag{2.16}$$

with

$$F_N(\mathbf{G}) = \sum_{\boldsymbol{d}} e^{i\boldsymbol{Q}.\boldsymbol{d}} \; b_{\boldsymbol{d}} \; . \tag{2.17}$$

Here $F_N(\boldsymbol{G})$ is called nuclear structure factor. For the elastic neutron scattering at finite temperature, we must include the Debye-waller factor e^{-W_d}, which accounts for the thermal motion of the atom. The expression for an elastic coherent scattering is then given by Eq. (2.16) with the nuclear structure factor

$$F_N(\boldsymbol{G}) = \sum_{\boldsymbol{d}} e^{i\boldsymbol{Q}.\boldsymbol{d}} \; b_{\boldsymbol{d}} \; e^{-W_{\mathbf{d}}} \; .$$

Now we will discuss the magnetic neutron scattering.

2.5.3 Magnetic Elastic Scattering

Since neutron has magnetic moment ($\hat{\mu}_n$ = -$\gamma\mu_N\hat{\sigma}$), it can interact with atomic magnetic moment via dipole-dipole interaction. The interaction can be expressed as

$$\hat{\mathcal{H}}_{int} = -\hat{\mu}_n.H_e \; . \tag{2.18}$$

Here $\gamma = 1.913$ is gyromagnetic ratio, μ_N is nuclear magneton, $\hat{\sigma}$ is pauli spin operator, and H_e is magnetic field created by unpaired electrons. For the transition metal ions, due to crystalline electric field, orbital angular momentum is normally quenched, we can therefore consider that atomic moment is purely due to the spin. For an atom with spin S, the magnetic moment is $gS\mu_B$, and the magnetic scattering amplitude is given by pS, with

$$p = (\frac{\gamma r_0}{2}) g f\,(\boldsymbol{Q}) \; . \tag{2.19}$$

Here r_0 is classical electron radius and $f(\boldsymbol{Q})$ is magnetic form factor (Fourier transformation of the spin density in an atom), given by,

$$f(\boldsymbol{Q}) = \int \rho_s(r) e^{i\boldsymbol{Q}.\boldsymbol{r}} d^3\boldsymbol{r} \ . \tag{2.20}$$

In an ideal paramagnet, magnetic moments are uncorrelated and completely independent. Differential scattering cross section for a paramagnet with only one type of magnetic ions is given by

$$(\frac{d\sigma}{d\Omega}) = \frac{2}{3} N p^2 e^{-2W} S(S+1) \ . \tag{2.21}$$

In this case, the scattering is Q-dependent due to magnetic form factor and Debye-Walller factor e^{-2W}.

For the magnetic elastic scattering, the coherent scattering cross-section is given by

$$(\frac{d\sigma}{d\Omega})_{coh} = N_M \frac{(2\pi)^3}{v_M} \sum_{\mathbf{G}_M} \delta(\mathbf{Q} - \mathbf{G}_M) |F_M(\mathbf{G}_M)|^2 \tag{2.22}$$

Here N_M is the total number of magnetic unit cells, v_M is the volume of the magnetic unit cell, and $\mathbf{G}_M$ is the magnetic reciprocal lattice vector. The magnetic structure factor F_M is given by

$$F_M(\mathbf{G}_M) = \sum_j p_j S_\perp e^{i\mathbf{G}_M.\mathbf{d}_j} e^{-W_j}. \tag{2.23}$$

Here $S_\perp$ is the component of the moment perpendicular to the scattering vector ($\boldsymbol{Q}$). In the case of a ferromagnet, magnetic and nuclear unit cell are identical, resulting in the same reciprocal lattice vector for magnetic and nuclear scattering. In the neutron diffraction experiment, magnetic reflections appears at the same position at which the nuclear reflections are observed. In the case of an antiferromagnet, magnetic and nuclear unit cell can be different, resulting in the new magnetic reciprocal lattice vectors (different from nuclear reciprocal lattice vectors). As a result, in the neutron diffraction experiment, magnetic reflections appear at positions different from the nuclear Bragg reflections.

2.5.4 Neutron Powder Diffractometers

In this thesis work, a variety of neutron powder diffractometers have been extensively used to get a deep insight into the crystal and magnetic structures. In the angle dispersive neutron powder diffraction measurements, a monochromatic neutron beam is incident on a powder sample. In a powder sample, some crystallite will be in the correct orientation to satisfy the Bragg's law, the diffracted neutron beam, therefore, lies on the surface of several cones, called Debye-Scherrer cones. The neutrons scattered out in the Debye-Scherrer cones are then detected by a detector bank, which cover a large angular range or solid angle. The neutron powder diffraction measurements were carried out at

- Dhruva reactor, Trombay, India
- Reactor source at the Institute Laue Langevin (ILL), France
- Continuous spallation source SINQ, Paul Scherrer Institute (PSI), Switzerland.

The high resolution neutron powder diffraction (NPD) method allows a precise measurement of lattice constants. However, for the crystal structure having a low crystal symmetry, the determination of the lattice constants is difficult because of the overlap of the Bragg peaks. The peak shape and width in the diffraction pattern determine the particle size and microstructure. Now we will mention the characteristics of the neutron powder diffractometers used in the present study.

2.5.4.1 The Powder Diffractometer-II

The Powder Diffractometer-II is installed on the beam tube TT-1013 at the Dhruva research reactor, Trombay, India. The schematic layout of the diffractometer is shown in the Fig. 2.4. The (311) Bragg reflection of the Ge single crystal is used to get the neutrons of wavelength 1.249 Å. The instrument is designed to study both crystal structure and magnetic structures providing a medium resolution ($\triangle d/d \sim 0.8 \times 10^{-3}$). The diffractometer is equipped with five linear position sensitive detectors (PSD) covering a scattering angle range of 5 - 140°. A closed cycle refrigerator covering the temperature range between 4.2 and 300 K is available on the diffractometer. More information about the instrument can be found in Ref. [4].

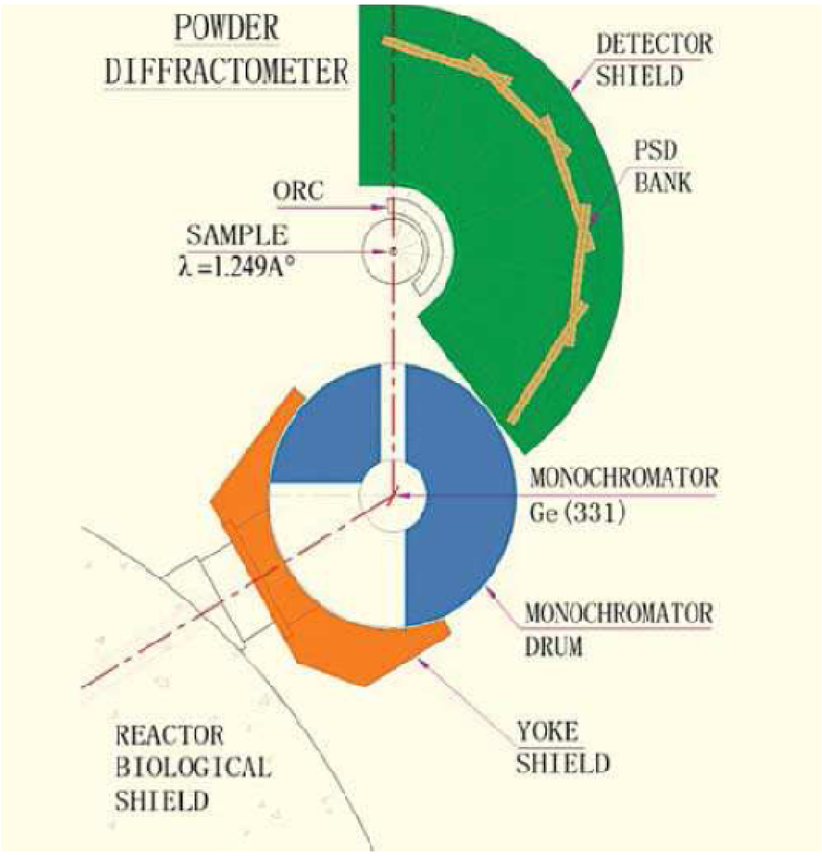

Figure 2.4: Schematic of the powder diffractometer II at Dhruva reactor, Trombay (adapted from Ref. [4]).

2.5.4.2 The DMC Powder Diffractometer

DMC is a high intensity neutron powder diffractoemter at SINQ, PSI, Switzerland, which is well suited for the determination of the magnetic structures. The instrument is located at the cold neutron guide RNR12. The diffractometer is equipped with a position sensitive BF_3 banana-type multi-detector array (400 single detectors with an angular separation of 0.2°). An radial oscillating collimator eliminates the parasitic coherent scattering peaks from components of sample environment equipments. The diffractometer is flexible to house a variety of sample environments and is capable to deliver the neutrons with the wavelength in the range of 2.3 Å to 5 Å. For the magnetic structure determination of the compounds studied in the present thesis, a constant wavelength of 2.46 Å has been used. The schematic layout of the DMC powder diffractometer is shown in Fig. 2.5. More information about the DMC

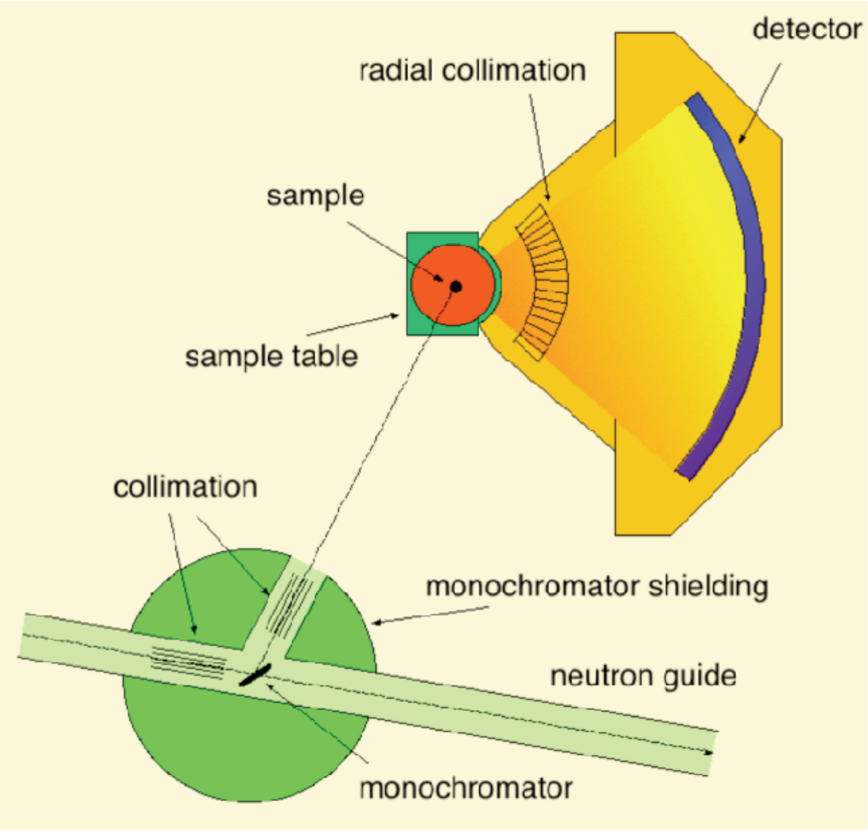

Figure 2.5: Schematic layout of the powder diffractometer DMC at SINQ (adapted from Ref. [5]).

instrument can be found on the PSI web page [5].

2.5.4.3 The D1B Powder Diffractometer

D1B is a high intensity neutron powder diffractometer at ILL, Grenoble. The instrument is extensively used by a larger user community for the determination of magnetic structures. The diffractometer is equipped with ^{3}He/CF$_4$ position-sensitive detectors covering the scattering angle (2θ) of 128° (from 0.8 to 128.8°). At small scattering angle, the instrument provides high resolution, FWHM $\sim 0.2°$ (for a sam-

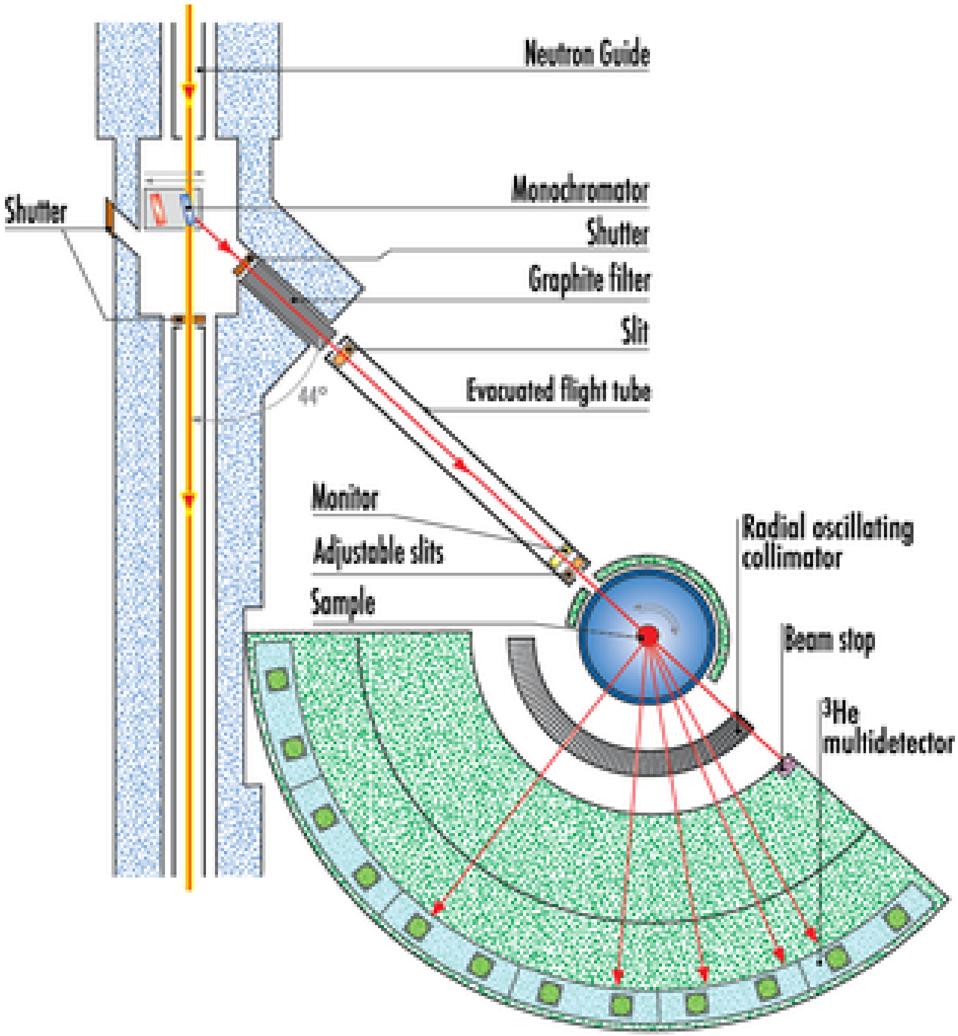

Figure 2.6: Schematic layout of the powder diffractometer D1B at ILL, Grenoble (adapted from Ref. [6]).

ple in 8 mm diameter vanadium can). A focusing pyrolytic graphite [(002) reflection] monochromator provides a neutron beam of wavelength 2.52 Å, with the neutron flux of 6.5 x 10^6 n $cm^{-2}s^{-1}$ at the sample position. The germanium monochromator [(311) reflection] provides a neutron beam of wavelengths 1.28 Å, with the neutron flux of 0.4 x 10^6 n $cm^{-2}s^{-1}$ at the sample position. For the magnetic structure determination of the compounds $Ca_{2.75}R_{0.25}Co_2O_6$ (R = Lu and Dy), studied in the present thesis, we have used the diffractometer in the high flux mode (λ = 2.52 Å) and data collection was performed over 1.5 - 30 K (Chapter 6). The schematic layout of the D1B powder diffractometer is shown in Fig. 2.6. More details about the instrument can be found on the ILL web page [6].

2.5.4.4 The D2B Powder Diffractometer

D2B diffractometer based at ILL, Grenoble is a very high-resolution ($\triangle d/d \sim 5 \times 10^{-4}$) two-axis powder diffractometer. The instrument is located at thermal beam tube H11. Different wavelengths on the diffractometer can be obtained by changing the Bragg reflection of the germanium monochromator. The take-off angle of the monochromator is 135°. The diffraction pattern can be recorded over a scattering angular range of 5 - 165°. A variety of the sample environment equipments (cryostat, furnace, pressure cell, *etc.*) can be mounted on this diffractometer. The schematic layout of the D2B powder diffractometer is shown in Fig. 2.7. More details about the instrument can be found on the ILL web page [7]. In the present study, data collection on D2B diffractometer was performed at 1.5 and 50 K on $Ca_{2.75}R_{0.25}Co_2O_6$ (R = Lu and Dy) samples (Chapter 6).

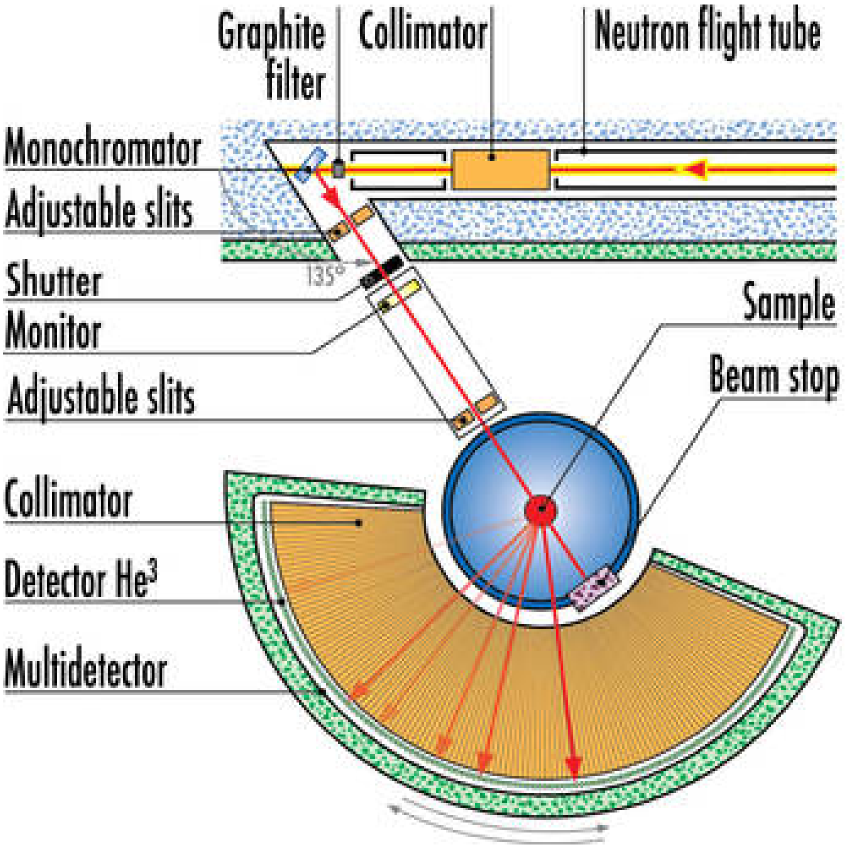

Figure 2.7: Schematic layout of the powder diffractometer D2B at ILL, Grenoble (adapted from Ref. [7]).

2.6 Magnetometer

Measurement of dc magnetization can provide an important information about the presence of a magnetic phase transition and the nature of dominant exchange interactions. In the present work, a vibrating sample magnetometer (VSM) has been used for dc magnetization measurements. The VSM operates on the principle of Faraday's law of induction. According to the Faraday's law of induction, when the magnetic flux associated with a coil changes, then an induced electromotive force (emf) is generated in the coil, which is given by

$$e = -N \frac{d\phi_B}{dt} \tag{2.24}$$

Here, e is the induced electromotive force, N is the number of turns in the coil, ϕ_B is the magnetic flux associated with the coil and t is the time. In the VSM, a sample is attached to the sample rod, which undergoes vertical sinusoidal motion, thereby yielding the sinusoidal motion of the sample. If the sample is magnetized (by an external magnetic field), then the oscillations will induce an electromotive force (electrical signal) in the pick-up coil (Fig. 2.8), which is given by Eq. (2.24). If the sample moves along the z-axis, then Eq. (2.24) can be written as,

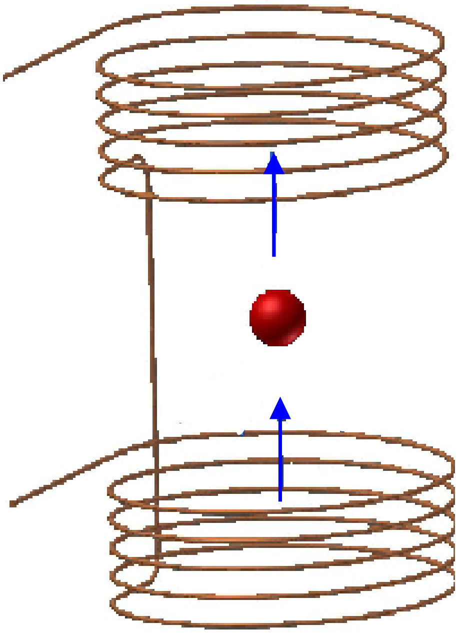

Figure 2.8: Schematic diagram of the sample and VSM pick-up coils (adapted from Ref. [8]).

$$e = -N \, \frac{d\phi_B}{dz} \, \frac{dz}{dt}. \tag{2.25}$$

If the sample vibrates with an amplitude A and frequency ω, then

$$\begin{aligned} z &= A \exp(i\omega t), \\ \frac{dz}{dt} &= A \, i \, \omega \, \exp(i\omega t); \end{aligned} \tag{2.26}$$

Therefore

$$e = -N\,A\,i\,\omega\,\frac{d\phi_B}{dz}\,\exp(i\omega t). \tag{2.27}$$

The VSM is calibrated with a Ni standard sample (Ni cylinder: Purity 99.99 %, 1 mm diameter × 1 mm length, weight = 0.006 mg with known magnetic moment of 0.329 emu at 300 K) to give a saturation magnetization of 55 ± 0.5 $\mathrm{Am^2/kg}$ at 0.5 T. The emu induced due to the Ni standard sample (V_{Ni} in Volts) with known magnetic moment (M_{Ni} in emu) has been stored as the calibration file. Then the magnetic moment of any unknown sample ($M_{unknown}$ in emu) can be calculated from the emf induced by that sample as

$$M_{unknown} = V_{unknown}\,\frac{M_{\mathrm{Ni}}}{V_{\mathrm{Ni}}}\;. \tag{2.28}$$

The schematic diagram of the VSM showing the position of the sample, supercon-

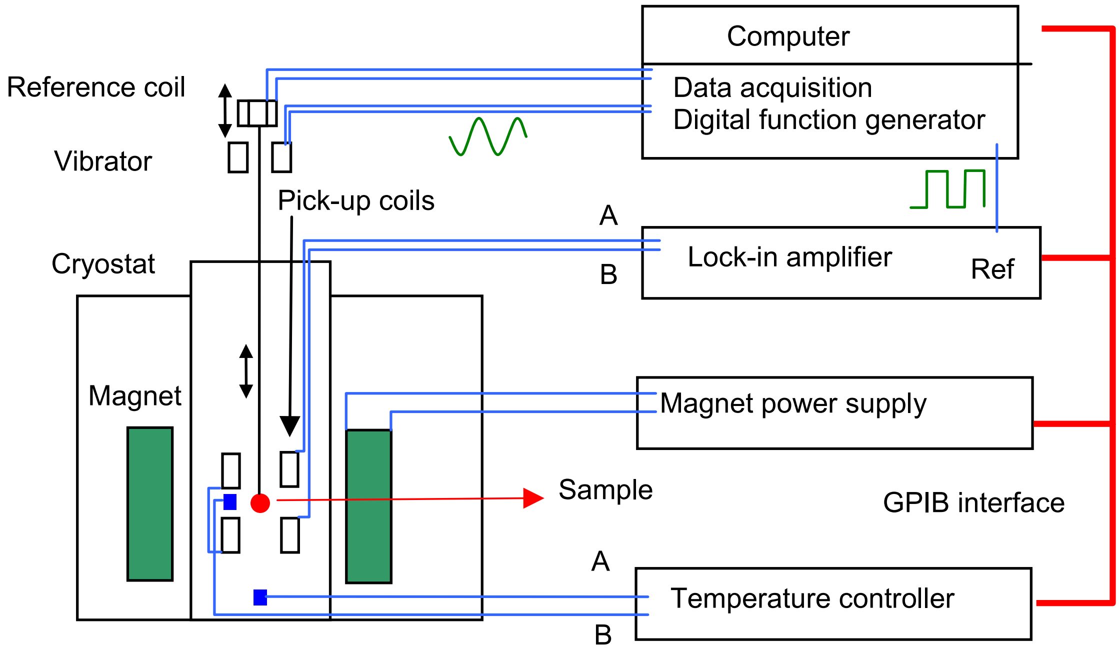

Figure 2.9: Schematic diagram of the VSM setup. The external magnetic field is created by the superconducting magnet (adapted from Ref. [8]).

ducting magnet, vibrator, temperature controller, and pick up coils for measuring the magnetic moment is shown in Fig. 2.9. In the present thesis work, we have used an Oxford Instruments VSM for the fields up to 12 T (temperature range 1.5 - 300 K) and a Cryogenic limited VSM for the fields up to 9 T (temperature range 1.8 - 300 K). For the measurement on the powder samples, powder is compressed into small pellet and loaded in the sample holder located at the end of the sample rod. The shapes of the sample are either elliptical or cylindrical.

2.7 Mössbauer Spectroscopy

The recoilless emission and resonant absorption of the γ-rays is known as Mössbauer effect. The effect was discovered by R. L. Mössbauer [36] in 1957, who received the Nobel prize [37] for this discovery in 1961. Mössbauer effect has been observed in many isotopes such as ^{57}Fe, ^{61}Ni, ^{99}Ru, ^{151}Eu, ^{155}Gd, ^{193}Ir, ^{195}Pt, and ^{197}Au. Among these, the isotope with the strongest recoilless resonant absorption is ^{57}Fe. The nuclear decay scheme of ^{57}Fe is shown in Fig. 2.10. The ^{57}Co having half life of 270 days serves as source of the excited ^{57}Fe nuclei. The excited ^{57}Fe nuclei (I = 3/2) decay to the ground state (I = 1/2) by emitting γ-ray photons of energy 14.4 keV. The emitted γ-ray can excite a second nucleus if it is absorbed resonantly. However, in the free nucleus, the conservation of the momentum imparts a recoil energy [$E_R = {E_\gamma}^2/2mc^2$, here m is the mass of the nucleus emitting, E_γ is the energy corresponding to the difference between nuclear energy levels of the nucleus (14.4 keV for the isotope ^{57}Fe), E_R is recoil energy, and c is the velocity of light] to the emitting nucleus. As a result, the energy of emitted γ-ray photon is not enough to excite another nucleus of the same isotope. The recoil energy (E_R) for the free nucleus ($\sim 10^{-2}$ eV) is found to be much larger than the line width ($\sim 10^{-9}$ eV).

In 1957, Mössbauer discovered that for nuclei in solid, under certain conditions

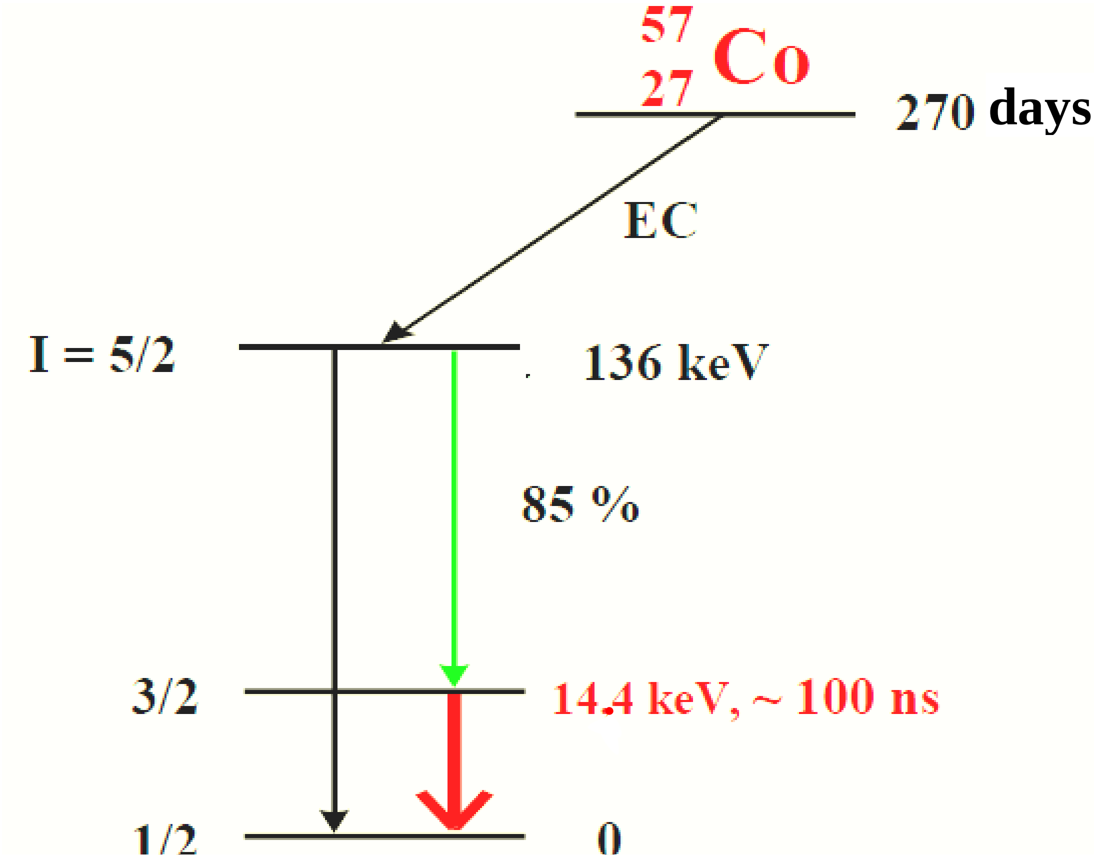

Figure 2.10: Nuclear decay scheme of ^{57}Fe isotope (adapted from Ref. [9]). Mössbauer spectroscopy involves the γ-ray of 14.4 keV.

(if phonon excitation does not occur during the γ-ray emission), the mass m in the expression of $E_R(= {E_\gamma}^2/2mc^2)$ could be equal to the mass of the crystal and the recoil momentum of the γ-ray is taken by the entire crystal. In such a case, the recoil energy is very small and γ-ray can be resonantly absorbed by the another nucleus of the same isotope. This recoilless emission and resonant absorption are the essential processes of the Mössbauer effect.

The hyperfine interactions, *i.e.* interactions between nucleus and its neighboring electrons, shifts the nuclear levels, resulting in a slight change in the transition energy for the emitting and absorbing nucleus. The perfect overlap can be obtained by making the use of the Doppler effect, *i.e.*, by moving the γ-ray source with respect to the absorber. Mössbauer spectra give a quantitative information about the hyperfine interactions. The quantitative information can be used to determine the local chemical environment, valence and spin states of the resonant atom. Three main hyperfine interactions are (i) electric monopole interaction, (ii) electric quadrupole interaction, and (iii) magnetic dipole interaction. In the present thesis work, ^{57}Fe Mössbauer spectroscopy has been used to study the structural and magnetic properties of iron containing compounds $Ca_3Co_{2-x}Fe_xO_6$ (x = 0.1, 0.2, 0.4, and 1.0). The discussion given below for the three hyperfine interactions is, therefore, limited to the ^{57}Fe isotope.

(i) Isomer shift (electric monopole interaction): The isomer shift arises due to the Coulomb interaction between protons of the nucleus and electrons (mainly s-electrons), over the volume of the nucleus. The radius of the nucleus is different in its ground and excited states, and the electron density at the nucleus depends upon the chemical environment. The difference in the chemical environment of the resonant atom, in the source and the absorber, thus produces a shift in the resonance energy.

(ii) Quadrupole splitting (electric quadrupole interaction) : It arises due to the interaction between quadrupole moment of the nucleus and electric field gradient (EFG) at the nucleus. The ground state of ^{57}Fe ($I = 1/2$) nucleus has zero quadrupole moment, however, the excited state ($I = 3/2$) has a finite quadrupole moment. The excited state ($I = 3/2$) is splitted in the doublet in the certain crystalline electric field environment (which has non zero EFG) and then two lines appear in the Mössbauer spectra as shown in Fig. 2.11.

(iii) Nuclear Zeeman interaction (magnetic dipole interaction) : It arises due to the interaction between magnetic moment of the nucleus and local magnetic field. The interaction energy of the nuclear system in a magnetic field B is given by, $E_M = -g_N \mu_N m_I B$. Here, g_N is the nuclear g-factor. Due to the four possible values of m_I, the ground state with $I = 1/2$ splits into two levels and the excited state ($I = 3/2$) splits into four levels, leading to the six possible lines in the Mössbauer spectrum due to the selection rule $\Delta m_I = 0, \pm 1$ (shown in Fig. 2.11). Thus the resonance lines of the iron will be splitted into a sextet in the presence of a magnetic field, with the splitting proportional to the magnetic field.

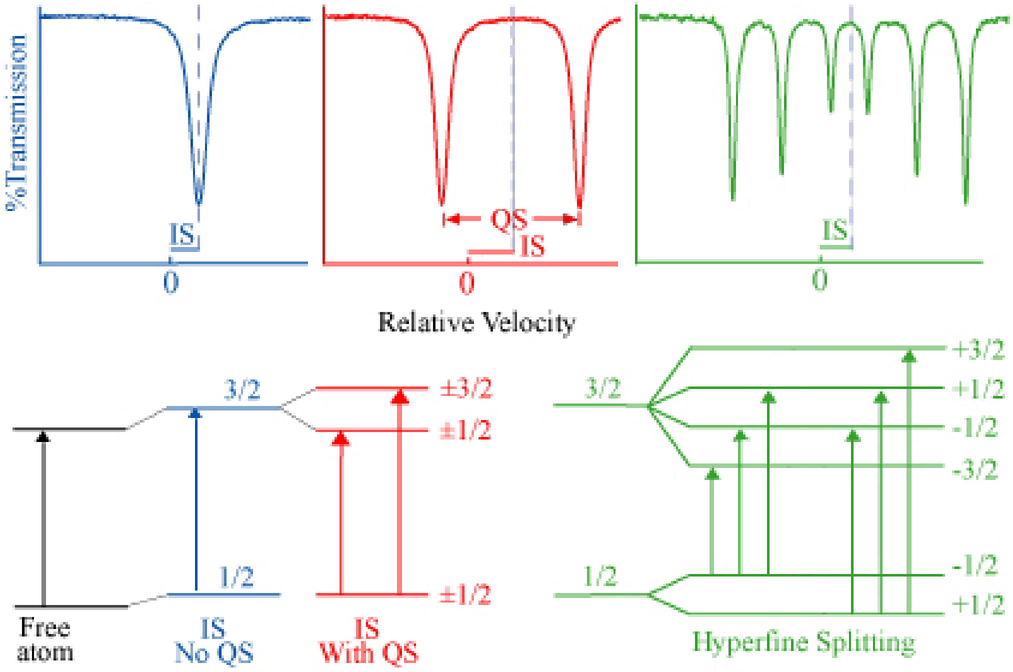

Figure 2.11: The effect of isomer shift, quadrupole splitting, and nuclear Zeeman interaction on the nuclear energy levels of ^{57}Fe (adapted from Ref. [10]).

2.7.1 Mössbauer Spectroscopy Instruments

The Mössbauer spectrometers used in the present work are situated at the Solid State Physics Division, Bhabha Atomic Research Centre, Trombay, India, and Racah Institute of Physics, Hebrew University, Jerusalem, Israel. The spectrometers were operated in constant acceleration mode (triangular wave) in transmission geometry. We used ^{57}Co in Rh matrix (strength $\sim$ 50 mCi) as Mössbauer source. The velocity calibration was done with a room temperature α-Fe absorber.

2.8 Rietveld Refinement

The crystal structural refinement techniques, which are mostly used today, are based on the formalism suggested by H. M. Rietveld [38] in 1969. Prior to Rietveld, the structure refinements from the powder diffraction patterns were performed using the integrated intensities of a set of Bragg reflections and converting them into the structure factors. The structure factors were then used to solve or refine the crystal structure, in the same way as one does for the single crystal data. This procedure works well when the diffraction peaks don't overlap. However, when the independent diffraction peaks overlap in a powder diffraction pattern, which may be due to poor resolution of the instrument or due to a lower symmetry of the crystal structure, useful information contained in the profile of these overlapping peaks is lost. This makes crystal structure refinement from the powder diffraction data difficult. In 1969, Rietveld developed a structure refinement method, which overcomes the problem of the peak overlaps by employing the entire diffraction pattern, with a variety of refinable parameters. This allows the extraction of maximum information because overlapping Bragg peaks are used for the structural analysis/refinement. Rietveld refinement is based on the weighted least square fit of the entire observed diffraction pattern to the calculated one. The quantity to be minimized in the least square refinement is

$$\chi^2 = \sum_{i=1}^{n} w_i \{y_{io} - y_{ic}(\beta)\}^2 \ . \tag{2.29}$$

Here w_i is the weightage of an individual observed intensity y_{io}, given by $w_i = 1/{\sigma_i}^2$, and ${\sigma_i}^2$ is the variance of "y_{io} ". The β's are the refinable parameters of the calculated profile. The calculated powder profile intensity at a given point i is given by

$$y_{ic} = s \sum_k L_k m_k \mid F_{hkl}^k \mid^2 \Omega(2\theta_i - 2\theta_k) P_k A + y_{ib} \tag{2.30}$$

Here s is the scale factor, L_k is the Lorentz-polarization factor, m_k is the multiplicity factor, ${F^k}_{hkl}$ is the structure factor, Ω is the profile function, P_k the preferred orientation function, and A is an absorption factor. The profile function is a convolution of the instrumental profile and the intrinsic profile of the sample. The θ_k is the calculated position of the Bragg peak and y_{ib} is the background intensity. The summation in Eq. (2.30) is over all possible reflections which contribute at the $2\theta_k$. The structure factor ${F^k}_{hkl}$ depends on the the positions j of the atoms in the unit cell, and is given by

$$F^k_{hkl} = \sum_{j=1}^{N} f_j \exp[2\pi i(hx_j + ky_j + lz_j)] \exp(-\frac{B_j \sin^2\theta}{\lambda^2}) \ . \qquad (2.31)$$

Here f_j is the scattering factor of the j^{th} atom and B_j is the isotropic temperature parameter. The sum in Eq. (2.31) is over all atoms in the unit cell, and (x_j, y_j, z_j) are the fractional positional coordinates of the j^{th} atom. The atomic scattering factor f_j is replaced by scattering length b_j in the case of neutron scattering.

Best estimate of the values of the parameters β's in Eq. (2.29) are obtained by setting the derivative to zero,

$$\sum_{i=1}^{n} w_i(y_{io} - y_{ic}) \frac{\partial y_{ic}}{\partial \beta} = 0 \ . \qquad (2.32)$$

This results in n "normal" equations. Because Eq. (2.29) is non-linear and transcendental in parameters, non-linear least-squares fitting has to be used to optimize (refine) the parameters. This means approximate values for all the parameters are required in the first cycle of the refinement. In the Rietveld method, more than one nuclear (and/or magnetic) phase can be refined simultaneously.

The quality of agreement between observed and calculated profiles is evaluated by residual functions defined as :

Profile factor,

$$R_p = 100 \sum_{i=1,n} \frac{\mid y_{io} - y_{ic} \mid}{\sum_{i=1,n} y_{io}} , \tag{2.33}$$

The weighted profile factor,

$$R_{wp} = 100[\frac{\sum_{i=1}^{n} w_i |y_{io} - y_{ic}|^2}{\sum_{i=1}^{n} w_i y_{io}^2}]^{1/2}, \tag{2.34}$$

The expected weighted profile factor,

$$R_{exp} = 100[\frac{n-p}{\sum_{i=1}^{n} w_i y_{io}^2}]^{1/2}, \tag{2.35}$$

Here, n and p are the total number of data points and the total number of refinable parameters used in the refinement, respectively. These agreement factors (R-factors) quantify how well the calculated pattern fits to the observed pattern. The R_p quantifies the difference between observed and calculated diffraction patterns on a point-by-point basis. The R_{wp} is most valuable index because it weights the residual (the quantity to be minimized in the refinement). The factor R_{exp} indicates the quality of the data. The value of R_{wp} can never be better than R_{exp}. One can also use goodness of fit (GOF), which compares R_{wp} to R_{exp},

$$GOF = \chi^2 = [\frac{R_{wp}}{R_{exp}}]^2. \tag{2.36}$$

The GOF should never be less than one. If the refinement results in GOF < 1, it means either one of the two things (i) the standard deviations for the data are overestimated and (ii) the model is trying to fit the noise. A important point to be noted here is that these agreement factors are statistically defined parameters, which don't account for poor or incorrect data. These factors are important when one tries to fit the different models to the same data. It is, therefore, necessary to make visual estimation of the fit by plotting the calculated, observed, and difference patterns, simultaneously. In the present thesis work, the program Fullprof [39, 40], in combination with the graphical user interface program WinPLOTR, has been used to refine the crystal structures and to determine the magnetic structures. The representation theory analysis for determining magnetic structures has been performed using the BASIREPS [39, 40] (built in WINPLOTR) and the SARAH [41] programs.

Chapter 3

Crystal Structure

3.1 Introduction

For several decades, A_3BO_3-type [A = alkali, alkaline-earth metal or rare-earth ions, and B = transition metal ions] perovskite oxides have received a lot of attention due to their interesting physical properties, such as, ferroelectricity, colossal magnetoresistance (CMR), metal-insulator transition, multiferroicity, *etc.* In addition, the composition of the perovskite oxides is highly flexible and can accommodate a variety of cations at both A and B sites. The crystal structure of an ideal cubic perovskite (as shown in Fig. 3.1) consists of corner sharing (BO_6) octahedra, with A cations occupying the cage created by eight (BO_6) octahedra. The A cations are in 6 fold oxygen co-ordination, and the B cations are in 12 fold oxygen co-ordination. Due to the size incompatibilities (which give rise to several modes of tilting of the BO_6 octahedra), several structural modifications of the ideal perovskite structure have been observed. The hexagonal perovskite structure is a variant of the oxygen packing in the perovskite oxides, leading to a structure containing chains of face sharing BO_6 octahedra, separated by the chains of A cations. The crystal structure of A_3MXO_6-type [A = Ca, Sr and (M, X) = alkali or transition metal ions] quasi-one-dimensional spin-chain compounds, studied in the present thesis, is a modification of the hexagonal perovskite structure. Both cubic and hexagonal perovskite structures can be described as the stacking of the closed pack [AO_3] layers and the subsequent filling of the generated octahedral sites by the B cations. An"-A-B-A-B-"

stacking sequence results in the hexagonal perovskite structure, however, an "-A-B-C-A-B-C-" stacking sequence results in the cubic perovskite structure. The crystal structure of the A_3MXO_6-type quasi-one-dimensional spin-chain compounds, can be generated from the stacking of the A_3MO_6 layers (obtained by tripling the $[AO_3]$ layers and replacing the three oxygen anions with one M cation) and by filling the generated octahedral sites with the X cations.

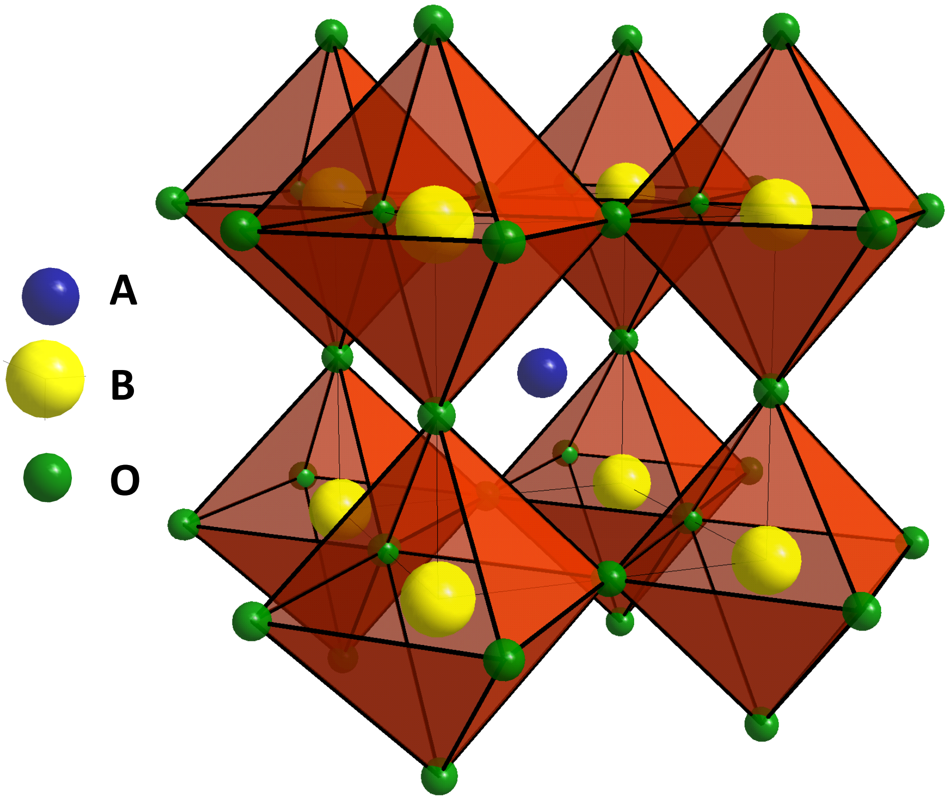

Figure 3.1: The crystal structure of an ideal cubic perovskite oxide. The cation A is located in the middle of eight interconnected BO_6 octahedra.

The compounds of A_3MXO_6 family crystallize in the K_4CdCl_6 type rhombohedral structure with space group $R\bar{3}c$. The crystal structure consists of chains of alternating face-sharing MO_6 trigonal prism (TP) and XO_6 octahedra (OCT) running along the crystallographic c axis [Fig. 3.2(a)]. These chains, separated by the non-magnetic A cations, are arranged on a triangular lattice in the ab plane with each chain surrounded by the six chains [Fig. 3.2(b)]. These chains are linear if no

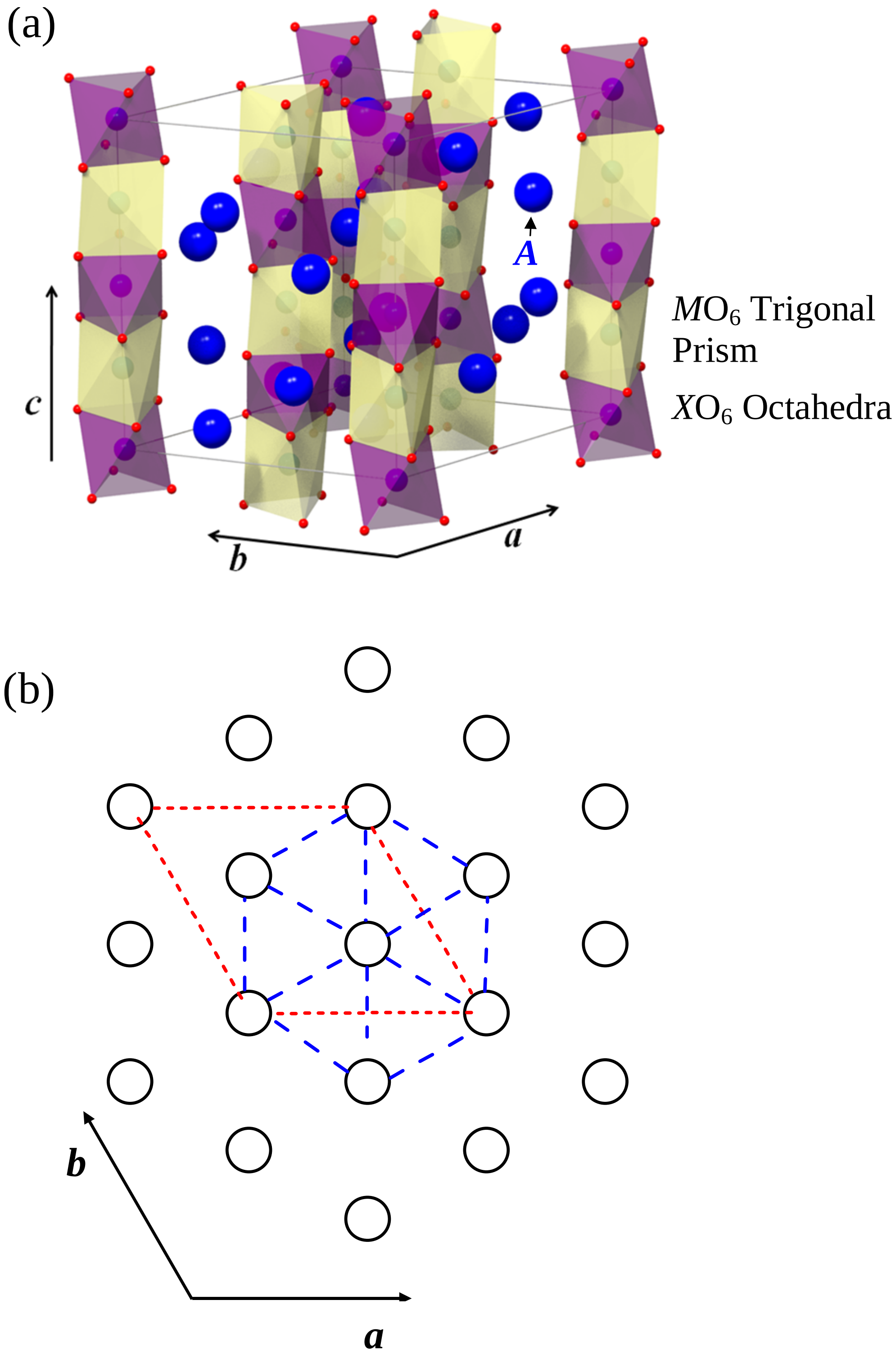

Figure 3.2: (a) Crystal structure of A_3MXO_6-type compounds. Atoms A and O are represented by blue (largest) and red (smallest) spheres, respectively. (b) A projection on the *ab* plane showing the triangular arrangement of the spin chains (blue long-dashed lines). The open circles in Fig.(b) represent the chains and the red short-dashed lines represent the unit cell in the *ab* plane.

structural distortion exists at the MO$_6$ trigonal prism and the XO$_6$ octahedra. The K$_4$CdCl$_6$ type rhombohedral structure undergoes a monoclinic distortion if ions at (M, X) position are Jahn-Teller ions. For example, Sr$_3$CuPtO$_6$ crystallizes in the monoclinic structure (space group $C2/c$) due to the presence of Cu^{+2} (Jahn-Teller) cation at the M site [42] resulting in the zigzag arrangement of Cu and Pt ions along the c axis. The compound Ca$_3$CuMnO$_6$ undergoes a further structural distortion and crystalizes in the triclinic structure [43, 44] with space group $P\bar{1}$, which is a subgroup of the space group $C2/c$. Similar to the perovskite structure, A_3MXO$_6$ family can accommodate a variety of cations at the $M$and X sites in a wide range of oxidation states. A list of the representative members of the A_3MXO$_6$ family is given in Ref. [45].

We will now describe in detail the structural characterization of the polycrystalline compounds, Ca$_3$Co$_{2-x}$O$_6$ (x = 0, 0.1, 0.2, 0.4, and 1) and Ca$_{2.75}R_{0.25}$Co$_2$O$_6$ (R= Lu and Dy) of the A_3MXO$_6$ family, which have been studied in the present thesis work. All compounds were prepared using the solid state reaction method (described in Chapter 2).

3.2 Experimental Details for Structural Study

Powder x-ray diffraction (XRD) measurements were performed on all the samples at room temperature using a Cu K_α radiation from scattering angle (2θ) 10° to 90° in equal 2θ steps of 0.02° [covering a scattering vector Q ($= 4\ \pi\ \sin\theta/\lambda$) range of 0.71 to 5.77 Å^{-1})].

For the compounds Ca$_3$Co$_{2-x}$Fe$_x$O$_6$ ($x = 0$, 0.1, 0.2, and 0.4), neutron diffraction patterns were recorded at room temperature using the five linear position sensitive detector (PSD) based powder diffractometer (λ = 1.249 Å) at Dhruva research reactor, Trombay [4] from scattering angle 6° to 138° covering a Q range of 0.53 to

9.398 Å^{-1}. Neutron diffraction patterns were converted in equal 2θ steps of 0.02° using the standard procedure.

For the compounds $Ca_{2.75}R_{0.25}Co_2O_6$(R = Lu and Dy), neutron diffraction measurements were carried out on the high-resolution powder diffractometer D2B at the Institut Laue-Langevin (ILL) in Grenoble (France)[7]. The diffraction patterns were collected at 50 K in an angular range $8^\circ < 2\theta < 150^\circ$ with 2θ step of 0.05°, using a wavelength of 2.39 Å. The x-ray and neutron diffraction data were analyzed by the Rietveld method using the FULLPROF program [40].

Mössbauer spectra for the compounds $Ca_3Co_{2-x}Fe_xO_6$ (x = 0.1, 0.2, 0.4, and 1.0) were measured at room temperature using a conventional constant acceleration spectrometer in transmission geometry. A γ-ray source of ^{57}Co in Rh matrix at room temperature was used. An α-Fe absorber was used at room temperature to calibrate the Doppler velocity V and also as the standard for the isomer shift (IS).

3.3 Results and Discussion

3.3.1 Crystal Structure of $Ca_3Co_{2-x}Fe_xO_6$ (x = 0, 0.1, 0.2, and 0.4)

3.3.1.1 X-ray and Neutron Diffraction Studies

The x-ray and the neutron powder diffraction patterns for the x = 0, 0.1, 0.2, and 0.4 compounds, recorded at 297 K, are shown in Figs. 3.3 and 3.4, respectively. The diffraction patterns were analyzed by the Rietveld refinement technique using the FULLPROF program [40]. Both x-ray and neutron diffraction patterns for each composition were refined simultaneously. In the Rietveld refinement of the neutron diffraction patterns, coherent scattering lengths (b_{coh}) 0.470×10^{-12}, 0.249×10^{-12}, 0.945×10^{-12}, and 0.580×10^{-12} cm for Ca, Co, Fe, and O, respectively, have been used. The refinement confirms that these compounds crystallize in the rhombohe-

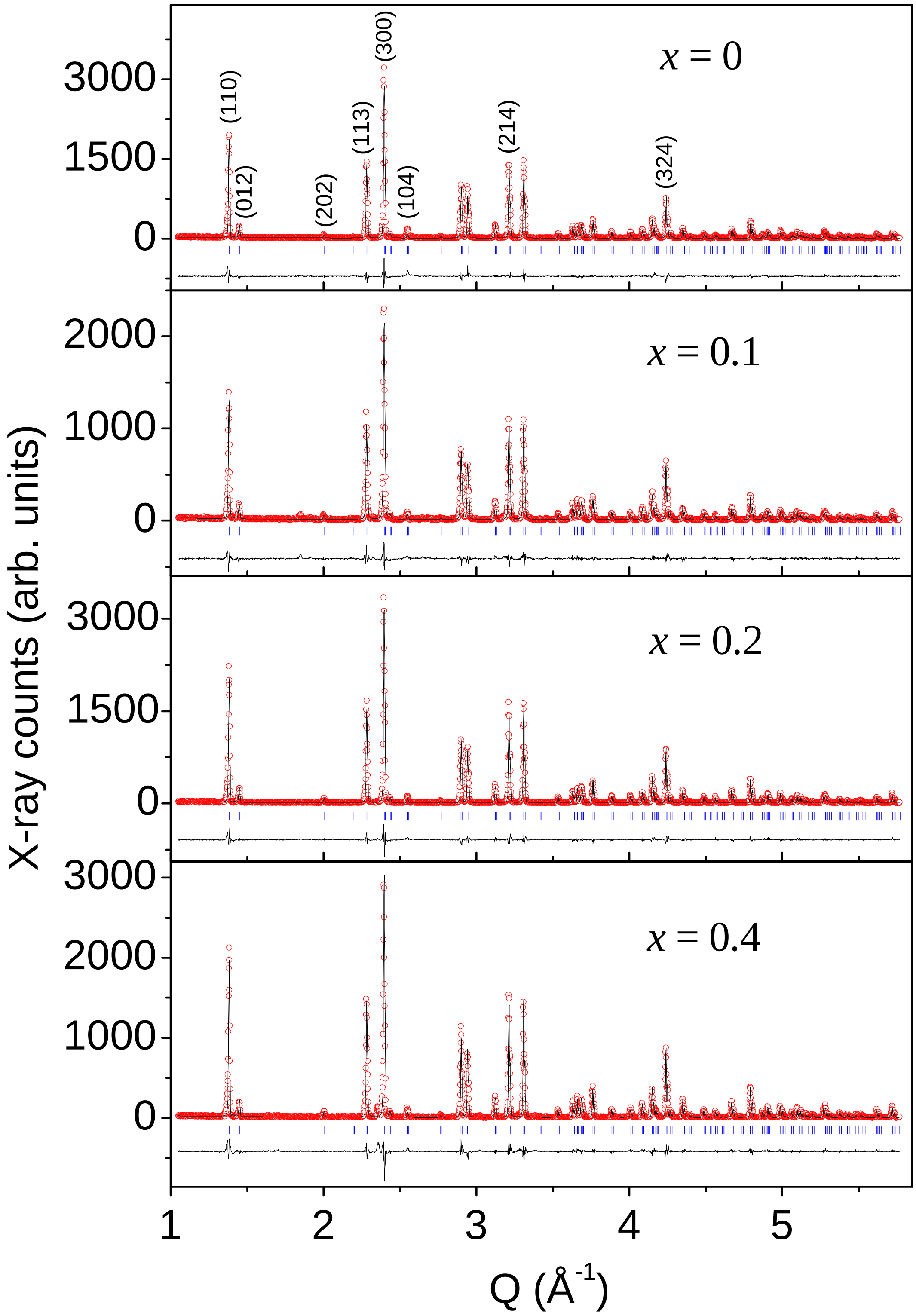

Figure 3.3: Observed (open circles) and calculated (solid lines) x-ray diffraction patterns of $Ca_3Co_{2-x}Fe_xO_6$ ($x = 0$, 0.1, 0.2, and 0.4) at 297 K. Solid line at the bottom of each panel shows difference between observed and calculated patterns. Vertical lines show the position of Bragg peaks. The (hkl) values corresponding to stronger Bragg peaks are also listed.

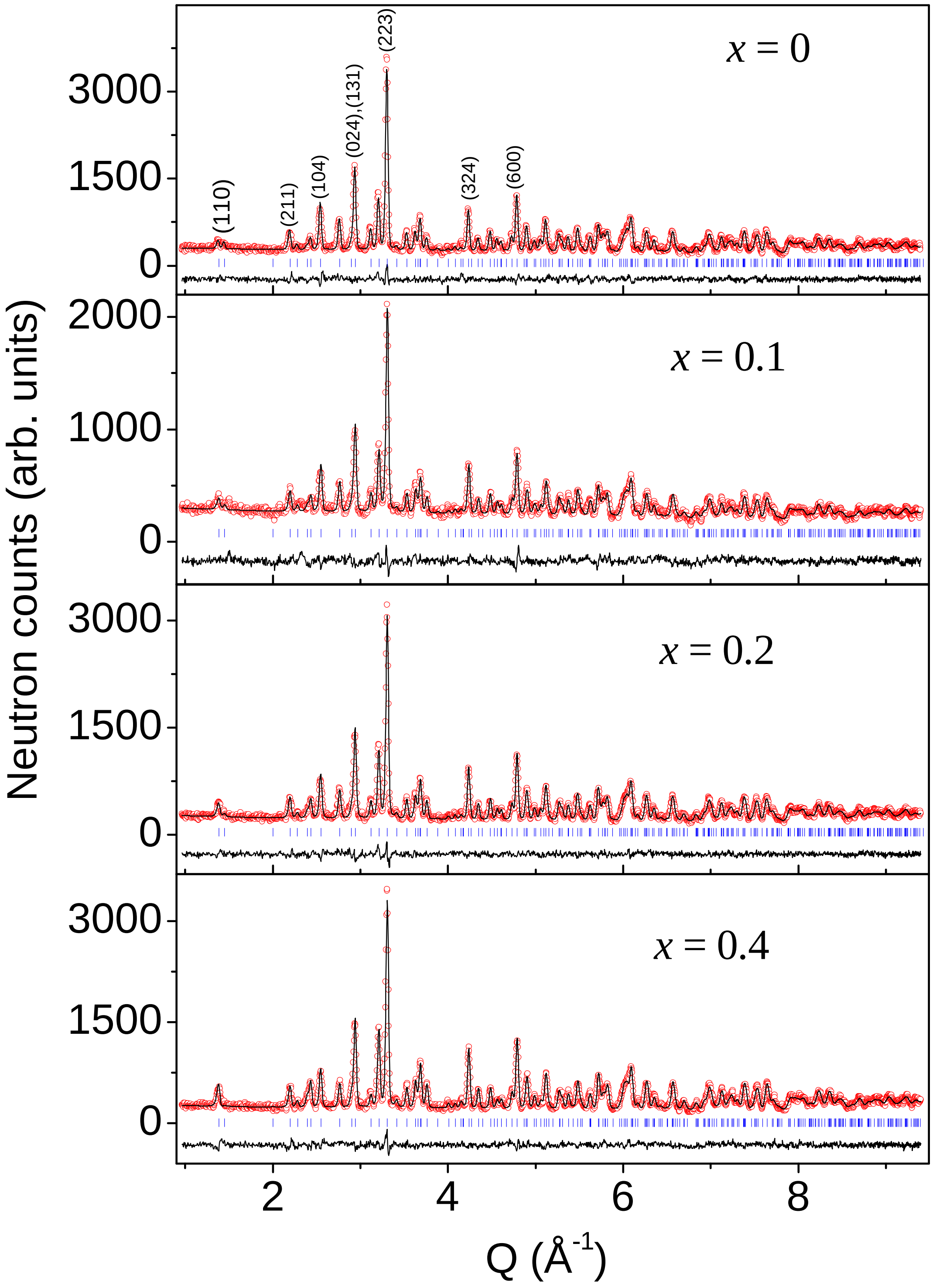

Figure 3.4: Observed (open circles) and calculated (solid lines) neutron diffraction patterns of $Ca_3Co_{2-x}Fe_xO_6$ ($x = 0$, 0.1, 0.2, and 0.4) at 297 K. Solid line at the bottom of each panel shows difference between observed and calculated patterns. Vertical lines show the position of Bragg peaks. The (*hkl*) values corresponding to stronger Bragg peaks are also listed.

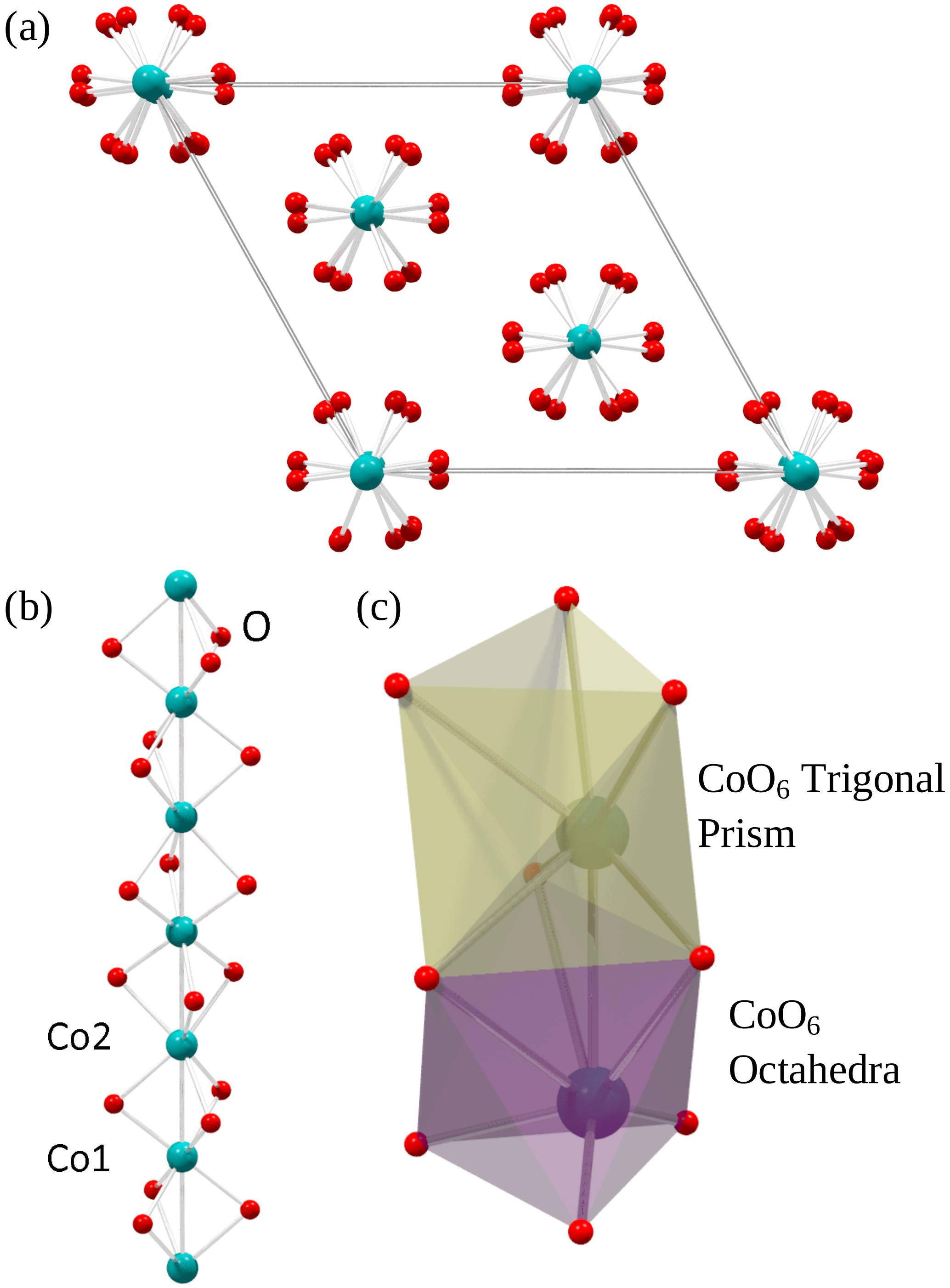

Figure 3.5: (a) Crystal structure of $Ca_3Co_2O_6$ projected on the *ab* plane. For clarity calcium atoms are not shown. (b) One-dimensional $[CoO_6]_\infty$ chains in $Ca_3Co_2O_6$. (c) Face-sharing octahedral and trigonal prismatic CoO_6 polyhydra.

dral structure (space group $R\bar{3}c$). There are six formula units per unit cell. The refinement also confirms that for all iron substituted compounds entire Fe is located at the TP site, $6a$ (0, 0, 1/4), with no trace of unreacted Fe. In these compounds,

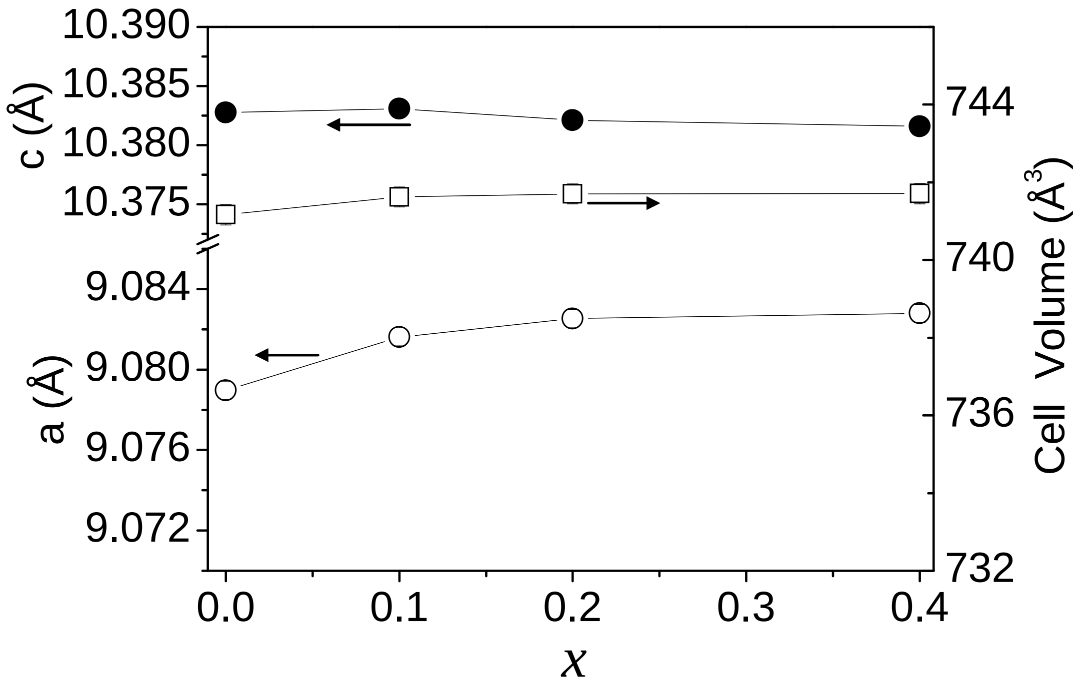

Figure 3.6: Lattice constants and unit cell volume for $Ca_3Co_{2-x}Fe_xO_6$ as a function of iron content. Solid lines are guide to the eye.

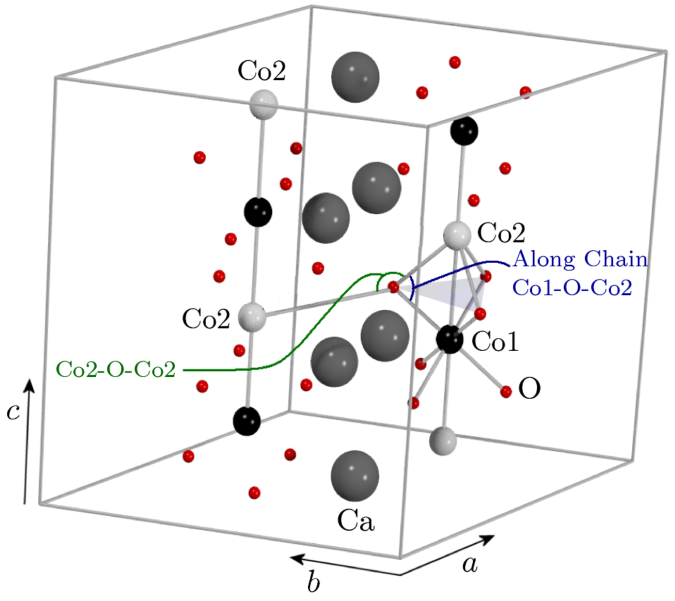

Figure 3.7: Unit cell of $Ca_3Co_{2-x}Fe_xO_6$ ($x = 0$, 0.1, 0.2, and 0.4), showing selected (Co1-O-Co2 and Co2-O-Co2) bond angles. Only selected atoms are shown for clarity.

Fe/Co ions, therefore, form the linear chain along the crystallographic *c* axis (shown in Fig. 3.5 for the compound $Ca_3Co_2O_6$). The refined unit cell parameters and other structural parameters are given in Table 3.1. Figure 3.6 depicts the Fe substitution dependence of the lattice constants and the unit cell volume. Selected interatomic distances and bond angles (along the chain and between chains) are shown in Fig. 3.7 and their values are given in Table 3.2. The values of the cell constants, interatomic distances, and bond angles obtained for the parent compound $Ca_3Co_2O_6$ match well with the values reported in the literature [46]. It is evident that there is no significant change in the lattice parameters (only slight increase in lattice constant *a*), unit cell volume, bond angles, and bond lengths by substitution of iron.

3.3.1.2 Mössbauer Study

Mössbauer spectra for $Ca_3Co_{2-x}Fe_xO_6$ (x = 0.1, 0.2, and 0.4) at room temperature are shown in Fig. 3.8. All spectra have been fitted well with an asymmetric doublet. An analysis of these spectra gives the quadruple splitting |QS|: 1.21, 1.23, 1.23 mm/s and isomer shift (IS): 0.41, 0.40, and 0.40 mm/s for x = 0.1, 0.2, and 0.4 samples, respectively. In the literature, the similar values of IS for high spin (HS) Fe^{3+} have been reported; 0.35, 0.39, and 0.43 mm/s for $LiFe_{0.5}Mn_{1.5}O_4$[47], α-LiF_5O_8 [48], and Ca_3FeRhO_6 [49], respectively. The QS values, observed for our compounds, are similar to the values reported in the literature for HS Fe^{3+} at TP site in the same class of compounds; 1.13 mm/s for Ca_3FeRhO_6 (Ref.[49]) and 1.23 mm/s for $Ca_3Co_{1.98}Fe_{0.02}O_6$[50]. For HS Fe^{3+} in the FeO_6 OCT, the reported QS values, are 0.02, 0.58 and 0.75 mm/s for α-LiF_5O_8 [48], α- $LiFeO_2$ [51], and $LiFe_{0.5}Mn_{1.5}O_4$[47], respectively, which are much lower than our experimentally observed values. Therefore, possibility of Fe^{3+} occupying octahedral site can be ruled out. From the observed values of IS and QS, we can conclude that HS Fe^{3+} is located

Table 3.1: Atomic positions, lattice constants, and thermal parameters for the compounds $Ca_3Co_{2-x}Fe_xO_6$. All crystallographic sites are fully occupied.

x	Atom	Site	x	y	z	B_{iso}
0	Ca	18e	0.3698(2)	0	1/4	0.39 (4)
	Co1	6b	0	0	0	0.37 (8)
	Co2	6a	0	0	1/4	0.48 (9)
	O	36f	0.1774(4)	0.0257 (5)	0.1145 (3)	0.53 (2)
0.1	Ca	18e	0.3697(6)	0	1/4	0.40 (5)
	Co1	6b	0	0	0	0.38 (9)
	Co2	6a	0	0	1/4	0.34 (9)
	Fe	6a	0	0	1/4	0.49 (8)
	O	36f	0.1779(6)	0.02377(6)	0.1133(6)	0.73 (4)
0.2	Ca	18e	0.3693(3)	0	1/4	0.49 (4)
	Co1	6b	0	0	0	0.45 (8)
	Co2	6a	0	0	1/4	0.5 (2)
	Fe	6a	0	0	1/4	0.5 (4)
	O	36f	0.1765(2)	0.0238(2)	0.1138(2)	0.69 (3)
0.4	Ca	18e	0.3692(2)	0	1/4	0.55 (4)
	Co1	6b	0	0	0	0.39 (9)
	Co2	6a	0	0	1/4	0.54 (7)
	Fe	6a	0	0	1/4	0.49 (7)
	O	36f	0.1759(3)	0.0235(3)	0.1139(2)	0.85 (4)

at the TP (Co2) site. This result (Fe is located at the TP site) is consistent with the outcome of our Rietveld refinement of x-ray and neutron diffraction patterns.

3.3.2 Crystal Structure of Ca_3CoFeO_6

3.3.2.1 X-ray Diffraction Study

The profile matching refinement of the x-ray diffraction pattern for $Ca_3Co_{2-x}Fe_xO_6$ ($x = 1.0$), using the FULLPROF [38], is shown in Fig. 3.9. The refinement confirms the formation of a single phase, in a triclinic structure (space group $P\bar{1}$). The unit

Table 3.2: Selected bond lengths and bond angles for $Ca_3Co_{2-x}Fe_xO_6$ samples.

x	Bond	Length (Å) along the chain		Bond angle
0	Ca-O	2.345(5)	2.459(2)	
		2.550(3)	2.470(1)	
	Co1-O	1.916(2)		
	Co2-O	2.070(1)	Co1-O-Co2	81.14(9)°
	Co1-Co2	2.59569		
			between the chains	
	Co2-O	3.905(2)	Co2-O-Co2	132.55(8)°
	Co2-Co2	5.52000		
0.1	Ca-O	2.339(4)	2.452(3)	
		2.476(3)	2.548(3)	
	Co1-O	1.919(3)	Co1-O-Co2	80.8(1)°
	Co2-O	2.079(3)		
	Co1-Co2/Fe	2.59570		
			between the chains	
	Co2-O	3.903(3)		
	Co2-Co2	5.52147	Co2-O-Co2	132.40(2)°
0.2	Ca-O	2.393(2)	2.463(2)	
		2.474(1)	2.552(3)	
	Co1-O	1.920(2)	Co1-O-Co2	81.25(3)°
	Co2-O	2.067(2)		
	Co1-Co2/Fe	2.59572		
			between the chains	
	Co2-O	3.912(1)		
	Co2-Co2	5.52191	Co2-O-Co2	132.44(6)°
0.4	Ca-O	2.346(3)	2.468(2)	
		2.551(3)	2.468(2)	
	Co1-O	1.922(2)	Co1-O-Co2	81.48(9)°
	Co2-O	2.062(2)		
	Co1-Co2	2.59573		
			between the chains	
	Co2-O	3.918(2)		
	Co1-Co2	5.52203	Co2-O-Co2	132.39(8)°

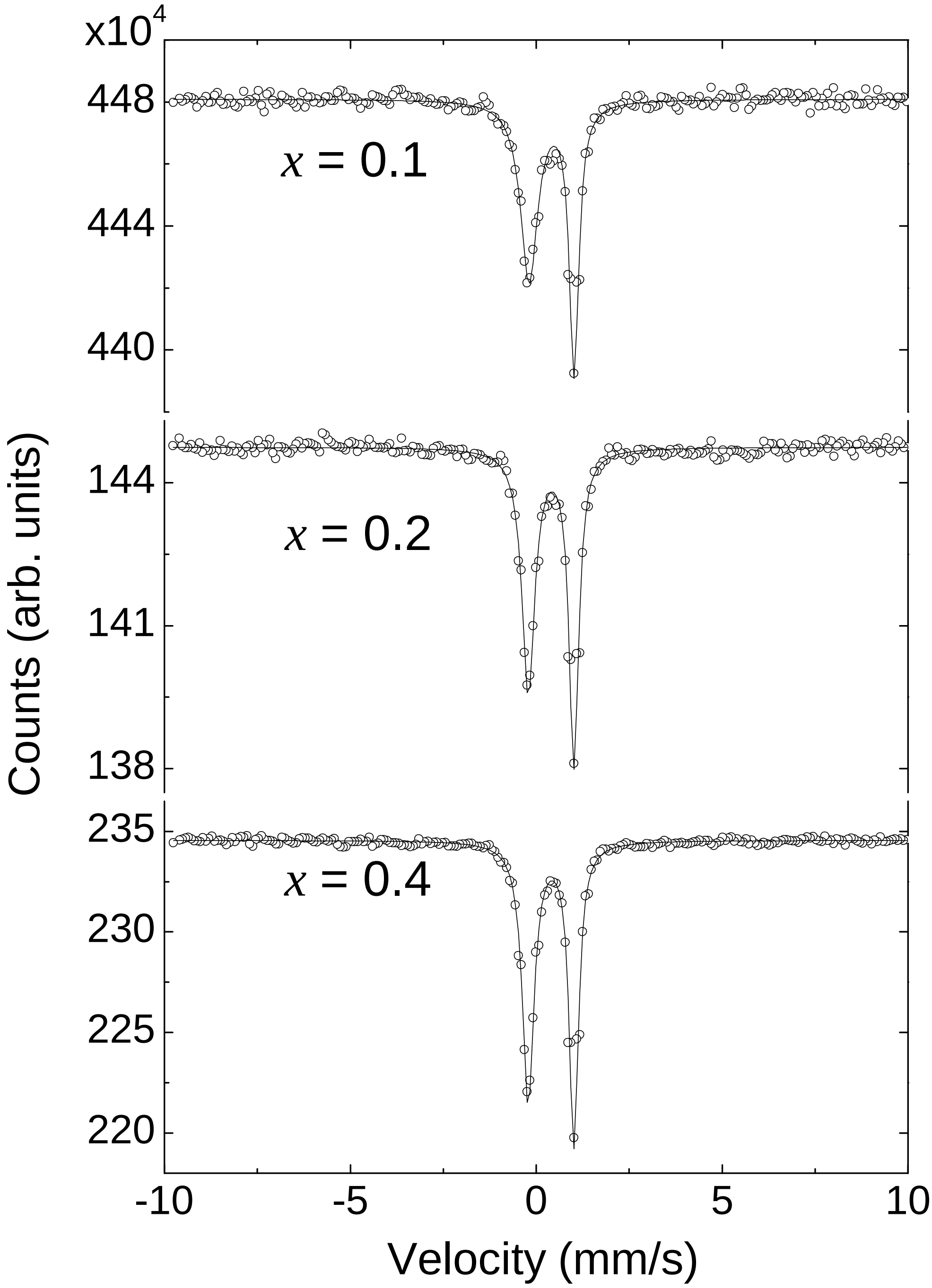

Figure 3.8: Mössbauer spectra for $Ca_3Co_{2-x}Fe_xO_6$(x = 0.1, 0.2, and 0.4) at room temperature. Solid lines are the fitted curves.

cell parameters are shown in the figure panel. The c axis is at angle of 18.47 ± 0.04° relative to the perpendicular to the ab plane. The unit cell volume is 523.3 Å^3. It may be mentioned here that the used profile matching refinement method [38] allows one to obtain only the crystal system, its space group, and the lattice parameters.

Since with this higher Fe substitution ($x = 1.0$), the crystal structure has completely changed from the known rhombohedral structure (for lower Fe substituted samples), it is not possible to use the Rietveld refinement method which needs position of all the atoms in the unit cell. Hence the used method, unlike the Rietveld profile refinement, does not give the refined position of the atoms in the unit cell. Hence, we are not in a position to give any further structural details. However, the present diffraction data analysis could clarify the single phase nature of the sample with the above mentioned crystallographic information.

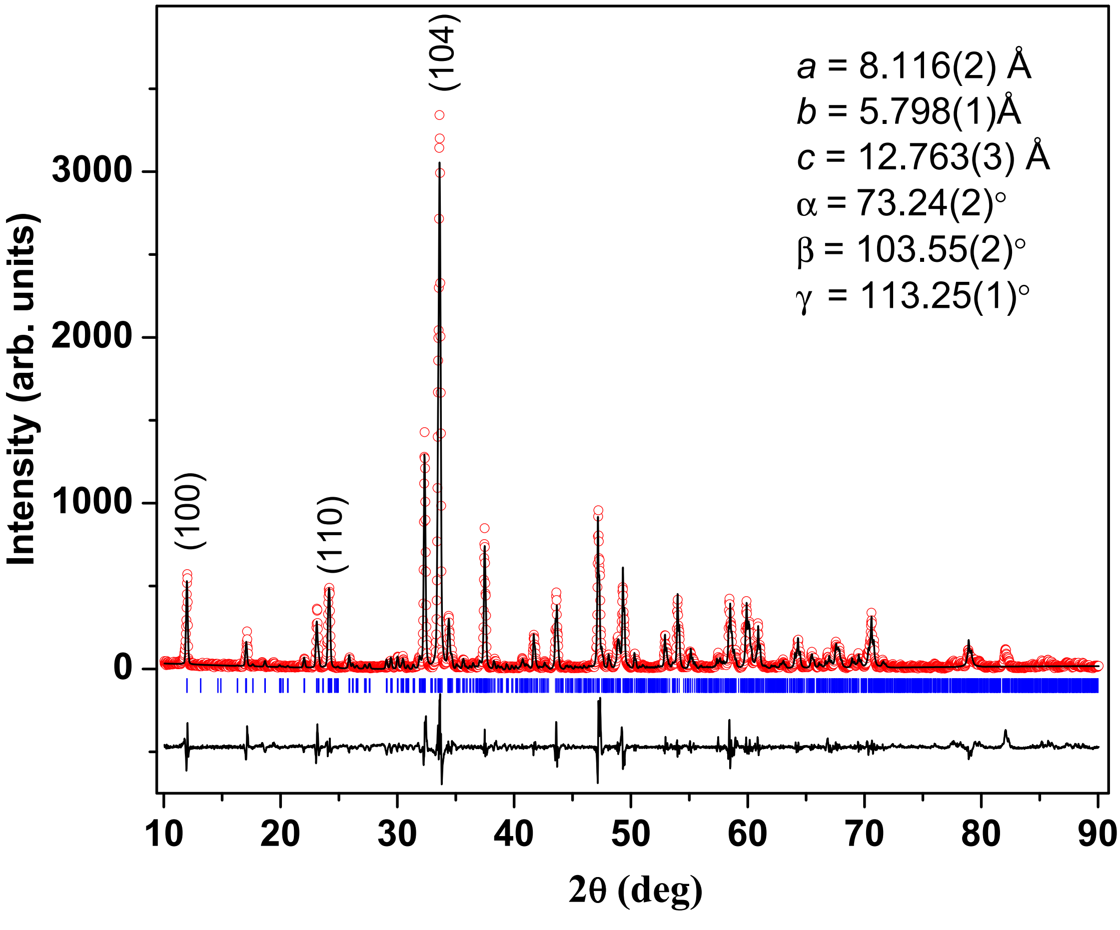

Figure 3.9: The x-ray diffraction pattern of Ca_3CoFeO_6 at 297 K. The solid line at the bottom of the figure shows the difference between the observed and the calculated patterns.

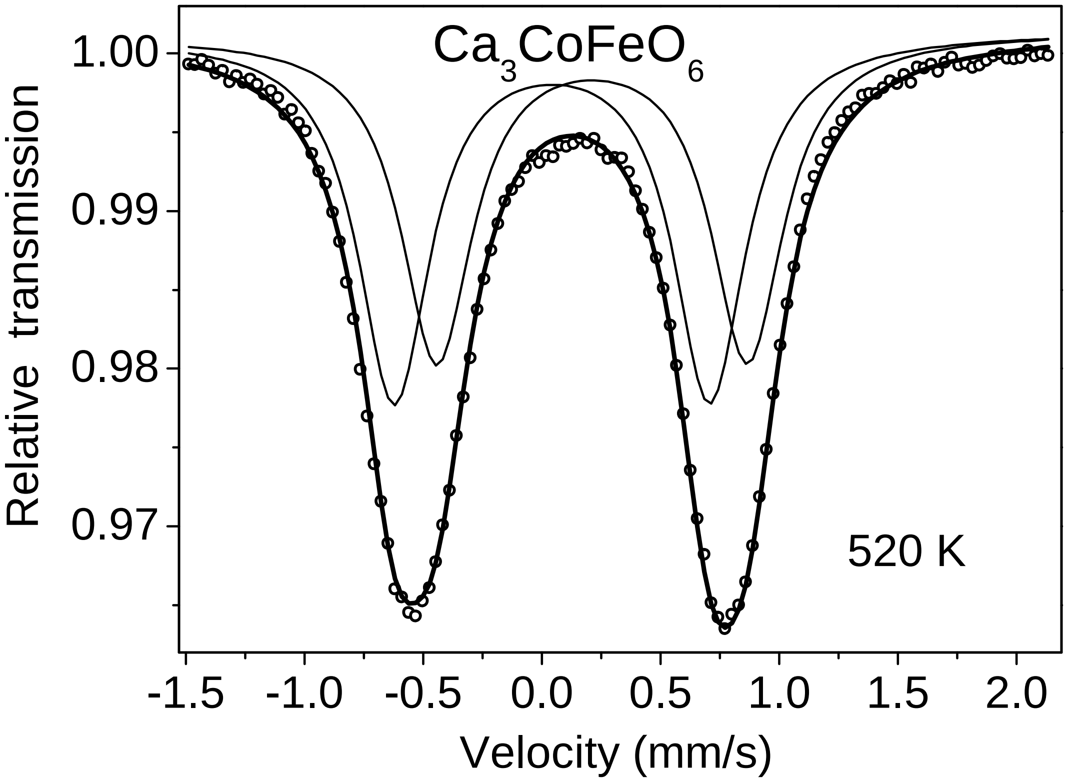

Figure 3.10: The Mössbauer spectra of Ca$_3$CoFeO$_6$ at 520 K.

3.3.2.2 Mössbauer Study

Figure 3.10 depicts the Mössbauer spectrum for the compound Ca$_3$CoFeO$_6$ at 520 K, above magnetic ordering temperature $T_N \sim 500$ K (discussed in Chapter 4). The spectrum is composed of two Fe subspectra associated with the two different crystallographic sites (Fig. 3.10). The one with the larger isomer shift and positive qaudrupole interaction is denoted arbitrarily as site "1". The derived values of the isomer shift and qaudrupole interaction are 0.22 and 0.64 mm/s for site "1", and 0.05 and -0.65 mm/s for site "2", respectively. The relative spectral area, which gives information about the relative occupation of "Fe", is almost equal for the site "1" and "2". Thus it is clear that in the compound Ca$_3$CoFeO$_6$, the iron occupies two different crystallographic sites with almost equal probability. The results of a detailed Mössbauer study below T_N will be presented in Chapter 4.

3.3.3 Crystal Structure of $\mathrm{Ca}_{2.75}\boldsymbol{R}_{0.25}\mathrm{Co}_2\mathrm{O}_6$

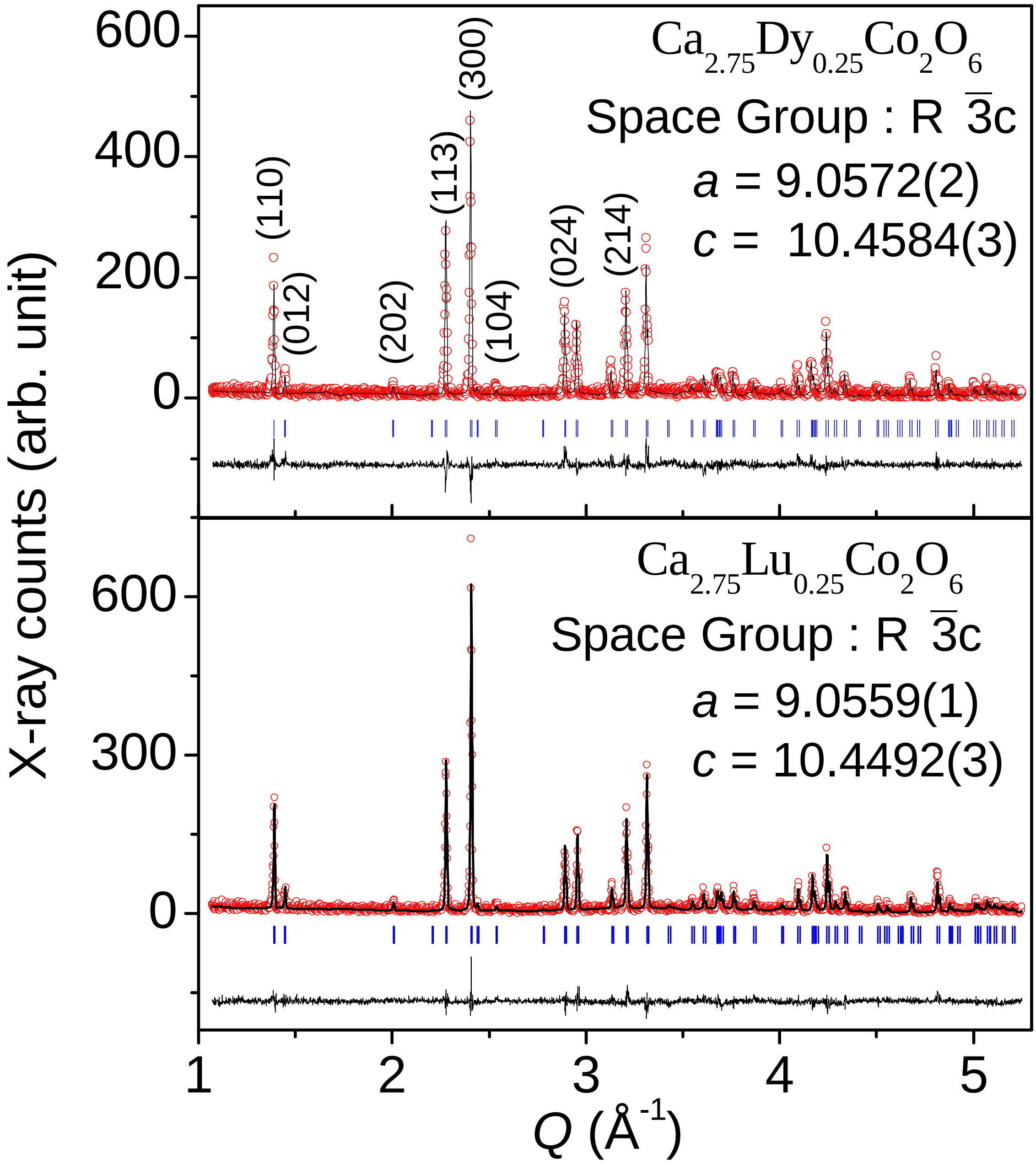

Figure 3.11: Observed (open circles) and calculated (solid lines) x-ray diffraction patterns of $\mathrm{Ca}_{2.75}R_{0.25}\mathrm{Co}_2\mathrm{O}_6$($R$ = Lu and Dy) at 297 K. Solid line at the bottom of each panel shows difference between observed and calculated patterns. Vertical lines show the position of the Bragg peaks. The (*hkl*) values corresponding to stronger Bragg peaks are also listed.

The crystal structure of the compounds $\mathrm{Ca}_{2.75}R_{0.25}\mathrm{Co}_2\mathrm{O}_6$ (R = Lu and Dy) has been investigated by combining the Rietveld refinement of x-ray and neutron diffraction patterns. The unit cell parameters with high precision were determined from

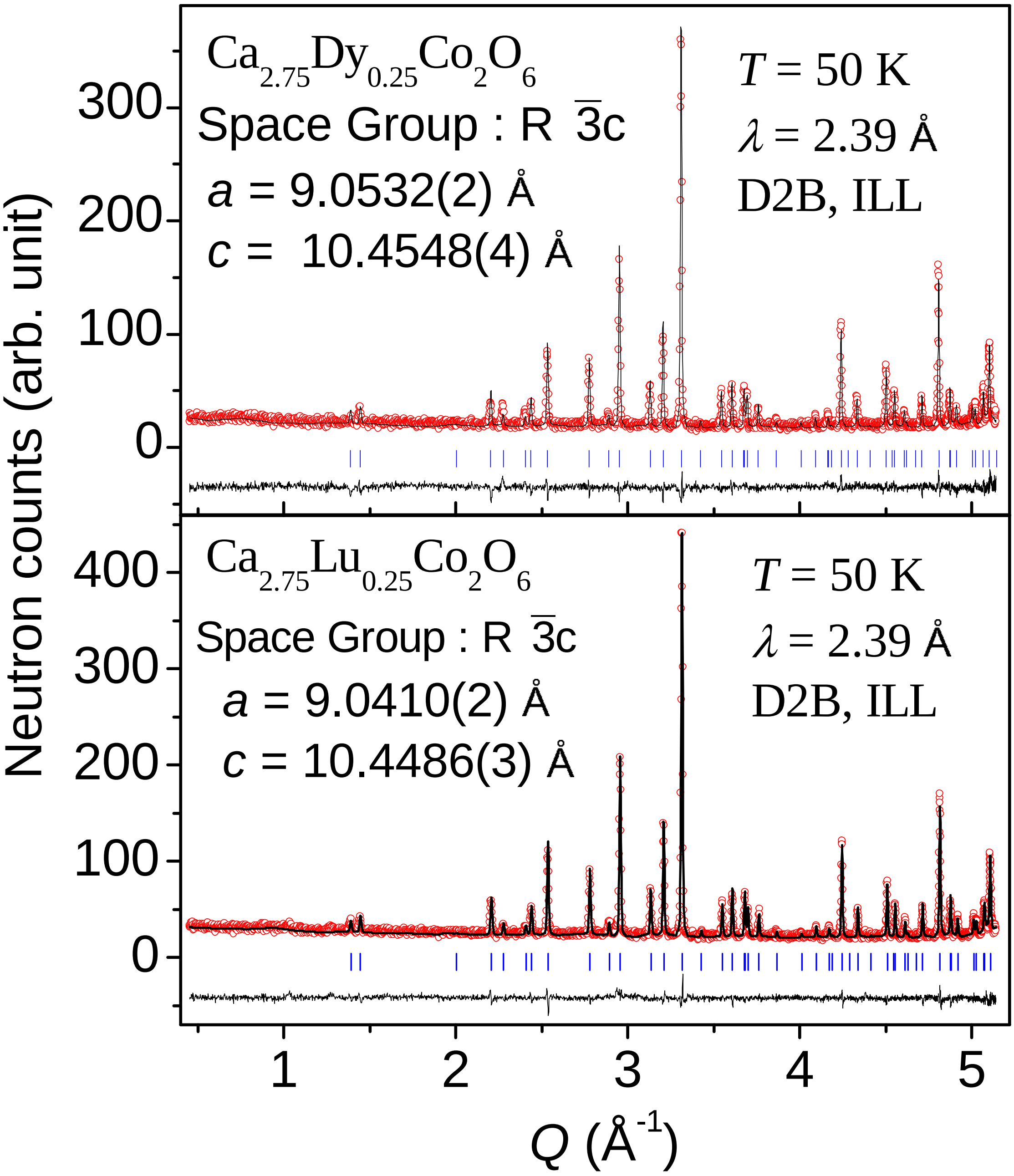

Figure 3.12: Observed (open circles) and calculated (solid lines) neutron diffraction patterns of $Ca_{2.75}R_{0.25}Co_2O_6$(R = Lu and Dy) at 50 K. Solid line at the bottom of each panel shows difference between observed and calculated patterns. Vertical lines show the position of the Bragg peaks.

the Rietveld refinement of the x-ray diffraction patterns at room temperature. The refined unit cell parameters were used as a starting point in the refinement of the neutron powder diffraction patterns. For the lighter atoms, the neutron scattering is more sensitive than the x-ray scattering, therefore, the positions of the oxygen atoms obtained from the refinement of the neutron diffraction patterns were included and fixed in the last step of the refinement of the room temperature x-ray diffraction patterns. Following this procedure, we have obtained reliable unit cell parameters. The Rietveld refined room temperature x-ray diffraction patterns are shown in Fig. 3.11, whereas the refined neutron diffraction patterns at 50 K are shown in Fig. 3.12. The Rietveld refinement of x-ray and neutron diffraction patterns confirms the single phase formation of both compounds in the rhombohedral structure (space group $R\bar{3}c$). The crystal structure contains linear chains that are made up of alternating face-sharing CoO_6 octahedra (with Co1) and CoO_6 trigonal prisms (with Co2), running along the crystallographic c axis. The refined unit cell parameters and other structural parameters obtained from the refinement of the room temperature x-ray patterns are given in Table 3.3. A comparison of the observed structural parameters with that for the parent compound $Ca_3Co_2O_6$ (Table 3.2) shows that with a substitution of rare-earth ions, the lattice constant c increases, however, the lattice constant a decreases. The bond lengths Co2-O and Co1-Co2 increase significantly, however, no significant change is observed in the bond length Co1-O. The observed increase in the bond lengths Co2-O with rare-earth substitution suggests that extra electrons are transferred to the Co ions at the TP site, which is further supported by dc magnetization, and low temperature neutron diffraction studies (discussed in Chapter 6). For the parent compound $Ca_3Co_2O_6$, the bond-valence sum (BVS) of $\sim$ 3.2 and 2.2 have been reported in the literature for the Co1 and Co2 ions, respectively [46]. For the rare substituted compounds, the calculated BVSs values using the program Bondstr [40] for the Co1 and Co2 are $\sim$ 3.21 and 1.91 for R = Dy, and 3.15 and 1.92 for R = Lu, respectively. The observed decrease in the BVSs confirms that the oxidation state of a fraction of the cobalt ions at the TP site is reduced from Co^{3+} to Co^{2+}.

Table 3.3: Structural parameters (atomic positions, thermal parameters, bond lengths, and bond angles) obtained from the refinement of the x-ray diffraction patterns at room temperature for $Ca_{2.75}R_{0.25}Co_2O_6$ (R = Lu and Dy). Both compounds crystallize in the space group $R\bar{3}$c. The lattice constants are $a = 9.0572(2)$Å, $c = 10.4584(3)$Å and $a = 9.0559(1)$Å, $c = 10.4492(3)$Å for R = Dy and Lu , respectively. All crystallographic sites are fully occupied.

Compound	Atom	Site	x	y	z	B_{iso}(Å^2)
R= Dy	Ca/Dy	18e	0.3692(3)	0	0.25	0.34(2)
	Co1	6b	0	0	0	0.39(6)
	Co2	6a	0	0	0.25	0.31(5)
	O	36f	0.1786(8)	0.0220(9)	0.1124(6)	0.78(3)
		Bond lengths (inÅ)				
	Co1-Co2	2.6146(2)				
	Co1-O	1.928(9)				
	Co2-O	2.099(6)				
		Bond angle				
	Co1-O-Co2	80.9(2)°				
R = Lu	Ca/Lu	18e	0.3692(3)	0	0.25	0.32(2)
	Co1	6b	0	0	0	0.33 (6)
	CO2	6a	0	0	0.25	0.35(5)
	O	36f	0.1783(8)	0.0254(9)	0.1120(6)	0.81(3)
		Bond lengths (inÅ)				
	Co1-Co2	2.6123(3)				
	Co1-O	1.913(7)				
	Co2-O	2.090(7)				
		Bond angle				
	Co1-O-Co2	81.4(3)°				

3.4 Summary and Conclusions

We have prepared single phasic polycrystalline samples of the spin-chain compounds $Ca_3Co_{2-x}Fe_xO_6$ (x = 0, 0.1, 0.2, 0.4, and 1.0) and $Ca_{2.75}R_{0.25}Co_2O_6$(R = Lu and

Dy). Rietveld refinement of x-ray and neutron diffraction patterns confirms that all compounds, except Ca_3CoFeO_6, crystallize in the rhombohedral structure (space group $R\bar{3}c$) and the crystal structure contains one-dimensional chains of alternating face-sharing CoO_6 octahedra (with Co1) and $(Co/Fe)O_6$ trigonal prisms (with Co2/Fe), running along the crystallographic c axis. With the Fe-substitution ($x \leq 0.4$), no significant changes in the lattice parameters, unit cell volume, bond angles, and bond lengths have been observed. For the compounds $Ca_3Co_{2-x}Fe_xO_6$ ($x = 0.1$, 0.2, and 0.4), the Rietveld refinement of neutron diffraction patterns, and Mössbauer study confirm that the Fe^{3+} ions (in the HS state) are located only at the TP site. For the rare earth substituted compounds $Ca_{2.75}R_{0.25}Co_2O_6$(R = Lu and Dy), the refinement shows that trivalent rare earth ions (R^{3+}) are located at the Ca^{2+} ($18e$) site, and bond lengths Co2-O and Co1-Co2 increase significantly, as compared to the parent compound $Ca_3Co_2O_6$. The observed increase in the bond lengths Co2-O, with rare earth substitution, suggests that extra electrons are transferred to the Co2 ions at the TP site. For the compound Ca_3CoFeO_6 ($x = 1$), the profile matching refinement of the x-ray diffraction pattern confirms the triclinic crystal structure (space group $P\bar{1}$).

Chapter 4

Magnetic Ground State of Spin-chain Compounds $Ca_3Co_{2-x}Fe_xO_6$

4.1 Introduction

Among the A_3MXO_6-type spin-chain compounds, which crystallize in the space group $R\bar{3}c$, the compound $Ca_3Co_2O_6$ and its derivatives are model systems for the triangular lattice antiferromagnets [42, 50, 52–57, 57–67]. In the $Ca_3Co_2O_6$, Co^{3+} ions are located at $6a$ [trigonal prisms (TP)] and $6b$ [octahedra (OCT)] crystallographic sites. Due to the crystalline electric field, the Co^{3+} ions in this compound have very strong Ising-like anisotropy with moment (for the TP sites), preferentially aligned along the crystallographic c direction. The Co^{3+} ions in the adjacent spin chains are shifted by 1/6 or 1/3 along the c axis, perpendicular to the ab plane. The compound $Ca_3Co_2O_6$ is reported to undergo two successive magnetic phase transitions at $T_{N1} \approx 25$ K and $T_{N2} \approx 10$ K [68]. In the temperature range between T_{N1} and T_{N2}, this compound would exhibit a partially disordered antiferromagnet (PDA) state [as shown in the Fig. 4.1 (a)], a state where 2/3 ferromagnetic Ising spin chains order with antiferromagnetic interchain interaction while the remaining 1/3 are left incoherent (disordered with zero net magnetization) [68]. There is sill an ambiguity regarding the nature of the magnetic state of this compound below T_{N2}, whether it is a frozen spin state (a state in which 1/3 incoherent spin chains freeze randomly) or a ferrimagnetic (FI) state [as shown Fig. 4.1 (b)]. The very

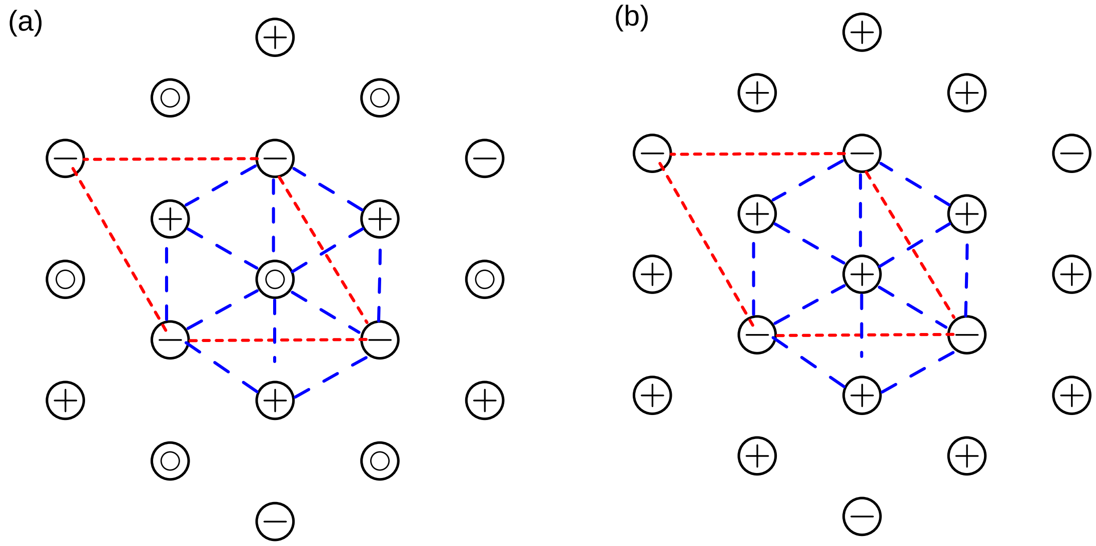

Figure 4.1: Schematic diagram of (a) PDA state and (b) ferrimagnetic (FI) state. The circles correspond to the Ising spin chains running along the crystallographic c axis. The plus and minus signs correspond to the direction of the magnetic moment along the crystallographic c axis; zero (0) represents the incoherent (the chain with net zero moment) spin chain. The red short-dashed lines represent the unit cell in the ab plane and the blue long-dashed lines represent the triangular arrangement of spin chains.

first low temperature neutron powder diffraction study for the compound $Ca_3Co_2O_6$ was carried out by Aasland *et al.* [52]. Based on the analysis of neutron diffraction patterns, Aasland *et al.* proposed a model for the magnetic structure; according to this model, the magnetic structure consists of chains (ordered ferrimagnetically) of alternating magnetic moments of (0.08 ± 0.04) μ_B and (3.00 ± 0.05) μ_B for Co^{3+} at OCT and TP sites, respectively. The moments in a single chain lie along the c axis (coupled ferromagnetically). Kageyama [63] *et al.* also proposed the same model and they ascribed a reduction in the intensity of the (100) peak below 13 K to a decrease in the ferrimagnetic domain size. The single crystal neutron diffraction study for the compound $Ca_3Co_2O_6$ was carried out by Petrenko *et al.* [62] in an applied magnetic field $H \| c$, and they proposed the existence of the PDA state. However, based on the ratio of intensity of antiferromagnetic peaks for field cooled and zero field cooled samples, they concluded that the ground state of $Ca_3Co_2O_6$ was not a simple PDA state. In zero field, they observed a decrease in the intensity of the AFM Bragg peak (100) below 15 K, which was ascribed to a possible appearance of the magnetic domains. According to Petrenko *et al.*, a model describing magnetic domains might include the xy spin components, *i.e.*, a small deviation of the Co^{3+} spins from an Ising-like behavior (moment along c axis) was possible [62]. Another important compound Ca_3CoRhO_6, in the family of A_3MXO_6, was reported (in the neutron powder diffraction study) to order in the PDA state below 90 K [66].

In order to investigate the variation in the crystal structure and magnetic properties associated with $3d$ electron filling at octahedral/trigonal prism sites in $Ca_3Co_2O_6$ compound, we substituted cobalt with iron. The choice of the iron substitution at the cobalt site was motivated by the fact that, in $Ca_3Co_2O_6$, the Co^{3+} ions at the TP site was reported to have an orbital moment of 1.7 μ_B [69], however, Fe^{3+} ions have a closed sub-shell, without an orbital degree of freedom, and therefore no orbital momentum for Fe^{3+} was expected. Moreover, the ionic radii of Co^{3+} and Fe^{3+} ions in the six oxygen coordination are very close, no lattice effect, therefore, was expected to be present. The magnetism of these Fe-substituted compounds is unique in the sense that spin chains are made up of different type of spins: Fe^{3+} (Heisenberg) and Co^{3+} (Ising). Rietveld refinement of x-ray and neutron diffraction patterns confirmed that the compounds $Ca_3Co_{2-x}Fe_xO_6$ (x = 0, 0.1, 0.2, and 0.4), crystallized in the space group $R\bar{3}c$ (Chapter 3). The Rietveld refinement of neutron diffraction patterns and Mössbauer study also confirmed that the Fe^{3+} ions (in the HS state) were located only at the TP site. Magnetic properties of the compounds $Ca_3Co_{2-x}Fe_xO_6$ ($x \leq 0.1$) have also been investigated by other groups[50, 64] using Mössbauer spectroscopy. In the Mössbauer study of the compound $Ca_3Co_{1.98}Fe_{0.02}O_6$, Kageyama *et al.*[50] observed that Fe spin behaves as an "isolated paramagnetic moment" in the ordered host spin system and there is no exchange interaction between Co and Fe spins. Based on the analysis of the Mössbauer spectra of the compounds $Ca_3Co_{2-x}Fe_xO_6$(x = 0.02, 0.04, and 0.1), Arai *et al.*[64] reported that Fe^{3+} spin remains in the "paramagnetic state" in the ferromagnetically ordered chains below the magnetic ordering temperature of 23 K, indicating that Fe spins are scarcely coupled with the Co spins having a strong Ising nature. The isolated electron state of Fe^{3+} with $g = 2.00$ has also been observed in the ESR study of the compound $Ca_3Co_{1.98}Fe_{0.02}O_6$ by Kageyama *et al.* [70].

In order to understand how the iron in the paramagnetic state [70] affects the spin structure, we have carried out a neutron powder diffraction study as a function of temperature for the compounds $Ca_3Co_{2-x}Fe_xO_6$ (x = 0, 0.2, and 0.4) and the results are discussed in the present Chapter. The aim of this study is to investigate the nature of the magnetic ground state of these iron-substituted compounds and to compare it with that of the parent compound $Ca_3Co_2O_6$.

For the compound Ca_3CoFeO_6, the results of x-ray diffraction study (Chapter 3) showed that the crystal structure has changed to triclinic (space group $P\bar{1}$). Mössbauer spectroscopy study showed that the iron resides almost equally in two different crystallographic sites. We do not have information about the positions of the atoms in the unit cell for this compound. Hence, we have not carried out any low temperature neutron diffraction study for this compound. However, the magnetic properties have been studied using the Mössbauer spectroscopy and the dc magnetization techniques (Section 4.3.6).

The results presented in this Chapter have been published [71–73] in international scientific journals.

4.2 Experimental Details

Polycrystalline samples of the compounds $Ca_3Co_{2-x}Fe_xO_6$ (x = 0, 0.2, 0.4, and 1) were prepared by the conventional solid-state reaction method as described in Chapter 2. Rietveld refinement of room-temperature x-ray powder diffraction patterns confirmed that all compounds, except Ca_3CoFeO_6, crystallized in the space group $R\bar{3}c$ (Chapter 3).

For the compounds with $x = 0$, 0.2, and 0.4, the neutron diffraction experiments in the temperature range of 1.5 - 100 K were performed on the cold neutron powder diffractometer DMC at the Paul Scherrer Institute (PSI), Switzerland. For these measurements, a vanadium can containing the sample was placed in a helium "orange" cryostat. A constant wavelength of 2.46 Å was used, and the diffraction data were analyzed by the Rietveld method using the FULLPROF program [40]. The representation theory analysis was performed using the BASIREPS software [40].

For the compound Ca_3CoFeO_6, which crystallized in the space group $P\bar{1}$ (Chapter 3), the magnetization measurements were carried out using a commercial (Oxford Instruments) vibrating sample magnetometer.

The Mössbauer study for the compounds with $x = 0.2$, 0.4, and 1.0 was performed using a conventional constant acceleration drive, a 50 mCi ^{57}Co: Rh source, and absorbers, putting in perspex holders for low temperatures (4.2 - 300 K) and in boron nitride holders for high temperature measurements (300 - 520 K). The velocity calibration was done with a room temperature α-Fe absorber. The experimentally observed spectra were least square fitted with calculated spectra according to various models. The spectra for the $x = 0.2$ and 0.4 samples, at 90 and 300 K, were fitted in terms of spin up-down relaxation theory formulas [74]. The spectra for the $x = 1$ sample were analyzed in terms of full diagonalization of the Hamiltonian of magnetic and quadrupole interactions, where the magnetic field is at an angle θ relative to the local axis of the electric field gradient (EFG), for simplicity, assuming axial symmetry for two different sites of iron.

4.3 Results and Discussion

4.3.1 Commensurate Magnetic Structure of $Ca_3Co_2O_6$

Figure 4.2 (a) depicts the Rietveld refined neutron diffraction patterns for the compound $Ca_3Co_2O_6$ at 100 K. The Rietveld refinement [Fig. 4.2(a)] confirms the single phase formation of the compound in the space group $R\bar{3}c$. The refined values of the structural parameters are in good agreement with the values reported in the literature [52]. The additional Bragg peaks in the neutron diffraction pattern at 20 K (Figs. 4.2 (b) and (c)), which is below the magnetic ordering temperature ($T_N \sim$ 25 K), indicate an antiferromagnetic ordering. These additional Bragg peaks can be indexed using the propagation vector $\boldsymbol{k} = \{0, 0, 1\}$ as described below. The magnetic structure has been analyzed using the standard irreducible representational theory as described by Bertaut [75, 76]. Following that methodology, we have determined the propagation vector group G_k (little group), which is formed by the set of symmetry operations and transforms the propagation vector into an equivalent vector differing by some arbitrary reciprocal lattice translation. In this particular case, it is important to take into account that $\boldsymbol{k}$ is not equivalent to -$\boldsymbol{k}$ and it is also necessary to use both vectors for calculating the magnetic moments (discussed later). For the propagation vector $\boldsymbol{k} = \{0, 0, 1\}$, the irreducible representations of the propagation vector group G^k are given in Table 4.1. The representations Γ_1 and Γ_2 are one-dimensional, while representation Γ_3 is two dimensional. In $Ca_3Co_2O_6$, Co1 and Co2 ions are located at the $6b$ (0, 0, 0) and $6a$ (0, 0, 1/4) sites, respectively.

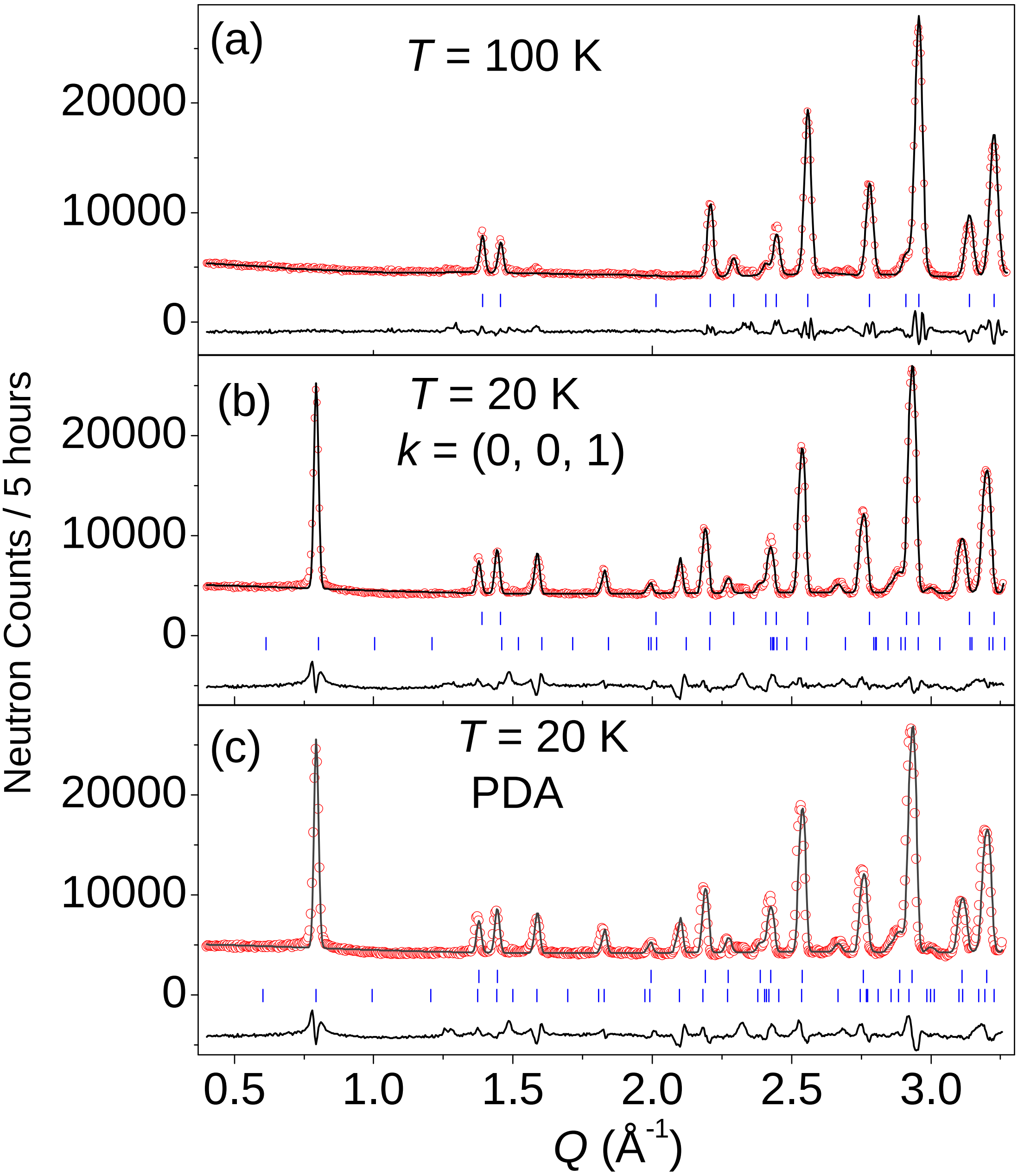

Figure 4.2: The Rietveld refined neutron powder diffraction patterns of $Ca_3Co_2O_6$ at (a) 100 K, (b) 20 K using the amplitude modulated $\{\boldsymbol{k} = 0, 0, 1\}$, and (c) 20 K using the PDA structure: experimental data (open circle), calculated curve (solid line), and difference (solid line at the bottom). Vertical marks correspond to the position of all allowed Bragg reflections for the crystal (top row) and magnetic (bottom row) reflections. Neutron diffraction pattern at 100 K show only nuclear Bragg reflections.

Table 4.1: Irreducible representation of the group of the propagation vector G_k, $a = /exp\ (2\ \pi\ i/3)$, $b = /exp\ (4\ \pi\ i/3)$.

Symmetry element G_k	1	$3_{(0,0,z)}{}^{+}$	$3_{(0,0,z)}{}^{-}$	(x, -x, z)	(x, 2x, z)	(2x, x, 2z)
Γ_1	1	1	1	1	1	1
Γ_2	1	1	1	-1	-1	-1
Γ_3	$\begin{pmatrix} 1 & 0 \\ 0 & 1 \end{pmatrix}$	$\begin{pmatrix} a & 0 \\ 0 & b \end{pmatrix}$	$\begin{pmatrix} b & 0 \\ 0 & a \end{pmatrix}$	$\begin{pmatrix} 0 & 1 \\ 1 & 0 \end{pmatrix}$	$\begin{pmatrix} 0 & b \\ a & 0 \end{pmatrix}$	$\begin{pmatrix} 0 & a \\ b & 0 \end{pmatrix}$

By using the great orthogonality theorem, the magnetic reducible representations $\Gamma(6b)$ and $\Gamma(6a)$ for these sites can be decomposed as direct sum of irreducible representations as

$$\Gamma(6b \mid Co1) = 1\Gamma_1^{(1)} + 1\Gamma_2^{(1)} + 2\Gamma_3^{(2)} \tag{4.1}$$

and

$$\Gamma(6a \mid Co2) = 1\Gamma_1^{(1)} + 1\Gamma_2^{(1)} + 2\Gamma_3^{(2)}. \tag{4.2}$$

According to the Bertaut method, in the first approximation, the vectors having the same representation of both sites may be coupled [75, 76]. Therefore, we shall first consider the representations Γ_1 and Γ_2 to describe the magnetic structure of the compound $Ca_3Co_2O_6$. The magnetic moment of the atom "j" in the asymmetric magnetic unit cell with the origin at the lattice point R_L, for a magnetic structure characterized by a set of propagation vectors $\{\boldsymbol{k}\}$, can be written as the Fourier series of the form

$$\boldsymbol{m}_{L,j} = \sum_{\mathbf{k}} \mathbf{S}_j^k\ exp(-2\pi i\boldsymbol{k}.\boldsymbol{R}_L). \tag{4.3}$$

If $\boldsymbol{k} = 1/2\boldsymbol{H}$, $\boldsymbol{H}$ being a reciprocal lattice vector, the Fourier coefficients are directly the magnetic moments. In a general case, the Fourier coefficients are complex vectors. If $\boldsymbol{k}$ is at the interior of Brillouin Zone, then $\boldsymbol{k}$ is not equivalent to -$\boldsymbol{k}$, and the vector sum must be extended to the pair $\boldsymbol{k}$ and -$\boldsymbol{k}$ taking into account that

$\boldsymbol{S}_j^k = \boldsymbol{S}_j^{-k}$. Moreover a 1/2 factor must be included in the calculations of the magnetic moments. These Fourier coefficients can be written as a linear combination of the basis vectors of the irreducible representation of the propagation vector group $\boldsymbol{G}_k$,

$$\boldsymbol{S}_j^{\mathbf{k}} = \sum_a C_{a,m}^j \Psi_{a,m}^{k,j} \ . \tag{4.4}$$

Here, $C_{a,m}^j$ are the coefficients (real or purely imaginary) and $\Psi_{a,m}^{k,j}$ are the unitary basis vectors for atom j. The index a varies from 1 up to the dimension of the irreducible representation. The index m varies from 1 to the number of times the irreducible representation is contained in the magnetic reducible representation. The Fourier coefficients, $\boldsymbol{S}_{js}^k$ for a site "js", in the orbit of the "j" atom can be calculated by transforming the $\boldsymbol{S}_j^k$ according to

$$\boldsymbol{S}_{js}^k = \boldsymbol{M}_{js} \boldsymbol{S}_j^k \exp(-2\pi i \phi_{js}^k) \ . \tag{4.5}$$

Where $\boldsymbol{M}_{js}$ is a transformation matrix and the phase ϕ_{js}^k is related with the centering and returning translations, and it is determined by symmetry. With all these ingredients the magnetic structure factor can be expressed as

$$\boldsymbol{F}_m(\mathbf{h}) = p \sum_{j=1}^{n} O_j f_j(\mathbf{h}) \sum_s T_{js} M_{js} \mathbf{S}_j^k exp\{2\pi i[\mathbf{h}\{S|\mathbf{t}\}_s \mathbf{r}_j - \varphi_{js}^{\boldsymbol{k}}]\} \ . \tag{4.6}$$

In this expression, $\boldsymbol{h} = \boldsymbol{H} + \boldsymbol{k}$, $p = 0.2695$, O_j is the occupation factor for the "j" orbit, $f_j(\mathbf{h})$ is the magnetic form factor of the atom j, T_{js} is the Debye-Waller factor for the atom placed in the position $\mathbf{r}_{js}$, $\{S|\mathbf{t}\}_s$ is the symmetry operator (rotational and translational part) that transform the atom in the position $\boldsymbol{r}_j$ to the atom in position $\boldsymbol{r}_{js}$. The φ_{js}^k phase factor includes the ϕ_{js}^k and a general phase Ψ_j^k which cannot be determined by symmetry and is same for all the atoms in the orbit "j" (

Table 4.2: Basis vectors of positions $6a$ and $6b$ for the representations Γ_1 and Γ_2.

IR	Basis vectors ${\psi_{a,m}}^{k,j}$ for $6b$ site		Basis vectors ${\psi_{a,m}}^{k,j}$ for $6a$ site	
	(0, 0, 0)	(0, 0, 1/2)	(0, 0, 1/4)	(0, 0, 3/4)
Γ_1	(0 0 1)	(0 0 -1)	(0 0 1)	(0 0 -1)
Γ_2	(0 0 1)	(0 0 1)	(0 0 1)	(0 0 1)

$\varphi_{js}^k = \phi_{js}^k + \Psi_j^k$).

The scattered intensity due to the magnetic periodicity, at the position given by $\boldsymbol{h}$, is proportional to the modulus square of the perpendicular component to the scattering vector $\boldsymbol{h}$ of the magnetic structure factor vector ($| \boldsymbol{F}_{m\perp}(\boldsymbol{h}) |^2$).

The basis vectors of special positions $6a$ and $6b$ for the representations Γ_1 and Γ_2 are given in Table 4.2. Figures 4.3 and 4.4(a) show the magnetic structures corresponding to the representations Γ_1 and Γ_2, respectively. In the representation Γ_1, the moments are aligned antiferromagnetically along the crystallographic c direction whereas, in the representation Γ_2, the moments are aligned ferromagnetically along the c direction. In both cases Γ_1 and Γ_2, the amplitudes of the site moments in the unit cell, labelled by the centring translation, t_1 = (2/3, 1/3, 1/3) and t_2 = (1/3, 2/3, 2/3), are modulated by a factor of $\cos(2\pi/3) = \cos(4\pi/3) = -0.5$. The observed neutron powder diffraction pattern at 20 K cannot be fitted with the magnetic structure corresponding to the representation Γ_1. However, the magnetic structure corresponding to the representation Γ_2, commonly referred to as amplitude modulated structure, is suitable to describe the observed neutron powder diffraction pattern. The Rietveld refined neutron diffraction pattern for the representation Γ_2 is shown in the Fig. 4.2(b). The magnetic moments for Co1 and Co2 ions located

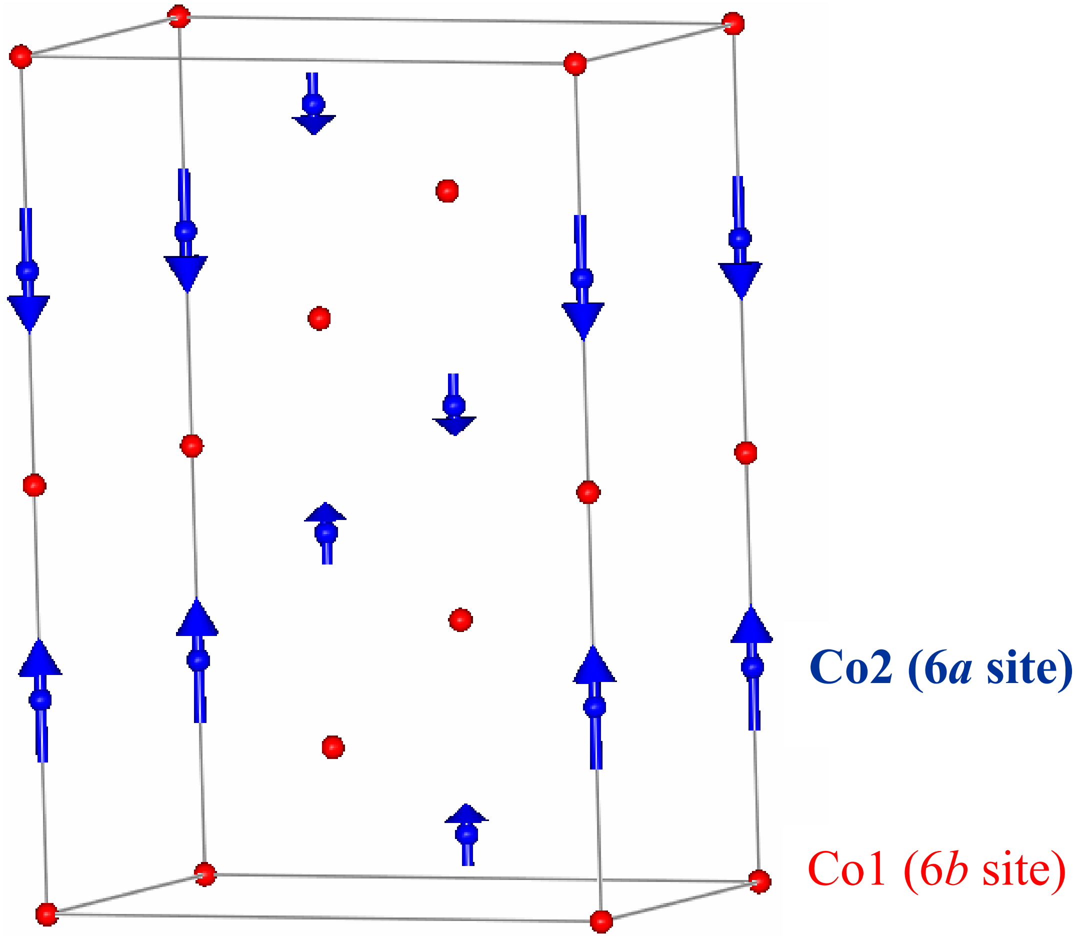

Figure 4.3: Magnetic structure corresponding to the representation Γ_1, where the moments are aligned antiferromagnetically along the crystallographic c direction. Sites $6a$ and $6b$ are in blue and red, respectively. Both $6a$ and $6b$ are occupied by Co^{3+} ions. The Co^{3+} ions at the $6b$ site are in low spin state (S = 0).

at the $6b$ (0, 0, 0) and $6a$ (0, 0, 1/4) sites, respectively, are given by:

$$\begin{aligned}
\mathbf{m}_{L,(j=6a,6b)} &= \sum_{(-\mathbf{k},+\mathbf{k})} \frac{1}{2}\mathbf{S}_j^k \exp(-2\pi i\mathbf{k}.\mathbf{R}_L) \\
&= \frac{1}{2}[\mathbf{S}_j^{\mathbf{k}} exp(-2\pi i\mathbf{k}.\mathbf{R}_L) + \mathbf{S}_j^{-\mathbf{k}} exp(-2\pi i\mathbf{k}.\mathbf{R}_L)] \\
&= \mathbf{S}_j^k \cos(2\pi\mathbf{k}.\mathbf{R}_L)\ . \qquad (4.7)
\end{aligned}$$

In the literature [58] it has been well established that the Co^{3+} ions at the $6b$ site are in low spin state ($S = 0$). In the present study, Rietveld refinement of the neutron diffraction patterns also yielded a magnetic moment value of $\sim 0.01(1)$

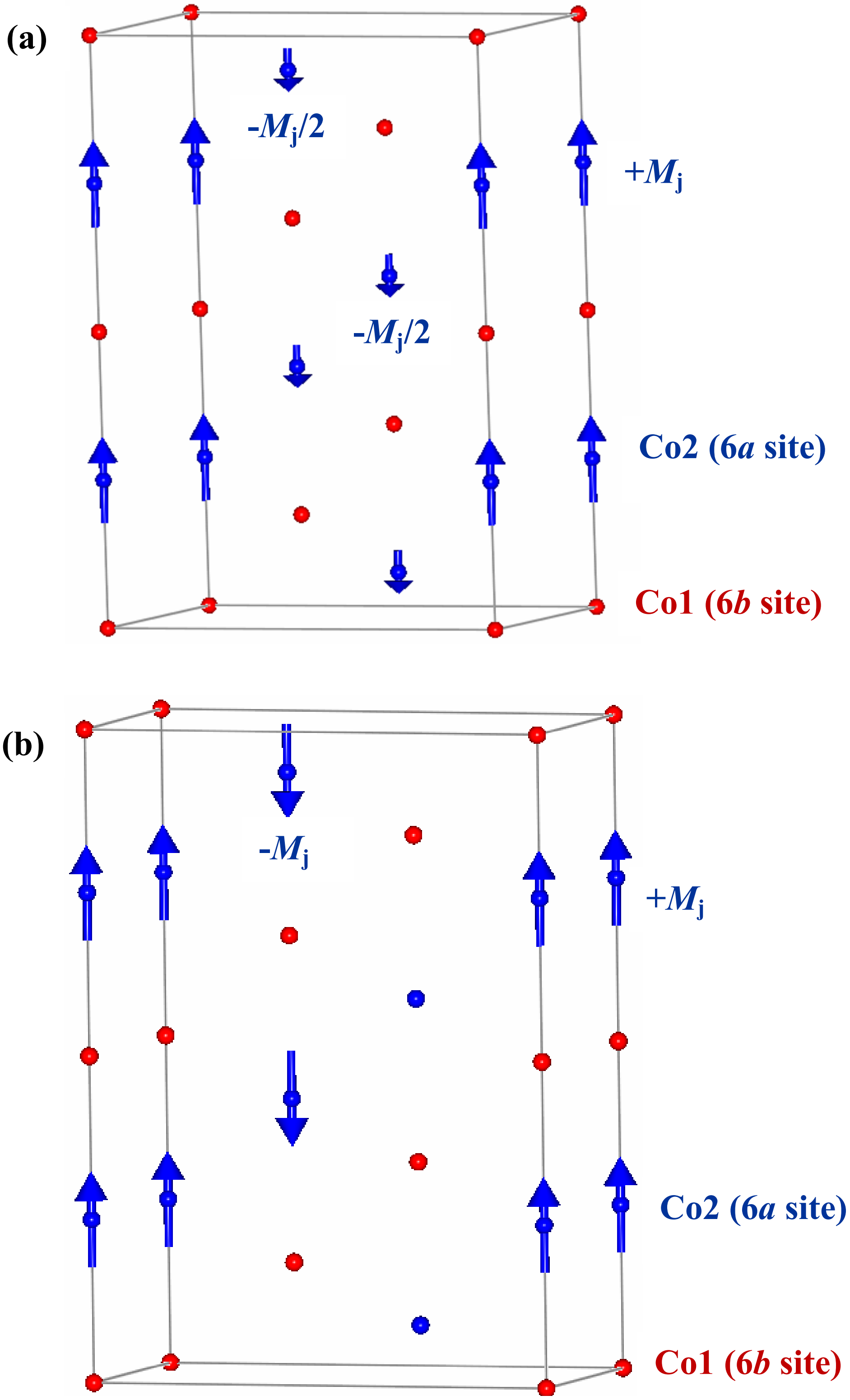

Figure 4.4: Magnetic structures corresponding to the representation (a) Γ_2 and (b) PDA model. Sites $6a$ and $6b$ are in blue and red, respectively. Both $6a$ and $6b$ are occupied by Co^{3+} ions. The Co^{3+} ions at the $6b$ site are in low spin state (S = 0). (a) In the representation Γ_2, the moments are aligned ferromagnetically along the c direction and are coupled antiferromagnetically in the ab plane. (b) The PDA model, similar to Γ_2 but with 1/3 of the sites with zero averaged magnetic moment.

μ_B/Co^{3+} ion at the 6b site. The maximum value of the ordered moment at the 6a site and its variation with temperature will be discussed later (in Sec. 4.3.4).

Here we would like to mention that the magnetic structure corresponding to the representation Γ_2 is different from the PDA structure reported in the literature for the compound $Ca_3Co_2O_6$, because in the PDA structure 1/3 chains are disordered. Therefore, in search of a possible PDA structure, we have tried to fit the observed neutron diffraction patterns using the space group $P\bar{1}$ and a propagation vector $\boldsymbol{k}$ = {0, 0, 0} referred to the nuclear cell. The Rietveld refined neutron diffraction pattern using the PDA structure is shown in Fig. 4.2(c) and the corresponding magnetic structure (PDA structure) is shown in Fig. 4.4(b).

Why are the two magnetic structures, the amplitude modulated structure and the PDA structure, able to fit the same neutron diffraction pattern will be discussed later (in Sec. 4.3.2). In addition, a time variation of the magnetic structure observed at lower temperatures (below $\sim$ 15 K) will also be discussed in detail (Sec. 4.3.4).

4.3.2 Commensurate Magnetic Structure of $Ca_3Co_{2-x}Fe_xO_6$

Figures 4.5 and 4.6 show, respectively, the Rietveld refined neutron powder diffraction patterns for the compounds $Ca_3Co_{2-x}Fe_xO_6$ with x = 0.2 and 0.4. The lattice parameters and refined atomic positions at 100 K for all atoms are listed in Table 4.3. The refined values of the structural parameters are in good agreement with those previously reported from independent x-ray and neutron diffraction studies [52, 77]. The Rietveld refinement of the neutron diffraction patterns confirmed that iron was located at the trigonal prism site (6a) which had already been confirmed by the Mössbauer spectroscopy study (Chapter 3). As shown in Figs. 4.5 - 4.7, the additional Bragg peaks start growing below 20 and 17 K for x = 0.2 and x = 0.4, respectively. These additional peaks, indexed with a propagation vector $\boldsymbol{k}$ =

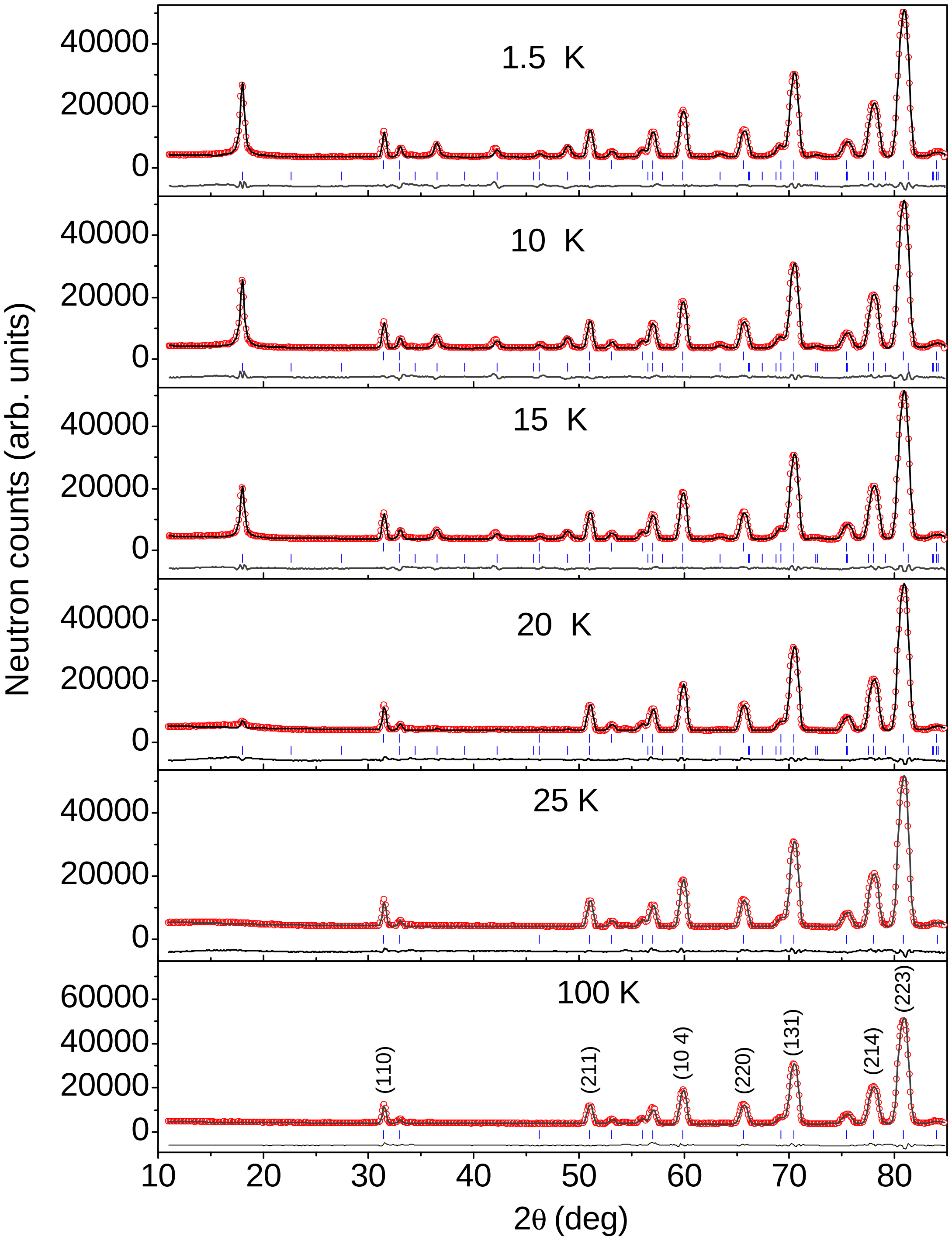

Figure 4.5: Observed (open circles) and calculated (solid lines) neutron diffraction patterns of $Ca_3Co_{1.8}Fe_{0.2}O_6$ using amplitude modulated structure $\{\boldsymbol{k} = 0,\ 0,\ 1\}$. Solid lines at the bottom of each panel shows the difference between the observed and the calculated patterns. The (hkl) values corresponding to stronger Bragg peaks are also listed. Vertical marks correspond to the position of all allowed Bragg reflections for the crystal (top row) and magnetic (bottom row) reflections. Neutron diffraction patterns at 100 and 25 K show only nuclear Bragg reflections.

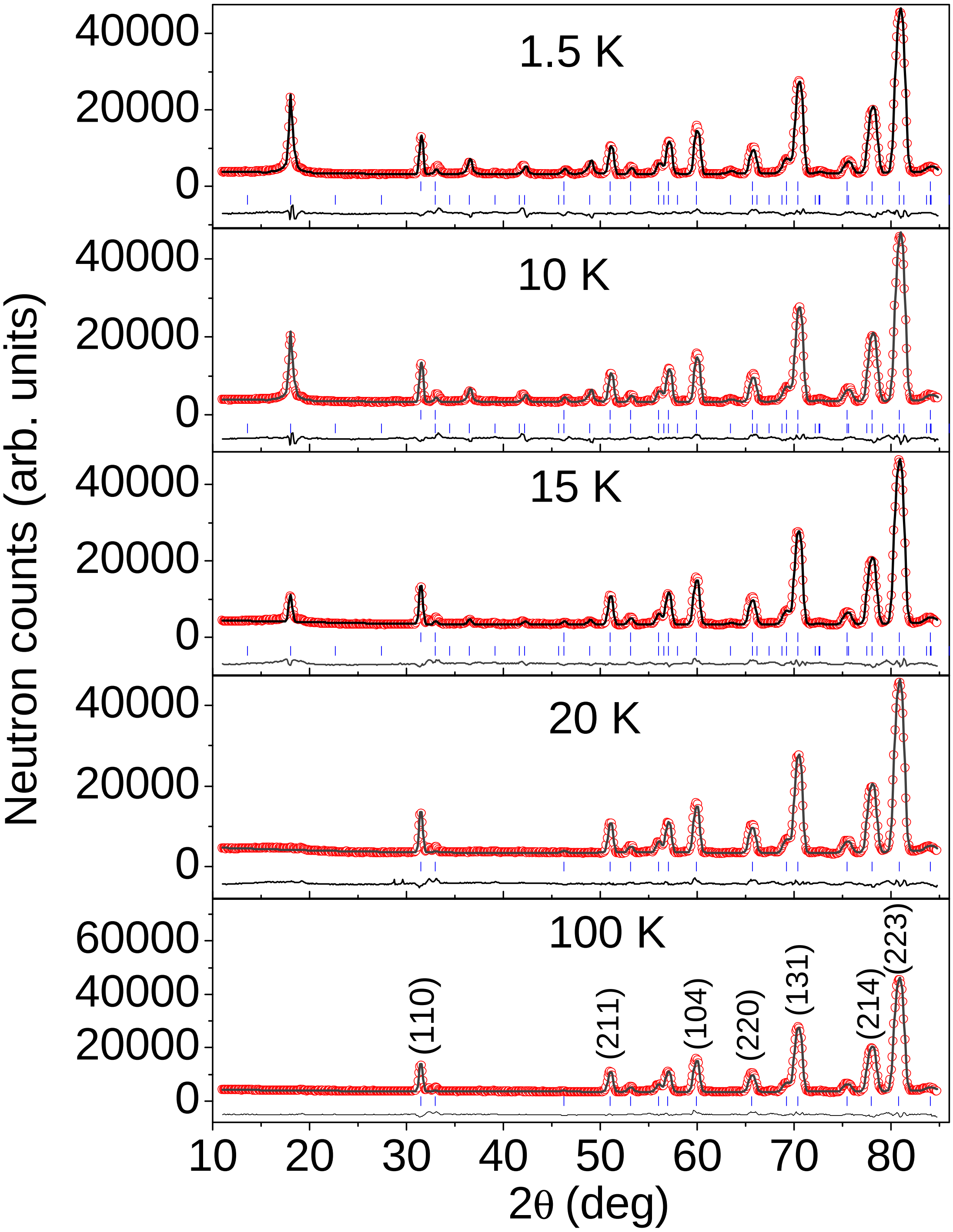

Figure 4.6: Observed (open circles) and calculated (solid lines) neutron diffraction patterns of $Ca_3Co_{1.6}Fe_{0.4}O_6$ using amplitude modulated structure $\{\boldsymbol{k} = 0,\ 0,\ 1\}$. Solid lines at the bottom of each panel shows the difference between the observed and the calculated patterns. The (*hkl*) values corresponding to stronger Bragg peaks are also listed. Vertical marks correspond to the position of all allowed Bragg reflections for the crystal (top row) and magnetic (bottom row) reflections. Neutron diffraction patterns at 100 and 25 K show only nuclear Bragg reflections.

Table 4.3: Results of the Rietveld refinement of neutron powder diffraction patterns at 100 K for $Ca_3Co_{2-x}Fe_xO_6$ (x = 0.2 and 0.4) samples. Atomic positions for the space group R$\bar{3}$c : Ca at 18e (x, 0, 1/4), Co1 at 6b (0, 0, 0), Fe/Co2 at 6a (0, 0, 1/4), and O at 36f (x, y, z).

	Lattice constants (Å)					
x	a	c	Atom	x	y	z
0.2	9.0774(1)	10.3821(3)	Ca	0.3717(3)	0	1/4
			O	0.1768(3)	0.0226(3)	0.1147(2)
0.4	9.0756(1)	10.3835(2)	Ca	0.3715(3)	0	1/4
			O	0.1772(2)	0.0236(2)	0.1142(2)

{0, 0, 1} referred to the space group $R\bar{3}c$, can be ascribed to an antiferromagnetic ordering of the Co^{3+} and Fe^{3+} spins in these compounds. The magnetic structure has been analyzed using the standard irreducible representational theory (discussed in Sec. 4.3.1) as described by Bertaut [75, 76]. For the propagation vector $\boldsymbol{k} = \{0, 0, 1\}$, the irreducible representations of the propagation vector group G^k are given in Table 4.1. The magnetic reducible representations for the sites 6b and 6a are given by Eqs. (4.1) and (4.2), respectively. The basis vectors of special positions 6a and 6b for the representations Γ_1 and Γ_2, are given in Table 4.2. Only the magnetic structure, corresponding to representation Γ_2, shown in Fig. 4.8(a), is suitable to describe the observed neutron powder diffraction patterns. The Rietveld refined neutron diffraction patterns for representation Γ_2 are shown in Figs. 4.5 and 4.6 for the $x = 0.2$ and $x = 0.4$ compounds, respectively. The magnetic moments for Co1 and Co2/Fe ions located at the 6b (0, 0, 0) and 6a (0, 0, 1/4) sites, respectively, are given by Eq. (4.7). The values of $\boldsymbol{m}_{6a}$ and $\mathbf{m}_{6b}$ for the $x = 0.2$ compound are 3.8(4) μ_B and 0.04(2) μ_B, respectively. While for the $x = 0.4$ compound, the values of $\boldsymbol{m}_{6a}$ and $\boldsymbol{m}_{6b}$ are 3.9(4) μ_B per site (6a) and 0.02(1) μ_B per site (6b),

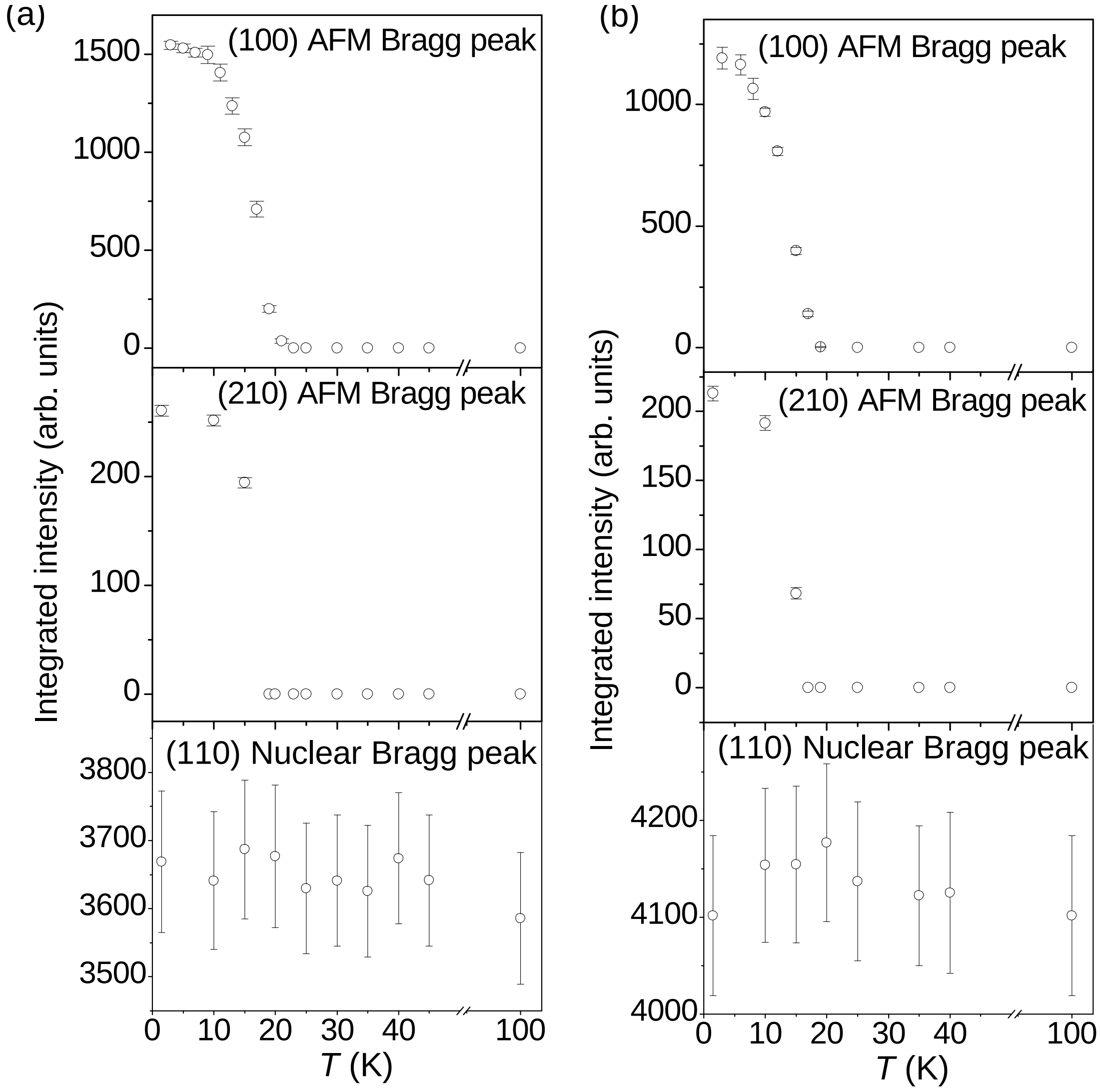

Figure 4.7: Temperature dependence of the integrated intensity of the antiferromagnetic reflections (100) and (210), and nuclear Bragg peak (110) for (a) $Ca_3Co_{1.8}Fe_{0.2}O_6$ (b) $Ca_3Co_{1.6}Fe_{0.4}O_6$.

respectively. The amplitudes of the site moments in the unit cell, labelled by the centring translation, $t_1 = (2/3, 1/3, 1/3)$ and $t_2 = (1/3, 2/3, 2/3)$, are modulated by a factor of $\cos(2\pi/3) = \cos(4\pi/3) = -0.5$ (as discussed in Section 4.3.1). This kind of magnetic structure may arise due to the presence of the competing interactions in the presence of the large axial anisotropy. In the present compounds, ferromagnetic intrachain and antiferromagnetic interchain interactions combined with the triangular lattice arrangement of the Ising spin chains give rise to the competing interactions. As mentioned in Section 4.1, a stronger crystalline electric field at the

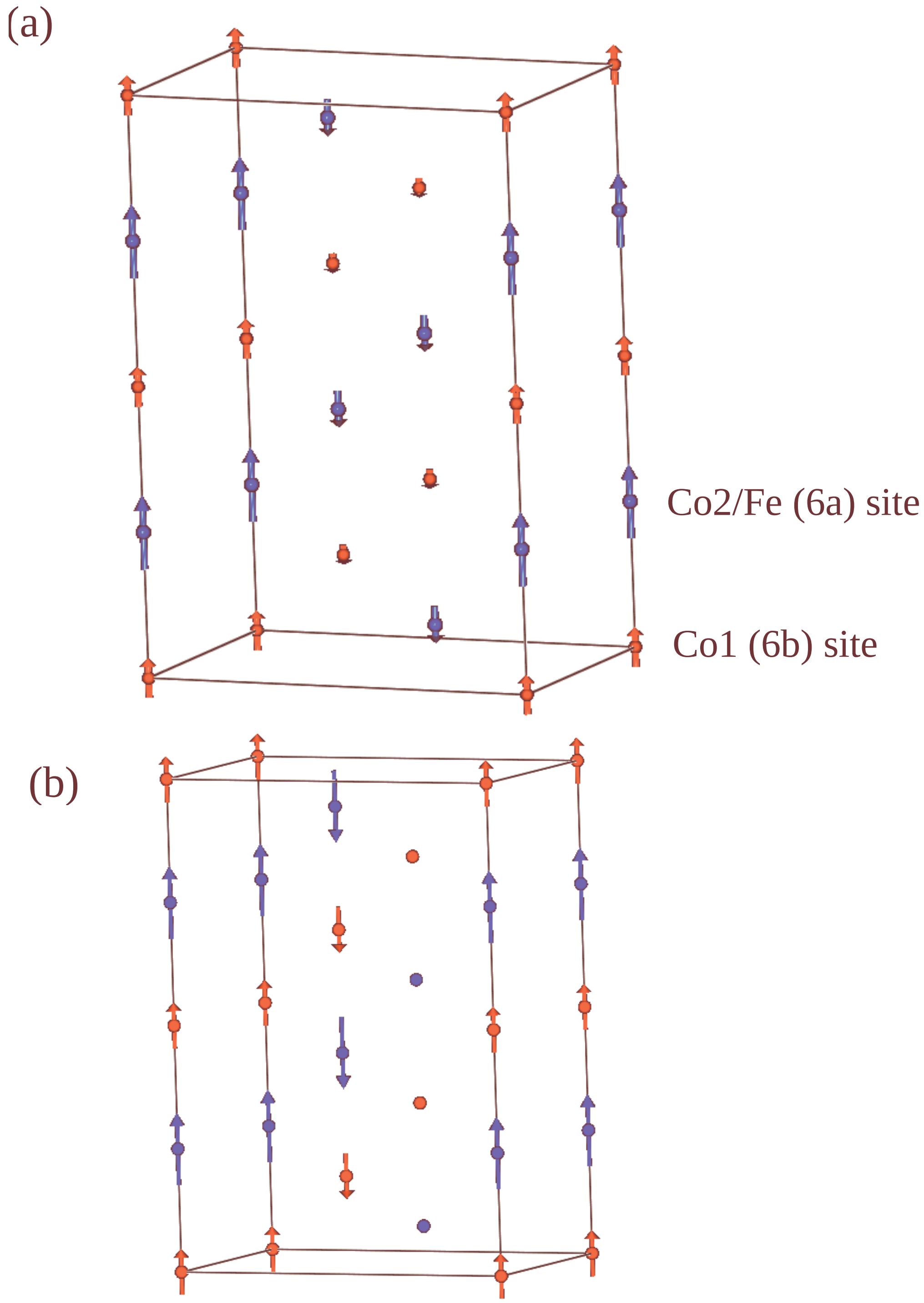

Figure 4.8: Magnetic structures corresponding to the representation (a) Γ_2 and (b) PDA model. Sites $6a$ and $6b$ are in blue and red, respectively. At $6a$ site there are two atoms Co and Fe with occupation factor (1-x) and x, respectively. At $6b$ there is only one atom Co with an occupation factor of 1. Magnetic moments are scaled in order to show the small magnetic moment at $6a$ sites. (a) In the representation Γ_2, the moments are aligned ferromagnetically along the c direction and are coupled antiferromagnetically in the ab plane. (b) The PDA model, similar to Γ_2 but with 1/3 of the sites with zero averaged magnetic moment. Long arrow: $6a$ site, short arrow: $6b$ site.

OCT site (6b site) can lead to the low spin state ($S = 0$) of the Co^{3+} ions in this compound [52] and, therefore, gives an explanation of the nearly zero value of the observed moment at the 6b site. For the 6a site, the observed value of the magnetic moments is less than the theoretically calculated value using the expression $\boldsymbol{m}_{6a} = [(1\text{-}x)\ \boldsymbol{m}_{Co} +\ x\ \boldsymbol{m}_{Fe}]$. Here $\boldsymbol{m}_{Co}$ and $\boldsymbol{m}_{Fe}$ are the spin only values of the ordered moment for Co^{3+} and Fe^{3+}. The theoretically expected ordered moment values with quenched orbital moment for $\mathbf{m}_{6a}$ (6a site) are 4.2 μ_B per site and 4.4 μ_B per site for $x = 0.2$ and 0.4, respectively. The R factors for the refinement are: $R_{Nuclear} = 1.35$ and $R_{Magnetic} = 9.24$ for the $x = 0.2$, and $R_{Nuclear} = 2.96$ and $R_{Magnetic} = 14.7$ for the $x = 0.4$ sample.

In a first inspection of the magnetic structure described above, it can be easily verified that the magnetic moments are not vanishing at any site and so no PDA model can be simulated using the propagation vector $\boldsymbol{k} = \{0, 0, 1\}$ and the space group $R\bar{3}c$. Therefore, in search of a possible PDA structure, we have tried to explain our experimental data using another model in which all the observed Bragg peaks have been indexed using the space group $P\bar{1}$ and a {0, 0, 0} propagation vector referred to the nuclear cell. The advantage of this model, in which we reduce the symmetry constraints, is that, for each site (6a or 6b), the six initial positions, earlier [for $\boldsymbol{k} = \{0, 0, 1\}$] related by the translations $t1 = (2/3, 1/3, 1/3)$ and $t2 = (1/3, 2/3, 2/3)$, and the operator (-y, -x, z+1/2) are decoupled in three pairs of sites only related now by (-y, -x, z+1/2). Then the low-temperature neutron powder diffraction patterns for all these iron-substituted compounds have been refined considering the PDA model. A schematic of the PDA magnetic structure has been shown in Fig. 4.8(b). In the PDA structure, 2/3 ferromagnetic Ising spin chains order with antiferromagnetic interchain interaction while the remaining 1/3 are left incoherent (disordered with zero net moment). Here it may be noted that the simi-

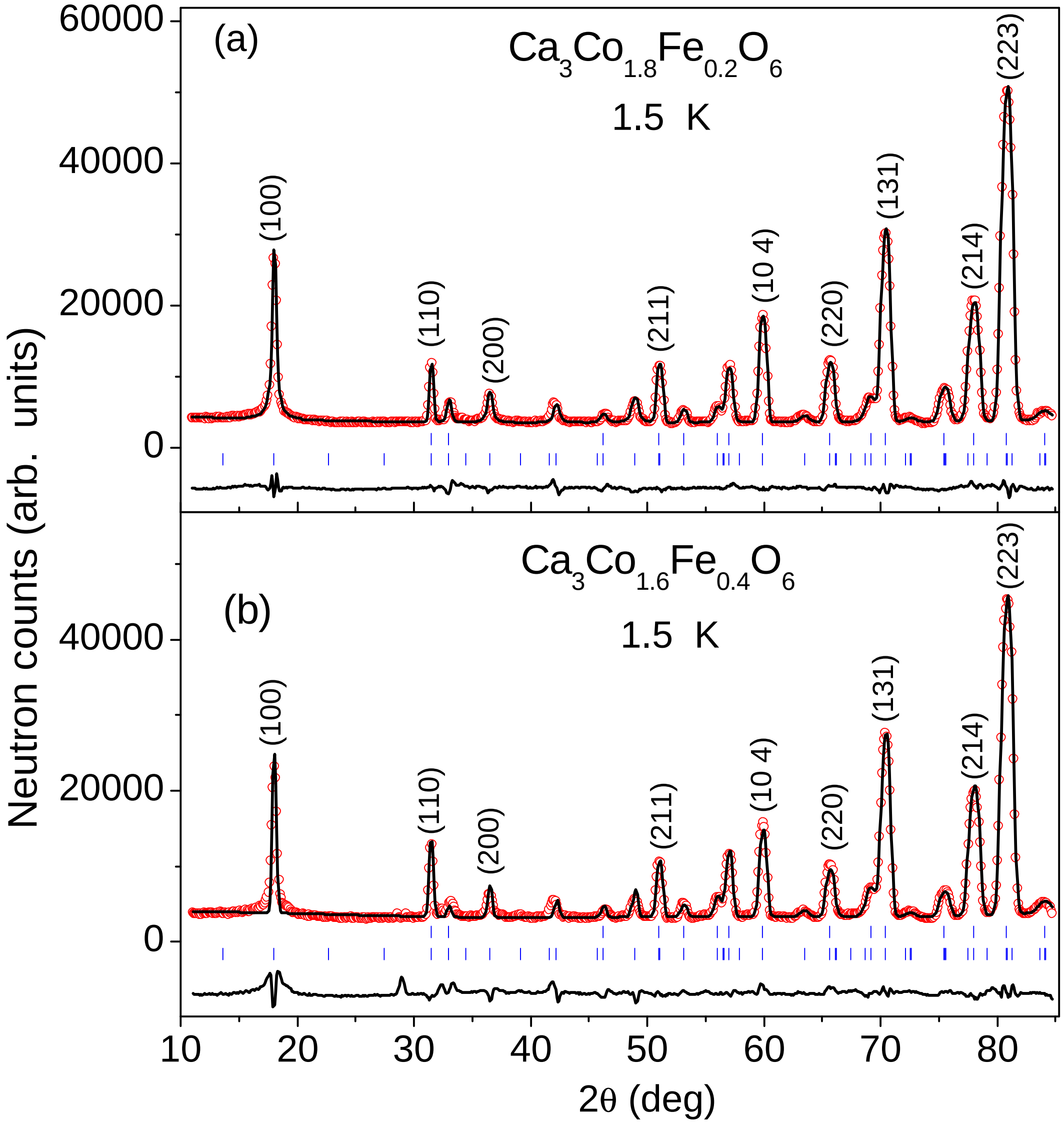

Figure 4.9: Observed (open circles) and calculated (solid lines) neutron diffraction patterns at 1.5 K using the PDA structure for the compounds (a) $Ca_3Co_{1.8}Fe_{0.2}O_6$ and (b) $Ca_3Co_{1.6}Fe_{0.4}O_6$. Solid line at the bottom of each panel shows the difference between the observed and the calculated patterns. The (*hkl*) values corresponding to stronger Bragg peaks are also listed. Vertical marks correspond to the position of all allowed Bragg reflections for the crystal (top row) and magnetic (bottom row) reflections.

lar PDA structure has been observed for the parent compound $Ca_3Co_2O_6$ (Section 4.3.1).

The Rietveld refined neutron diffraction patterns at 1.5 K using the PDA structure for the $x = 0.2$ and the $x = 0.4$ samples are shown in the Figs. 4.9(a) and 4.9(b), respectively. The results of the magnetic Rietveld refinement are given in Table 4.4.

The moments for both sites $6a$ and $6b$ lie along the c axis. Both $6a$ and $6b$ sites for this compound are fully occupied. The refined values of the site averaged order moment for the $6a$ site (four out of six) at 1.5 K are 3.8(2) and 3.7(6) μ_B per site for $x = 0.2$ and 0.4, respectively. The refined values of the ordered moment for the $6b$ site are very small for both compounds (Table 4.4). The R factors are: $R_{Nuclear}$ = 1.73 and $R_{Magnetic}$ = 9.98 for $Ca_3Co_{1.8}Fe_{0.2}O_6$, and $R_{Nuclear}$ = 3.06 and $R_{Magnetic}$ = 15.2 for $Ca_3Co_{1.6}Fe_{0.4}O_6$. In this model also, the observed ordered moments for $6a$ site at 1.5 K are less than the calculated spin only values.

Hence, we realize that two different magnetic structures, one in the $R\bar{3}c$ and the other in $P\bar{1}$, are able to fit our experimental intensities. In fact they are not so different because their Fourier coefficients are only differing in a global phase factor of ${\psi^k}_j = \pi/6$, which cannot be fixed by symmetry and it is the same for the two different sites. That is, ${S_{js}}^{\boldsymbol{k}=(001)} = {S_{js}}^{\boldsymbol{k}=(000)}$ exp(-$i\pi/6$) where "js" is $6a$ or $6b$. Another important common point in the two structures is that the total magnetization, independent of the model, is zero in the unit cell, which excludes a possible ferrimagnetic configuration. In Fig. 4.10, the effect of this global phase shift is represented.

As described in literature [62, 63], both PDA and ferrimagnetic structures have been observed for the parent compound $Ca_3Co_2O_6$. The PDA state for the parent compound $Ca_3Co_2O_6$ has also been confirmed by muon spin relaxation study [50, 61–64, 77, 78]. The important point here is that if the iron-substituted compounds adopt the ferrimagnetic structure then some of the fundamental Bragg peaks, especially the fundamental (110) Bragg peak, should have a magnetic contribution below the magnetic ordering temperature. A simple calculation shows that magnetic contribution in the intensity of (110) Bragg peak is zero in the PDA state, while in the ferrimagnetic state the magnetic contribution is finite. Figure 4.7 shows the

Table 4.4: Fourier coefficients (vector and phase), and results of the magnetic Rietveld refinement of neutron powder diffraction patterns at 1.5 K for $Ca_3Co_{2-x}Fe_xO_6$ using (a) amplitude modulated $\{\boldsymbol{k} = 0,\ 0,\ 1\}$ (model 1) , and (b) PDA structure (model 2). At $6a$ site there are two atoms Co and Fe with occupation factor (1-x) and x, respectively. At $6b$ there is only one atom Co with an occupation factor of 1. The moments are aligned in the c direction for both sites; as a result m_x and m_y are zero for both sites. (Constant is $c = 1$ and $c = 2/\sqrt{3}$ for the amplitude modulated $\{\boldsymbol{k} = 0,\ 0,\ 1\}$ and the PDA structure, respectively).

		$S_{js}{}^{k} = m_z(0\ 0\ c)\exp(-i2\pi\varphi_{js}{}^{k})$					
		$\varphi^{k}{}_{js}/2\pi$		m_z/μ_B			
		$\varphi^{k}{}_{js} = \phi^{k}{}_{js} + \psi^{k}{}_{j}$		$x = 0.2$		$x = 0.4$	
		Model 1	Model 2	Model 1	Model 2	Model 1	Model 2
$6a$	(0, 0, 1/4) (0, 0, 3/4)	0	1/12	3.8(2)	3.8(2)	3.9(4)	3.7(6)
	(2/3, 1/3, 7/12) (2/3 ,1/3, 1/12)	1/3	1/4	-1.9	0.0	-1.95	0.0
	(1/3, 2/3, 11/12) (1/3, 2/3, 5/12)	2/3	7/12		-3.8(2)		-3.7(6)
$6b$	(0, 0, 0) (0, 0, 1/2)	0	1/12	0.04(2)	0.04(2)	0.02(1)	0.02(1)
	(2/3, 1/3, 1/3) (2/3, 1/3, 5/6)	1/3	1/4	-0.02	0.0	-0.01	0.0
	(1/3, 2/3, 2/3) (1/3, 2/3, 1/6)	2/3	7/12		-0.04(2)		-0.02(1)
R_{mag}				9.24	9.98	14.7	15.2

temperature dependence of the integrated intensity of peak (110) for the $x = 0.2$ and 0.4 samples. It is evident from the figures that there is no change in the integrated intensity of the (110) peak down to 1.5 K for both compounds. This clearly rules out the possibility of the ferrimagnetic or ferromagnetic state. The observed reduction in the value of the ordered moment for the $6a$ site in both the models

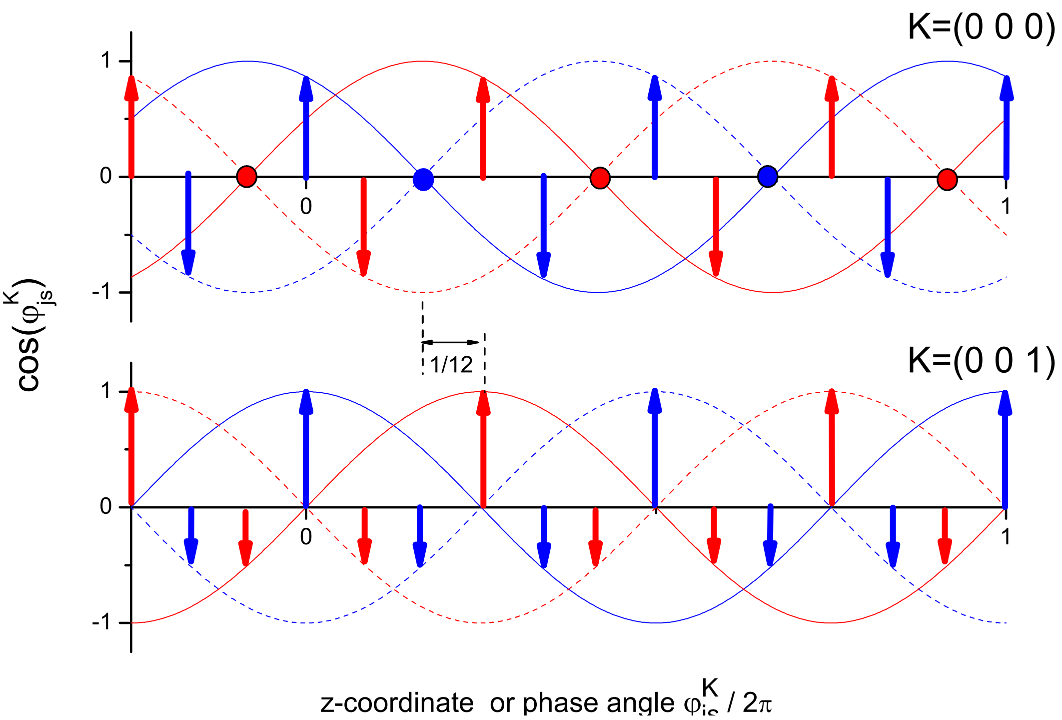

Figure 4.10: Magnetic moment modulation as function of the z coordinate (or equivalently, as can be observed in Table 4.4, the $\psi^k{}_{js}/2$ phase angle) for $6a$ (red; thick line) and $6b$ (blue; thin line) sites. From the figure it is easily observed that an $\pi/6$ global phase shift, the same for all the sites, allows to pass from model with $\boldsymbol{k} = \{0, 0, 0\}$ on the top, to model with $\boldsymbol{k} = \{0, 0, 1\}$ at the bottom. For that reason the two models give the same magnetic pattern in powder neutron diffraction experiments. Lines are guides to the eyes to better show the modulation of each site. Also it is observed that the averaged magnetic moment along a unit cell is zero following, for each site ($6a$ and $6b$), the sequence ...$\sqrt{3}/2$, 0, -$\sqrt{3}/2$, $\sqrt{3}/2$, 0, -$\sqrt{3}/2$... for the model $\boldsymbol{k} = \{0, 0, 0\}$ and ...,1, -1/2, -1/2, 1, -1/2, -1/2,... for the model with $\boldsymbol{k} = \{0, 0, 1\}$.

may be due to spin-orbit coupling and covalence effects [79–83] . The small moment on the $6b$ site may come from the spin state transition of some of the Co^{3+} ions at octahedral site ($6b$ site) from low spin ($S = 0$) to high spin ($S = 2$)/ intermediate spin ($S = 1$) state.

Now we discuss an important point which goes beyond the models used here. Figure 4.7 shows the temperature dependence of the integrated intensity of the prominent antiferromagnetic Bragg peak (100) for the present iron-substituted compounds. The (100) peak appears below 20 and 17 K for $x = 0.2$ and $x = 0.4$ samples. Here it may be noted from literature [52, 62, 63] that for the parent compound

$Ca_3Co_2O_6$, the intensity of the (100) peak first increases with decreasing temperature; however, below 18 K the intensity of the (100) peak decreases with decreasing temperature. This has been ascribed to a transition from the PDA to the ferrimagnetic structure for $Ca_3Co_2O_6$. In the present study, the observed intensity variation (Fig. 4.7) combined with no change in the intensity of the (110) fundamental peak, indicates that there is no phase transition to a ferrimagnetic or ferromagnetic state (in the zero applied magnetic field) for the iron-substituted compounds.

In summary, the Rietveld refinement of the neutron diffraction patterns suggests that the PDA structure as well as the amplitude modulated structure [$\boldsymbol{k} = \{0, 0, 1\}$], is suitable for the magnetic structure of the compounds $Ca_3Co_{2-x}Fe_xO_6$ ($x =$ 0, 0.2, and 0.4). However, a more detailed analysis (given below) shows that these compounds order (below their respective T_N) into an incommensurate spin density wave state.

4.3.3 Incommensurate Magnetic Structure of $Ca_3Co_{2-x}Fe_xO_6$

Now we turn our attention to Figs. 4.11 and 4.12, which depict temperature dependence of the neutron diffraction patterns for $x = 0.2$ and 0.4 compounds, respectively. In the first approximation, the observed neutron powder diffraction patterns at 1.5 K have been fitted with two different magnetic structures: (i) PDA structure and (ii) amplitude-modulated structure with a propagation vector $\boldsymbol{k} = \{0, 0, 1\}$ as discussed in Section 4.3.2. However, a careful inspection of the observed and calculated neutron diffraction patterns shows that the antiferromagnetic (AFM) Bragg peaks observed at $Q \sim 0.79$, 1.60, and 1.84 Å^{-1} are not well fitted by either of the above-mentioned two magnetic structures, as shown in Figs. 4.13(a), 4.13(b), 4.14(a), and 4.14(b). A detailed analysis of the neutron powder diffraction patterns at 1.5 K reveals that the magnetic structure is not a commensurate, but it

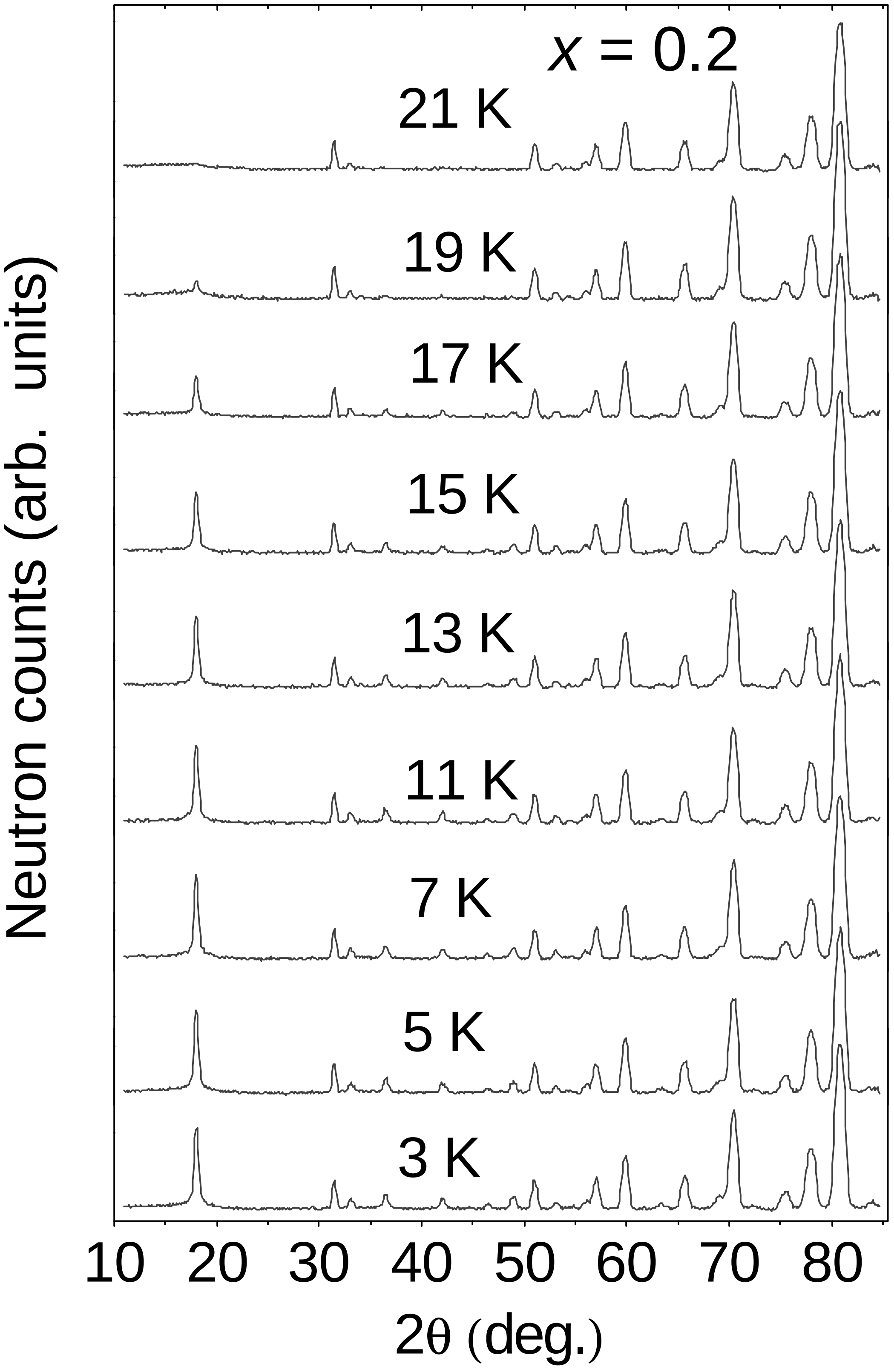

Figure 4.11: Temperature evolution of the neutron powder diffraction patterns of the compound $Ca_3Co_{1.8}Fe_{0.2}O_6$. The additional peaks appear below 20 K, due to the onset of an antiferromagnetic ordering.

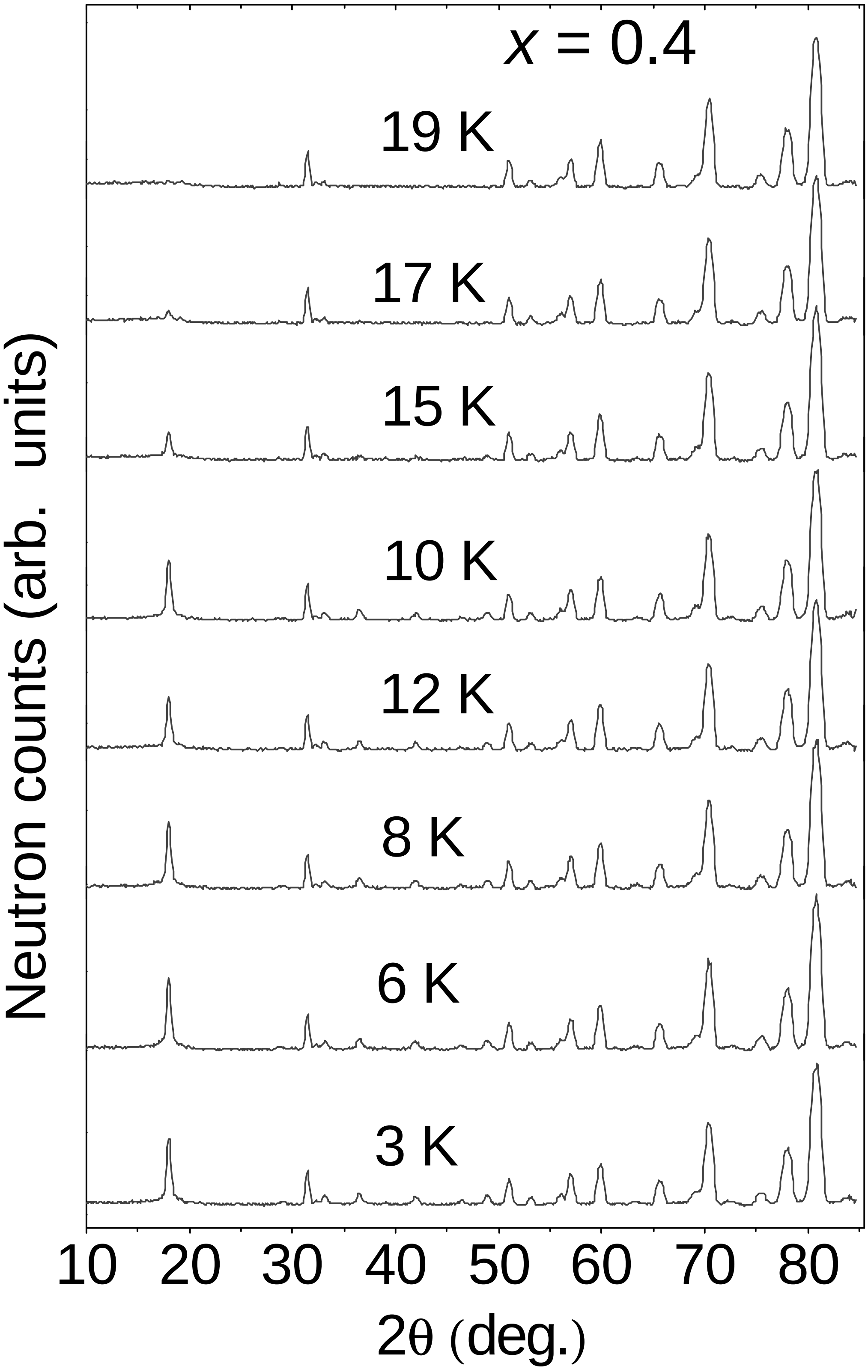

Figure 4.12: Temperature evolution of the neutron powder diffraction patterns of the compound $Ca_3Co_{1.6}Fe_{0.4}O_6$. The additional peaks appear below 17 K, due to the onset of an antiferromagnetic ordering.

corresponds to an incommensurate structure with propagation vector $\boldsymbol{k} = \{0, 0, 1.0182(9)\}$, as shown in Figs. 4.13(c) and 4.14(c).

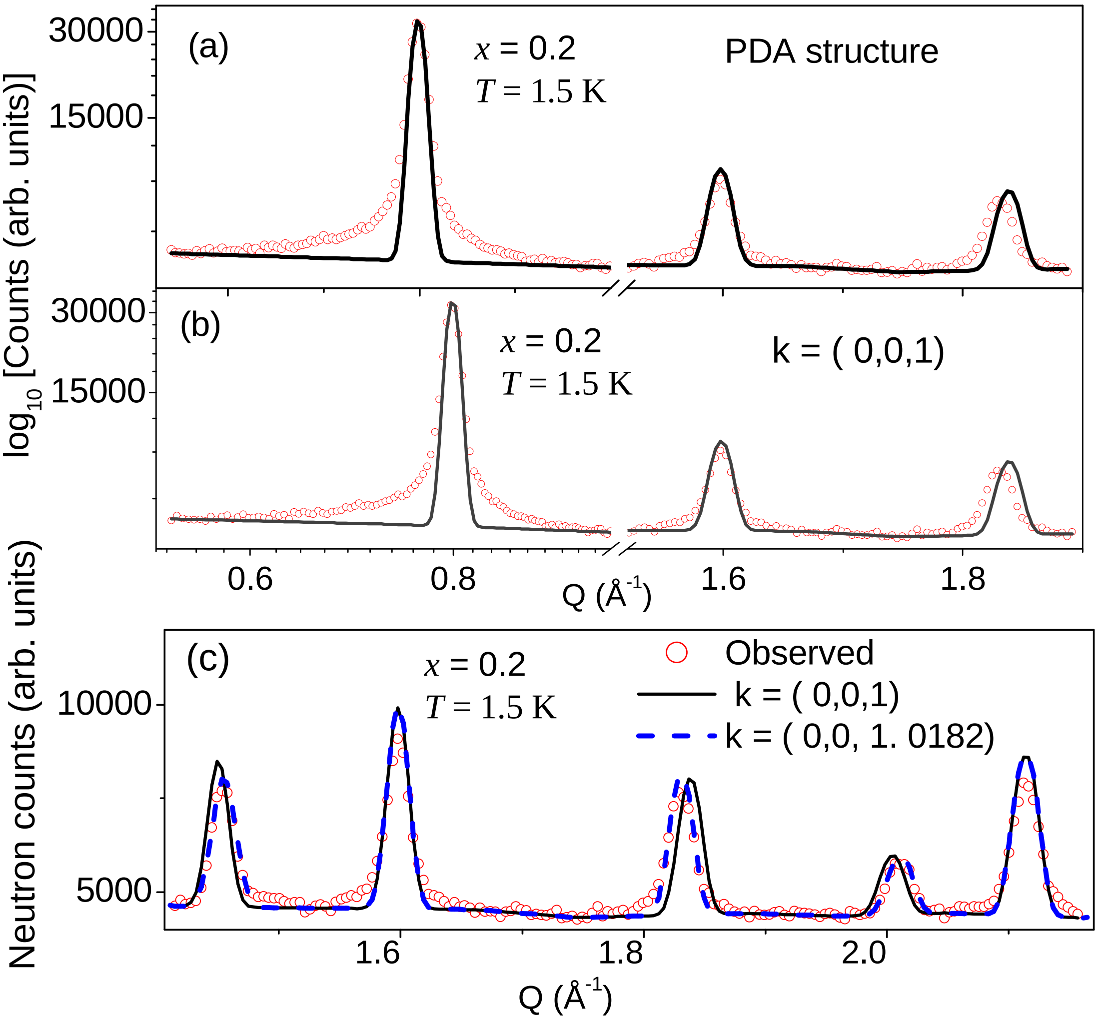

Figure 4.13: The Rietveld refined neutron powder diffraction patterns (only AFM peaks at $Q \sim 0.79$, 1.60, and 1.84 Å^{-1} are shown) for $Ca_3Co_{1.8}Fe_{0.2}O_6$ at 1.5 K using (a) the partially disordered antiferromagnet (PDA) structure and (b) the amplitude modulated structure with $\boldsymbol{k} = \{0, 0, 1\}$. (c) The Rietveld refined patterns for $Ca_3Co_{1.8}Fe_{0.2}O_6$ at 1.5 K are shown for two different values of the propagation vector $\boldsymbol{k} = \{0, 0, 1\}$ (solid line) and $\{0, 0, 1.0182(9)\}$ (dashed line). On each plot, the open circles and solid line represent the experimental data points and the calculated diffraction pattern, respectively.

Symmetry analysis (using the representation theory mentioned in Section 4.3.1) shows that the magnetic representation for $6a$ and $6b$ can be written as

$$\Gamma(6a) = 1\Gamma_1^{(1)} + 1\Gamma_2^{(1)} + 2\Gamma_3^{(2)} \tag{4.8}$$

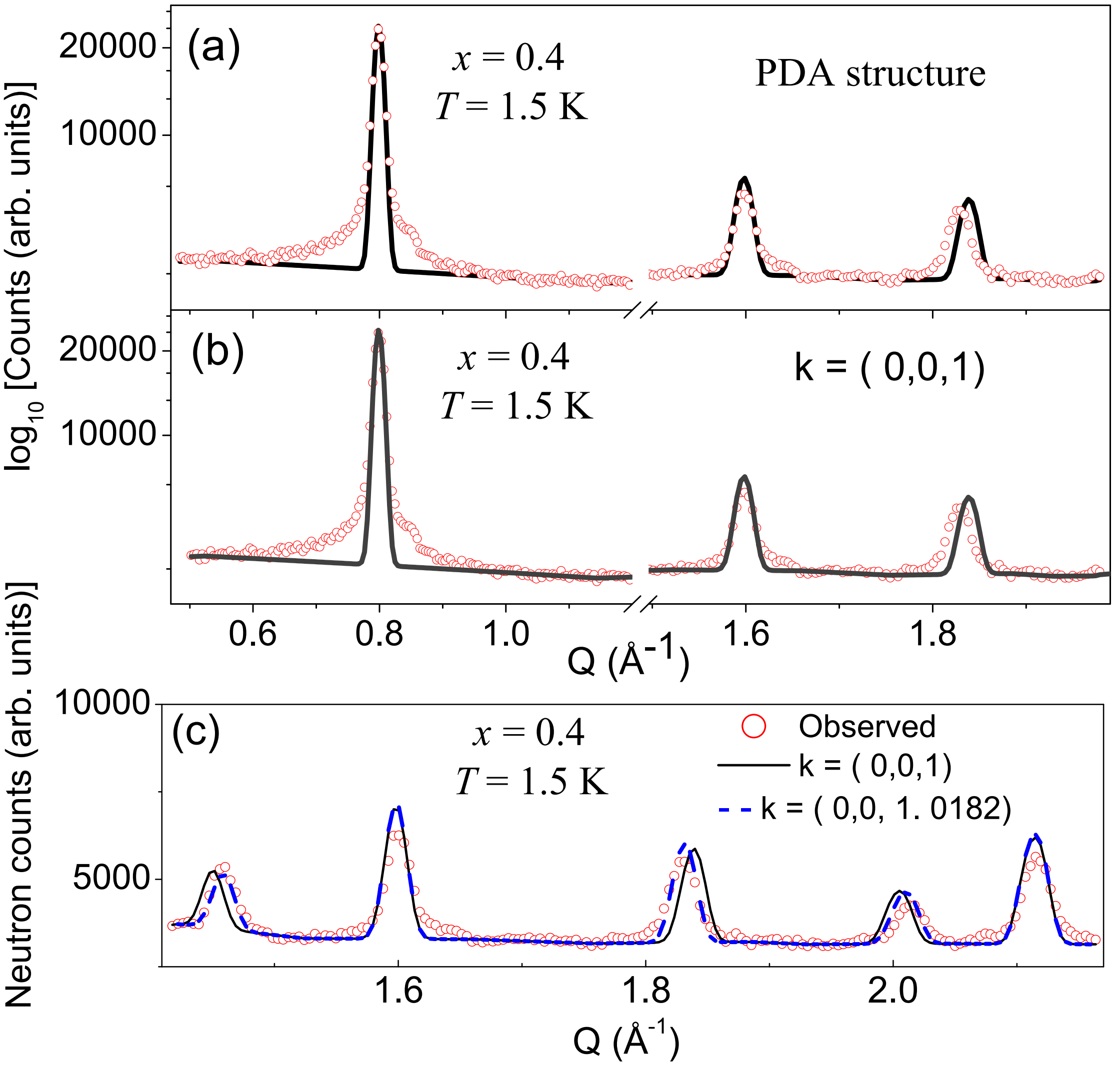

Figure 4.14: The Rietveld refined neutron powder diffraction patterns (only AFM peaks at $Q \sim 0.79$, 1.60, and 1.84 Å^{-1} are shown) for $Ca_3Co_{1.6}Fe_{0.4}O_6$ at 1.5 K using (a) the partially disordered antiferromagnet (PDA) structure and (b) the amplitude modulated structure with $\boldsymbol{k} = \{0, 0, 1\}$. (c) The Rietveld refined patterns for $Ca_3Co_{1.6}Fe_{0.4}O_6$ at 1.5 K are shown for two different values of the propagation vector $\boldsymbol{k} = \{0, 0, 1\}$ (solid line) and $\{0, 0, 1.0182(9)\}$ (dashed line). On each plot, the open circles and solid line represent the experimental data points and the calculated diffraction pattern, respectively.

and

$$\Gamma(6b) = 1\Gamma_1^{(1)} + 1\Gamma_2^{(1)} + 2\Gamma_3^{(2)} \ . \tag{4.9}$$

Here, the representations Γ_1 and Γ_2 are one dimensional, while representation Γ_3 is two dimensional. Only the magnetic structure corresponding to the representation Γ_2 is suitable to describe the observed neutron powder diffraction patterns.

The magnetic moments at $6a$ (0, 0, 1/4) and $6b$ (0, 0, 0) sites are given by $\mathbf{m}_{L,(j=6a,6b)} = \mathbf{S}_j^k \cos(2\pi\mathbf{k}.\mathbf{R}_L)$. The magnetic structure corresponds to a longitudinal amplitude-modulated structure (incommensurate), with a modulation and alignment of the moments along the crystallographic c axis as shown in Fig. 4.15. The observed and calculated neutron diffraction patterns (convoluted with the instrumental resolution function), corresponding to the representation Γ_2 with single magnetic correlation length, are shown in Figs. 4.16(a) and 4.17(a) for $x = 0.2$ and 0.4 samples, respectively. It is clear from Figs. 4.16(a) and 4.17(a) that the magnetic Bragg peak centered at $Q \sim 0.79$ Å^{-1} is broader [full width at half maximum (FWHM) = 0.489(2)° and 0.493(3)° for $x = 0.4$ and 0.2 compounds, respectively] than that expected (FWHM = 0.414° at $Q \sim 0.79$ Å^{-1}) from the instrumental resolution. In general, a broadening of Bragg reflections arises due to microstructure and/or magnetic domain size effects. In case of broadening due to microstructural effect, both nuclear and magnetic Bragg peaks are broadened, whereas domain size effect leads to a broadening of the magnetic Bragg peaks only. In the present study, we have observed that Bragg peaks of magnetic origin only are broadened. Therefore, for the present Fe-substituted compounds, magnetic domain size effect is responsible for the observed peak broadening.

To account for the magnetic domain size effect, domains with needle-like shape (parameter IsizeModel= -1 in refinement) are considered. However, the observed neutron diffraction patterns (especially the lower Q region of the magnetic Bragg peaks) cannot be fitted well by considering the needle shape domains, as shown in Figs. 4.16 (b) and 4.17 (b) for $x = 0.2$ and 0.4 samples, respectively. In order to improve the fitting further, domains with platelet-like shape are considered. The size model No. 1 has been used to determine the magnetic structure (parameter IsizeModel=1)[40] . This model corresponds to a magnetic structure, for the representation Γ_2, in which a long-range magnetic ordering (LRO) exists in the ab plane along with a finite spin-spin correlation length along the c direction (ξ^c). For this

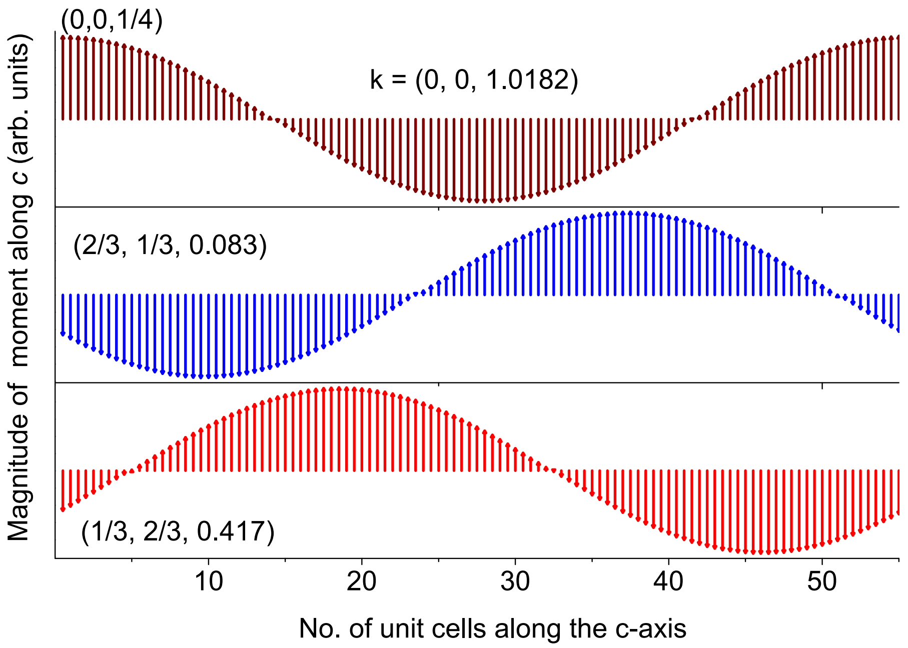

Figure 4.15: Schematic of the proposed longitudinal amplitude modulated magnetic structure [incommensurate, $\boldsymbol{k} = \{0,\ 0,\ 1.0182(9)\}$] for 55 unit cells, with a modulation and alignment of the moments along the crystallographic c axis, corresponding to the model used to calculate the diffraction patterns shown in Figs. 4.13(c) and 4.14(c) for $x = 0.2$ and 0.4 samples, respectively. The magnitude and direction of spins in the three adjacent spin chains with the (x, y) coordinate as (0, 0), (2/3, 1/3), and (1/3, 2/3) are shown. It can be viewed that the PDA structure (up - down - zero spin configuration in the neighboring spin chains) appears only at some specific lattice points.

purpose, the Thompson-Cox-Hastings pseudo-Voigt function was used for the peak shape in the refinement [40]. This peak-shape function is a linear combination of Gaussian and Lorentzian peak-shape functions. The FWHM of Gaussian (H_G) and Lorentzian (H_L) components of the peak profile are given, respectively, by

$$H_G^2 = (U + D_{ST}^2)\tan^2\theta + V\tan\theta + W + \frac{I_G}{\cos^2\theta} \tag{4.10}$$

and

$$H_L = X\tan^2\theta + \frac{Y + F(S_Z)}{\cos^2\theta}, \tag{4.11}$$

where U, V, and W are the half width parameters characterizing the instrumental resolution function (IRF), D_{ST} is an anisotropic Gaussian contribution to micros-

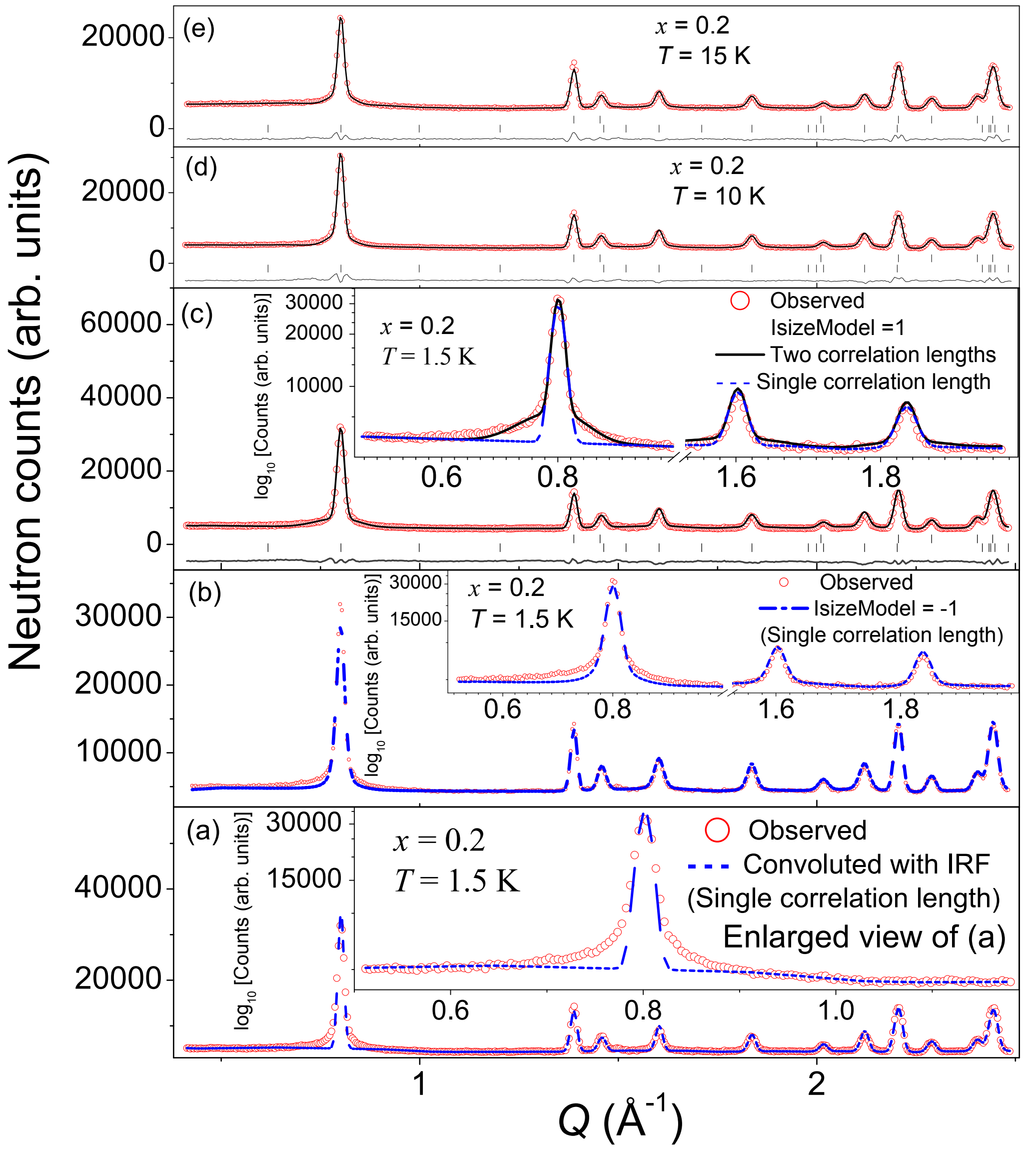

Figure 4.16: The Rietveld refined neutron powder diffraction patterns for the compound $Ca_3Co_{1.8}Fe_{0.2}O_6$ corresponding to the representation Γ_2 of the incommensurate propagation vector $\boldsymbol{k} = \{0, 0, 1.0182(9)\}$ with (a) single correlation length at 1.5 K, convoluted with the instrumental resolution function (IRF), the inset (with neutron counts on a $\log_{10}$ scale) zooms in on the AFM peak at $Q \sim 0.79$ Å^{-1} , (b) single correlation length at 1.5 K (with IsizeModel = -1 in the magnetic phase), the inset (with neutron counts on a $\log_{10}$ scale) zooms in on the observed and calculated patterns, and (c) two correlation lengths at 1.5 K (with IsizeModel = 1 in the magnetic phase), the inset zooms in on the observed (open circles) and calculated patterns with both two correlation lengths (black solid line) and single correlation length (blue dashed line) using the IsizeModel = 1 over the selected Q range. The Rietveld refined patterns for $Ca_3Co_{1.8}Fe_{0.2}O_6$ with two magnetic correlation lengths at (d) 10 K and (e) 15 K with IsizeModel = 1 as in (c). On each plot, the open circles and the solid/dashed line represent the experimental data points and the calculated diffraction patterns, respectively, and the difference is shown at the bottom as a solid line in (c), (d) and (e). The vertical marks correspond to the position of all allowed Bragg reflections for the crystal (top row) and magnetic (bottom row) reflections.

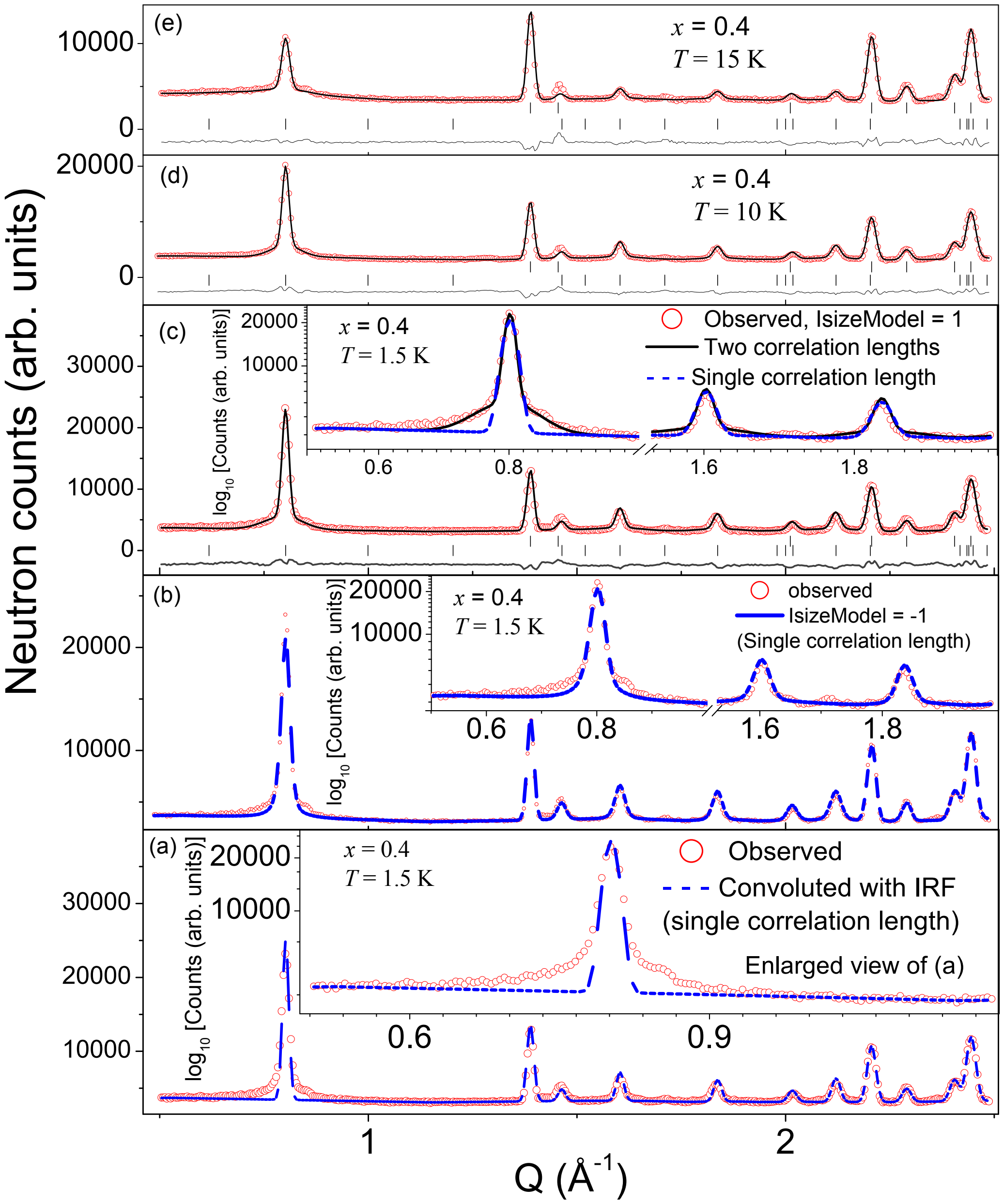

Figure 4.17: The Rietveld refined neutron powder diffraction patterns for the compound $Ca_3Co_{1.6}Fe_{0.4}O_6$ corresponding to the representation Γ_2 of the incommensurate propagation vector $\boldsymbol{k} = \{0,\ 0,\ 1.0182(9)\}$ with (a) single correlation length at 1.5 K, convoluted with the instrumental resolution function (IRF), the inset (with neutron counts on a $\log_{10}$ scale) zooms in on the AFM peak at $Q \sim 0.79$ Å^{-1}, (b) single correlation length at 1.5 K (with IsizeModel = -1 in the magnetic phase), the inset (with neutron counts on a $\log_{10}$ scale) zooms in on the observed and calculated patterns, and (c) two correlation lengths at 1.5 K (with IsizeModel = 1 in the magnetic phase), the inset zooms in on the observed (open circles) and calculated patterns with both two correlation lengths (black solid line) and single correlation length (blue dashed line) using the IsizeModel = 1 over the selected Q range. The Rietveld refined patterns for $Ca_3Co_{1.6}Fe_{0.4}O_6$ with two magnetic correlation lengths at (d) 10 K and (e) 15 K with IsizeModel = 1 as in (c). On each plot, the open circles and the solid/dashed line represent the experimental data points and the calculated diffraction patterns, respectively, and the difference is shown at the bottom as a solid line in (c),(d), and (e). The vertical marks correspond to the position of all allowed Bragg reflections for the crystal (top row) and magnetic (bottom row) reflections.

train, I_G is a Gaussian isotropic size parameter, X is a Lorentzian isotropic strain parameter, Y is a Lorentzian isotropic size parameter, and $F(S_z)$ is an anisotropic Lorentzian contribution arising from particle size. The functions D_{ST} and $F(S_z)$ have different expressions depending on the particular model used for the strain and size contributions to the broadening. The Rietveld refined neutron diffraction patterns using this model are shown in the insets of Figs. 4.16(c) and 4.17(c) for the $x = 0.2$ and $x = 0.4$ compounds, respectively. Here, single magnetic correlation length along the c axis is considered. However, agreement between calculated and observed patterns is still not satisfactory.

In order to improve the refinement further, instead of the single magnetic correlation length along the c direction, we consider two different magnetic correlation lengths (${\xi_I}^c$ and ${\xi_{II}}^c$) along the c direction. As shown in Figs. 4.16(c) and 4.17(c), Rietveld refinement using such a model, with two different magnetic correlation lengths, satisfactorily described the observed neutron diffraction patterns at 1.5 K. For the $x = 0.2$ compound, the values of ${\xi_I}^c$ and ${\xi_{II}}^c$ at 1.5 K are $\sim$ 1027 and 60 Å, respectively, whereas for the $x = 0.4$ sample, the values of ${\xi_I}^c$ and ${\xi_{II}}^c$ at 1.5 K are 1021 and 47 Å, respectively. The correlation lengths ${\xi_I}^c$ and ${\xi_{II}}^c$, therefore, correspond to long-range (LRO) and short-range magnetic ordering (SRO), respectively. Here we would like to mention that the magnetic ordering in the ab plane is always long-range for both LRO and SRO below their respective magnetic ordering temperatures ($\sim$ 20 and 17 K for $x = 0.2$ and 0.4, respectively). The ratios of relative contributions of LRO (with correlation length ${\xi_I}^c$) and SRO (with correlation length ${\xi_{II}}^c$) to the magnetic Bragg peaks at 1.5 K are 13:7 and 3:2 for the $x = 0.2$ and 0.4 samples, respectively. For both compounds, the observed neutron powder diffraction patterns at all other temperatures (below their magnetic ordering temperatures), have been fitted with the same magnetic structure model [Figs.

4.16(d), 4.16(e), 4.17(d), and 4.17(e)]. The relative contribution of the LRO and SRO in the magnetic Bragg peaks also remains constant over the entire temperature range. Figures 4.18(a) and (b) show the fitted profiles at various temperatures for the strongest magnetic Bragg peak at $Q = 0.79$ Å^{-1}. The derived temperature dependence of the magnetic correlation lengths $\xi_I{}^c$(LRO) and $\xi_{II}{}^c$(SRO) for both compounds is depicted in Figs. 4.18(c) and 4.18(d). It is evident that for both compounds, the correlation length $\xi_I{}^c$ (LRO) decreases with increasing temperature, whereas the correlation length $\xi_{II}{}^c$ (SRO) remains approximately constant for both compounds.

The values of the maximum ordered magnetic moments $\mathbf{m}_{6a}$ and $\mathbf{m}_{6b}$ (at 1.5 K) for the $x = 0.2$ compound are $4.82(3)\mu_B$ per ($6a$) site and $0.04(2)\mu_B$ per ($6b$) site, respectively. For the $x = 0.4$ compound, these values are $5.11(2)\mu_B$ per ($6a$) site and $0.02(1)\mu_B$ per ($6b$) site. It is interesting to note that the values of the ordered magnetic moment $\mathbf{m}_{6a}$ (4.82 μ_B and 5.11 μ_B for $x = 0.2$ and 0.4 compounds, respectively) are equal for LRO and SRO. The nearly zero value of the ordered magnetic moment for Co^{3+} ions at the $6b$ site (OCT site) may be ascribed to a stronger crystalline electric field [77]. For the $6a$ site, the observed values of the magnetic moments are higher than the theoretically calculated values using the expression $\mathbf{m}_{6a}$ =[(1-x) $\mathbf{m}_{Co}$ + x $\mathbf{m}_{Fe}$]. Here $\mathbf{m}_{Co}$ and $\mathbf{m}_{Fe}$ are the spin-only values of the ordered moment for Co^{3+} and Fe^{3+}, respectively. The theoretically expected ordered moment values with fully quenched orbital moment for $\mathbf{m}_{6a}$ are 4.2 μ_B per site and 4.4 μ_B per site for $x = 0.2$ and 0.4, respectively. A high value of the effective paramagnetic moment has been observed in our dc magnetization study, 5.72 μ_B and 5.97 μ_B for $x = 0.2$ and 0.4 compounds, respectively (mentioned in Chapter 5) [77]. The observed high value of magnetic moment at the $6a$ site in these Fe-substituted compounds may be ascribed to the presence of an orbital moment for

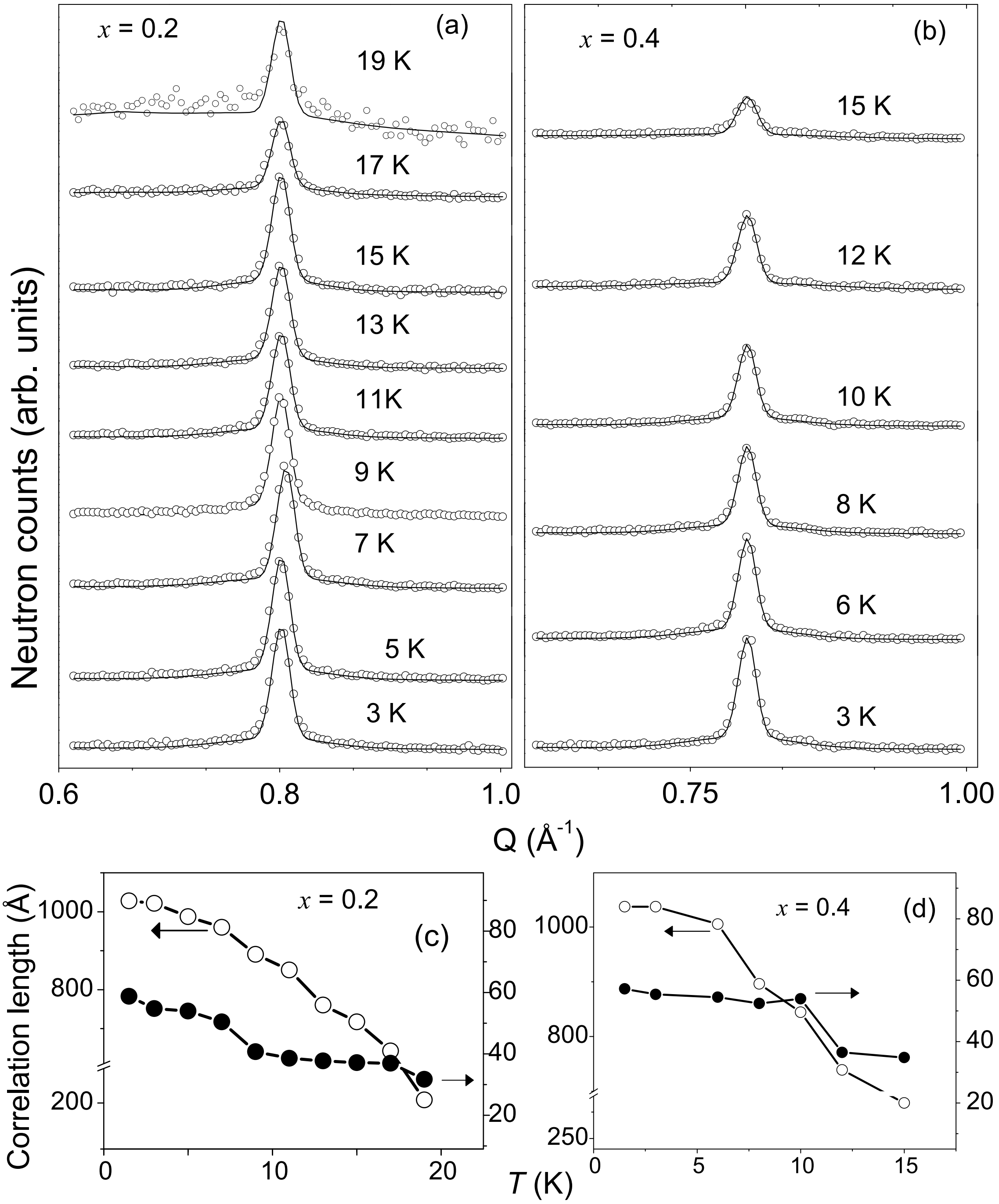

Figure 4.18: Observed (open circles) and calculated (solid lines) patterns with parameter IsizeModel = 1 and two magnetic correlation lengths $\xi_I{}^c$ and $\xi_{II}{}^c$ at different temperatures for the strongest magnetic Bragg peak for (a) $x = 0.2$ (left top) and (b) 0.4 (right top) compounds. The variation of correlation lengths for LRO ($\xi_I{}^c$, open circle) and SRO ($\xi_{II}{}^c$, solid circle) for (c) $x = 0.2$ (Left bottom) and (d) $x = 0.4$ (right bottom) compounds. Solid lines in (c) and (d) are guides to the eye.

Co^{3+} ions. From magnetic dichroism measurements [69], an orbital moment of 1.7 μ_B was reported for Co^{3+} ions at the $6a$ (TP) site for the compound $Ca_3Co_2O_6$.

Now we discuss about the observed incommensurate amplitude modulated structure and the coexistence of two correlation lengths ${\xi_I}^c$ and ${\xi_{II}}^c$ for the studied compounds $Ca_3Co_{2-x}Fe_xO_6$ ($x = 0.2$ and 0.4). In the structure of these compounds, each spin chain is surrounded by six chains, forming a triangular lattice in the *ab* plane [as shown in Fig. 4.1(a)]. The magnetic ions in the neighboring spin chains (in a triangular lattice) are shifted by 1/6 or 1/3 along the crystallographic *c* axis. In a triangular lattice, the spin configurations in the neighboring spin chains are up - down - down/zero. This kind of spin arrangement gives rise to a competition between ferromagnetic intrachain and antiferromagnetic interchain exchange interactions. These competing interactions give rise to a noncollinear spin arrangement if single ion anisotropy is weak. However, if the single-ion anisotropy is strong, these competing interactions may give rise to an incommensurate amplitude-modulated structure as observed for the present Fe-substituted compounds (Fig. 4.15). In the studied iron-substituted compounds, Fe^{3+} ($3d^5$) ions carry zero orbital moment, so it cannot have a local Ising anisotropy in the presence of a cubic crystalline field (Co^{3+} ions have local Ising anisotropy). Different spin characters of host (Ising, Co^{3+}) and impurity (Heisenberg, Fe^{3+}) spins have been observed in the Mössbauer [50, 64] and ESR [70] studies where Fe^{3+} ions remain in the paramagnetic state in the ferromagnetically ordered chains. The observed two correlation lengths in the present study also suggest that the iron spin (Heisenberg) breaks the ferromagnetic chains and its (Fe^{3+}) spin remains either in the paramagnetic state or freezes randomly (due to the competing exchange interactions) at low temperatures. No change in the ratio of intensity of the long-range and the short-range ordering also suggests that the magnetic ordering in the ferromagnetic chains is stable down to

1.5 K. We have also observed that the correlation lengths for both SRO and LRO do not differ much with varying concentrations of Fe. It is, therefore, evident that a higher concentration (for $x = 0.4$) of Fe hardly breaks the ferromagnetic bonds further as compared to that for the lower concentration of Fe (for $x = 0.2$). More than one spin-spin correlation length has been observed in the neutron diffraction studies of the other frustrated magnets $Tb_2Sn_2O_7$ [84] and $LiMn_2O_4$ [85].

For the parent compound $Ca_3Co_2O_6$, Agrestini *et al.* [86] have shown that the magnetic propagation vector $\boldsymbol{k} = \{0,\ 0,\ k_z\ {\sim}1.01\}$ is incommensurate with the crystal structure. They described the physical origin of modulation in the magnetic structure in terms of the competition between ferromagnetic intrachain (due to direct Co-Co overlap) and antiferromagnetic interchain exchange interactions. Agrestini *et al.* have fitted only the (100) magnetic Bragg peak using two Gaussian functions with significantly different widths, the narrower of which corresponds closely to the instrumental resolution. The broad Gaussian peak corresponds to the SRO. However, in the present study, we have carried out a detailed analysis of the neutron diffraction patterns and established the coexistence of LRO and SRO. Moreover, in our analysis, we have taken a wide Q range (magnetic Bragg peaks observed at $Q \sim 0.79$, 1.6029, 1.8365, 2.1204, and 2.6881 Å^{-1}), unlike in Ref. [86] where only the (100) magnetic Bragg peak was considered, to estimate the correlation lengths for SRO and LRO. For the compound $Ca_3Co_2O_6$, the estimated correlation length in the *ab* plane for the short-range order at 5 K is 180 Å [86]. However, for the present Fe-substituted compounds, a long-range magnetic ordering always exists in the *ab* plane. We have defined LRO and SRO based upon the extent of the correlation length along the *c* axis. For the compound $Ca_3Co_2O_6$ [73], below 18 K, a reduction in the intensity of the strongest magnetic reflection (100) was observed in the powder as well as single crystal neutron diffraction studies. At 21 K, the ratio of intensity contribution of the short-range and the long-range magnetic ordering to the magnetic Bragg peaks is 0.2; this ratio increases to 0.7 at low temperatures. This indicates the instability of the long-range magnetic order at lower temperatures. For the present Fe-substituted compounds, we have also observed a long-range as well as short-range magnetic ordering down to 1.5 K. However, we have not observed any reduction in the intensity of the strongest magnetic reflection (100) at $Q \sim 0.79$ Å^{-1}. The ratio of intensity of the long-range and the short-range ordering also remains constant down to 1.5 K. It is, therefore, evident that unlike for the compound $Ca_3Co_2O_6$, for the present Fe-substituted compounds $Ca_3Co_{2-x}Fe_xO_6$, the short-range magnetic correlation does not grow at the expense of the long-range magnetic correlation.

Niitaka *et al.*[66], based on the analysis of the neutron diffraction patterns, reported that compound Ca_3CoRhO_6 ordered magnetically below 100 K in a PDA state, in which 1/3 ferromagnetic spin chains (in a triangle) are spin up ($+M$), 1/3 ferromagnetic spin chains are spin down ($-M$), and the remaining 1/3 are incoherent (disordered). Below 30 K, the 1/3 incoherent spin chains freeze and give rise to a frozen PDA state. On the contrary, the magnetic structure of the present Fe-substituted compounds is incommensurate with an amplitude modulation of the moments along the c axis, where the magnetic configuration of the neighboring spin chains (arranged in a triangle) is ($+M$, $-M$, 0) at specific lattice points only (Fig. 4.15). This is different from the PDA state, where ($+M$, $-M$, 0) structure is present for all lattice points. On the contrary, to the reported frozen-PDA state (below 30 K) for the compound Ca_3CoRhO_6, no phase transition has been observed at low temperature for the present Fe-sustituted compounds. Loewenhaupt *et al.* [65] also proposed the PDA state for the magnetic structure of the compound Ca_3CoRhO_6 below 100 K. In addition, they observed a diffuse magnetic peak, superimposed over the strongest magnetic Bragg peak (100) below as well as above the ordering temperature of 100 K. The estimated correlation lengths for the diffuse magnetic ordering above and below 100 K are 16 and 23 Å, respectively, indicating that with the establishment of the long-range magnetic ordering, the correlation length for diffuse magnetic scattering increases. The intensity of the diffuse magnetic peak increases with lowering of the temperature, reaching a maximum around 100 - 150 K, and then decreases at lower temperatures. The position of the diffuse magnetic peak shifts to a larger scattering angle with decreasing temperature. For the present Fe-substituted compounds, a diffuse magnetic peak, superimposed over the strongest (sharper) magnetic Bragg peak, has been observed only below the long-range ordering temperature. Here the relative contribution of LRO and diffuse magnetic scattering (SRO) in the magnetic phase remains constant (below transition temperature) down to 1.5 K with no change in the position of the diffuse magnetic peak. Besides, the correlation length, corresponding to the diffuse magnetic scattering for the present Fe-substituted compounds, also remains approximately constant below the long-range magnetic ordering temperature. It is, therefore, evident that the substitution of the Ising Co spins by the Heisenberg Fe spins stabilizes the incommensurate amplitude-modulated magnetic phase over the entire temperature range.

The low-temperature neutron diffraction study for the compound Sr_3HoCrO_6 was carried out by Hardy *et al.* [87]. The extra peaks in the neutron diffraction patterns have been observed below 15 K. Hardy *et al.* have proposed the PDA state for the magnetic structure of this compound. The magnetic short-range ordering coexists with the long-range ordering below the long-range ordering temperature (15 K). A decrease in the correlation length with decreasing temperature from 9 to 1.5 K has been observed for long-range ordering. Moreover, a high background in the small-angle part of the neutron diffraction patterns has been observed at temperatures above as well as below the long-range ordering temperature (10 K), the reason of which is not reported. In sharp contrast, the LRO correlation length for the present Fe-substituted compounds increases with decreasing temperature. The coexistence of the long-range and the short-range magnetic order for the compound Sr_3HoCrO_6 is similar to the present Fe-substituted compounds. However, as mentioned earlier, the observed PDA structure for the compound Sr_3HoCrO_6 is very much different from the observed amplitude-modulated incommensurate structure for the present Fe-substituted compounds. It is, therefore, clear that the magnetic correlations for the present Fe-substituted compounds are very much different from the compound Sr_3HoCrO_6, except for a coexistence of the long-range and the short-range order. The magnetic structures of the present Fe-substituted compounds are significantly different than those for the compounds $Ca_3Co_2O_6$ and Ca_3CoRhO_6 as well, despite the fact that all these spin-chain compounds crystallize in the rhombohedral structure with space group $R\bar{3}c$. A comparison of the magnetic structures of the compounds of the $A_3MX\mathrm{O}_6$ family is given in Table 4.5.

4.3.4 Incommensurate Magnetic Structure of $Ca_3Co_2O_6$ and its Time Dependence

Figure 4.19 shows the Rietveld refined neutron diffraction patterns for the compound $Ca_3Co_2O_6$ at 20 K (below $T_N \sim 25$ K). In the first approximation, the observed neutron powder diffraction patterns at 20 K can be fitted with two different magnetic structures: (i) PDA structure and (ii) amplitude-modulated structure with a propagation vector $\boldsymbol{k} = \{0, 0, 1\}$ as described in Section 4.3.1. However, a careful inspection of the observed and calculated neutron diffraction patterns shows that the propagation vector is incommensurate $\boldsymbol{k}_1 = [\{0, 0, \delta\}$ with $\delta = 1.009$ (3)] in the hexagonal setting of the space group $R\bar{3}c$ and the magnetic structure [Fig.

Table 4.5: Magnetic structures of the compounds of A_3MXO_6 family (determined from neutron diffraction studies).

	Compounds			
Properties	$Ca_3Co_2O_6$	Ca_3CoRhO_6	Sr_3HoCrO_6	$Ca_3Co_{2-x}Fe_xO_6$
T_N(K)	25	100 (T_{N1}) 30 (T_{N2})	15	20 ($x = 0.2$) 17 ($x = 0.4$)
Magnetic structure	Modulated PDA structure with $\boldsymbol{k}$ = {0, 0, 1.01}	PDA (30 K $\leq T \leq$ 100 K) Frozen-PDA ($T \leq$ 30K)	PDA	Modulated structure with $\boldsymbol{k}$ = {0, 0, 1.0182(9)}
Temperature dependence of intensity of the magnetic reflection (100)	Below 18K, intensity decreases with decreasing temperature	Increases with decreasing temperature (below T_{N1}) and then constant below 30 K	Below 9 K, intensity decreases with decreasing temperature	Below T_N, increases with decreasing temperature
Coexistence of short-range and long-range ordering	Below 21 K	Above as well as below T_{N1}	Below T_N	Below T_N
Ratio of intensity contribution from short-range and long-range	0.2 at 21 K 0.7 at 5 K	Not reported	Not reported	0.54 ($x = 0.2$) and 0.67($x = 0.4$). Remains constant below T_N .
Correlation lengths	180 Å for SRO (at 5 K)	16 Å($T \geq 100$ K) for SRO 6.415 Å at 3 K (SRO)	400 Å for LRO (at 9 K) 40 Å for SRO (at 9 K)	1027Å (LRO) and 60 Å (SRO) along c axis at 1.5 K ($x = 0.2$). For both cases, LRO in the ab plane. 1021 Å (LRO) and 47 Å (SRO) along c axis at 1.5 K ($x = 0.4$). For both cases, LRO in the ab plane.
References	[86]	[65, 66]	[87]	**Present study**

4.20] corresponds to a spin density wave (SDW) structure. The Co^{3+} moments (at

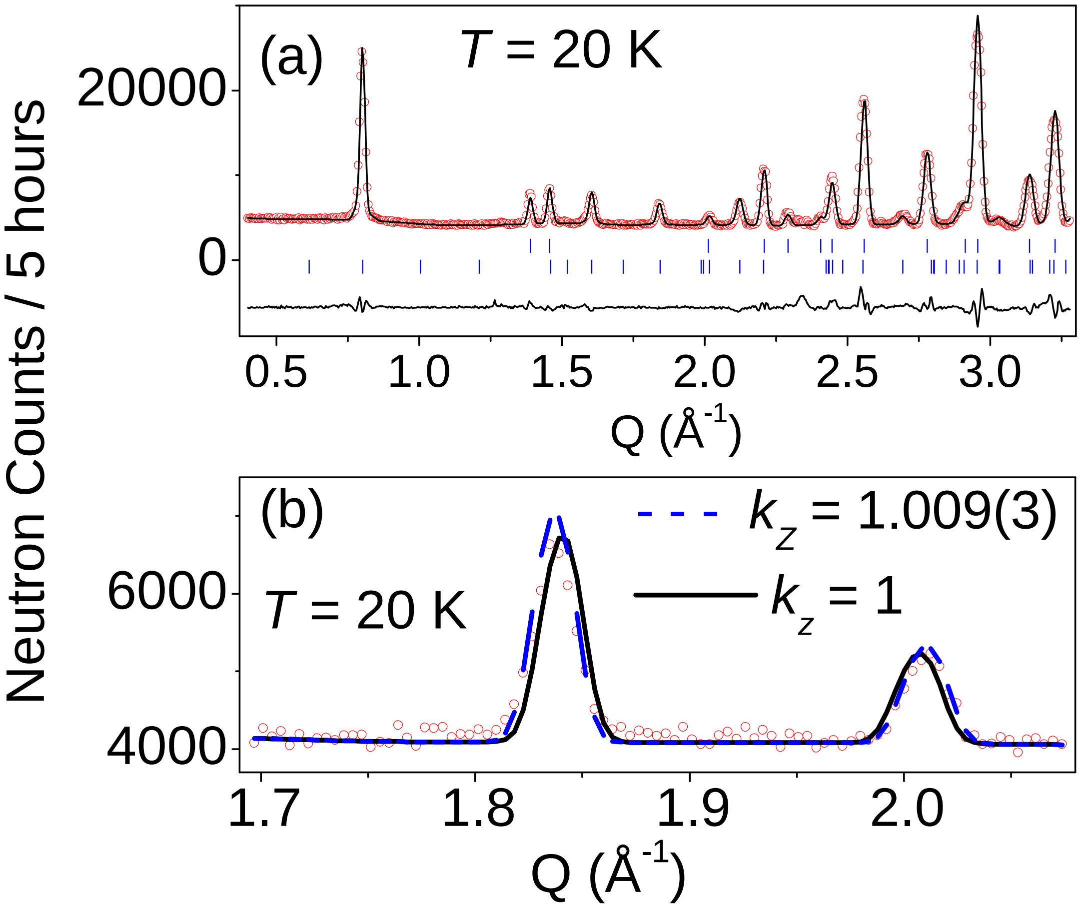

Figure 4.19: (a) The Rietveld refined neutron powder diffraction patterns of $Ca_3Co_2O_6$ at 20 K : experimental data (open circle), calculated curve (solid line), and difference (solid line at the bottom). The upper vertical marks are the nuclear Bragg reflections and the lower vertical marks are the reflections arising from the propagation vector $\boldsymbol{k}_1 = 0, 0, 1.009(3)$.(b) Rietveld refined pattern at 20 K are shown for two different values of the propagation vector $\boldsymbol{k} = (0, 0, k_z)$ with $k_z = 1$ (solid line) and $k_z = 1.009$ (3) (dashed line).

the $6a$ site) are aligned along the crystallographic c axis, as described previously by Agrestini *et al.* [86]. Figure 4.21(a) depicts the temperature dependence of the full width at half maximum (FWHM) for the strongest AFM Bragg peak (1, 0, 1 - δ) [at $Q \sim 0.8$ Å^{-1}]. Interestingly, the widths of the observed magnetic Bragg peaks, at all temperatures below T_N, are greater than that expected from the instrument resolution, indicating the presence of SRO. The FWHM expected from the instrumental resolution function (DMC, PSI, Switzerland) over the Q-range of 0.7 - 0.8 Å^{-1} is $\sim$

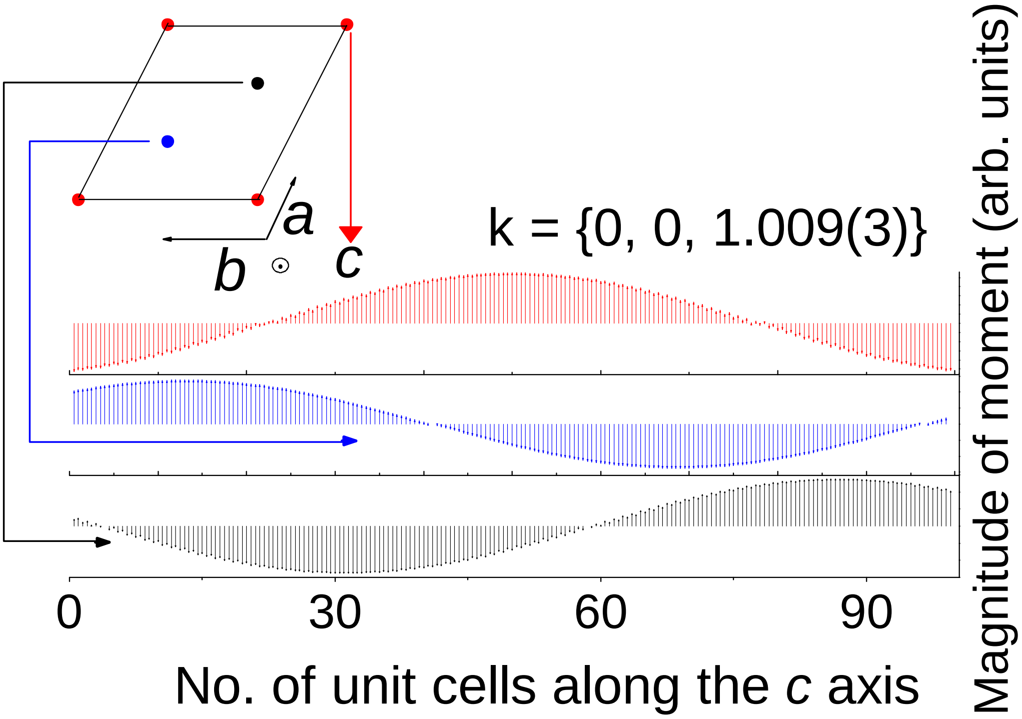

Figure 4.20: The schematic of the SDW structure with a modulation and alignment of the moments along the crystallographic c axis for 100 unit cells (the magnitude and direction of the spins in the three adjacent spin chains are given).

0.39°. We also note that the FWHM at 1.5 K is less than the FWHM at 5 K. To account for the observed broadening of the magnetic Bragg peaks (SRO), the magnetic domains of platelet-like shape are assumed, and the Thompson-Cox-Hastings pseudo-Voigt profile function is used in the refinement as described in Sec. 4.3.3 for the Fe-substituted compounds $Ca_3Co_{2-x}Fe_xO_6$. We have considered the magnetic Bragg peaks as a sum of two pseudo-Voigt peaks, having different widths (FWHMs). The width (FWHM) of the narrow peak is equal to the FWHM of the instrumental resolution function (Fig. 4.21 (b)). An analysis of the width of the broader peak, which corresponds to magnetic short-range ordering (SRO), reveals that the magnetic correlation length for the platelet shape domains is ~ 72 Å at 20 K. The ratio of relative contributions of the LRO and SRO (I_{LRO}/I_{SRO}) to the magnetic Bragg peaks is 7/3; and the maximum value of the ordered moment at the $6a$ site (M_{6a}), same for the LRO and SRO, is 4.82(3) μ_B at 20 K. However, at 15 K, the values of correlation length (ξ), intensity ratio (I_{LRO}/I_{SRO}), and the maximum moment (M_{6a}) are 130 Å, 3/7, and 5.14 (2) μ_B, respectively. The observed presence of the SRO at all temperatures below T_N is surprisingly different from the results reported in the literature, where SRO was observed only below 21 K [86].

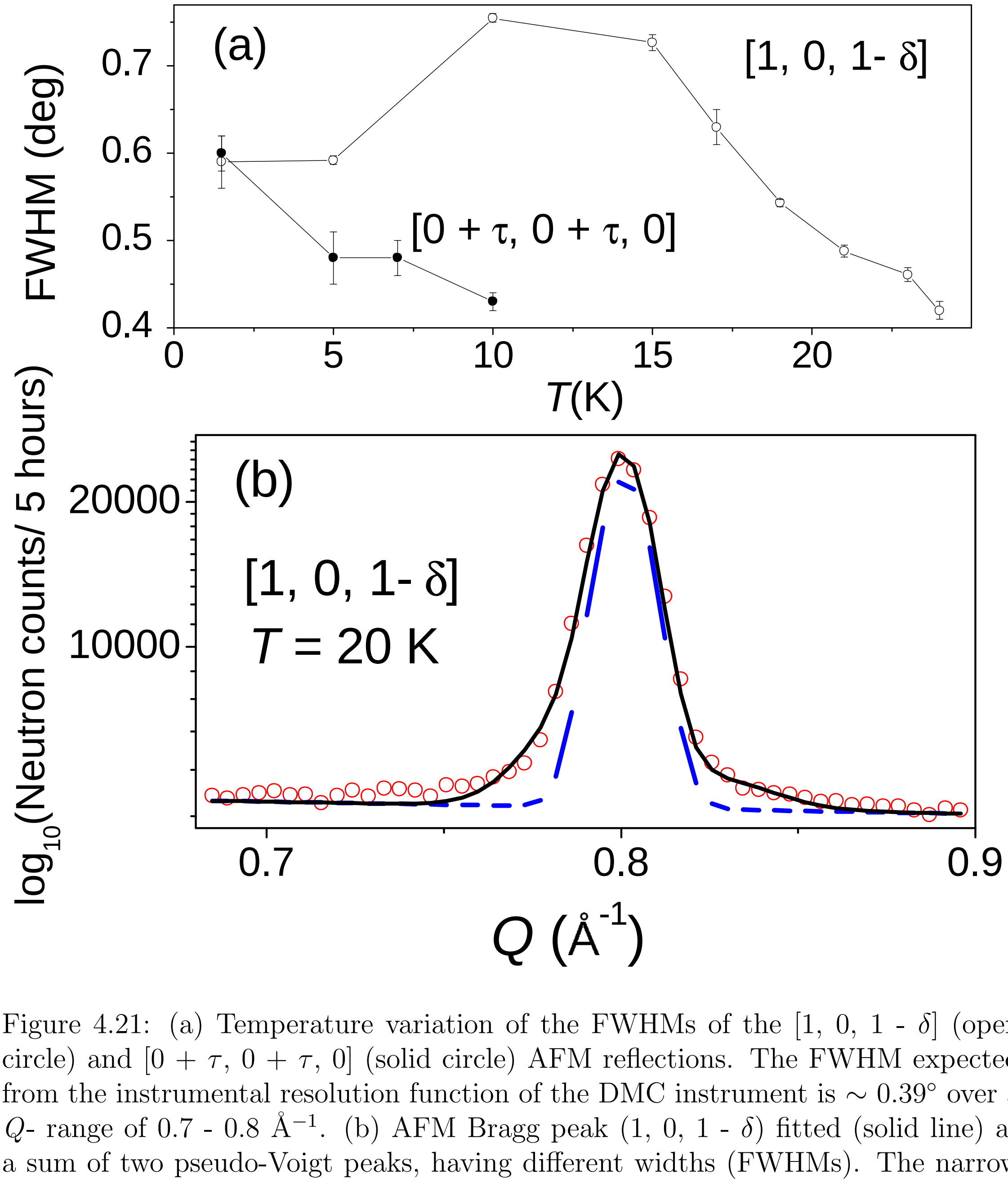

Figure 4.21: (a) Temperature variation of the FWHMs of the [1, 0, 1 - δ] (open circle) and [0 + τ, 0 + τ, 0] (solid circle) AFM reflections. The FWHM expected from the instrumental resolution function of the DMC instrument is ~ 0.39° over a Q- range of 0.7 - 0.8 Å^{-1}. (b) AFM Bragg peak (1, 0, 1 - δ) fitted (solid line) as a sum of two pseudo-Voigt peaks, having different widths (FWHMs). The narrow peak (dashed line) having FWHM of the instrumental resolution function is also shown. The solid lines are guides to the eye.

Interestingly, in addition to the SDW transition with the propagation vector $\boldsymbol{k}_1$,

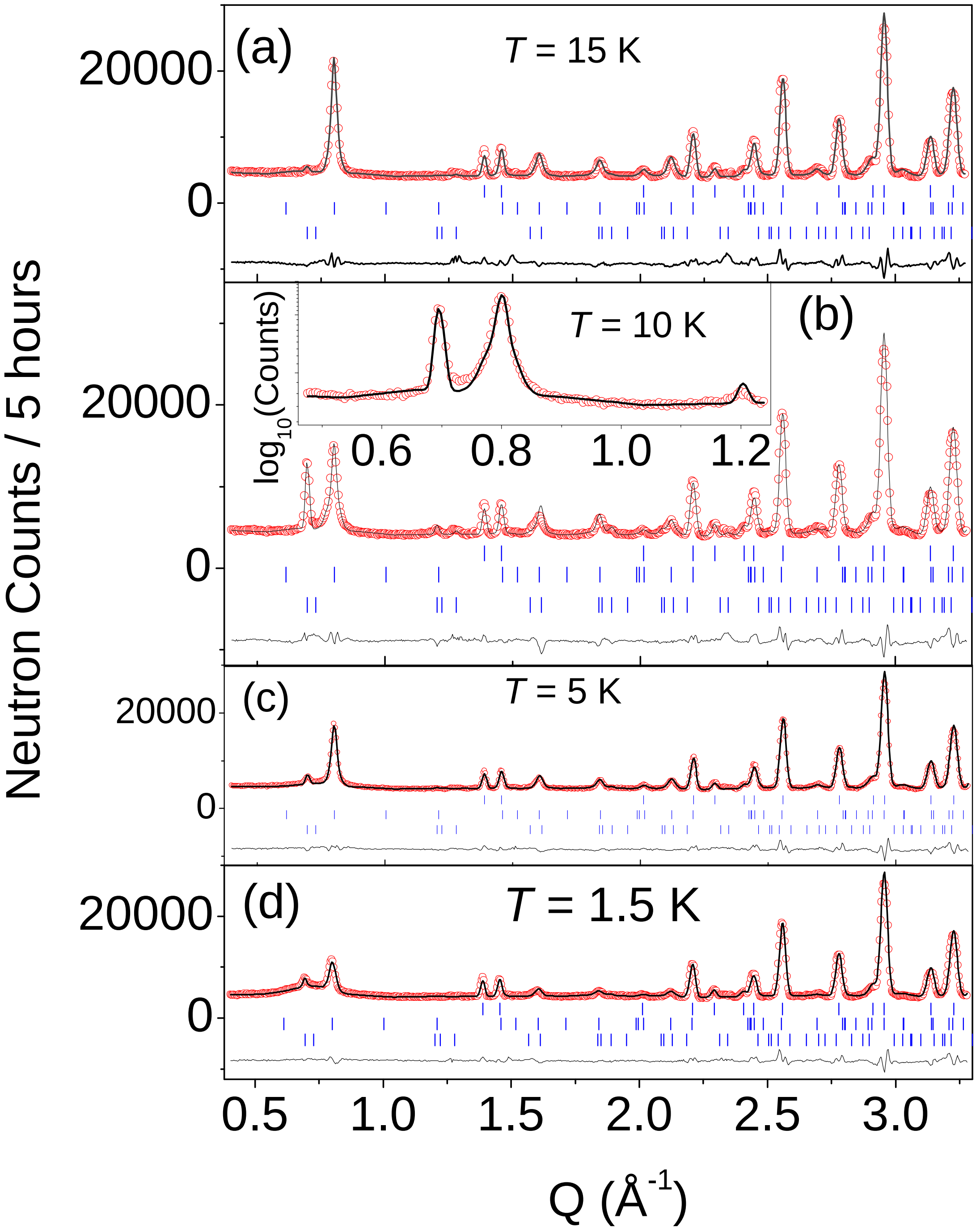

Figure 4.22: The Rietveld refined neutron powder diffraction patterns of $Ca_3Co_2O_6$ at (a) 15 K, (b) 10 K, (c) 5 K, and (d) 1.5 K: experimental data (open circle), calculated curve (solid line), and difference (solid line at the bottom). The upper vertical marks are the nuclear Bragg reflections, middle vertical marks are the reflections arising from the propagation vector $\boldsymbol{k}_1 = 0, 0, 1.009(3)$, and the lower vertical marks show the reflections from the propagation vector $\boldsymbol{k}_2 = (0.5, 0.5, 0)$. Inset in (b) shows the strongest magnetic reflections arising from the propagation vectors $\boldsymbol{k}_2$ [at $Q \sim 0.69$ and 1.20 Å^{-1}] and $\boldsymbol{k}_1$ [at $Q \sim 0.8$ Å^{-1}].

a second set of magnetic peaks appear in the neutron diffraction patterns for $T \leq 15$ K [Figs. 4.22(a) - (d)]. The strongest magnetic reflections arising from the propagation vectors $\boldsymbol{k}_2$ [at $Q \sim 0.69$ and 1.20 Å^{-1}] and $\boldsymbol{k}_1$ [at $Q \sim 0.8$ Å^{-1}] are shown in the inset of Fig. 4.22(b). Agrestini *et al.*[88] also observed the second set of magnetic peaks below 12 K, but only if the sample was held at 10 K for some time while cooling. The second set of magnetic reflections can be indexed using the propagation vector $\boldsymbol{k}_2 = [\{\tau, \tau, 0\}$ with $\tau = 0.5]$ in the hexagonal setting of the space group $R\bar{3}c$. The magnetic structure defined by the propagation vector $\boldsymbol{k}_2$ is called commensurate antiferromagnetic (CAFM) structure.

In order to clarify the relation between the two magnetic structures appearing below 15 K, we have measured the integrated intensity of the two strongest magnetic Bragg peaks (1, 0, 1 - δ) [at $Q \sim 0.8$ Å^{-1}] and (0 + τ, 0 + τ , 0) [at $Q \sim 0.69$ Å^{-1}] , which stands for the $\boldsymbol{k}_1$ (SDW) and $\boldsymbol{k}_2$ (CAFM) type magnetic structures, respectively, at a series of temperatures below 35 K, as shown in Fig. 4.23. The intensity of the Bragg peak (1, 0, 1 - δ) increases with decreasing the temperature, reaches a maximum value at ∼ 15 K, and thereafter decreases monotonically with a further decrease in temperature. The intensity of the magnetic Bragg peak (0 + τ, 0 + τ, 0), which appears at ∼ 15 K, increases with decreasing temperature, reaches a maximum at ∼ 10 K, and then starts decreasing with decreasing temperature down to lowest measurement temperature of 1.5 K . From the temperature dependence of FWHM of the AFM Bragg peak (1, 0, 1 - δ), shown in Fig 4.21(a), we note that magnetic Bragg peak (0 + τ, 0 + τ, 0) gets significantly broadened below 8 K, indicating the presence of SRO (down to 1.5 K).

Symmetry analysis using the group of propagation vector (little group) shows that the magnetic representation for the site $6a$ (for the propagation vector $\boldsymbol{k}_2$) can

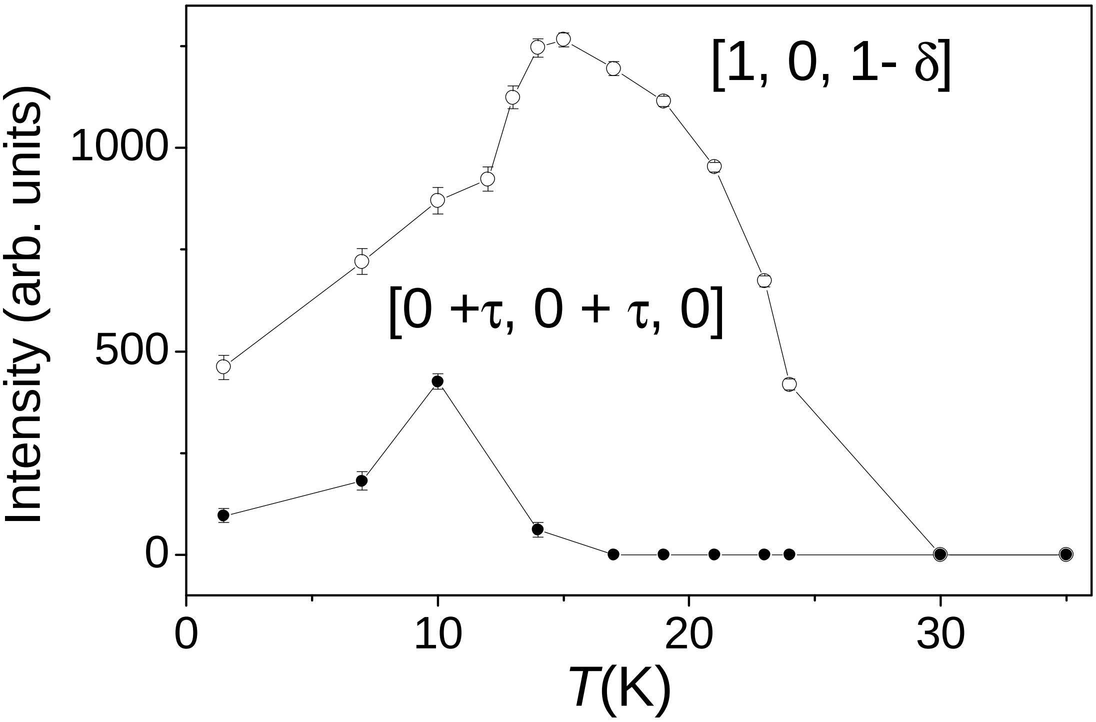

Figure 4.23: Temperature dependence of the integrated intensity of [1, 0, 1 - δ] (open circle) and [0 + τ, 0 + τ, 0] (solid circle) AFM Bragg peaks. The solid lines are guides to the eye.

be written as

$$\Gamma(6a) = 1\Gamma_1^{(1)} + 1\Gamma_2^{(1)} + 2\Gamma_3^{(1)} + 2\Gamma_4^{(1)}. \tag{4.12}$$

Here all the representations are one dimensional. The observed strongest magnetic peaks at $Q \sim 0.69$ and 1.20 Å^{-1} can be fitted with the representation Γ_3, containing two basis vectors ψ_1 = (1 -1 0) and ψ_2 = (0 0 1). For the basis vector ψ_1, the moment has component in the *ab* plane, however, for the basis vector ψ_2, moment has component along the *c* axis. Agrestini *et al.* [88] have considered only the basis vector ψ_2 [moment along *c* axis] for the refinement of the neutron diffraction patterns. A simple calculation shows that the magnetic Bragg peak ($\bar{1} + \tau$, $0 + \tau$, 2) at $Q \sim 1.27$ Å^{-1} has finite intensity if one considers only the basis vector ψ_2 in the refinement. However, the calculated intensity is weaker than the standard deviation of the background if one consider both ψ_1 and ψ_2 in the refinement as shown in Fig. 4.24(a). In the observed neutron diffraction patterns, shown in Figs. 4.24 (b) and (c), no observable change in the intensity at $Q \sim 1.27$ Å^{-1}, below 15 K, suggests that both basis vectors should contribute in the magnetic structure. The schematic of the magnetic structure having both propagation vectors, called CAFM structure, is shown in Fig. 4.25. Here, the size of the magnetic unit cell, along both *a* and *b* axes, is double than the size of the nuclear unit cell. In the magnetic structure, amplitude of the moments at the TP site is constant and the moment has component in the *ab* plane as well as along the *c* axis.

We now turn our attention on the nature of the SDW and CAFM phases. An unusual aspect of the neutron diffraction patterns is a time dependence of the strongest magnetic Bragg peaks of the SDW and CAFM structures. Figures 4.26(a), (b), and (c) show the neutron diffraction patterns for the strongest magnetic reflections collected in 30 minutes at 10, 7, and 1.5 K. For the measurement at 1.5, 7, and 10 K, the sample was cooled from 100 K at a cooling rate of 2 K/min, and then data collection was started. We have binned the data for every 30 minutes. In Fig. 4.26, we show data for three representative binning modules corresponding to an effective time gap of 15, 165, and 295 minutes, after the measurements were started at the respective temperatures. It is evident from Figs. 4.26 (a), (b), and (c) that the magnetic Bragg peaks exhibit a time dependence, which is most prominent at 10 K. However, at every temperature, the system reaches in the equilibrium after $\sim$ 165 minutes. The time dependence of these magnetic Bragg peaks was also observed by Agrestini *et al.* [88] in the temperature range of 8 - 12 K (above 12 K, magnetic Bragg peaks corresponding to the CAFM structure was not present). They observed that if the sample was cooled rapidly from 18 to 2 K, then data contained only the features corresponding to the SDW and SRO (belonging to the SDW structure) phases. On the other hand, if the sample was held at 10 K for some time while

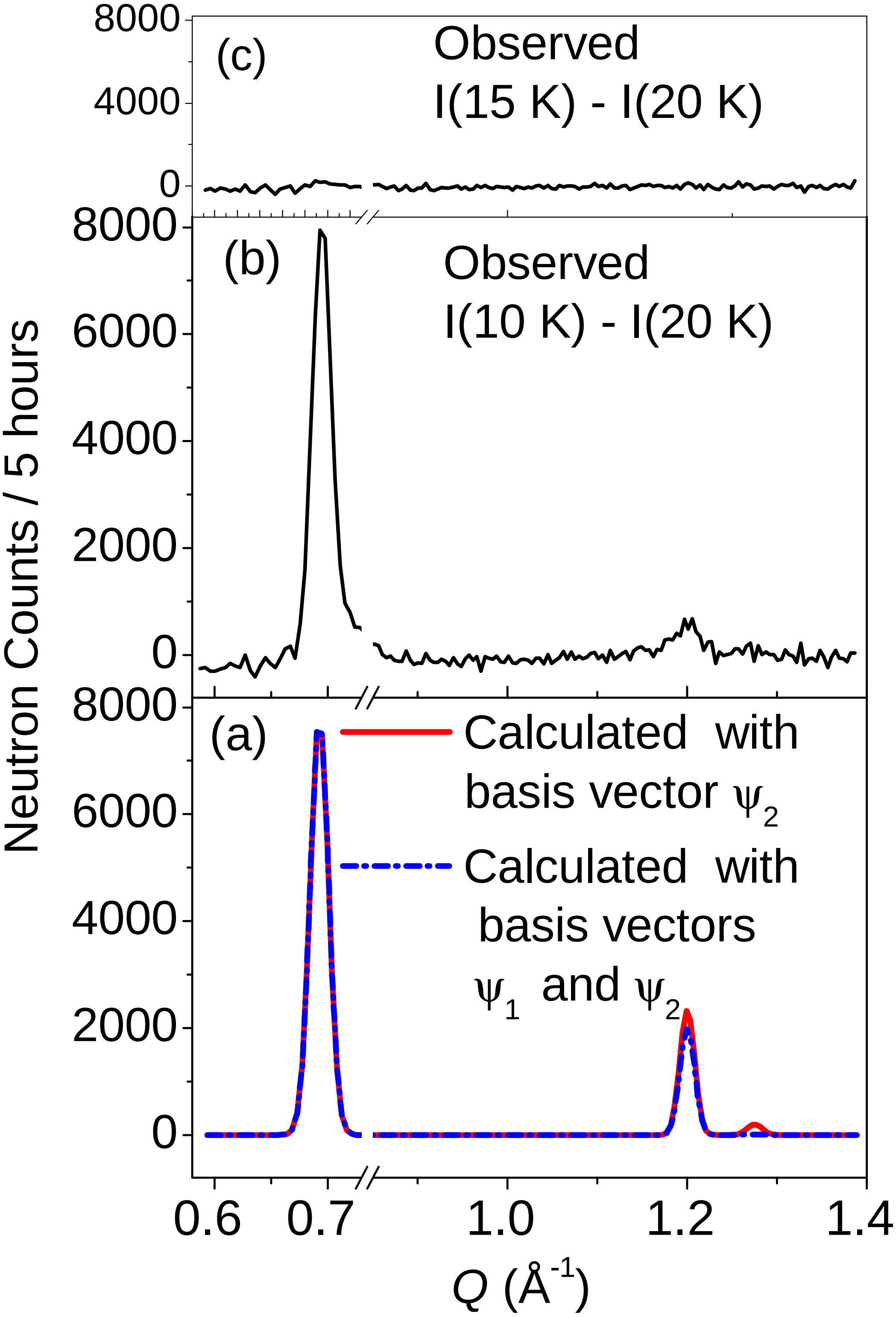

Figure 4.24: (a) The calculated neutron diffraction patterns for the CAFM structure by considering two cases: (i) only the basis vector ψ_2 (solid line) and (ii) both basis vectors ψ_1 and ψ_2 (dashed line). A selection of the observed magnetic neutron diffraction patterns at (b) 15 K and (c) 10 K. In Figs. (b) and (c) nuclear and magnetic background at 20 K has been subtracted out.

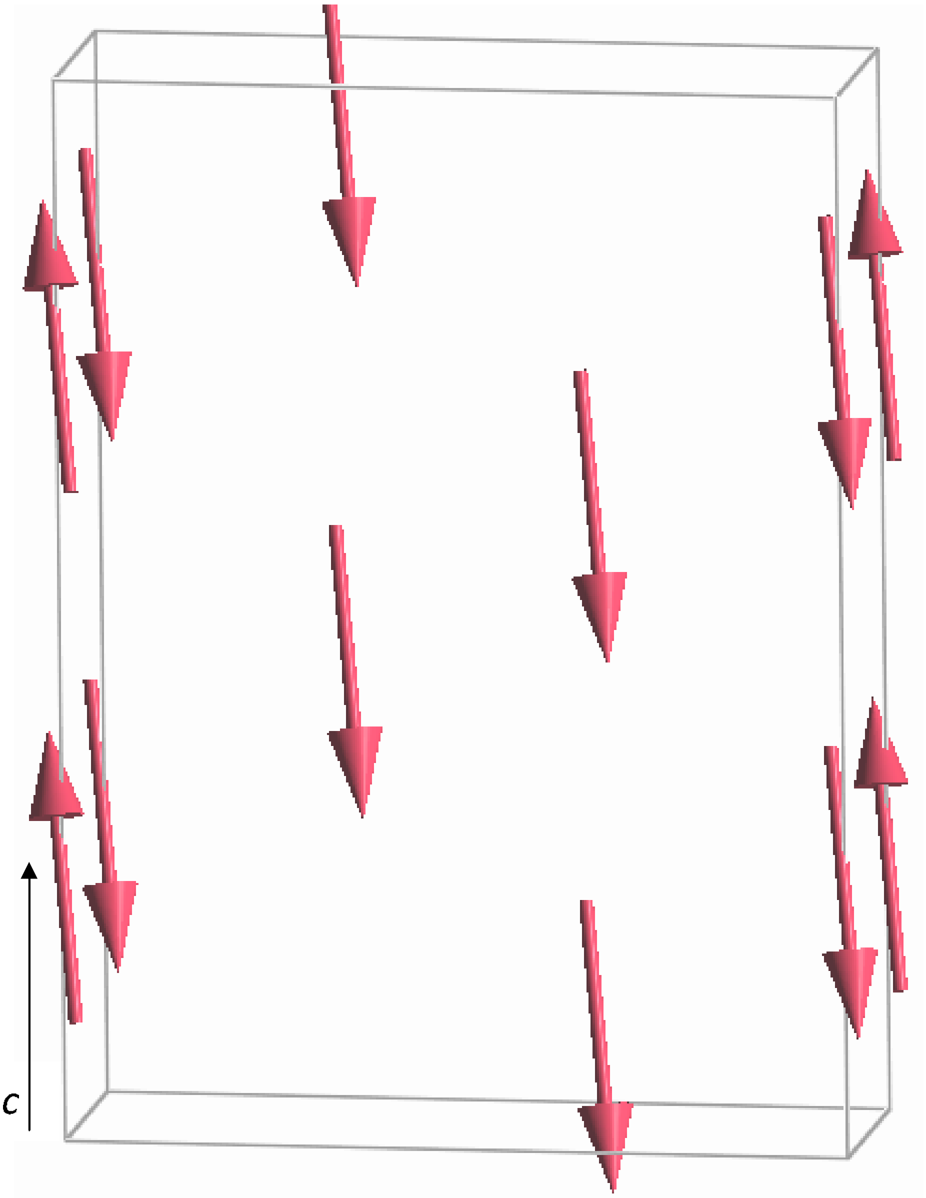

Figure 4.25: The schematic of the CAFM structure, having moment component along the c axis as well as in the ab plane.

cooling, then the magnetic Bragg peaks corresponding to the CAFM structure were observed. However, in the present study, we have observed the magnetic Bragg peaks corresponding to the same CAFM structure, even though the sample is cooled from 100 K to 1.5 K, 5 K and 7 K with no waiting time at 10 K. We note here that a cooling rate of 2 K/min was used by us. The magnetic Bragg peaks corresponding to the SDW structure are always present below T_N, as reported in literature [88]. No thermal hysteresis in the neutron diffraction patterns has been observed in the

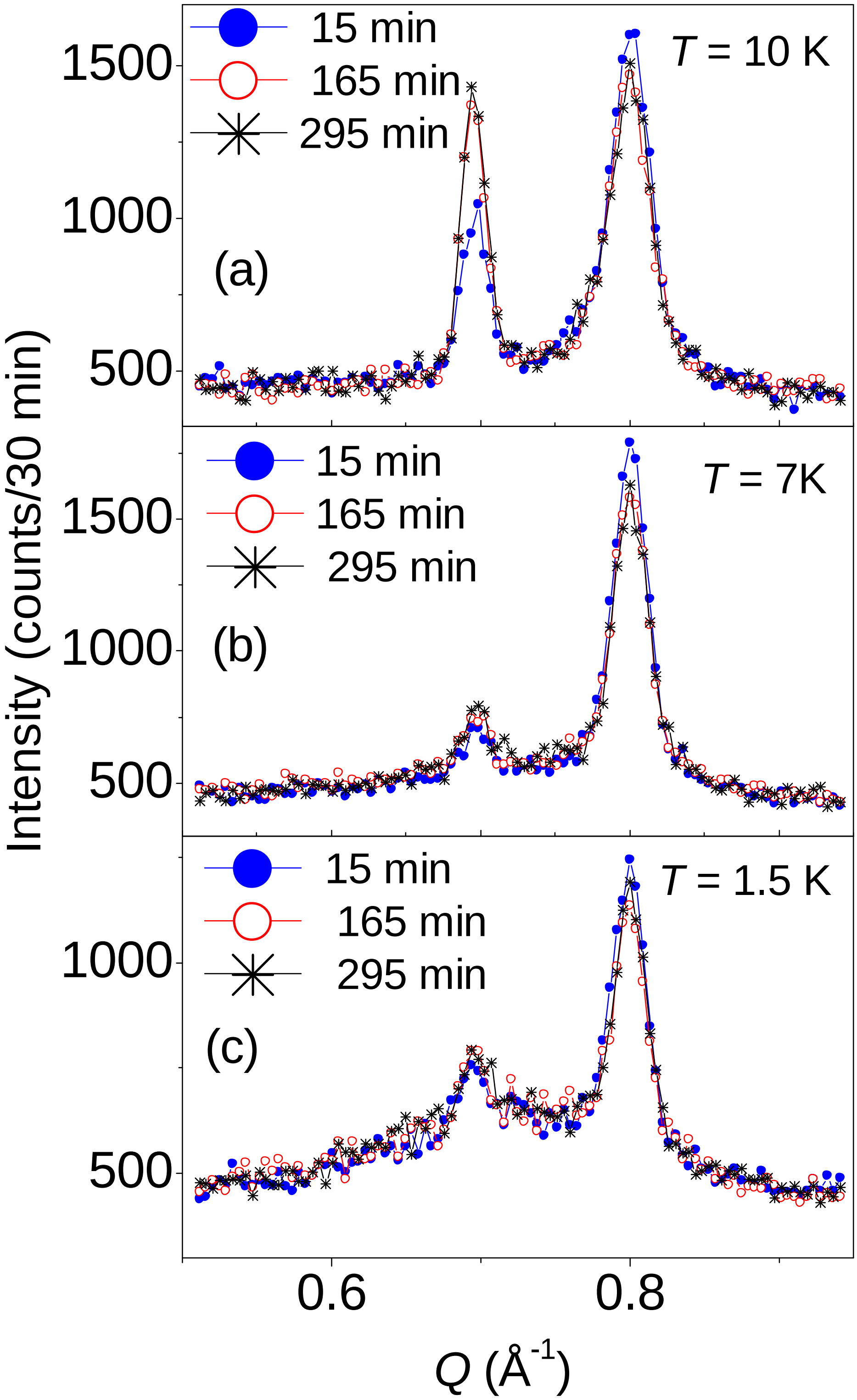

Figure 4.26: Neutron diffraction patterns collected in 30 minutes after an effective time gap of 15 (solid circle), 165 (open circle), and 295(star) minutes, after the measurement was started at (a) 10 K, (b) 7 K, and (c) 1.5 K. The magnetic Bragg peaks at $Q \sim 0.69$ and 0.8 Å^{-1} correspond to the CAFM and SDW type magnetic structures, respectively. The solid lines are guides to the eye.

present study.

Now we discuss that both SDW and CAFM magnetic structures can be interpreted by a single magnetic phase. We consider that the two propagation vectors $\boldsymbol{k}_1$ and $\boldsymbol{k}_2$ correspond to a single magnetic phase, in which the magnetic ordering can be described by a commensurate propagation vector which is being modulated by an incommensurate component. For the magnetic structures belonging to both propagation vectors, we have used the same scale factors (equal to the scale factor of the nuclear phase) in the refinement. If we consider that the magnetic transition at 15 K is of second order, no thermal hysteresis is expected in the neutron diffraction patterns (as observed in the present study). The finding from the present study is in mark contrast with the reported results in literature [88], where two different magnetic phases were considered in two different regions of the sample.

The refinements at 1.5, 5, and 7 K after the different time gaps are shown in Figs. 4.26 (a), (b), and (c), respectively. The Rietveld refined neutron diffraction patterns in the temperature range 1.5 - 15 K, with no waiting time at the respective temperatures, are shown in Figs. 4.22 (a) - (d). For both magnetic structures, the ratio of the intensities contribution of the LRO and SRO is 3:7 at $T = 5$ and 7 K, which decreases to 1: 9 at 1.5 K (indicating an increase in the volume fraction of the SRO). The amplitudes of the ordered moments are different for the CAFM and SDW structures. However, for both LRO and SRO, the amplitudes are same. Here it may be noted that for $15 < T < 25$ K, only the magnetic reflections corresponding to the propagation vector $\boldsymbol{k}_1$ are present. However, for $T < 15$ K, the magnetic reflections corresponding to both SDW and CAFM structures are present.

Now we will derive the value of the maximum ordered magnetic moment at 1.5 K. For the magnetic structure belonging to the propagation vector $\boldsymbol{k}_1$ (the SDW structure), the Co^{3+} ions (at the $6a$ site) have moment components of $M_x = 0$, M_y

= 0, and M_z = 2.82(4) μ_B, with a total moment of 2.82(4) μ_B. For the magnetic structure with propagation vector $\boldsymbol{k}_2$ (the CAFM structure), the Co^{3+} ions have moment components of M_x = - 0.32(3), M_y = 0.32(3), and M_z = 2.81(2) μ_B, with a net moment of 2.85(3) μ_B. The total maximum moment, calculated as a vector sum of the magnetic structures belonging to the propagation vectors $\boldsymbol{k}_1$ and $\boldsymbol{k}_2$, reaches to a value of 5.65(6) μ_B, with components of M_x = - 0.32 (3), M_y = 0.32 (3), and M_z = 5.63 (6) μ_B.

Finally, we discuss the results of the neutron diffraction studies reported in literature (in zero field) and bring out the importance of the present study. In the present study, the proposed ground state magnetic structure (below 15 K), is a coherent superposition of the magnetic structures belonging to the propagation vectors $\boldsymbol{k}_1$ (SDW) and $\boldsymbol{k}_2$ (CAFM), in which the ordered moment has components in the *ab* plane as well as along the *c* axis. We have also observed the magnetic Bragg peaks corresponding to the CAFM structure even when the sample is cooled rapidly (cooling rate: 2 K/ min) from 100 K to 1.5, 5, 7, and 10 K. The proposed magnetic structure is very much different from the reported ferrimagnetic as well as the PDA structure [52, 62, 63]. The proposed magnetic structure is also very much different from the square-wave magnetic structure (in which the moments with a constant amplitude of 5.3 ± 0.2 μ_B are aligned along the *c* axis) reported in the literature [89], however, the refined value of the maximum moment at the 6*a* site for the proposed magnetic structure in the present study, 5.65(6) μ_B at 1.5 K, is very much close to value reported in the literature for the square-wave structure. The reported results in the present study are very much different from the results available in literature, where the magnetic Bragg peaks corresponding to the CAFM were observed, only if the sample was kept at 10 K for some time while cooling from 18 K. In the literature, it was reported that sample contained three magnetic phases (i.e. different kind of magnetic ordering is present in the different regions of the sample), a SDW phase, a CAFM phase, and a phase exhibiting SRO. Moreover, it was assumed that the moment at the TP site was saturated to 5.1 ± 0.1 μ_B below 20 K. The temperature variation of the moment was not considered to evaluate the phase fraction of the CAFM, SDW, and SRO phases. In the CAFM phase (belonging to the propagation vector $\boldsymbol{k}_2$), the magnetic moments were reported to be aligned along the c axis. The CAFM phase was reported to be the true ground state of the compound. We, therefore, conclude that the magnetic structure reported in the present study is very much different from the results of the neutron diffraction studies reported in the literature. A comparison of the magnetic structures is given in Table 4.6.

4.3.5 Mössbauer Study of Spin Relaxation of Fe^{3+} in $Ca_3Co_{2-x}Fe_xO_6$

Figure 4.27 depicts the Mössbauer spectra for the $x = 0.2$ and 0.4 samples. The spectra (Fig. 4.27) were analyzed in terms of the spin relaxation theory [74], and it yields perfect fits in terms of χ^2 values, and confirms the earlier conclusions [77] that the iron occupies only the TP site (Co2), with a negative quadrupole interaction, EQ $= 1/4e^2qQ$ (= -0.62 mm/s at 90 K). The analysis also yields (assuming a fluctuating magnetic hyperfine field of 45 T) the room temperature spin relaxation rates, which are 1.5×10^{11} and 7.7×10^{10} s^{-1} for $x = 0.4$ and $x = 0.2$, respectively, indicating the dominance of Fe-Fe spin-spin relaxation. The ratio of the relaxation rates (∼2) equals the ratio of iron concentration, expected for spin-spin relaxation. Also the fact that the $x = 0.4$ sample at 90 K exhibits a spectrum with a relaxation rate of 5.5×10^{10} s^{-1}, not very much smaller than that at 300 K, indicates the dominance of the spin-spin relaxation process. The relaxation rate certainly does not follow a high temperature power law expected for spin-lattice relaxation.

Table 4.6: Magnetic structures of the compound $Ca_3Co_2O_6$ determined from the neutron powder diffraction (NPD) and single crystal neutron diffraction (SXND) studies.

	Properties				
	Magnetic structure	Maximum moment at the $6a$ site	Coexistence of the SRO and LRO	Time variation of the AFM reflections	Ref.
NPD	Ferrimagnetic ($T_N \sim 24$ K)	(3.00 ± 0.05) μ_B at 10 K, and moment ∥ c axis	Not reported	Not reported	[52]
NPD	Ferrimagnetic ($T \leq 25$ K)	Not reported	Not reported	Not reported	[63]
SXND	Not a simple PDA	Not reported	Not reported	Not reported	[62]
SXND and NPD	SDW	(5.0 ± 0.1) μ_B at 20 K, and spin ∥ c axis	Below 21 K	Not reported	[86]
SXND	Square-wave ($T \leq 13$ K)	(5.3 ± 0.2) μ_B at ~ 10 K, and spin ∥c axis	Not reported	(1, 0, ± δ) move to (1, 0, 0) with time ($T \leq 13$ K)	[89]
NPD	SDW ($12 \leq T \leq 25$ K) Coexistence of SDW, CAFM, and SRO ($8 \leq T \leq 12$ K) CAFM($T = 2$ K)	(5.1 ± 0.1)μ_B For $T < 20$ K, and spin ∥ c axis for all phases	Below 21 K	Inter-conversion of the SDW and CAFM phases ($8 \leq T \leq 12$ K)	[88]
NPD	SDW ($15 \leq T \leq 25$ K) Coherent superposition of the CAFM and SDW structures ($15 \leq T$)	5.65(6) μ_B at 1.5 K, and spins have component along the c axis as well as in the ab plane	At all the temperature below T_N	AFM peaks of the SDW and CAFM structure show time dependence	**Present Study**

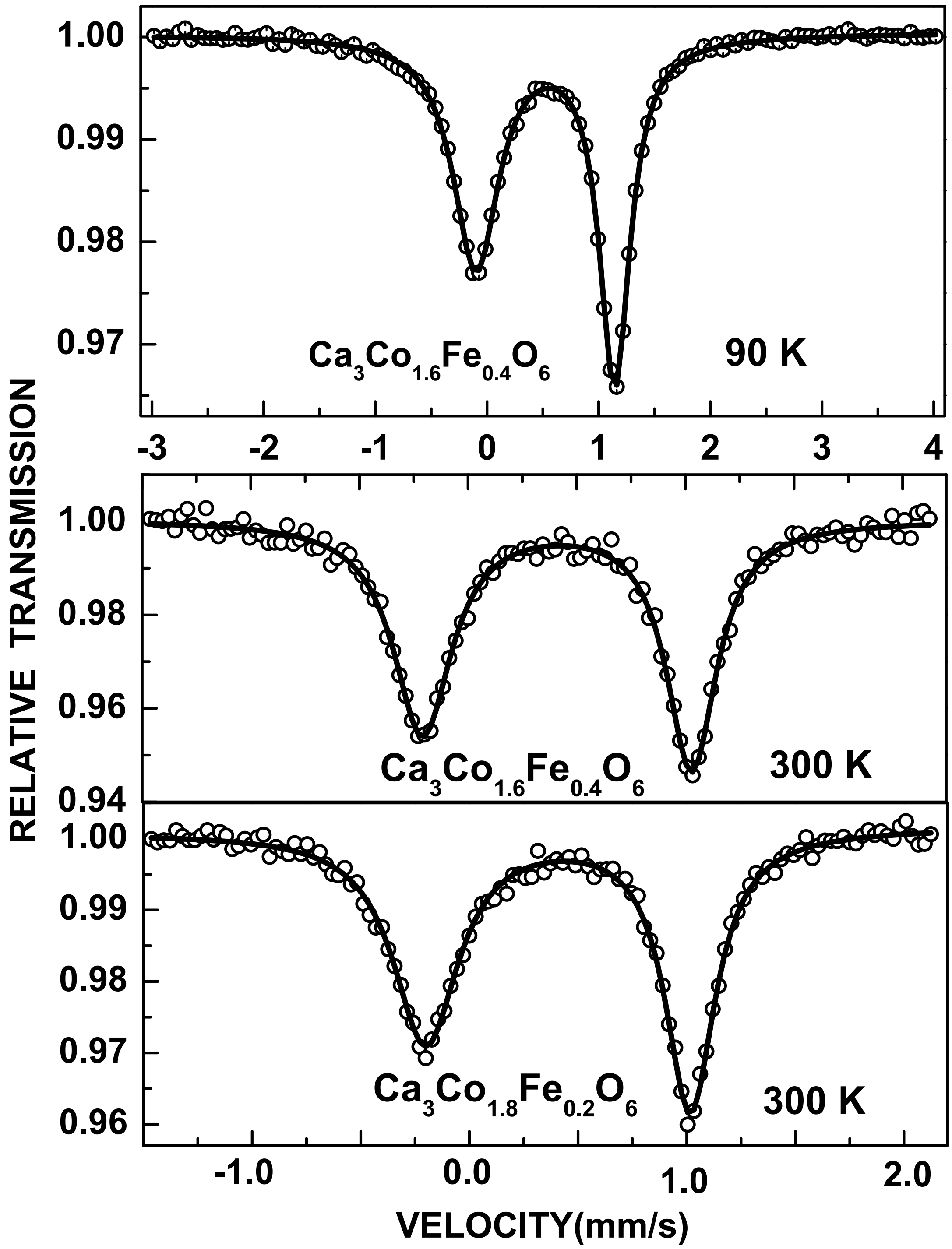

Figure 4.27: The Mössbauer spectra of $Ca_3Co_{2-x}Fe_xO_6$ for the $x = 0.2$ and 0.4 samples.

4.3.6 Magnetic Properties of Ca_3CoFeO_6

Figures 4.28 and 4.29 depict the Mössbauer spectra for the compound Ca_3CoFeO_6 at different temperatures in the range of 4.2- 520 K. The compound Ca_3CoFeO_6

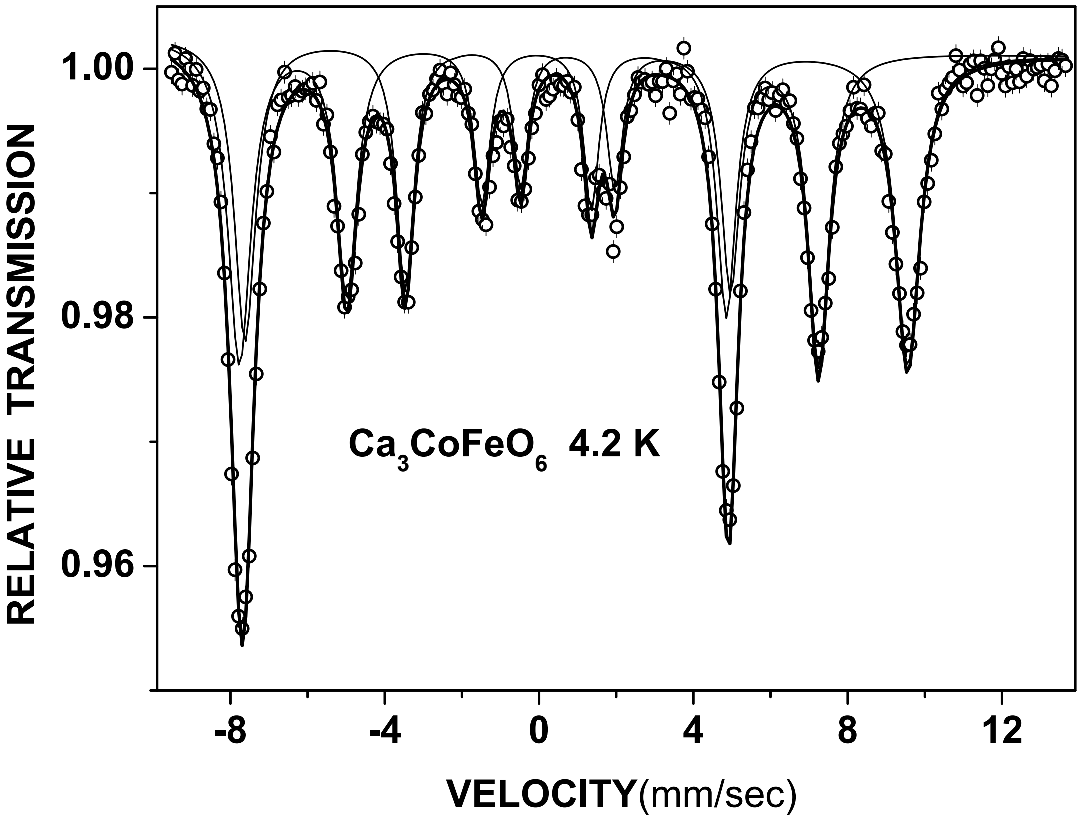

Figure 4.28: The Mössbauer spectra of Ca_3CoFeO_6 at 4.2 K.

exhibits spectra displaying magnetic order up to 500 K. Just by counting the number of absorption lines in the spectra (Fig. 4.28) it is obvious that they are composed of two Fe subspectra of different crystallographic sites. The one with the larger hyperfine field, larger isomer shift, and positive qaudrupole interaction is denoted arbitrarily as site 1. Table 4.7 depicts the parameters that are obtained from the analysis of the spectra in terms of full diagonalization of the Hamiltonian of magnetic and quadrupole interactions, where the magnetic field is at an angle θ relative to the axis of the EFG for two different crystallographic Fe sites. The solid lines in the figures show the least square fit simulated spectra. Figure 4.30 depicts the temperature dependence of the relative spectral areas under the two subspectra, giving approximately the relative occupation of Fe in the two sites. One observes that they are almost of equal intensity; the slight difference may be the result of a

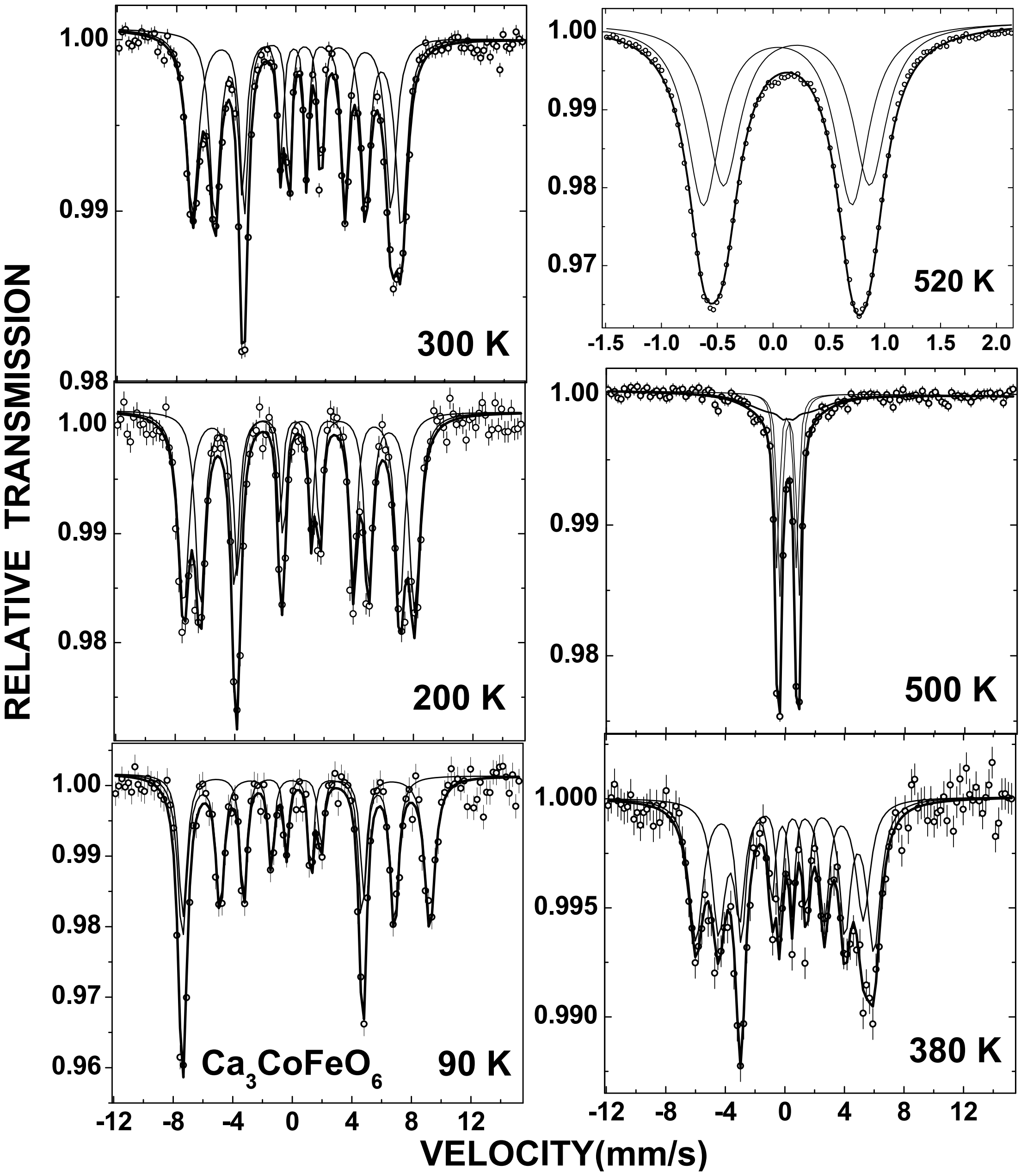

Figure 4.29: The Mössbauer spectra of Ca_3CoFeO_6 at various temperatures.

slightly different recoil free fraction for the two sites. Thus it is clear that for this concentration of iron ($x = 1.0$), the iron occupies two different crystallographic sites with almost equal probability. In Fig. 4.31, we show the temperature dependence of the isomer shift for the two sites. Except for the fact that the isomer shift is different for the two sites, there is nothing unusual in these behaviors, displaying the normal high temperature linear shift.

Table 4.7: The parameters derived from the analysis of the Ca_3CoFeO_6 Mössbauer spectra. The error bars of these parameters are shown in the corresponding figures. The isomer shifts (IS1 and IS2) are relative to that of iron at room temperature. EQ1 and IN1 stand for the quadrupole interaction and the relative intensity of site “1”.

Temp. (K)	IN1 (%)	IS1 (mm/s)	EQ1 (mm/s)	HF1 (T)	θ_1 (deg)	IS2 (mm/s)	EQ2 (mm/s)	HF2 (T)	θ_2 (deg)
4.2	54	0.42	0.68	53.3	25	0.28	-0.64	45.7	23
90	56	0.42	0.60	51.5	18	0.26	-0.64	43.7	20
150	54	0.43	0.60	49.9	29	0.26	-0.68	42.8	35
185	50	0.41	0.60	48.9	48	0.26	-0.61	42.2	51
200	51	0.40	0.59	48.0	61	0.24	-0.70	41.2	64
225	52	0.39	0.60	47.1	79	0.21	-0.73	40.5	80
250	51	0.37	0.62	46.0	82	0.2	-0.7	39.2	81
300	54	0.35	0.56	43.2	80	0.16	-0.67	36.3	85
350	53	0.32	0.54	40.3	90	0.15	-0.65	33.5	90
380	54	0.28	0.56	36.8	90	0.11	-0.62	29.7	90
450	53	0.24	0.56	28.6	90	0.07	-0.57	21.9	90
500	52	0.23	0.62	0		0.08	-0.65	0	
520	46	0.22	0.64	0		0.05	-0.65	0	

In Fig. 4.32, the temperature dependencies of the quadrupole interactions are shown. Here we observe a surprising result, the Fe quadrupole interaction in the two sites is almost equal in strength, yet of opposite sign. The quadrupole interactions change very little with temperature, as expected for an ionic Fe^{3+} ($S_{5/2}$ state), where the electric field gradient is due to lattice charges.

Figure 4.33 displays the temperature dependence of the two hyperfine fields. We observe that the hyperfine field for two different sites varies smoothly with temperature, the value of hyperfine field changing from 52 and 43 T, respectively, at

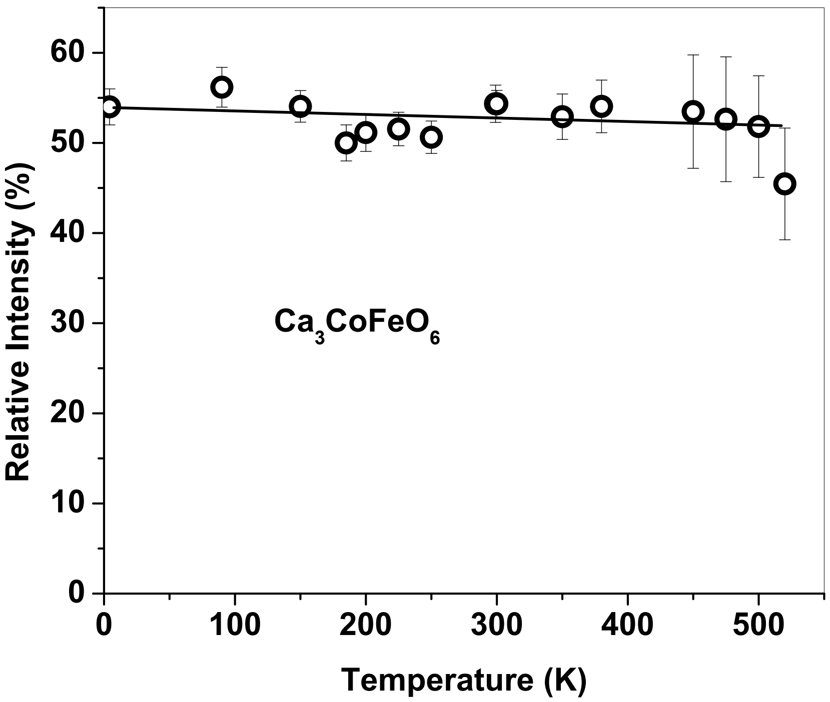

Figure 4.30: The relative intensity of one of the subspectra of Fe (“1”).

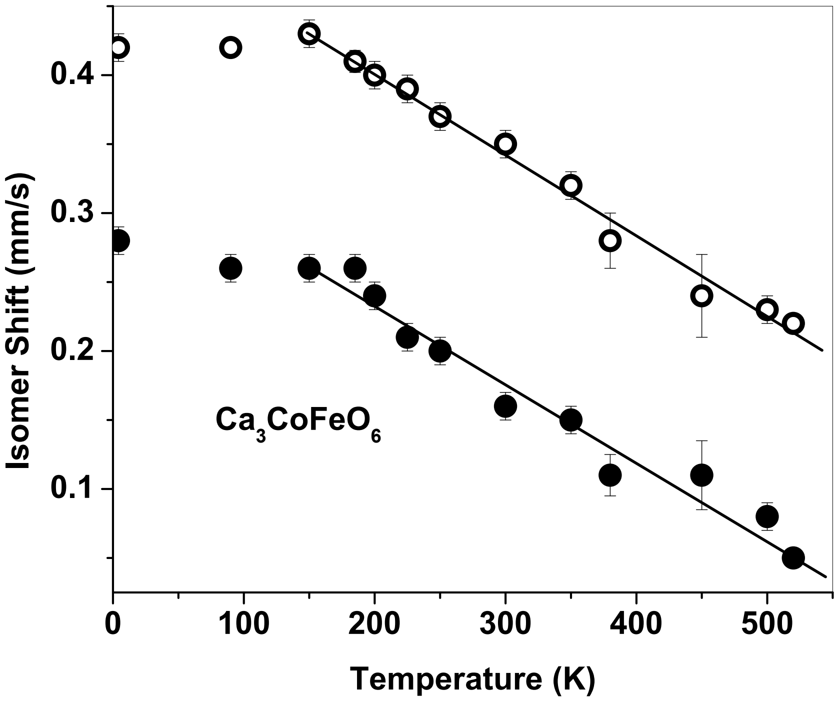

Figure 4.31: The temperature dependence of the isomer shifts of the two Fe sites, (“1” open circles).

low temperature to zero above 500 K. The solid lines in Fig. 4.33 represent the parameterless (except for the normalization of the fields to 52 and 43 T at low temperatures) pure spin 5/2 Brillouin functions, indicating almost identical temperature

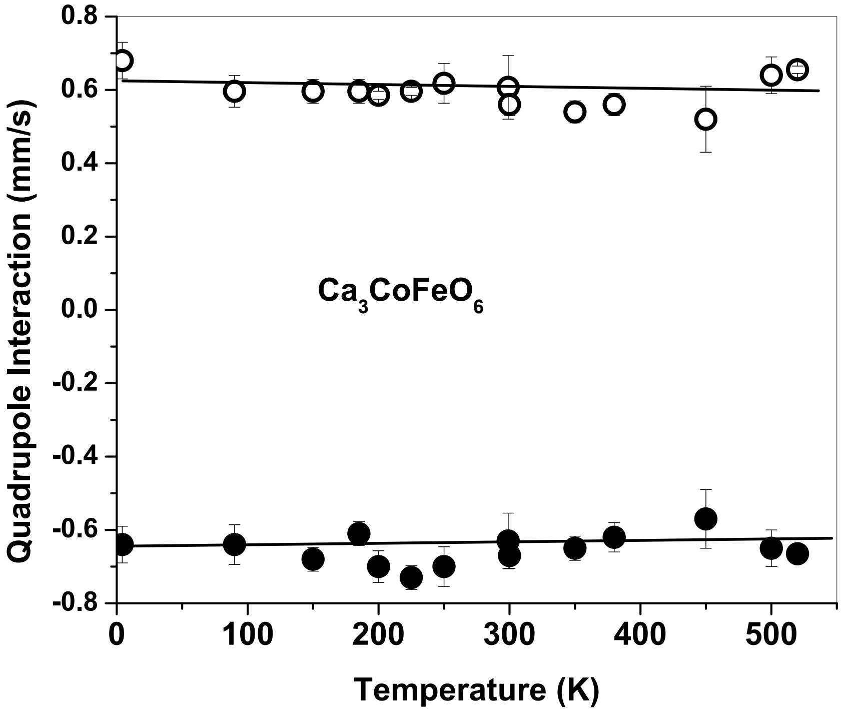

Figure 4.32: The temperature dependence of the two quadrupole interactions in the two Fe sites ("1" open circles).

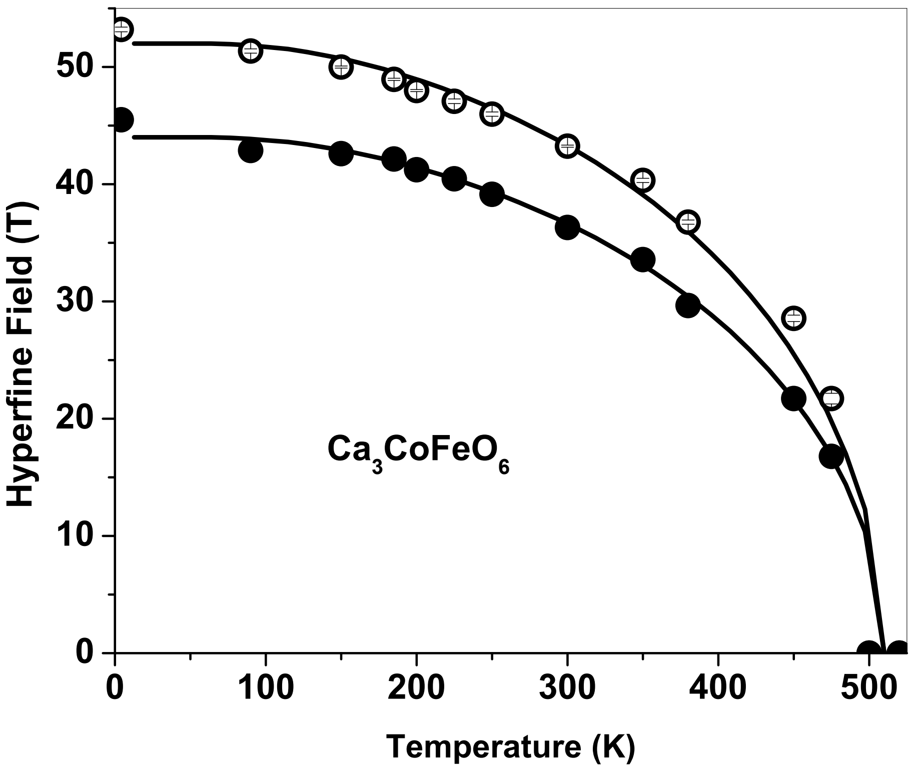

Figure 4.33: The temperature dependence of the two hyperfine fields. The solid lines are pure spin 5/2 Brillouin functions.

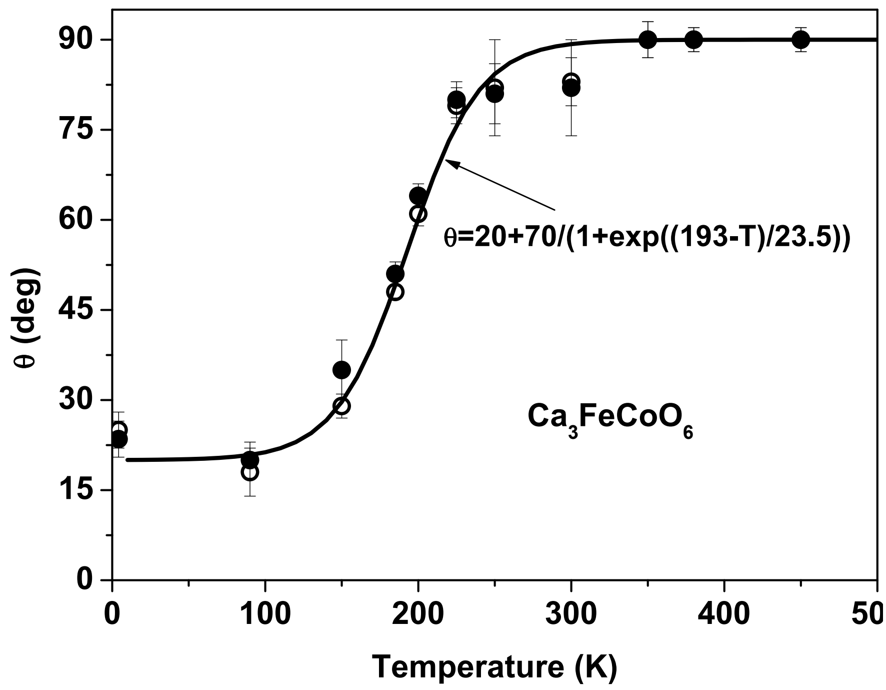

Figure 4.34: The temperature dependence of the angles θ_1 and θ_2.

dependencies of the magnetic moments in the two sites. The spectrum at 520 K, shown in Fig. 4.29, was analyzed in terms of two pure quadrupole doublets. A very interesting result is displayed in Fig. 4.34, in which the temperature dependence of the angles θ_1 and θ_2 at which the hyperfine fields point relative to the local EFG axis are displayed. One observes that θ_1 and θ_2 are equal to each other and change drastically with temperature. While at low temperatures, below 150 K, the moments in both sites are aligned at an angle of 20±3° relative to the EFG axis, above 230 K they are perpendicular to the EFG axis. Here it may be noted that in the x-ray diffraction study (Chapter 3), it has been observed that *c* axis is at an angle of 18.5° relative to the perpendicular to the *ab* plane. The results of Mössbauer and x-ray diffraction studies, therefore, indicate that the axis of the EFG in both sites is perpendicular to the unit cell basal plane (*ab* plane) and at low temperatures the moments are probably along the unit cell *c* axis. At the high temperatures the magnetization lies in the basal plane. The solid line in Fig. 4.34 is a least square fit of the step function formula: $\theta = \theta_0 + (90.0 - \theta_0) / [1.0 + \exp\{(T_{sr}-T)/W\}]$, yielding $\theta_0 = 20 \pm 3°$, $T_{sr} = 193 \pm 5$ K, and $W = 23 \pm 2$ K. The relative alignment of the magnetic moments for the two sites is depicted schematically in Fig. 4.35.

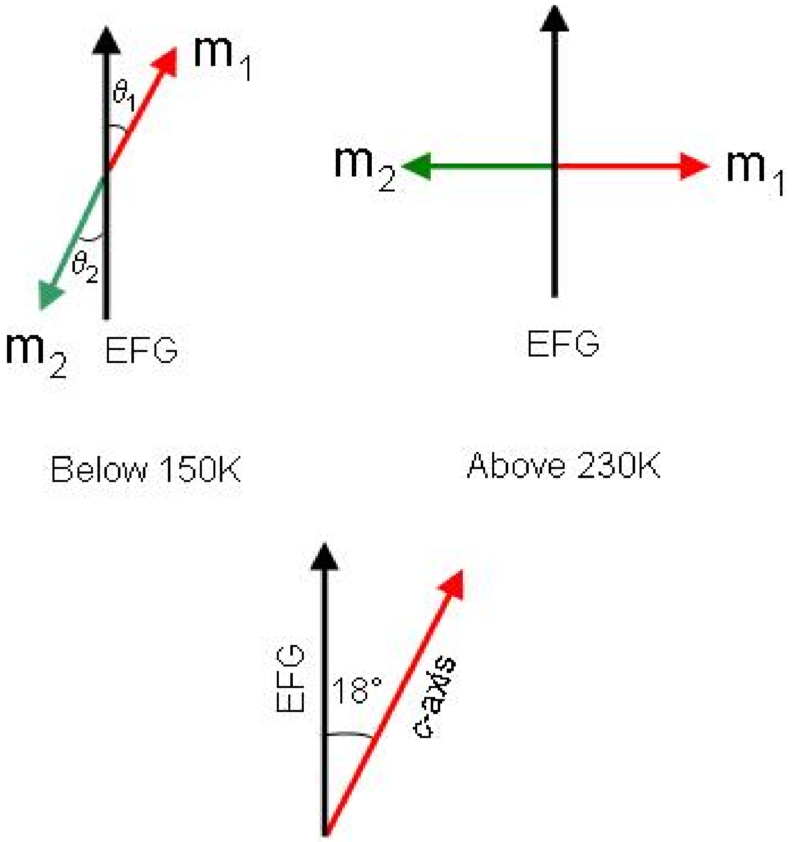

Figure 4.35: A schematic diagram of the relative alignment of two site moments with respect to the EFG and the crystallographic c axis.

The temperature dependent dc magnetization curves in the temperature range 5 - 320 K are shown in Fig. 4.36. It is clear that the magnetic ordering temperature is above the highest recorded temperature. The zero field cooled and field cooled magnetization curves do not merge even at 320 K, in agreement with the Mössbauer studies. Around 200 K, one observes a sharp drop in magnetization, which can be associated with the spin reorientation found in the Mössbauer studies. The magnetic field dependence of magnetization at 1.5 K presented in Fig. 4.37 indicates that at high magnetic fields, the magnetization varies linearly

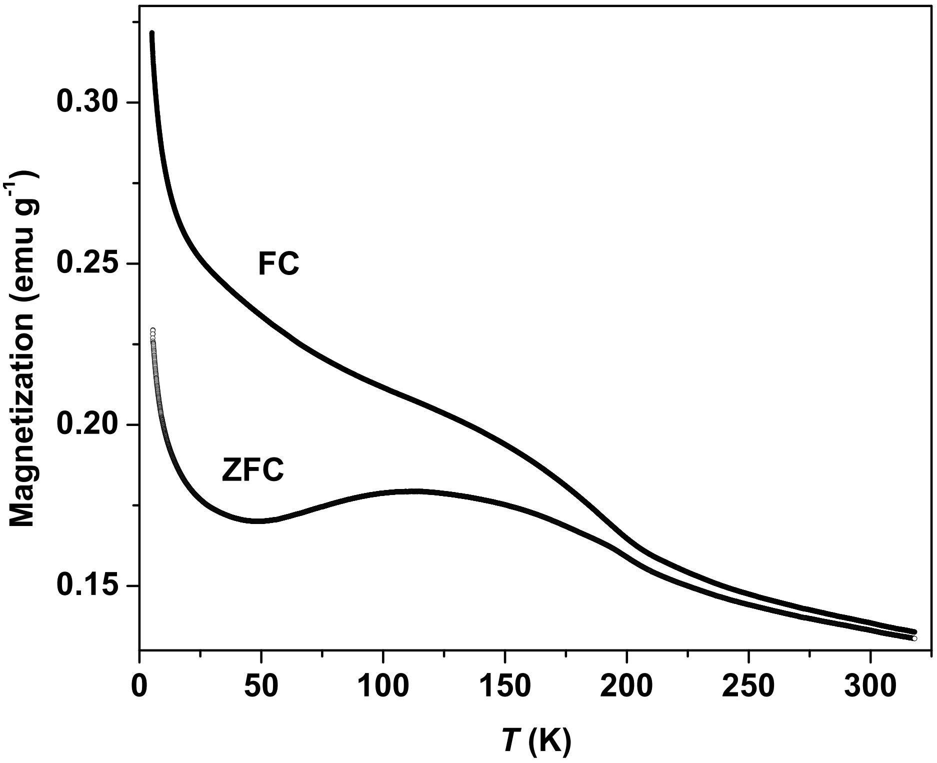

Figure 4.36: The temperature dependence of the field cooled and zero field cooled magnetizations of Ca_3CoFeO_6 in 1 T.

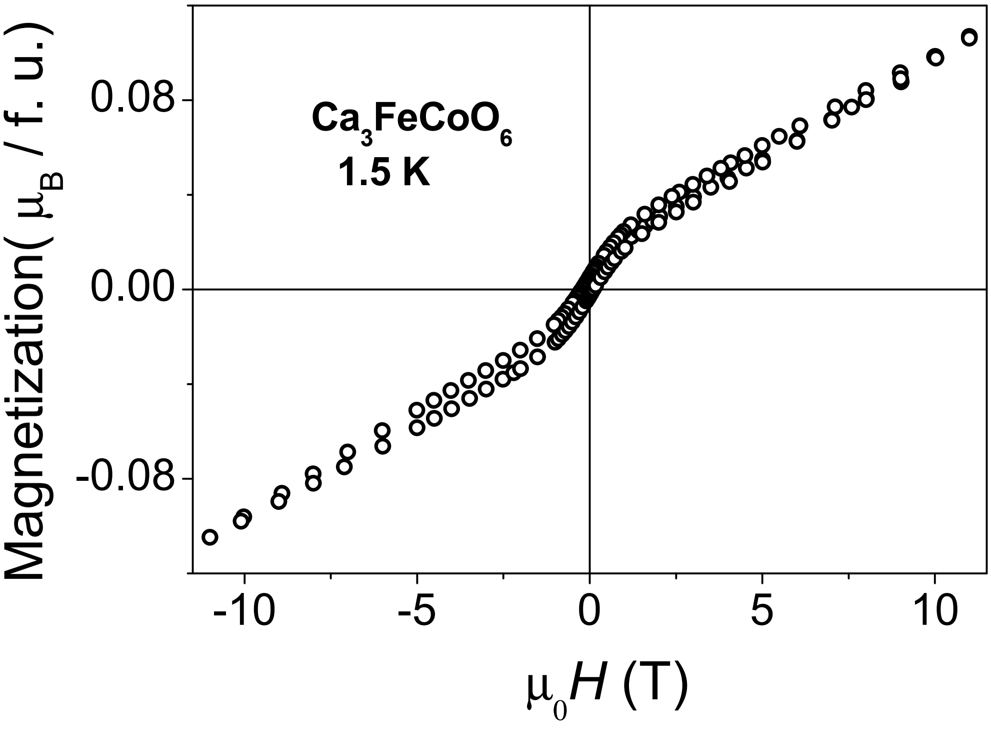

Figure 4.37: Magnetic field dependence of the Ca_3FeCoO_6 magnetization at 1.5 K.

with magnetic field, as expected for an antiferromagnet; however, a small ferromagnetic component, displaying hysteresis, is also present. It seems that the magnetic coupling between intrasite irons is ferromagnetic while the intersite sublattices are coupled antiferromagnetically. The small ferromagnetic component observed in Fig. 4.37 may be due to an unequal iron concentration in the two sites (shared with cobalt). A difference of $\sim 0.2\%$ in the concentration is enough to explain the observed ferromagnetic component. Alternatively a very small canting (only $\sim 0.2°$) of the moments in the antiferromagnetic structure may also produce the observed ferromagnetic component.

Here it may be noted that the magnetic properties of Ca_3CoFeO_6 are very much different from that of the isostructural compound Ca_3CuMnO_6 [43]. For the Ca_3CuMnO_6, two transitions for long-range magnetic ordering (not a common feature in a quasi-one-dimensional system), one at 5.5 K and other below 3.6 K, have been reported in the literature [43]. The transition at 5.5 K has been ascribed due to the antiferromagnetic ordering. Recently, the magnetic and electronic properties of Ca_3FeRhO_6 [90], with the chemical formula similar to the present compound Ca_3FeCoO_6 but with a crystal structure like that of $Ca_3Co_2O_6$, have been studied. It was found that the ordering temperature of Ca_3FeRhO_6 is only $T_N = 20$ K. The iron occupies the trigonal prism site, similar to the iron substituted $Ca_3Co_2O_6$ and an equal strength of quadrupole interaction for both Ca_3FeRhO_6 and Ca_3FeCoO_6 has been found in the Fe Mössbauer study. These similarities and differences between the two compounds Ca_3FeRhO_6 and Ca_3FeCoO_6 prove that the local oxygen environment of Fe in the two compounds is very similar; however, due to the different crystal structure, the Fe-Fe exchange interactions are very different, T_N observed to be approximately 20 and 500 K for Ca_3FeRhO_6 and Ca_3FeCoO_6, respectively.

4.4 Conclusions

In the present Chapter, the author has investigated the magnetic structure of the compounds $\mathrm{Ca_3Co_{2-x}Fe_xO_6}$ by neutron powder diffraction (for $x = 0$, 0.2, and 0.4) and Mössbauer spectroscopy (for $x = 0.2$, 0.4, and 1.0) studies. Additional magnetic diffraction peaks in the neutron powder diffraction patterns below their respective Néel temperatures ($T_N = 25$, 20 and 17 K, for $x = 0$, 0.2, and 0.4 compounds, respectively) indicate the presence of the antiferromagnetic structure.

In the first approximation, two different commensurate magnetic structures, (i) amplitude-modulated structure with a propagation vector $\boldsymbol{k} = \{0, 0, 1\}$ and (ii) partially disordered antiferromagnetic (PDA) structure, are able to fit the same neutron diffraction patterns for the $x = 0$, 0.2, and 0.4 compounds, below T_N. The common point is that magnetization in the unit cell is zero for both magnetic structures. However, a detailed analysis reveals that these compounds order magnetically in an incommensurate spin density wave (SDW) structure, having a modulation and an alignment of the spins along the crystallographic c axis, below T_N.

A detailed analysis for the Fe- substituted compounds ($x = 0.2$ and 0.4) shows that the magnetic ground state is an incommensurate spin density wave, with the propagation vector $\boldsymbol{k} = \{0, 0{,}1.0182(9)\}$. Further, Rietveld refinement of neutron diffraction patterns confirmed a coexistence of short-range and long-range incommensurate magnetic structures with an amplitude modulation of the moments along the c axis, below $\sim$ 20 and 17 K for $x = 0.2$ and 0.4, respectively. A model of platelet-like-shaped magnetic crystallites, disorderly stacked along crystallographic c direction [Isize model=1 in FULLPROF], describes the observed magnetic short-range as well as the long-range order satisfactorily. The maximum values of ordered magnetic moments at the $6a$ site (at 1.5 K) are 4.82 μ_B and $5.11\mu_B$ for $x = 0.2$

and 0.4 compounds, respectively. The same values of the ordered magnetic moment (4.82 μ_B and 5.11 μ_B for $x = 0.2$ and 0.4 compounds, respectively) are observed for both LRO and SRO. The nearly zero value of the ordered moment has been observed for the 6*b* site for both compounds. The magnetic correlation lengths along the *c* axis, at 1.5 K, for the LRO ($\xi_I{}^c$) and SRO ($\xi_{II}{}^c$) are $\sim$ 1027 and 60 Å for the compound $x = 0.2$; and 1021 and 47 Å for the compound $x = 0.4$, respectively. For both compounds, the magnetic correlation length for the LRO increases with decreasing temperature, while for the SRO, it remains approximately constant down to 1.5 K. The relative contributions of the LRO and SRO in the magnetic Bragg peaks are in the ratio of 13:7 and 3:2 for $x = 0.2$ and 0.4, respectively. This ratio remains unchanged down to 1.5 K for both compounds, indicating that the volume fractions of the compound exhibiting the short-range order and long-range order remain constant. The coexistence of SRO and LRO incommensurate magnetic structures can be a good model to understand the spin-spin correlations for other compounds of the $A_3MX\mathrm{O}_6$ family, especially for the compounds $\mathrm{Ca_3CoRhO_6}$ (Refs. [65] and [66]) and $\mathrm{Sr_3HoCrO_6}$ (Ref. [87]). A single crystal neutron diffraction study will be of great help to provide further insight on the microscopic nature of the magnetic ordering in these compounds.

For the parent compound $\mathrm{Ca_3Co_2O_6}$, a detailed analysis shows that the magnetic ground state is a coherent superposition of the SDW and CAFM structures. For both magnetic structures (the SDW and CAFM), a SRO coexists with the LRO. The ratio of the intensities contribution (in both SDW and CAFM structures) of the LRO and SRO is 3:7 over 5 - 7 K and the ratio decreases to 1: 9 at 1.5 K. In the proposed ground state magnetic structure, the ordered moment has component in the *ab* plane as well as along the *c* axis. The observed ordered moment components in the *ab* plane questions the very strong Ising-like magnetic anisotropy of the Co^{3+}

spins at TP site.

In the Mössbauer study, the compounds with $x = 0.2$ and 0.4, show a paramagnetic behavior at 90 K and the iron exhibits slow spin relaxation phenomena even at room temperature. The compound Ca_3CoFeO_6, where the iron resides almost equally in two different crystallographic sites, exhibits a very high magnetic ordering temperature, $T_N \sim 500$ K. At $T_{sr} \sim 193$ K, a spin reorientation of the iron magnetic moments is observed. Below T_{sr}, the moments in the two sites are aligned along the crystallographic c axis, whereas above T_{sr} they are aligned in the basal ab plane. The magnetic order is ferromagnetic within each iron site and antiferromagnetic between the sites. A small ferromagnetic component observed in the magnetization studies is probably due to a very small difference in the occupation of the two iron sites. The unique magnetic properties of Ca_3CoFeO_6 ($x = 1$) compare to the compounds with lower x values, or Ca_3FeRhO_6, are due to its different crystal structure, which may have some importance for its practical applications.

CHAPTER 5

Effect of Magnetic Field on the Ground State Magnetic Properties of $Ca_3Co_{2-x}Fe_xO_6$

5.1 Introduction

In the zero field neutron diffraction study of the compounds $Ca_3Co_{2-x}Fe_xO_6$ ($x =$ 0, 0.2 and 0.4), described in Chapter 4, it is observed that these compounds ordered magnetically in an incommensurate spin density wave (SDW) structure, having a modulation and an alignment of the spins along the crystallographic c axis, below their respective Néel temperatures ($T_N =$ 25, 20 and 17 K, for $x =$ 0, 0.2, and 0.4 compounds, respectively). Further, a coexistence of the magnetic long-range and short-range ordering has been observed down to 1.5 K (below T_N).

In the present chapter, the effect of an external magnetic field on the nature of magnetic ordering in the compounds $Ca_3Co_{2-x}Fe_xO_6$ ($x =$ 0, 0.1, 0.2, and 0.4) is described. First (in Sec. 5.3.1), the author discusses the results of the dc magnetization study, where, an indication of the presence of a field-induced transition from a ferri-to-ferromagnetic state is observed. Field induced transitions generally arise from a competition between Zeeman energy and exchange energy or crystal-field anisotropy. The microscopic understanding of the field induced transitions in these geometrically frustrated compounds with a triangular lattice arrangement of spin chain is of fundamental interest because an interplay between geometrical frustration and high magnetic field results in many novel magnetic states.

In order to achieve a microscopic understanding of the effect of an external magnetic field on the magnetic correlations at microscopic length scale in these quasi-1D spin-chain compounds, the author has carried out a detailed neutron powder diffraction study down to 1.5 K and up to a field of 4 T for the compound $\mathrm{Ca_3Co_{1.8}Fe_{0.2}O_6}$. A field-induced phase transitions from the zero field incommensurate spin density wave (SDW) structure ($T_N \sim 20$ K) to a commensurate amplitude modulated (AM) structure, and then to a ferrimagnetic structure have been observed. Besides, the effect of an applied field on the observed short-range spin-spin correlation has been brought out. The results of the neutron diffraction study are described in Sec. 5.3.2. The results have been published [77] in international scientific journals.

Here it may be noted that in the present chapter, the effect of an external magnetic field on the magnetic properties of these compounds has been investigated using the powder samples. In powder sample, the direction of the field relative to the easy axis changes due to the powder averaging. The analysis of the $M(H)$ curves is difficult because of the presence of a strong magnetic anisotropy, which can spoil many interesting features. However, in the neutron powder diffraction study, by analyzing the field and temperature dependence of the integrated intensities of the antiferromagnetic reflections, one can get a useful qualitative information regarding the field-induced magnetic phase transitions. The measurements on twin-free single crystals of these compounds will be of great help to provide further insight on the microscopic nature of the magnetic ordering in these compounds. Moreover, in single crystals, one can apply a magnetic field transverse to the Ising axis (c axis for the studied compounds in the present thesis) and obtain an experimental transverse field magnetic phase diagram, which can be compared with the theoretical results of the transverse field Ising model.

5.2 Experimental Details

Polycrystalline samples of the compounds $\mathrm{Ca_3Co_{2-x}Fe_xO_6}$ (x = 0, 0.1, 0.2, and 0.4) were prepared by the conventional solid-state reaction method as described in

Chapter 2.

The dc magnetization measurements were carried out on all the samples using a commercial (Oxford Instruments) vibrating sample magnetometer. For the zero-field-cooled (ZFC) magnetization measurements, the samples were first cooled from room temperature down to 2 K in zero field. After applying the magnetic field of 1 kOe at 2 K, the magnetization was measured in the warming cycle with the field on. Whereas, for the field-cooled (FC) magnetization measurements, the samples were cooled down to 2 K in the same field (1 kOe) and the FC magnetization was measured in the warming cycle under the same field. The hysteresis curves were recorded at 1.5 K over +110 to -110 kOe applied field.

The neutron diffraction experiments on the compound $Ca_3Co_{1.8}Fe_{0.2}O_6$ were performed by using the cold neutron powder diffractometer DMC at the Paul Scherrer Institute (PSI), Switzerland (λ = 2.46 Å). In zero magnetic field, diffraction patterns were recorded in the temperature range of 1.5 - 100 K. The diffraction patterns by applying an external magnetic field up to 4 T were recorded over the temperature range of 4.2 - 50 K using the pressed-powder pellets. The diffraction data were analyzed by the Rietveld method using the FULLPROF program [40] The representation theory analysis was performed using the SARAH software [41].

5.3 Results and Discussion

5.3.1 Dc-magnetization Study

5.3.1.1 ZFC and FC Magnetization vs Temperature

The temperature dependence of the ZFC and FC dc magnetization for all samples under $H = 1$ kOe is shown in Fig 5.1. Inverse magnetic susceptibility vs temperature has been plotted in the inset of Fig 5.1. It is clear from Fig. 5.1 that the high tem-

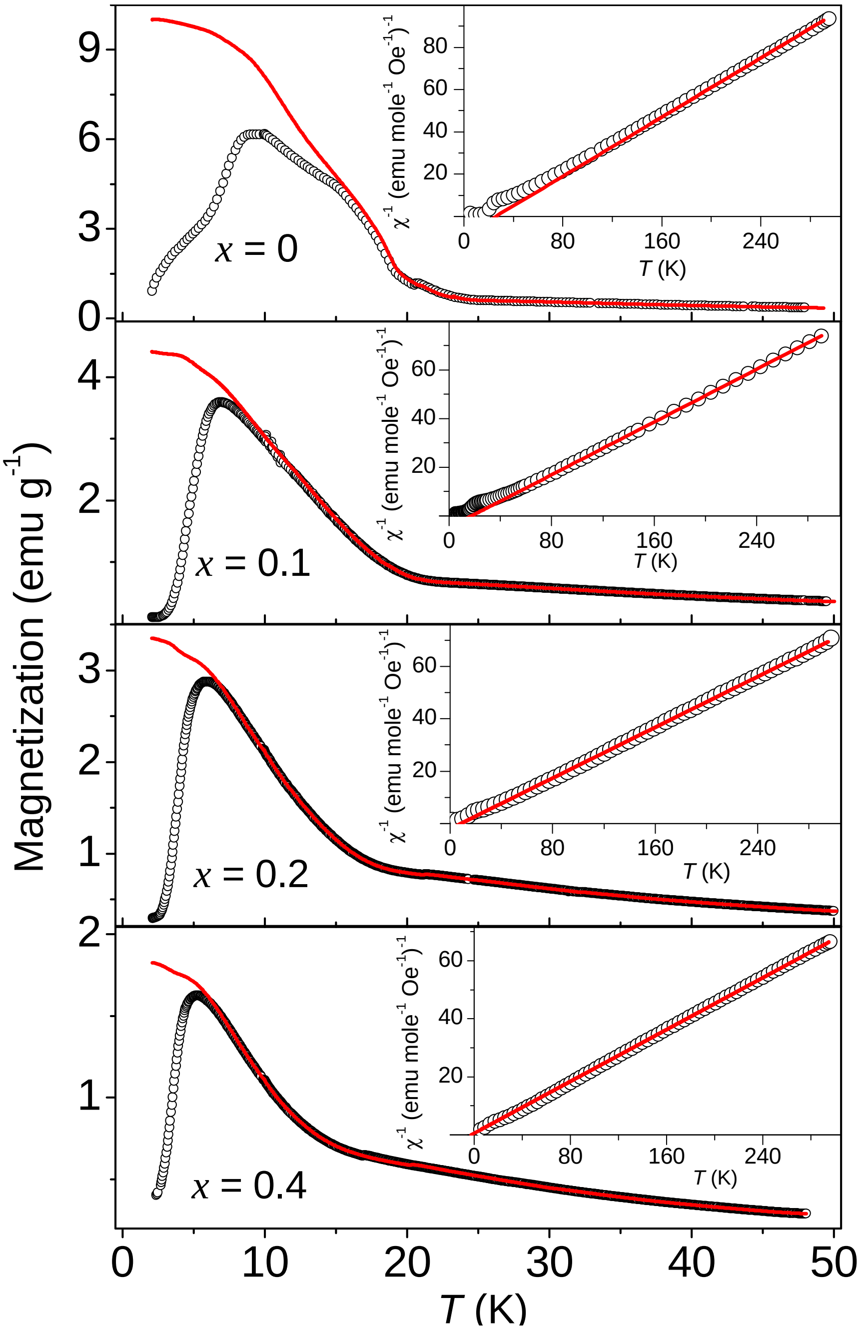

Figure 5.1: Dc magnetization versus temperature curves under 1 kOe field for $Ca_3Co_{2-x}Fe_xO_6$ (x = 0, 0.1, 0.2, and 0.4). The open circles and the solid line correspond to ZFC and FC modes, respectively. Insets show inverse dc susceptibility vs temperature curves fitted with the Curie-Weiss law.

perature magnetic susceptibility obeys the Curie-Weiss law [$\chi_{mol} = C_{mol}/(T - \theta_p)$], here C_{mol} is molar Curie constant and θ_p is the paramagnetic Curie temperature. The value of θ_p decreases as the concentration of iron increases; reaching 17.6 and 7.5 K for $x = 0.1$ and 0.2, respectively against $\theta_p = 27.9$ K for $x = 0$ and it becomes negative (-1.6 K) for x = 0.4 sample, which indicates that at this higher concentration of iron, antiferromagnetic (AFM) interaction dominates over ferromagnetic (FM) interaction. The effective paramagnetic moment μ_{eff} [=$(3C_{mol}k_B/N_A{\mu_B}^2)^{1/2}$ ≈ $(8\ C_{mol})^{1/2}$, where k_B stands for Boltzmann constant and N_A stands for Avogadro number], obtained from the slope of χ^{-1} vs T curves, are depicted in Fig. 5.2. Theoretically expected (spin-only) values of the μ_{eff} using the expression

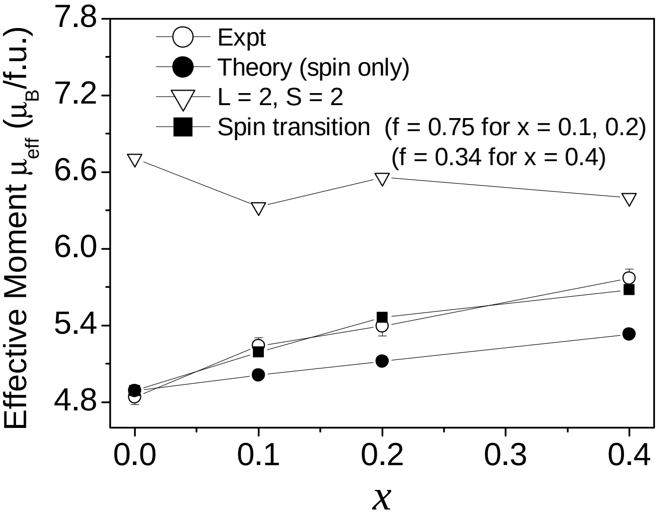

Figure 5.2: Theoretical and experimental μ_{eff} vs iron concentration. Solid lines are guide to the eye.

$$\mu_{eff} = [\sqrt{(1-x)g^2 S^{TP}_{Co}(S^{TP}_{Co}+1) + x\, g^2 S^{TP}_{Fe}(S^{TP}_{Fe}+1)}]\ \mu_B$$

with g = 2 are also shown in Fig. 5.2. Here μ_{eff} has been calculated (assuming spin only contribution) by considering Co^{3+} at octahedra (OCT) site in the low spin (LS) state (S = 0), Co^{3+} at trigonal prisms (TP) site in the high spin (HS) state (S = 2), and Fe^{3+} at TP site in the HS state (S = 5/2) [50]. For the parent compound $Ca_3Co_2O_6$, experimental value (4.8 μ_B per formula unit) matches with the theoretical value (4.89 μ_B per formula unit) and for iron substituted samples, experimental μ_{eff} values are higher than the theoretically expected values. If we assume that the orbital moment of Co^{3+} is not quenched in the TP site (orbital moment of Fe^{3+} is zero since it has half filled $3d$ shell), the calculated values of μ_{eff} are higher than the observed values (Fig. 5.2). If we consider that orbital momentum is partially quenched, theoretical values of the μ_{eff} (considering different values of L) do not match with the experiment values. Another possibility of observing higher experimental values of effective paramagnetic moment as compared to the theoretically expected spin only values for Fe substituted compounds may be LS to HS transition of octahedral Co^{3+} ions that are located near Fe^{3+} ions [91], which could also be responsible for the slight increase of cell constants for the present Fe substituted compounds. An increase of cell parameters by such a spin transition has been reported in literature [91]. Such a transition is possible [91] because covalency of the Fe-O bond is higher than the covalency of Co-O bond (i.e. electronegativity of Fe^{3+} is higher than that of Co^{3+}; 1.9 and 1.8 respectively [92]). Under the framework of spin transition for Co^{3+} at the octahedral site, the μ_{eff} can be calculated using the expression

$$\mu_{eff} = [\sqrt{(1-x)g^2 S_{Co}^{TP}(S_{Co}^{TP}+1) + x\, g^2 S_{Fe}^{TP}(S_{Fe}^{TP}+1) + x\, f\, g^2 S_{Co}^{OCT}(S_{Co}^{OCT}+1)}]\ \mu_B$$

with $g = 2$ (Fig. 5.2). Here f is the fraction of Co^{3+} ions (at the octahedral site) that undergo LS to HS transition for each Fe^{3+} substituted ion. The experimental and the theoretical values match for $x = 0.1$ and 0.2 by taking $f = 0.75$ (Fig. 5.2). For $x = 0.4$, the experimental and the theoretical values match by taking $f = 0.34$. The observed lower value of f for the $x = 0.4$ sample can be explained by the fact that for a higher concentration of iron, there could be pairs/sequence of Fe^{3+} ions along the chain, so the effective number of Co^{3+} ions (with Fe^{3+} ions as nearest neighbors) showing transition from LS to HS is small. For the parent compound $Ca_3Co_2O_6$, there is a sudden increase in the magnetization at around

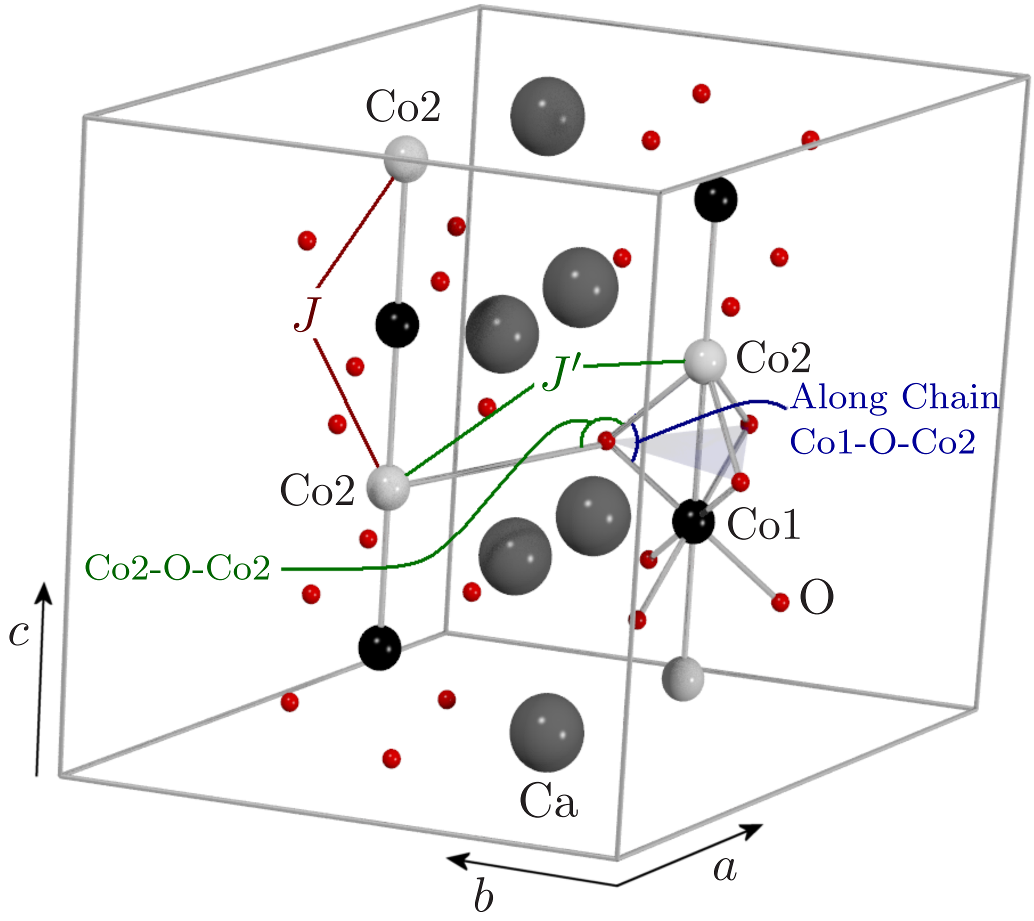

Figure 5.3: Unit cell of $Ca_3Co_{2-x}Fe_xO_6$ ($x = 0$, 0.1, 0.2, and 0.4), showing selected (Co1-O-Co2 and Co2-O-Co2) bond angles. Paths of interchain and intrachain exchange interactions are also shown as J' and J, respectively. Only selected atoms are shown for clarity.

25 K and also there exists a peak in the magnetization at around 10 K. These observations are consistent with the reported results for this compound [42, 53]. In literature, two kinds of magnetic exchange interactions have been considered for this spin-chain compound [59]. The exchange interaction J between the magnetic Co2 ions located at TP site along the chain axis (c axis) is FM and the superexchange interaction J' between the magnetic Co2 ions (via oxygen ions) is AFM (Fig. 5.3). Sudden increase in the magnetization at around 25 K has been ascribed in literature [42, 46, 52–61, 93–97] as due to the combined effect of FM ordering along the chain and AFM ordering between chains. This argument is supported by the simultaneous

appearance of AFM and FM Bragg peaks in the neutron diffraction pattern at $T \sim$ 25 K [62, 63] and sharp peak in the specific heat (under zero fields) [54] at the same temperature. This type of spin configuration has been described as the onset of the partially disordered antiferromagnetic (PDA) state and it is supported by the muon spin relaxation study [78]. While peak in the magnetization curve at around 10 K is considered as an indicative of magnetic transition to the ferrimagnetic (FIM) state [68].

From the temperature dependence of FC and ZFC dc-magnetization (shown in the Fig. 5.1) it is evident that for all the samples, a bifurcation between FC and ZFC magnetization is found at lower temperatures. This bifurcation in FC and ZFC magnetization may be taken as the signature of geometrical frustration due to triangular lattice of Ising Co moments in the *ab* plane. Results of the reported low temperature Mössbauer study [64] show that Fe^{3+} remains in the paramagnetic state in the FM ordered chains below 25 K. Figure 5.1 also indicates that as the concentration of iron increases, magnetization decreases. This decrease in the magnetization and θ_p (negative for $x = 0.4$) indicates that as the concentration of iron increases the long range FM ordering along the chain is reduced (due to reduced correlation length between Co moments along the chain) and AFM interchain interaction dominates over the FM intrachain interaction. This has been ascribed to a different magnetic character of Co host (Ising) and Fe impurity (Heisenberg) spins [50].

Figure 5.4 depicts the temperature dependence of molar susceptibility, where χT vs T is plotted. It reveals four main features (i) in the high temperature range (150 - 300 K), χT approaches its paramagnetic limit, (ii) as temperature is decreased below 150 K, χT starts increasing giving the signature of a short-range ordering along the chains, (iii) with further decreasing the temperature, a dip in χT vs T

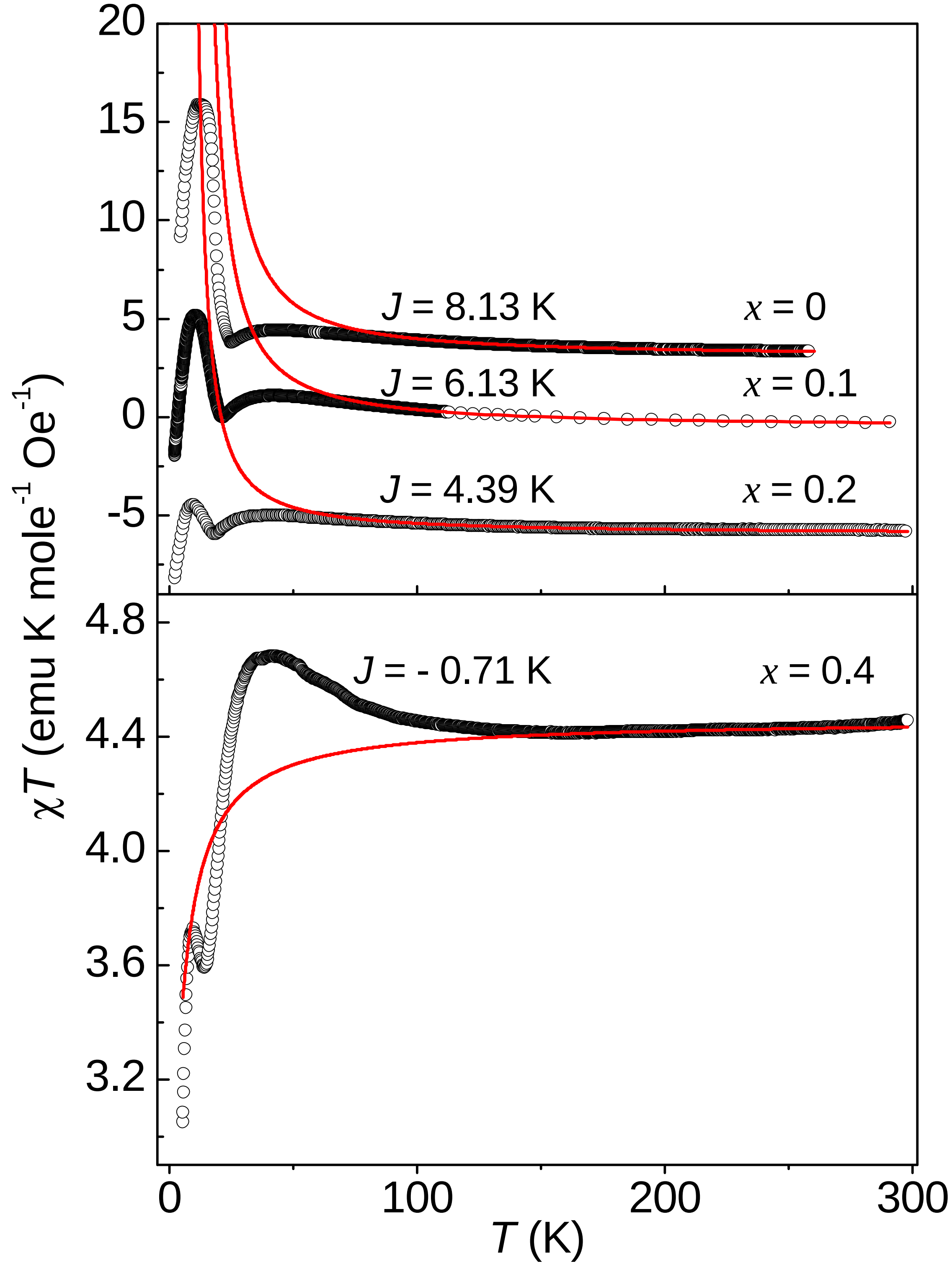

Figure 5.4: Plots of χT vs T for $Ca_3Co_{2-x}Fe_xO_6$($x = 0$, 0.1, 0.2, 0.4) derived from FC magnetization curves. Solid lines represent the fitted curve using Eq. (5.3). For $x = 0.1$ and 0.2, χT values are shifted down by 5 and 10 emu K mol^{-1} Oe^{-1}, respectively for clarity.

plot is found, and (iv) a sharp increase in the χT below the dip temperature and then again a decrease of χT at lower temperatures down to 2 K. The temperature corresponding to the dip varies with x (24.83 K for $x = 0$ and 3.59 K for $x = 0.4$). The dip in the χT vs T plot may be ascribed to a FIM ordering at low temperatures [98]. The decrease in the χT at low temperature ($T < 7$ K) has been assigned to a spin frozen state in literature [99] for the parent compound $Ca_3Co_2O_6$.

5.3.1.2 Intrachain and Interchain Exchange Interactions

The intrachain exchange constant can be determined by fitting the experimental χT vs T curves [99, 100]. Theoretical studies show that the parallel [99] and the perpendicular [101] susceptibilities for, $S = 2$, 1D Ising spin chain are given by

$$\chi_{\parallel} T = \frac{3}{4}\, g^2 \exp(8J/k_B T) \tag{5.1}$$

and

$$\chi_{\perp} T = \frac{3}{4}\, g^2 \ . \tag{5.2}$$

Here g is the Lande factor, k_B stands for the Boltzmann constant, and J is the intrachain exchange constant. For polycrystalline (powder) sample, susceptibility can, therefore, be written as

$$\chi_p T = 1/3\ \chi_{\parallel} T + 2/3 \chi_{\perp} T \ . \tag{5.3}$$

Equation (5.3) is strictly valid for the $S = 2$, Ising spin-chain. But our system (except $Ca_3Co_2O_6$) is not $S = 2$, 1D Ising spin-chain system (for Fe^{3+} ions, value of S is 5/2). In literature, no theoretical expression is available for $S = 2$ and $S = 5/2$ mixed spin system. We have, therefore, used Eq. (5.3) to estimate the approximate value of the exchange constant J. This type of approximate method has already been used in literature [97] for $\mathrm{Ca_3Co_{2-x}Cr_xO_6}$, where $\mathrm{Co^{3+}}$ ions are in the HS and the LS states at the TP and OCT sites, respectively, and $\mathrm{Cr^{3+}}$ ions at the OCT site are in the HS ($S = 3/2$) state. By fitting the high temperature part of the $\chi_P T$ vs T curves using Eq. (5.3) (Fig. 5.4) as per the procedure followed in literature [97], we have estimated the value of intrachain exchange constant J (shown in Table 5.1). It is found that as the concentration of iron increases, J decreases. For instance as x increases from 0 to 0.2, J decreases from 8.1 to 4.3 K, and for $x = 0.4$ it becomes negative (J = -0.7 K). Positive value of J refers that intrachain interaction is FM while negative value of J indicates that interaction is AFM. The derived negative value of J for the $x = 0.4$ sample is consistent with the negative value of θ_p for this sample. Here we give some physical argument to explain the negative value of J. For $\mathrm{Ca_3Co_{2-x}Fe_xO_6}$, when concentration of Fe is low (small value of x), the probability of having Fe pairs or clusters in a Co chain is very small and $\mathrm{Fe^{3+}}$ ions are mainly isolated. For small value of x, iron limits the correlation length by breaking FM ordering between $\mathrm{Co^{3+}}$ ions along the c axis and reduces the strength of intrachain exchange coupling constant J. When x increases (> 0.2), the formation of pairs of $\mathrm{Fe^{3+}}$ ions along the chain is probable. There may be AFM exchange interaction (via oxygen) between $\mathrm{Fe^{3+}}$ ions along the chain (Fig. 5.3) which can give the negative value of J. This can lead to a FIM ordering (with negative θ_p) at low temperatures. For the $x = 0.2$ and 0.4 compounds, a coexistence of magnetic short-range and long-range ordering, below T_N, has been confirmed from the zero field neutron diffraction study (Chapter 4). We have observed that the correlation lengths for both magnetic short-range ordering (SRO) and long-range ordering (LRO) do not differ very much for the $x = 0.2$ and 0.4 compounds, indicating that Fe ions in a chain are located preferentially very close to each other for higher concentration of iron (x= 0.4).

This confirms that a higher concentration (for x = 0.4) of Fe hardly breaks the ferromagnetic bonds further as compared to that for the lower concentration of Fe (for x = 0.2).

Interactions between the chains in the *ab* plane give deviation from the 1D spin system. The deviation from the ideal 1D character of Ising chain can be taken into account by introducing the mean field correction to the ideal 1D Ising spin model. Mean field correction to the $S = 1/2$, 1D Ising spin-chain is available in literature, and it has been used [101] to evaluate the interchain exchange constant. However, in literature no mean field expressions, either for $S = 2$ Ising spin-chain or for $S = 2$ and $S = 5/2$ mixed spin system, exist. It will be of great importance to evaluate the interchain interaction if the mean field corrections for such spin systems are available. An alternate option to calculate interchain interaction is by using ferri-to-ferromagnetic transition field (H_{FIM-FM}). A field induced FIM to FM-like transition is found in our M vs. H study (Fig. 5.5). In a model of Ising spin-chain [97], interchain interaction is related to H_{FIM-FM} through the relation $J' = \frac{g\mu_B H_{FIM-FM}}{12S}$. For the present system of mixed spins ($S = 2$ and $S = 5/2$), assuming $S = 2$ and $g = 2$, we have derived the value of J' as used for $S = 2$ and $S = 3/2$ mixed spin-chain system in literature [97]. The value of J' varies from -0.20 K for $x = 0$ to -0.32 K for $x = 0.4$. Therefore, as the concentration of iron increases from 0 to 0.4, interchain interaction increases. Since the distance between magnetic ions perpendicular to the chain axis, and the bond angle via oxygen do not change by iron substitution, the increase in the value of J' can be understood by assuming that the strength of exchange coupling for Co2/Fe-O-Co2/Fe pathway is greater than that of the Co2-O-Co2. This is consistent with the fact that Fe is known to introduce negative exchange interactions. Fe^{3+} has five electrons in the *d* orbital, while Co^{3+} has six, and also spin character of host (Co) is Ising while impurity (Fe)

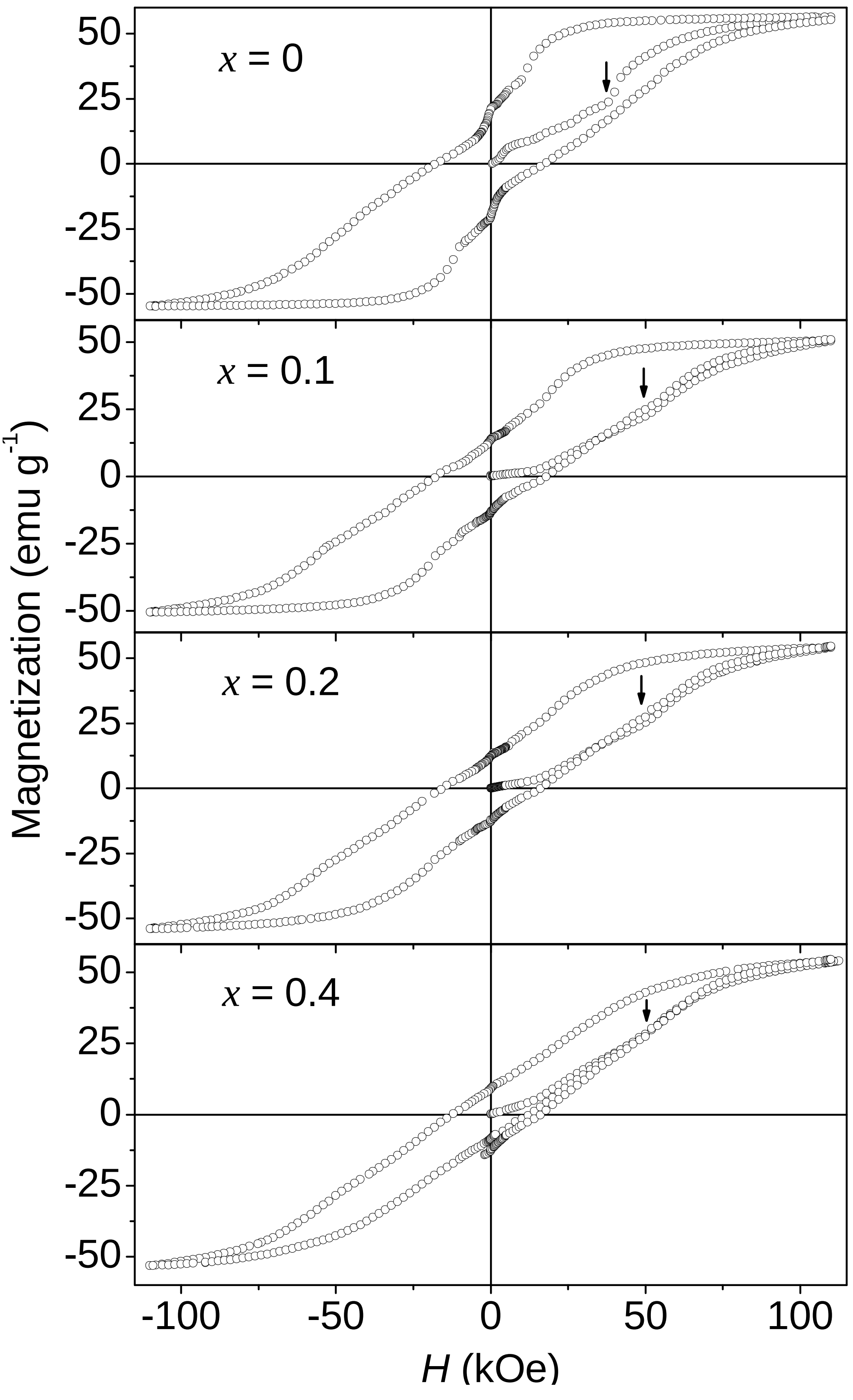

Figure 5.5: Hysteresis curves at 1.5 K for $\mathrm{Ca_3Co_{2-x}Fe_xO_6}$($x = 0$, 0.1, 0.2, and 0.4). Virgin magnetization curves (first leg) show a possible field induced FIM to FM transition (marked by arrows).

Table 5.1: Magnetic exchange constants for $\mathrm{Ca_3Co_{2-x}Fe_xO_6}$ samples.

x	J(K)	J'(K)	$\lvert J'/J\rvert$
0	8.13	-0.20	0.025
0.1	6.13	-0.27	0.044
0.2	4.39	-0.30	0.068
0.4	-0.71	-0.32	0.451

is of Heisenberg nature. The ratio $|J'/J|$ characterizes the "one dimensionality" of the magnetic system. It varies from 0.025 for $x = 0$ to 0.451 for $x = 0.4$ as shown in the Table 5.1. In literature, Clardige *et al.* reported $J'/J \sim 0.33$ for $\mathrm{Sr_3CuPtO_6}$ (Heisenberg chain compound) [102] and they concluded that it should not be considered as 1D magnetic system due to a higher value of J'/J. Since for the present $x = 0.4$ compound $|J'/J| \sim 0.451$, this compound should also not be considered as 1D magnetic system. The ratio is very small for $\mathrm{Ca_3Co_2O_6}$ hence it has predominantly a one dimension character. We can, therefore, conclude that as the concentration of iron increases, the one dimensional character of Ising spin chains is reduced.

The previous report by Flahaut *et al.* [97] on substitution of $\mathrm{Co^{3+}}$ by $\mathrm{Cr^{3+}}$ in $\mathrm{Ca_3Co_2O_6}$ shows that as the concentration of Cr increases from $x = 0$ to $x = 0.1$ in $\mathrm{Ca_3Co_{2-x}Cr_xO_6}$, both J and J' decrease. Here we would like to point out that effects of substitution of Cr are much different from the present study where Fe is substituted. The $\mathrm{Cr^{3+}}$ substitutes the LS $\mathrm{Co^{3+}}$ at octahedral site and it is in the HS state ($S = 3/2$). In $\mathrm{Ca_3Co_{2-x}Cr_xO_6}$, solubility range of $\mathrm{Cr^{3+}}$ is limited to about 10 at. % occupation of octahedral site. In the Cr substitution case, cell constants a and c change by $\sim$ 0.14 % and 0.08 %, respectively, for the change in x from 0 to 0.15, whereas in the present case, the cell constant a changes only by 0.01 % for the change in x from 0 to 0.4.

5.3.1.3 Field Dependent Magnetization

Figure 5.5 depicts hysteresis loops (field up to 110 kOe) at 1.5 K for all the samples. It is evident from Fig. 5.5 that virgin magnetization (M) varies linearly with field in a small field region. It is also found that a large hysteresis exists in M versus H curves of all samples but as the concentration of iron increases, these curves become less hysteric. The magnetization saturates for $x = 0$ but for $x = 0.1$, 0.2, and 0.4 samples the magnetization does not saturate even under the highest applied field. Experimentally observed values of the remanent magnetization and the coercive fields are shown in Fig. 5.6. It is clear that as the concentration of iron increases both remanent magnetization and coercive field decrease. It is, therefore, evident that the magnetic hardness decreases with Fe substitution. This is consistent with the observed fact that with increasing Fe concentration, the 1D character of Ising spin chains is reduced.

The spatial dimensionality (d) of arrangement of magnetic ions in the present system can be deduced from the approach of the magnetization to its saturation value (M_S) in the high field region [103, 104]. This dependency is given by

$$\frac{M_s - M}{M_s} \propto (H)^{(d-4)/2} \tag{5.4}$$

Here, the proportionality constant is given by $\delta = (C/M_s)^{(4-d)/2}$ with C as magnetocrystalline anisotropy constant. According to Eq. (5.4), approach of magnetization to its saturation value $\triangle M/M_s$ (here $\triangle M = M_S - M$) obeys $H^{-3/2}$ and $H^{-1/2}$ dependence for the 1D and three-dimensional (3D) interaction of magnetic ions, respectively. Figure 5.7 depicts the variation of $\triangle M/M_S$ with $H^{-3/2}$ and

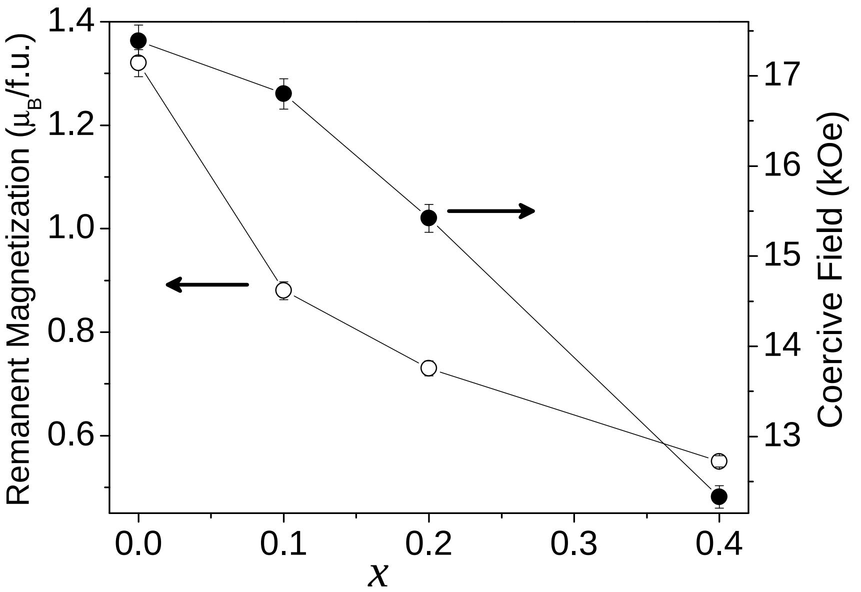

Figure 5.6: Variation of remanent magnetization and coercive fields with composition. Solid lines are guide to the eye.

$H^{-1/2}$ for all the samples at 1.5 K. Inset of Fig. 5.7 depicts variation of anisotropy constant (C) with composition, derived from the slope [$= (C/M_s)^{3/2}$] of $\triangle M/M_S$ vs $H^{-3/2}$ curves. The results show that for x = 0, 0.1, and 0.2 samples, $\triangle M/M_S$ is proportional to $H^{-3/2}$ and hence imply the 1D character of the spatial arrangement of magnetic ions in these samples. For x = 0.4 sample, $\triangle M/M_S$ deviates from $H^{-3/2}$ dependence, which can be ascribed as deviation from ideal 1D character of this sample (consistent with highest derived value of $|J'/J|$). The decrease of anisotropy constant (C) with the increase of iron concentration (inset of Fig. 5.7) is also consistent with the aforesaid argument.

5.3.2 Neutron Diffraction Study of Field-induced Magnetic Phase Transitions in $Ca_3Co_{1.8}Fe_{0.2}O_6$

Figure 5.8 (a) depicts the Rietveld refined neutron diffraction pattern for the compound $Ca_3Co_{1.8}Fe_{0.2}O_6$ at 1.5 K (well below $T_N \sim 20$ K) in zero applied field. As shown in the inset of Fig. 5.8 (a), the antiferromagnetic reflections appearing in

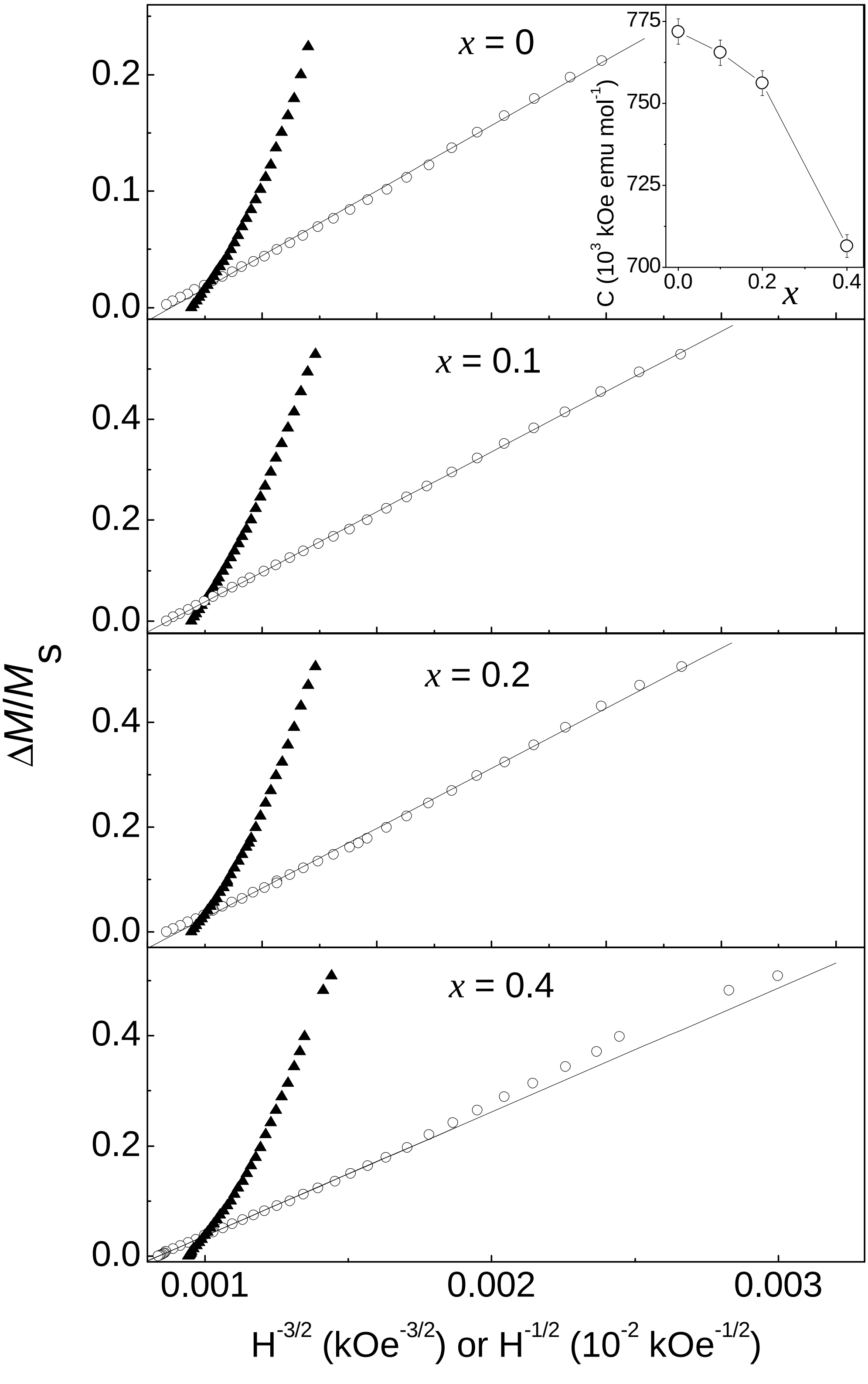

Figure 5.7: Plots of $\triangle M/M_S$ vs $H^{-3/2}$ (open circles) and $\triangle M/M_S$ vs $H^{-1/2}$ (solid triangles) obtained from high field region of virgin magnetization curves. Straight lines represent linear fit of $\triangle M/M_S$ vs $H^{-3/2}$. Inset shows variation of anisotropy constant with composition.

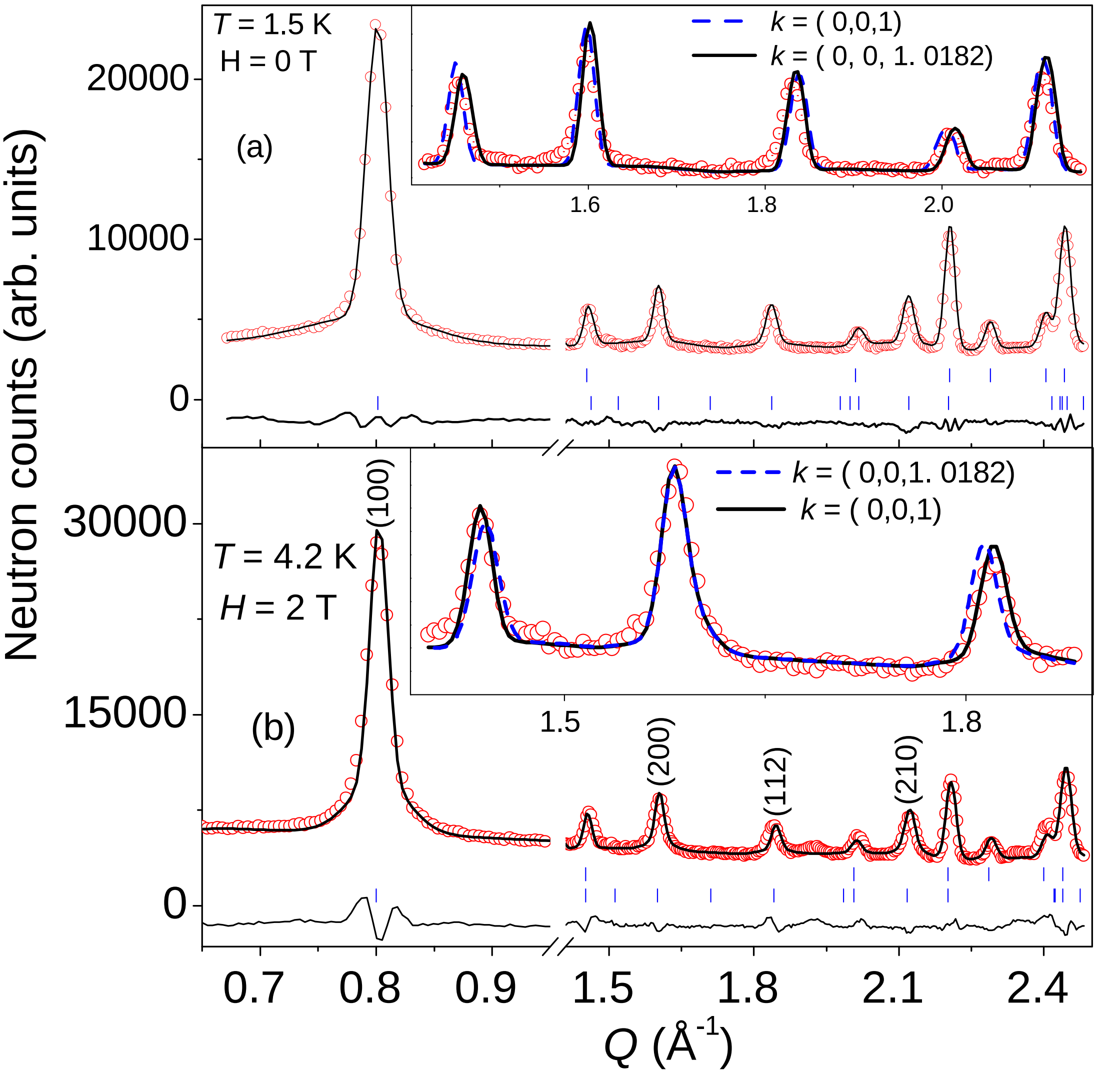

Figure 5.8: The Rietveld refined neutron diffraction patterns of $Ca_3Co_{1.8}Fe_{0.2}O_6$ at (a) 1.5 K under zero applied field, (b) 4.2 K under an applied field of 2 T : experimental data (open circle), calculated curve (solid line), and difference (solid line at bottom). The upper vertical marks are the nuclear Bragg reflections, lower vertical marks are the magnetic reflections. The (*hkl*) values for the satellite peaks which appear below T_N are also listed. The insets in (a) and (b) show the Rietveld refined patterns for two different values of the propagation vector.

the neutron diffraction pattern can be indexed with the incommensurate propagation vector $\boldsymbol{k} = \{0, 0, 1.0182\ (9)\}$, and the magnetic structure corresponds to the SDW structure [105]. Moreover, in zero applied field, a magnetic short-range ordering (SRO) coexists with the long-range ordering (LRO) at all temperatures below T_N, as described in Chapter 4. Figure 5.8(b) depicts the Rietveld refined neutron diffraction pattern at 4.2 K under an applied field of 2 T. As shown in the inset

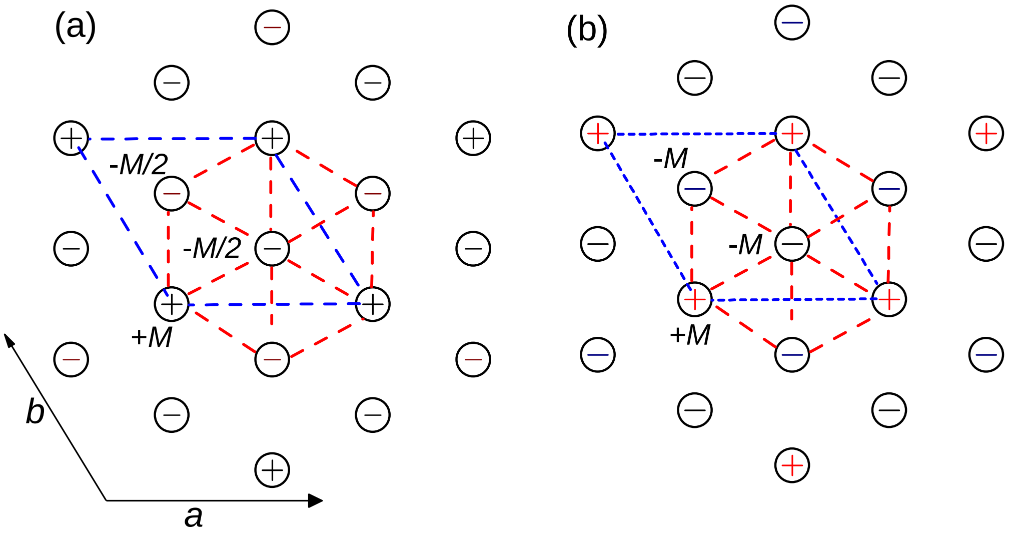

Figure 5.9: Schematic diagram of (a) AM state and (b) ferrimagnetic state, projected on the ab plane. In Figs. (a) and (b), the circles represent the Ising spin chain, and the plus (+) and minus (-) signs correspond to the direction (along the positive c axis and negative c axis, respectively) of representative moments in the spin chains. The values of the moments within the three nearest spin chains are marked.

of Fig. 5.8(b), the observed antiferromagnetic reflections can be indexed with the commensurate propagation vector $\boldsymbol{k} = \{0, 0, 1\}$ and the magnetic structure corresponds to the AM structure, in which moments lie along the crystallographic c axis. The amplitude of the moments in the unit cell is given by $\boldsymbol{M}_{L,j(j=6a,6b)} = M_j$ $\cos(2\pi\boldsymbol{k}.\boldsymbol{R}_L)$. Here M_j is the maximum moment and $\boldsymbol{R}_L$ is the translation vector with respect to the zeroth-cell. The amplitudes of the site moments in the unit cell, labelled by the centring translation, $\boldsymbol{R}_L = (2/3, 1/3, 1/3)$ and $(1/3, 2/3, 2/3)$, are modulated by -0.5. The observed amplitude modulated (commensurate) magnetic structure is very much different from the zero field spin-density wave (SDW) magnetic structure, having incommensurate propagation vector $\boldsymbol{k} = \{0, 0, 1.0182(9)\}$. In the SDW magnetic structure, the values of the moments in the lattice varies between $+M_j$ and -M_j, however, in the amplitude modulated structure (Fig. 5.9(a)), the values of the moments within the three nearest spin-chains with the (x, y) coordinate as $(0, 0)$, $(2/3, 1/3)$, and $(1/3, 2/3)$ are $+M_j$, -$M_j/2$, -$M_j/2$, respectively.

The observed crossover from incommensurate to commensurate magnetic ordering indicates a reduction of the spin frustration on the triangular lattice.

To describe further the effect of the magnetic field on the magnetic structure of the compound $Ca_3Co_{1.8}Fe_{0.2}O_6$, the observed magnetic Bragg peaks have been considered in two groups; (i) the first group corresponds to the satellite peaks, such as (100), (200), and (210) reflections which appear below T_N, and (ii) the second group corresponds to the peaks such as (110), (220), and (012) whose intensities appear on the top of the nuclear (fundamental) Bragg peaks. The temperature dependences of the integrated intensities of these Bragg peaks play a crucial role in determining the nature of the magnetic ordering of the compound in an applied magnetic field. A simple calculation using the Fullprof program [40] shows that the magnetic contribution in the intensity of fundamental (110) Bragg peak is zero in the case of the SDW/AM structure (Fig. 5.9 (a)), while the contribution is finite in the case of a ferromagnetic/ferrimagnetic (Fig. 5.9 (b)) structure [in each case, the moment was considered along the crystallographic c axis]. In Fig. 5.10, we show the temperature dependence of the integrated intensities of the fundamental peaks (110) and (220) under magnetic fields of 0, 2, and 4 T. In magnetic fields of 0 and 2 T, the intensities of the two peaks show no enhancement below 20 K (Figs. 5.10 (a) and (b)). Under an applied field of 2 T, no enhancement in the intensity of these two peaks, confirms an AM-type magnetic structure. Whereas, in the absence of an external magnetic field, no enhancement in the intensities of these two peaks, corresponds to the SDW structure, as mentioned in Chapter 4 [73]. In the magnetic field of 4 T, below $\sim$ 20 K, the intensity of (110) peak increases gradually with decreasing the temperature (Fig. 5.10 (c)), indicating that the magnetic structure is ferrimagnetic/ferromagnetic at a field of 4 T. We indeed find that magnetic structure at H = 4 T is ferrimagnetic, as evident from the following discussion. Figure 5.11

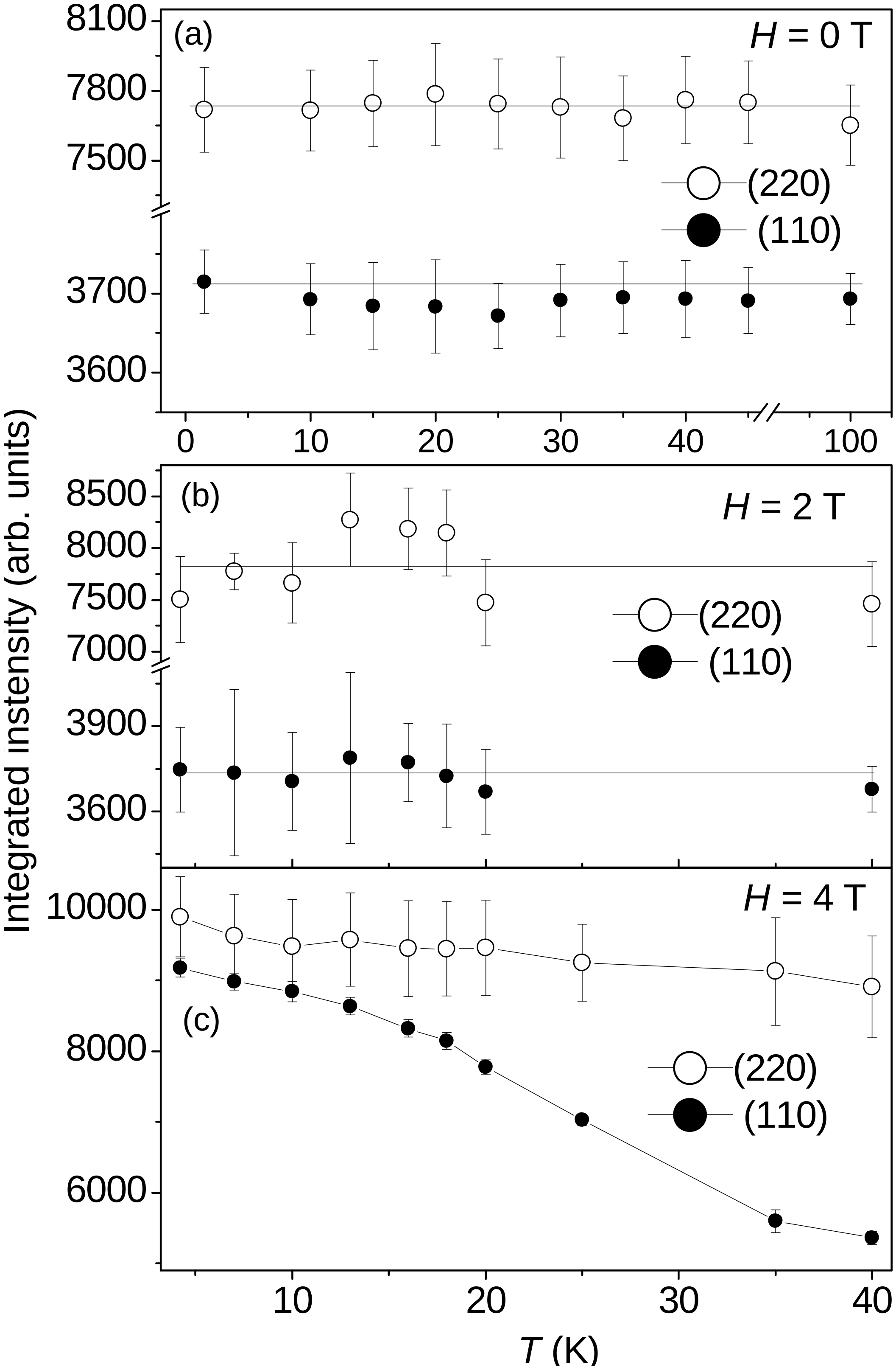

Figure 5.10: Temperature dependence of the integrated intensity of the Bragg peaks (110) (solid circle) and (220) (open circle) in an applied magnetic field of (a) 0 T, (b) 2 T, and (c) 4 T. The solid lines are guides to the eye.

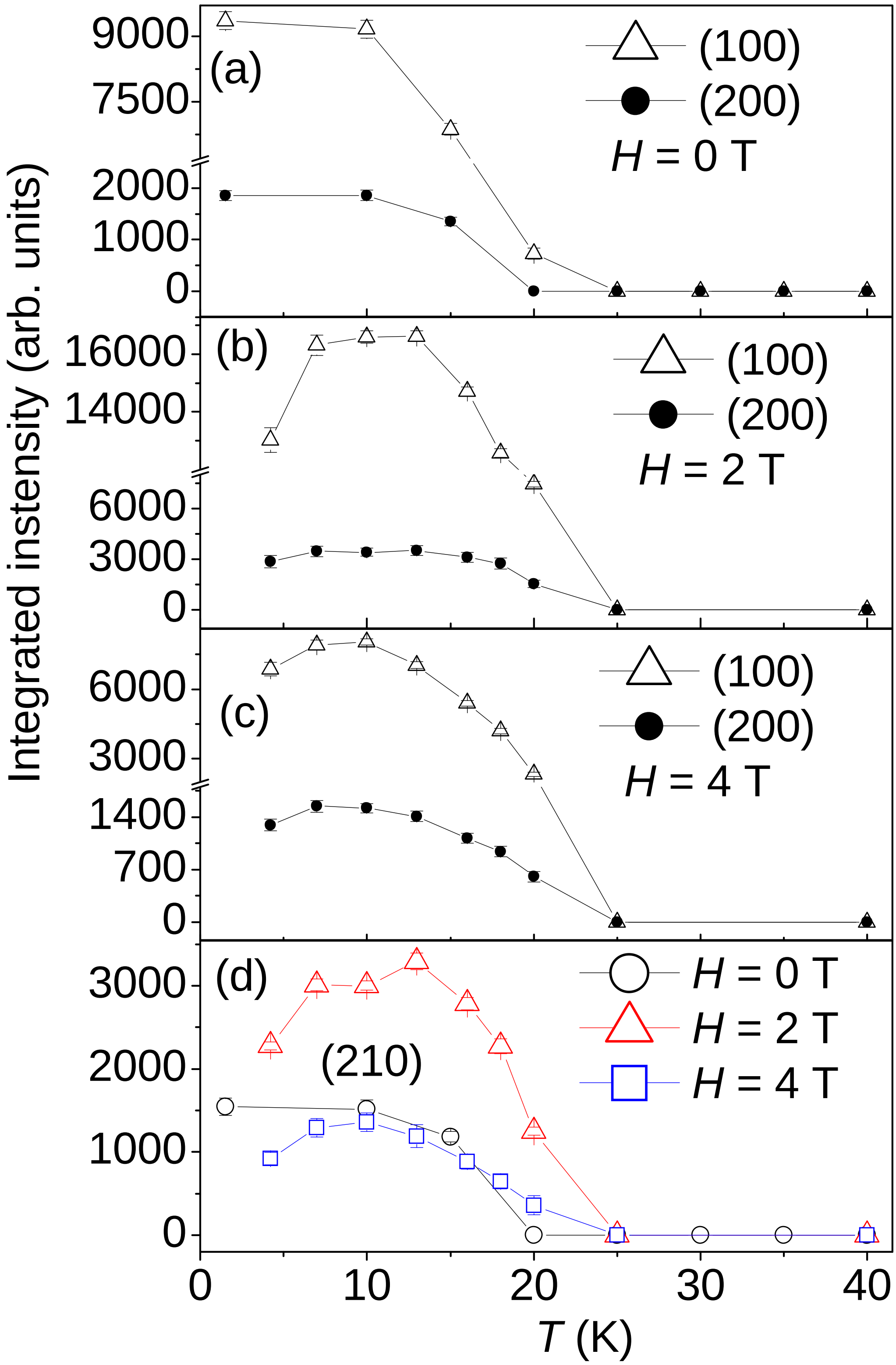

Figure 5.11: Temperature dependence of the integrated intensity of the Bragg peaks (100) (open triangle) and (200) (solid circle) in an applied magnetic field of (a) 0 T, (b) 2 T, and (c) 4 T. (d) Temperature dependence of the integrated intensity of the Bragg peak (210) in an applied magnetic field of 0 T (open circle), 2T (open triangle), and 4 T (hollow square). The solid lines are guides to the eye.

depicts the temperature dependences of the integrated intensities of the satellite Bragg peaks (100), (200), and (210) in applied magnetic fields. It is important to mention here that the application of magnetic field does not change the number of the additional magnetic Bragg reflections, it only affects their intensities and positions. In an applied field of 4 T, the observed non zero intensities of the peaks (100), (200), (210) [Figs. 5.11(c) and (d)] and an increase in the intensity of the fundamental Bragg peak (110) [Fig. 5.10 (c)], below T_N, suggest that magnetic structure is ferrimagnetic as shown in Fig. 5.9 (b). However, the intensity of the satellite peaks (100), (200), and (210) in the ferrimagnetic phase is small compared to the AM structure [Fig. 5.11]. This suggests that the AFM correlations between spin chains are weakened or broken when field is increased to 4 T. When the field is increased further (> 5 T), the spin system with the "broken spin chains" approaches to its fully field induced ferromagnetic state as found in our earlier dc magnetization study [77]. A similar field induced ferrimagnetic structure and/or ferromagnetic structure has been reported in literature for the most intensely studied compounds $Ca_3Co_2O_6$ and Ca_3CoRhO_6 of the A_3MXO_6 family [62, 66]. In the zero applied magnetic field [Figs. 5.11(a) and (d))], the intensities of the peaks (100), (200), and (210) increase gradually with decreasing temperature, corresponding to the SDW structure, as reported earlier [73]. In magnetic fields of 2 and 4 T (Figs. 5.11(b), (c), and (d)), a pronounced drop in the intensities of the peaks (100), (200), and (210) has been observed at lower temperatures (below $\sim$ 12 K). The origin of the observed reduction in the intensities of these peaks will be discussed later.

Figure 5.12 describes the effect of magnetic field on the short-range magnetic order. In zero applied field, the SRO is present at all temperatures below T_N with a constant volume ratio 13:7 of the magnetic Bragg intensities for the LRO and the SRO, as mentioned in Chapter 4 [73]. Even under magnetic fields of 2 and 4 T,

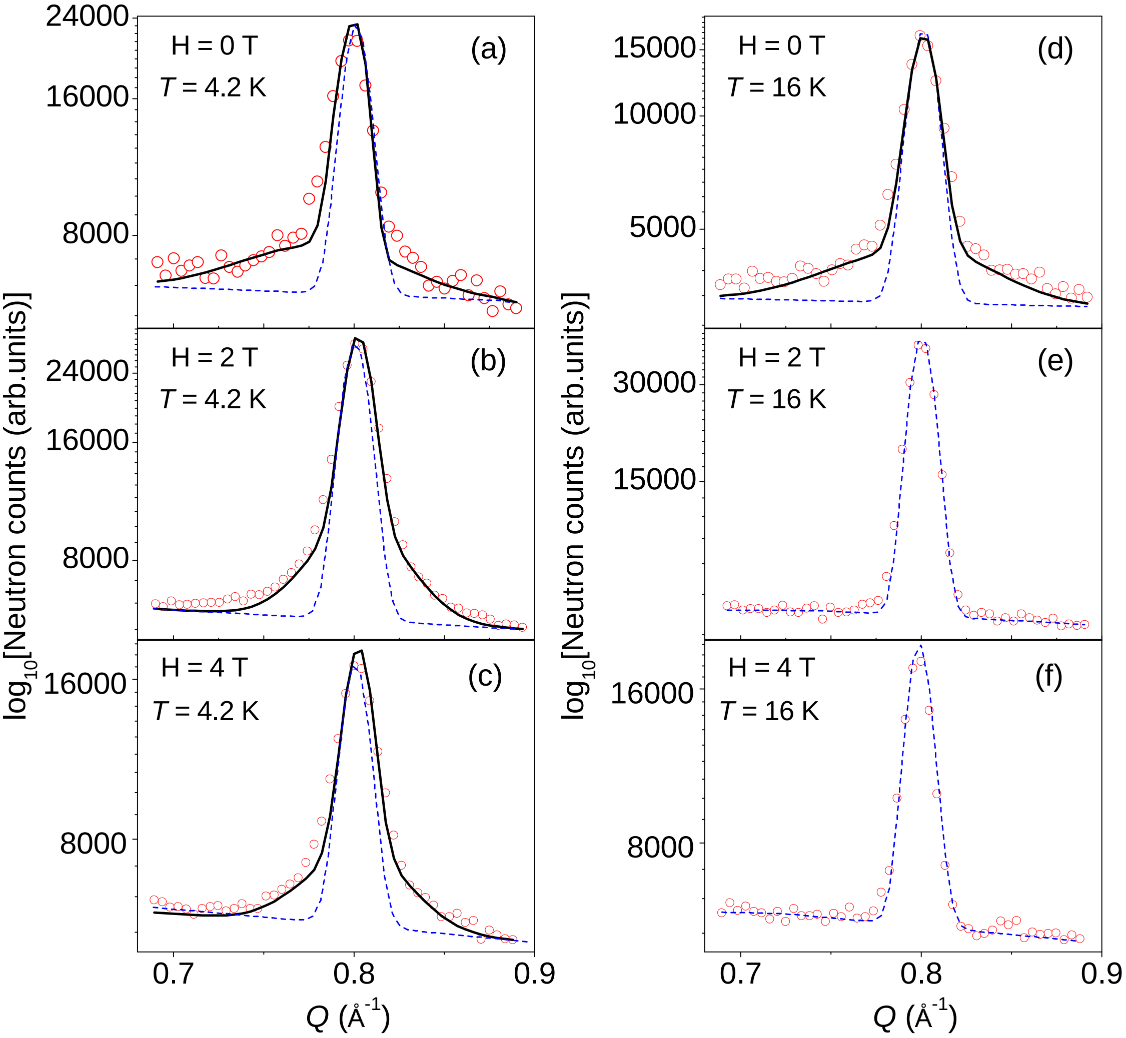

Figure 5.12: The observed Bragg peak (100) (open circle) under an applied field of (a) 0 T, (b) 2 T, and (c) 4 T at 4.2 K; and (d) 0 T, (e) 2 T, and (f) 4 T at 16 K. In Figs. (a) - (d), the Bragg peak (100) is fitted (solid line) as a sum of two pseudo-Voigt peaks, where the width of the narrow peak (dotted line) is limited by the instrumental resolution function. In Figs. (e) and (f), the Bragg peak (100) is fitted with a single pseudo-Voigt profile having a width limited by the instrumental resolution function.

a broadening (Bragg peak width larger than that expected from the instrumental resolution function) of the satellite Bragg peak (100) persists below ∼ 12 K. However, the nature of the SRO (below 12 K) in applied magnetic field is different from that in zero applied field (discussed later). The profiles of the observed satellite Bragg peak (100) at all temperatures below T_N (∼ 20 K) under zero applied field , and below ∼ 12 K under applied fields, have been fitted using a combination of two pseudo-Voigt

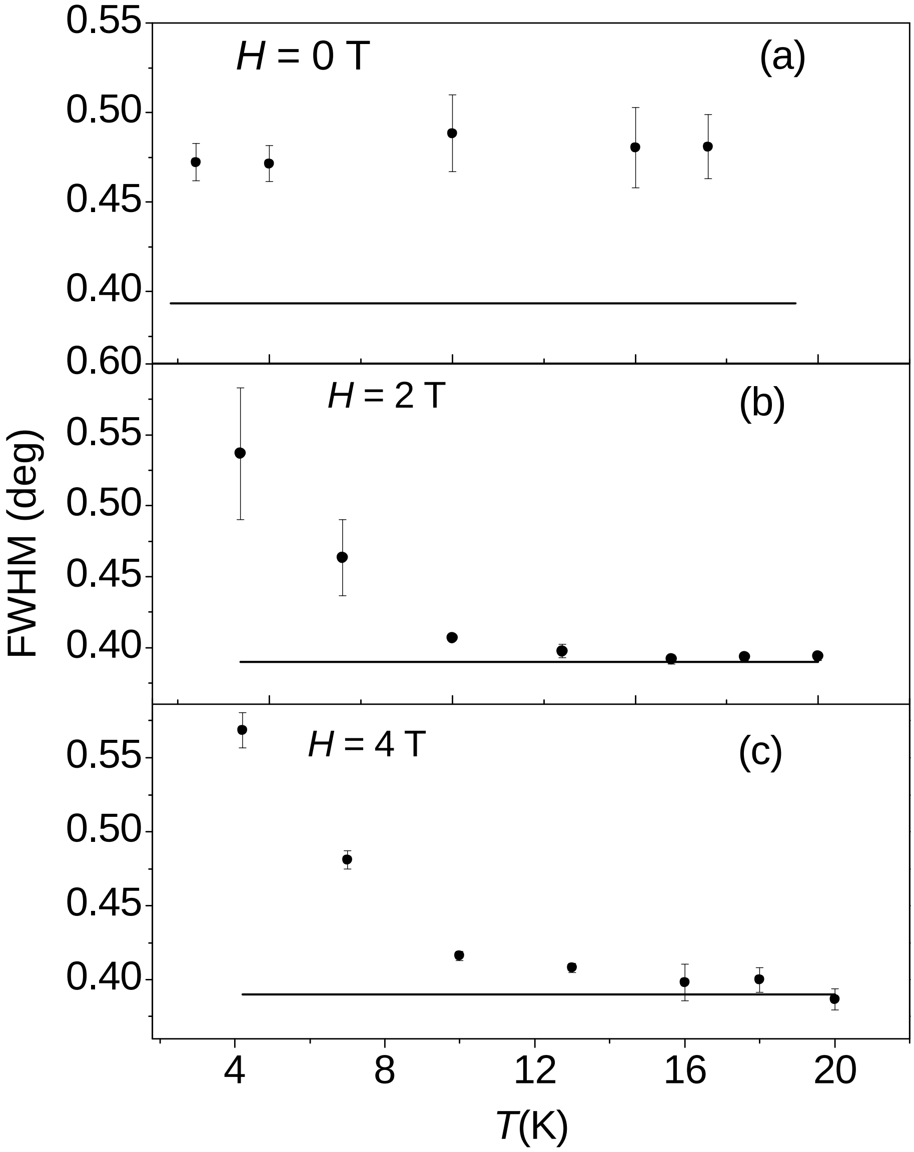

Figure 5.13: Temperature variation of the FWHM of the Bragg peak (100) in an applied field of (a) 0 T (b) 2 T and (c) 4 T. The FWHM expected from the instrumental resolution function is shown as solid horizontal line.

peaks, where the width of only one peak is limited by the instrumental resolution function. The derived temperature variation of the full width at half maximum (FWHM, convoluted peak width by considering both narrow and broad peaks), is plotted in Figs. 5.13 (a), (b), and (c). In zero applied field, the nature of the SRO is same as mentioned in Chapter 4 [73]. Figures 5.12 (a), (b), and (c) depict the fitted profiles at 4.2 K in the magnetic fields of 0, 2, and 4T, respectively. Above 12 K, under fields of 2 and 4 T, the width is limited by the instrumental resolution indicating that the short-range magnetic order is converted into the long-range magnetic order. The profile of the Bragg peak corresponding to this long-range ordering [Figs. 5.12 (e) and (f)] has been fitted well using a single pseudo-Voigt function. In zero applied field, the SRO correlation length is $\sim$ 54 Å at 4.2 K and it gets affected by the magnetic field. The SRO correlation lengths are $\sim$ 149 and 110 Å at 4.2 K, and 86 and 62 Å at 7 K in an applied field of 2 and 4 T, respectively. Besides, the application of magnetic field affects the volume ratio of the LRO and SRO contributions (13:7 and 3:2 at 7 and 4.2 K, respectively, under applied field of 4 T). We also note that similar behaviour has been observed for the other peaks (200) and (210). Under an applied fields of 2 and 4 T, the enhancement of the SRO volume fraction with lowering of temperature could be responsible for the observed reduction in the intensity of the satellite Bragg peaks (100), (200), and (210) below $\sim$ 12 K, shown in Fig. 5.11. Here it may be noted that in Chapter 4 [73], the presence of the SRO at all temperatures (below T_N), in zero applied field, was attributed to the different spin character of the Co^{3+} (Ising) and Fe^{3+} (Heisenberg) spins, due to which the Fe^{3+} ions remains in the paramagnetic phase or freeze randomly at low temperatures. In the present study, we have observed that in magnetic fields of 2 and 4 T, the SRO is present only at low temperatures ($<$ 12 K). This suggests that in applied fields, in a spin-chain, the Fe^{3+} spins are aligned parallel to the Co^{3+} spins for $12 < T < 20$ K. However, at low temperatures (below $\sim$ 12 K), both Co^{3+} and Fe^{3+} spins possibly freeze randomly as the SRO volume fraction increases. Such a spin freezing is different form the spin freezing in zero field (mentioned in Chapter 4) [73], where only the Fe^{3+} spins freeze randomly, resulting in the different nature of the SRO in the presence of field.

Now we compare the observed field induced transitions for the present compound with one of the well studied compounds of A_3MXO_6 family, *viz.* the compound

Ca_3CoRhO_6 [62, 66, 106]. The compound Ca_3CoRhO_6 was reported to order in the PDA state below 90 K. However, the present compound $Ca_3Co_{1.8}Fe_{0.2}O_6$ orders in the SDW structure below T_N. Besides, for the compound Ca_3CoRhO_6, a magnetic contribution to the intensity of the (110) peak was observed in an applied field of 2 T below 90 K, which was ascribed to a field induced ferrimagnetic state. Further, a drop in the intensity of the Bragg peak (100) was observed below $\sim$ 30 K for the measurements in a field of 2 T. The observed drop in the intensity of the (100) peak was ascribed to a magnetic phase transition from the ferrimagnetic state to a frozen PDA (FPDA) state, below 30 K. In the present study for the compound $Ca_3Co_{1.8}Fe_{0.2}O_6$, two field induced transitions, first from the zero field SDW structure to a commensurate amplitude modulated (AM) structure, and second from the AM structure to a ferrimagnetic structure have been observed. The observed SDW structure and AM structure are very much different from the PDA and FPDA structures of the compound Ca_3CoRhO_6. The observed reduction in the intensities of the satellite peaks (in applied fields) for the present compound has been ascribed to the presence of the SRO at low temperatures.

Now we compare the observed field induced transitions in the present study with the parent compound $Ca_3Co_2O_6$. In absence of magnetic field, the parent compound $Ca_3Co_2O_6$, was reported to order in a modulated PDA structure with the propagation vector $\boldsymbol{k} = \{0, 0, 1.01\}$ below 25 K [86]. A field induced transition to a ferrimagnetic state was observed, in the magnetic field of 1.7 T, and then a transition to a ferromagnetic state was reported in the magnetic field of 3.6 T [62]. However, for the present compound $Ca_3Co_{1.8}Fe_{0.2}O_6$, we have observed a field induced incommensurate (SDW structure at $H = 0$ T) to commensurate (AM structure at $H = 2$ T) magnetic phase transition, followed by another magnetic phase transition to a ferrimagnetic state at a higher field. Further, for the parent compound $Ca_3Co_2O_6$, a SRO (of antiferromagnetic nature) along with a LRO was reported only below $\sim$ 15 K (T_N = 25 K). Moreover, no change in the degree of antiferromagnetic disorder (SRO) was reported at magnetic fields of 1.2 and 2.4 T [106]. For the present compound $Ca_3Co_{1.8}Fe_{0.2}O_6$, in zero applied field the SRO coexists with LRO at all the temperatures below T_N ($\sim$ 20 K). An application of magnetic field converts the SRO into the LRO above 12 K. We, therefore, conclude that the magnetic properties of the compound $Ca_3Co_{1.8}Fe_{0.2}O_6$ are very much different from the well studied compounds $Ca_3Co_2O_6$ and Ca_3CoRhO_6 of the A_3MXO_6 family.

5.4 Summary and Conclusion

The author has studied the effect of an external magnetic field on the nature of the magnetic ordering in the compounds $Ca_3Co_{2-x}Fe_xO_6$ (x = 0, 0.1, 0.2, and 0.4) using dc magnetization and neutron diffraction techniques. For all compounds, the high temperature magnetic susceptibility obeys the Curie-Weiss law. The values of paramagnetic Curie temperature decrease as the concentration of iron increases (θ_p = 27.8 for x = 0 compound) and it becomes negative (-1.6 K for x = 0.4) for higher concentration of iron. From the dc-magnetization study, we have derived the values of the intrachain (positive) and interchain (negative) exchange constants for the compounds $Ca_3Co_{2-x}Fe_xO_6$ (x = 0.0, 0.1, 0.2, and 0.4). The values of intrachain exchange constant J derived by fitting the high temperature χT vs T curves with the theoretical model indicates that as the concentration of iron increases, J decreases and for higher concentration of iron ($x > 0.2$) it becomes negative. These results can be understood by considering the formation of pairs of Fe^{3+} ions along the chain for higher concentration of iron (x = 0.4) and negative exchange interaction between Fe^{3+} ions along the chain (via oxygen). A coexistence of the SRO and

LRO (for the $x = 0.2$ and 0.4 compounds), has been confirmed from the zero field neutron diffraction study (Chapter 4). It is observed that the correlation lengths for both SRO and LRO do not differ very much for the $x = 0.2$ and 0.4 compounds, indicating that Fe ions in a chain are located preferentially very close to each other for higher concentration of iron (x= 0.4). A field induced ferri-to-ferromagnetic like transition is found in the M vs H study. An estimate of the interchain exchange constant J', derived from the ferri-to-ferromagnetic like transition under field, indicates that J' increases with increasing the Fe concentration. This indicates that the strength of negative exchange interaction for Co2/Fe-O-Co2/Fe pathway is greater than that of the Co2-O-Co2 which can be ascribed to the different spin nature of Co^{3+} and Fe^{3+} ions. Deviation from $\triangle M/M_S = \delta \ H^{-3/2}$ behavior with increasing iron concentration indicates the deviation form quasi-1D character of spins for higher Fe substituted compounds. The observed results (in the dc magnetization study) have been ascribed to a breaking of the ferromagnetically ordered linear spin-chains along the crystallographic c axis with iron substitution and strengthening of antiferromagnetic exchange interaction between Fe^{3+} ions.

Neutron diffraction study has been carried out to study the spin-spin correlations in the compound $Ca_3Co_{1.8}Fe_{0.2}O_6$, by directly investigating the evolution of the magnetic structures as a function of applied magnetic field (0, 2 and 4 T) and temperature (1.5 - 100 K). At low temperatures, in the zero field, the magnetic structure corresponds to the SDW structure with an incommensurate propagation vector [k = {0, 0, 1.0182(9)}]. An application of magnetic field up to 4 T does not change the number of the additional magnetic Bragg reflections in the neutron diffraction patterns, it only affects their intensities and positions. A change in the propagation vector from an incommensurate [$\boldsymbol{k}$ = {0, 0, 1.0182 (9)}] to a commensurate [$\boldsymbol{k}$ = {0, 0, 1}] is found, when the magnetic field is increased to 2 T. In an applied field of 2 T, the magnetic structure corresponds to an amplitude modulated structure with $\boldsymbol{k} = \{0, 0, 1\}$. The observed change in the propagation vector, from the incommensurate to the commensurate, indicates a reduction of the spin frustration on the triangular lattice in an applied field of 2 T. A further increase of the magnetic field ($H = 4$ T) leads to a magnetic phase transition from the amplitude modulated structure to a ferrimagnetic structure. In the ferrimagnetic phase, intensities of the satellite peaks (100), (200), and (210) are low compared to the SDW and the AM structures, indicating that the AFM correlations between spin chains are weakened or broken, before the system reaches to a fully polarized ferromagnetic phase at higher magnetic fields ($>$ 5 T). The application of magnetic field affects the SRO volume fraction as well as the spin-spin correlation length. The applied magnetic field also converts the SRO (which was present in zero field) into LRO above 12 K, however, below 12 K, the SRO still persists. In the magnetic fields of 2 and 4 T, the observed reduction in the intensities of the peaks (100), (200), and (210) [below $\sim$ 12 K] has been attributed to an increase in the volume fraction of the SRO (different from the zero field SRO). This is in contrast with the zero field neutron diffraction study, where a SRO coexists with LRO in a constant volume ratio of 13:7 at all temperatures below T_N. The derived results would be useful to understand the effect of an external magnetic field on the nature of the magnetic ordering in other geometrically frustrated triangular lattice spin systems. The results would also be useful to develop theoretical models to describe the effect of magnetic field on the degenerate magnetic ground states of such quasi-1D spin-chain systems. However, a single crystal neutron diffraction study would be required for a complete elucidation of a magnetic phase diagram of the compound $Ca_3Co_{1.8}Fe_{0.2}O_6$ in the temperature-magnetic field plane.

CHAPTER 6

Magnetic Properties of the Rare-earth Substituted Compounds $Ca_{2.75}R_{0.25}Co_2O_6$

6.1 Introduction

The magnetic properties of the compound $Ca_3Co_2O_6$ have been studied extensively in literature (discussed in Chapter 4). However, the effect of electron doping on electronic and magnetic properties of the compound $Ca_3Co_2O_6$ has not been studied in detail. Vidya *et al.* [95] have carried out a first principle calculations, based on density functional theory, with generalized gradient corrections, to study the effect of electron doping on the electronic and magnetic properties of the compound $Ca_3Co_2O_6$ [95]. They [95] predicted that electronic and magnetic properties of the compound $Ca_3Co_2O_6$ can be tuned by an electron doping. The ground states of the compounds $Ca_{2.25}Y_{0.25}Co_2O_6$ and $Ca_{2.7}Y_{0.3}Co_2O_6$ were predicted to be insulating ferromagnet [95]. However, the experimentally reported magnetic ground state for the compound $Ca_{2.7}Y_{0.3}Co_2O_6$ was ferrimagnetic [107]. It was found that as the concentration of Y increased, the Curie-Weisss temperature and the effective paramagnetic moment decreased, indicating a reduction in the strength of ferromagnetic intrachain exchange interaction (J). For the concentration of Y greater than 0.3, no magnetic ordering was observed [108]. The effect of other rare-earth (R) substitution at the Ca site on the structural and magnetic properties of the compounds $Ca_{3-\nu}R_\nu Co_2O_6$ ($\nu \leq 0.9$) was investigated by Hervoches *et al.* [108]

using dc -magnetization and x-ray diffraction techniques. The unit-cell dimensions were reported to vary linearly with increasing the concentration of R^{3+} (R = Y, Pr, Nd, Sm, Eu, Gd, Tb, Dy, Ho, Yb, and Lu) [108]. A reduction in the magnetic moment of the cobalt ions at TP site was observed, similar to that reported for the Y substituted compounds [107]. The compounds $\mathrm{Ca_{2.70}R_{0.30}Co_2O_6}$ were found to order magnetically for R = Pr, Nd, Sm, Eu, Tb, Ho, and Lu. However, no magnetic ordering was observed for the compounds $\mathrm{Ca_{2.70}Dy_{0.30}Co_2O_6}$, $\mathrm{Ca_{2.70}Gd_{0.30}Co_2O_6}$, and $\mathrm{Ca_{2.70}Yb_{0.30}Co_2O_6}$ [108].

Motivated by the above mentioned studies, we have prepared polycrystalline samples of the compounds $\mathrm{Ca_{2.75}}R_{0.25}\mathrm{Co_2O_6}$ (R = Lu and Dy). This particular concentration of rare-earths has been chosen by keeping in mind that the compounds should have maximum electron doping but at the same time order magnetically. This would allow us to investigate the effect of electron doping on the magnetic ground state. We have chosen Lu and Dy substituted compounds because of a significant difference in the Shannon ionic radii [109] of $\mathrm{Lu^{3+}}$ and $\mathrm{Dy^{3+}}$ (0.977 and 1.027 , respectively). In the parent compound $\mathrm{Ca_3Co_2O_6}$, the crystal structure contains spin-chains, made up of alternating face sharing $\mathrm{CoO_6}$ octahedra (OCT) and $\mathrm{CoO_6}$ trigonal prism (TP), running along the crystallographic c axis. These chains are arranged on a triangular lattice in the ab plane and are separated by non-magnetic $\mathrm{Ca^{2+}}$ ions (ionic radii of $\mathrm{Ca^{2+}}$ is 1.12 Å). The substitution of Lu^{3+} and Dy^{3+} ions at the $\mathrm{Ca^{2+}}$ site, due to a significant difference in the ionic radii, may change the distance between magnetic ions. The difference in the oxidation state of the R^{3+} and $\mathrm{Ca^{2+}}$ would vary the oxidation and spin states of $\mathrm{Co^{3+}}$ ions in the compound $\mathrm{Ca_3Co_2O_6}$. These factors are expected to change the intrachain and interchain magnetic exchange interactions, which can modify the magnetic properties of these spin-chain compounds. Moreover, $\mathrm{Dy^{3+}}$ is magnetic and $\mathrm{Lu^{3+}}$ ($4f^{14}$) is non-magnetic. The Dy-substituted compound would, therefore, enable us to investigate the possible microscopic changes in the nature of magnetic ordering due to the presence of magnetic ions between chains.

In the present work, the magnetic properties of rare-earth substituted compounds $\mathrm{Ca}_{2.75}R_{0.25}\mathrm{Co}_2\mathrm{O}_6$ (R = Lu and Dy) have been studied using low temperature neutron diffraction and dc magnetization techniques. The results of the dc magnetic susceptibility and neutron diffraction study confirm that extra electrons in these compounds are transferred to the cobalt ions at the TP site. Both compounds order magnetically in the incommensurate spin density wave (SDW) below their respective Néel temperatures. The observed decrease in the values of the T_N ($\sim$ 25 K for the parent compound $\mathrm{Ca}_3\mathrm{Co}_2\mathrm{O}_6$), with rare earth substitution, indicates a reduction in the dominant intrachain (J) ferromagnetic interaction.

6.2 Experimental Details

Polycrystalline compounds $\mathrm{Ca}_{2.75}R_{0.25}\mathrm{Co}_2\mathrm{O}_6$ (R = Lu and Dy) were prepared using the conventional solid state reaction method as described in Chapter 2. Rietveld refinement of room-temperature x-ray powder diffraction patterns confirmed the single phase formation of both compounds in the space group $R\bar{3}c$.

The neutron diffraction experiments were carried out on high-resolution powder diffractometer D2B at the Institut Laue-Langevin (ILL) in Grenoble (France). The diffraction patterns were collected at selected temperatures (T = 1.5 and 50 K) in an angular range $8^\circ < 2\theta < 150^\circ$ with 2θ step of 0.05°, using a wavelength of 2.39 Å. Neutron diffraction patterns between 1.5 and 25 K were measured using the high intensity D1B diffractometer (λ = 2.52 Å) at ILL, Grenoble (France). Diffraction data analysis was done by the Rietveld method using the FULLPROF [40] refinement package. The representation theory analysis was performed using the BASIREPS software [40].

Magnetization measurements were carried out using a commercial (Cryogenic Limited, UK) vibrating sample magnetometer. For the zero-field-cooled (ZFC) magnetization measurements, the samples were cooled down to 2 K in zero field, then a magnetic field of 1kOe was applied, and the data were recorded in the warming cycle, with field on. Whereas, for the field cooled (FC) magnetization measurements, after applying the magnetic field of 1kOe at 300 K, samples were cooled down to 2 K, and FC magnetization was measured in the warming cycle. The hysteresis curves were recorded at various temperatures over + 9 to -9 Tesla applied field.

6.3 Results and Discussion

6.3.1 Magnetic Susceptibility

The temperature dependencies of the FC and ZFC susceptibilities for both compounds are shown in Fig. 6.1. The ZFC susceptibility (χ) increases gradually with decreasing the temperature down to $\sim$ 7 K, below which it drops. However, the FC susceptibility increases continuously with decreasing the temperature down to 2 K. A bifurcation between FC and ZFC susceptibility has been observed at low temperatures ($\sim$ 8 K). A small kink in the ZFC susceptibility curve, has been observed at $\sim$ 17 K for $Ca_{2.75}Lu_{0.25}Co_2O_6$, however, no such kink has been observed for $Ca_{2.75}Dy_{0.25}Co_2O_6$ (insets of Fig. 6.1). The observed kink can be attributed to a 3D magnetic ordering in $Ca_{2.75}Lu_{0.25}Co_2O_6$. Here we would like to mention that a 3D magnetic ordering has been observed below $\sim$ 16 K for both compounds in the neutron diffraction study (Section 6.3.2). The observed behavior is similar to that observed for the parent compound $Ca_3Co_2O_6$ and Fe-substituted compounds (described in Chapter 4). In literature, a similar behavior has been reported for other

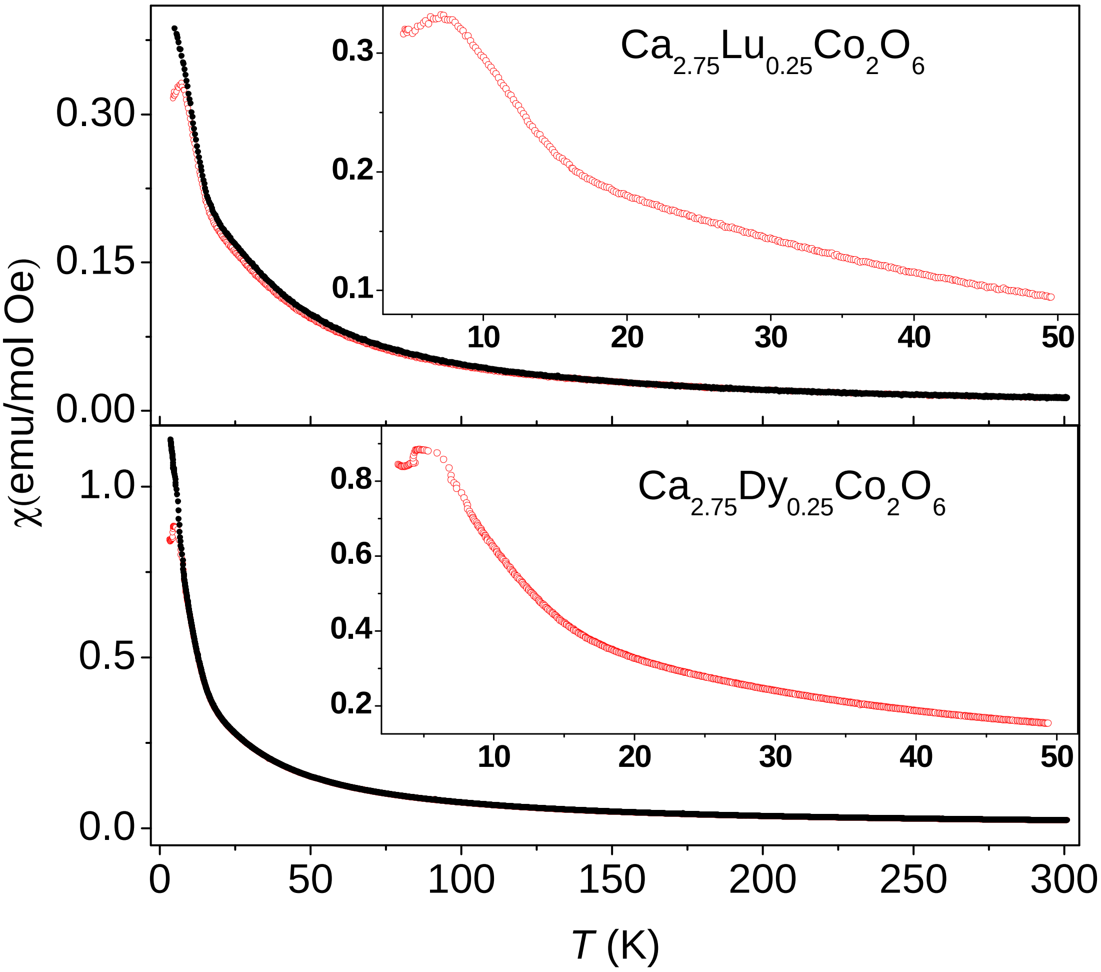

Figure 6.1: Dc magnetic susceptibility vs temperature curves under 1 kOe field for $Ca_{2.75}R_{0.25}Co_2O_6$ (R = Lu and Dy). The (red) open and (black) solid circles correspond to ZFC and FC modes, respectively. Insets show zoomed-in view of the ZFC susceptibility at low temperatures.

compounds of the A_3MXO_6 family, *viz.* Ca_3CoRhO_6 [94] and Sr_3NiRhO_6 [110] . The observed bifurcation (between FC and ZFC susceptibilities) can be ascribed to the spin freezing phenomenon, which may arise due to the presence of a geometrical frustration in these compounds. For both compounds, high temperature (in the paramagnetic region) magnetic suitability obeys the Curie-Weiss law [$\chi_{mol} = C_{mol}/T - \theta_p$], here C_{mol} is molar Curie constant and θ_p is the paramagnetic Curie temperature. The temperature dependencies of the inverse susceptibilities (χ^{-1}) and the fitted curves with Curie-Weiss law are shown in Fig. 6.2. The derived values of the θ_p for the compounds $Ca_{2.75}Lu_{0.25}Co_2O_6$ and $Ca_{2.75}Dy_{0.25}Co_2O_6$ are 28.4 and

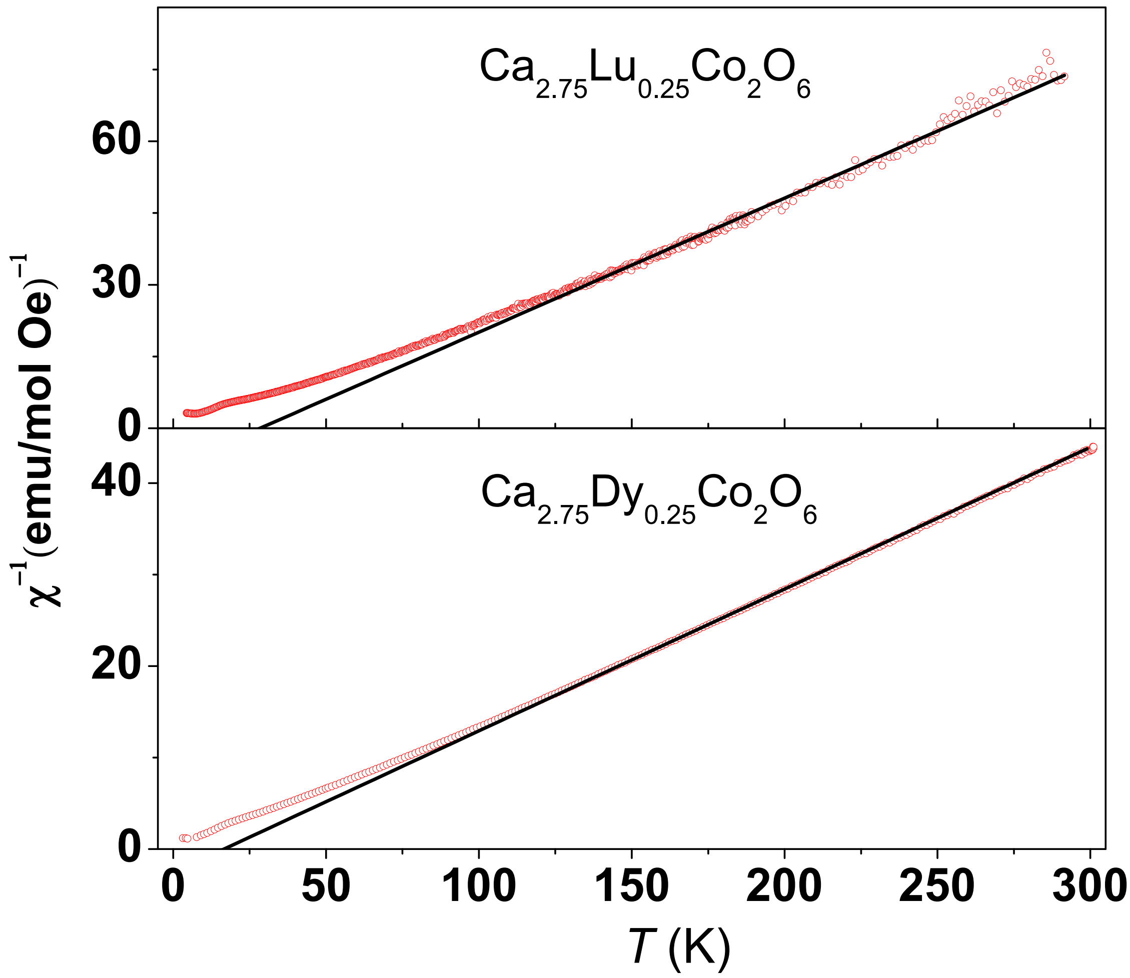

Figure 6.2: Inverse ZFC susceptibility (H = 1 kOe) vs temperature curves fitted with the Curie-Weiss law for $Ca_{2.75}R_{0.25}Co_2O_6$ (R = Lu and Dy).

16.6 K, respectively. The positive value of θ_p indicates a ferromagnetic nature of the dominant exchange interaction. Here it may be noted that for the parent compound $Ca_3Co_2O_6$, the reported value of the θ_p is ~ 30 K [77]. The observed decrease in the values of the θ_p with rare earth substitution indicates a reduction in the dominant ferromagnetic intrachain exchange interaction. The derived values of the molar Curie constant C_{mol} for the compounds $Ca_{2.75}Lu_{0.25}Co_2O_6$ and $Ca_{2.75}Dy_{0.25}Co_2O_6$ are 3.56 and 6.45 emu K/mol-Oe, respectively. The effective paramagnetic moment (μ_{eff}) per formula unit has been derived from the experimental molar curie constant C_{mol} using the relation $\mu_{eff} \approx \sqrt{8C_{mol}}$. The derived values of the μ_{eff} are 5.34 and 7.18 μ_B/f.u. for the compounds with R = Lu and Dy, respectively. For the Co ions at the TP and OCT sites, one expects a quenching of the orbital momentum, so that $L = 0$, $J = S$, and $g = 2$ [77]. For the rare earth ions R^{3+}, the spin-orbit coupling is stronger than the crystalline electric field and the magnetic moment can be associated with the total angular momentum J. The values of J for Lu^{3+} and Dy^{3+} are 0 and 15/2 , respectively. For the parent compound $Ca_3Co_2O_6$, due to the crystalline electric field (t_{2g} and e_g splitting), Co^{3+} ions at the OCT site are reported to be in the low spin ($S = 0$) state [52]. The reported value of the effective moment is 5.5 μ_B per formula unit. In the present rare earth substituted compounds, the extra electrons can be transferred to the cobalt ions at either TP or OCT site. The transfer of extra electrons is expected to change the oxidation state of some of cobalt ions from 3+ ($3d^6$) to 2+ ($3d^7$). If the extra electrons are transferred to the cobalt ions at the OCT site, the spin configuration of 25 percentage of cobalt ions at the OCT site (low spin site) will change from $S = 0$ ($3d^6$) to S = 1/2 ($3d^7$), which would result in an increase (compared to $Ca_3Co_2O_6$) in the value of μ_{eff} per formula unit. On the other hand, if extra electrons are transferred to the cobalt ions at the TP site, the spin configuration of 25 percentage of cobalt ions at the TP site (high spin site) will change from $S = 2$ ($3d^6$) to $S = 3/2$ ($3d^7$). This would result in an decrease in the value of μ_{eff} per formula unit, provided the rare earth ions carry a zero moment (which is the case of Lu^{3+}). The observed lower value of the μ_{eff} for the compound $Ca_{2.75}Lu_{0.25}Co_2O_6$ (5.34 μ_B/f.u.) compared to the value reported in the literature for the parent compound $Ca_3Co_2O_6$ (5.5 μ_B/f.u.) suggests that extra electrons are transferred to the cobalt ions at the TP site. The expected values of the μ_{eff}, considering extra electrons are transferred to the cobalt ions at the TP site, can be calculated using the expression

$$\mu_{eff} = \sqrt{0.25 g_J^2 J(J+1) + 0.75 \times 2^2 \times 2 \times 3 + 0.25 \times 2^2 \times 3/2 \times 5/2} \, .$$

Here g_J is Landé factor. For R = Lu and Dy compounds, theoretically expected (considering spin only values of the moment for cobalt ions) values of μ_{eff} are 4.66 and 7.077 μ_B/f.u., respectively. The higher experimental values of the μ_{eff} can be due to a partial quenching of the Co^{3+} angular momentum. Here it may be noted that for the parent compound $Ca_3Co_2O_6$, an orbital momentum of 1.7 μ_B has been reported for the Co^{3+} ions at the TP site [69].

6.3.2 Magnetic Structure

Rietveld refined neutron diffraction patterns for both compounds at 50 K are shown in Fig. 6.3. The refined values of the structural parameters, given in Table 6.1, are consistent with the values obtained from the Rietveld refinement of room temperature x-ray diffraction patterns mentioned in Chapter 3 (except the variation in the structural parameters due to the temperature factor).

The low temperature neutron diffraction experiments were carried out to investigate the nature of magnetic ordering in these compounds. Figures 6.4 and 6.5 depict the neutron diffraction patterns for the compounds $Ca_{2.75}R_{0.25}Co_2O_6$ with R = Lu and Dy, respectively, in the temperature range 1.5 - 25 K, measured on the high flux D1B diffractometer. Additional Bragg peaks in the neutron diffraction patterns appear for both compounds below $\sim$ 16 K, indicating the onset of an antiferromagnetic ordering. For the parent compound $Ca_3Co_2O_6$, a 3D magnetic ordering is reported to occur below the Néel temperature ($T_N \sim$ 25 K) due to a combined effect of a stronger intrachain ferromagnetic (J) and a weaker interchain antiferromagnetic (J') interactions [88]. The observed decrease in the 3D magnetic ordering temperature with the rare-earth substitution indicates a lower values of J, which is consistent with our structure studies, where a increase in the lattice constant c, with the substitution of the rare earth ions, has been observed. The increase

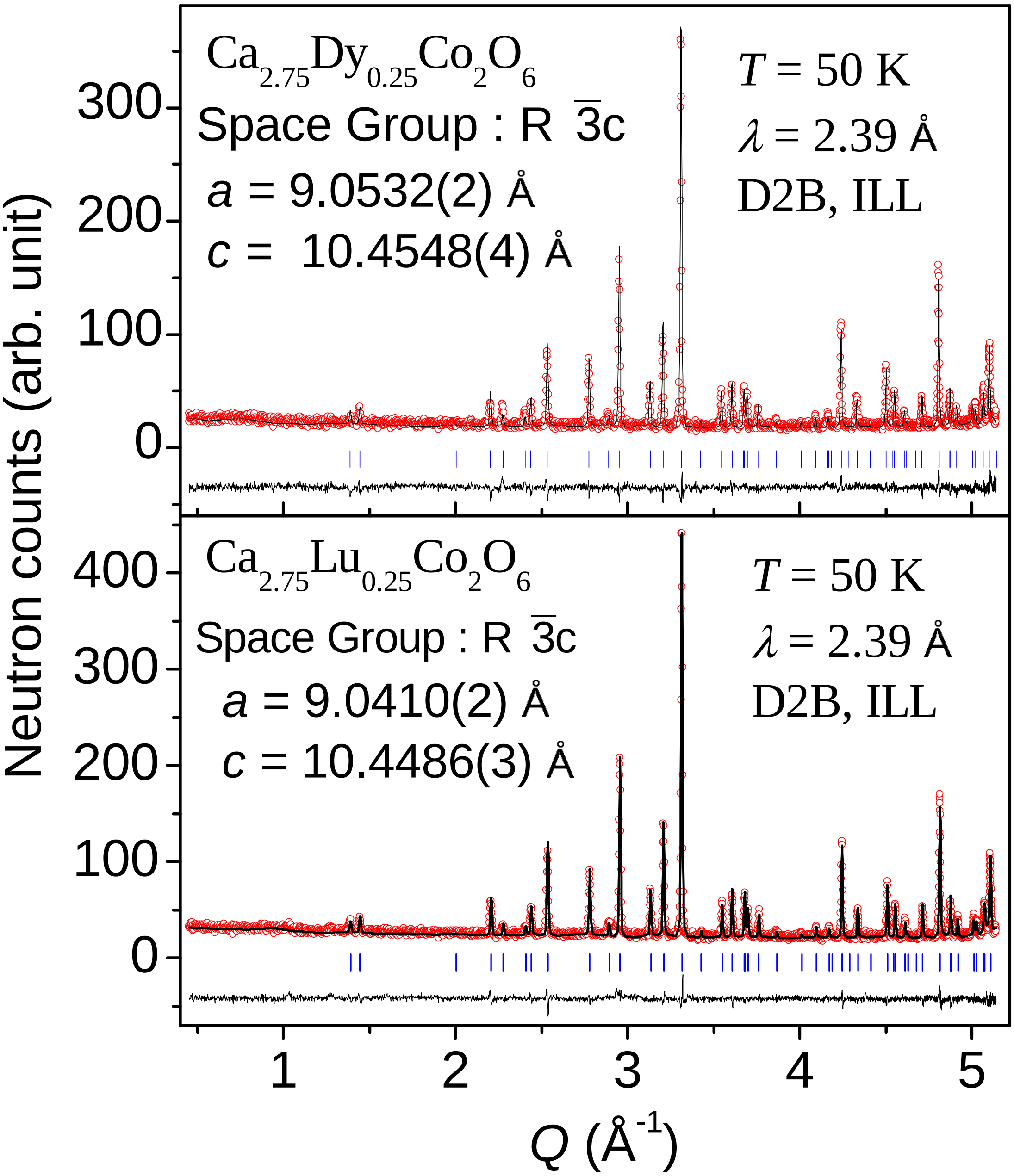

Figure 6.3: Observed (open circles) and calculated (solid lines) neutron diffraction patterns of $Ca_{2.75}R_{0.25}Co_2O_6$(R = Lu and Dy) at 50 K. Solid lines at the bottom of each panel show difference between observed and calculated patterns. Vertical lines show the position of Bragg peak.

in the separation between magnetic ions along a chain, gives a weaker ferromagnetic intrachain exchange interaction (J).

To analyze the precise nature of the antiferromagnetic ordering (exact values of the propagation vector), neutron powder diffraction patterns have been measured at 1.5 K for both compounds on the high resolution D2B diffractometer. The magnetic

Table 6.1: Structural parameters (atomic positions, thermal parameters, bond lengths, and bond angles) obtained from the refinement of the neutron diffraction patterns at 50 K for the compounds $Ca_{2.75}R_{0.25}Co_2O_6$ (R = Lu and Dy). Both compounds crystallize in the space group $R\bar{3}$c. The lattice constants are $a = 9.0532(2)$Å, $c = 10.4548(4)$Å and $a = 9.0410(2)$Å, $c = 10.4486(3)$Å for R = Dy and Lu, respectively. All crystallographic sites are fully occupied.

Compound	Atom	Site	x	y	z	B_{iso}(Å^2)
R = Dy	Ca/Dy	18e	0.3684(5)	0	0.25	0.24(2)
	Co1	6b	0	0	0	0.25 (6)
	Co2	6a	0	0	0.25	0.28(5)
	O	36f	0.1769(4)	0.0254(3)	0.1113(2)	0.38 (3)
		Bond lengths (inÅ)				
	Co1-Co2	2.6137(1)				
	Co1-O	1.898(3)				
	Co2-O	2.086(3)				
		Bond angle				
	Co1-O-Co2	81.8(3)°				
R = Lu	Ca/Lu	18e	0.3692(3)	0	0.25	0.26(2)
	Co1	6b	0	0	0	0.28(3)
	Co2	6a	0	0	0.25	0.21(3)
	O	36f	0.1785(2)	0.0254(2)	0.1120(1)	0.36(3)
		Bond lengths (inÅ)				
	Co1-Co2	2.6121(2)				
	Co1-O	1.912(2)				
	Co2-O	2.089(2)				
		Bond angle				
	Co1-O-Co2	81.37(7)°				

Bragg peaks at 1.5 K have been indexed using the incommensurate propagation vector $\boldsymbol{k} = \{0, 0, 1.02\}$ referred to the rhombohedral setting of the space group $R\bar{3}c$ (Fig. 6.6). The magnetic structure has been analyzed using the standard irreducible

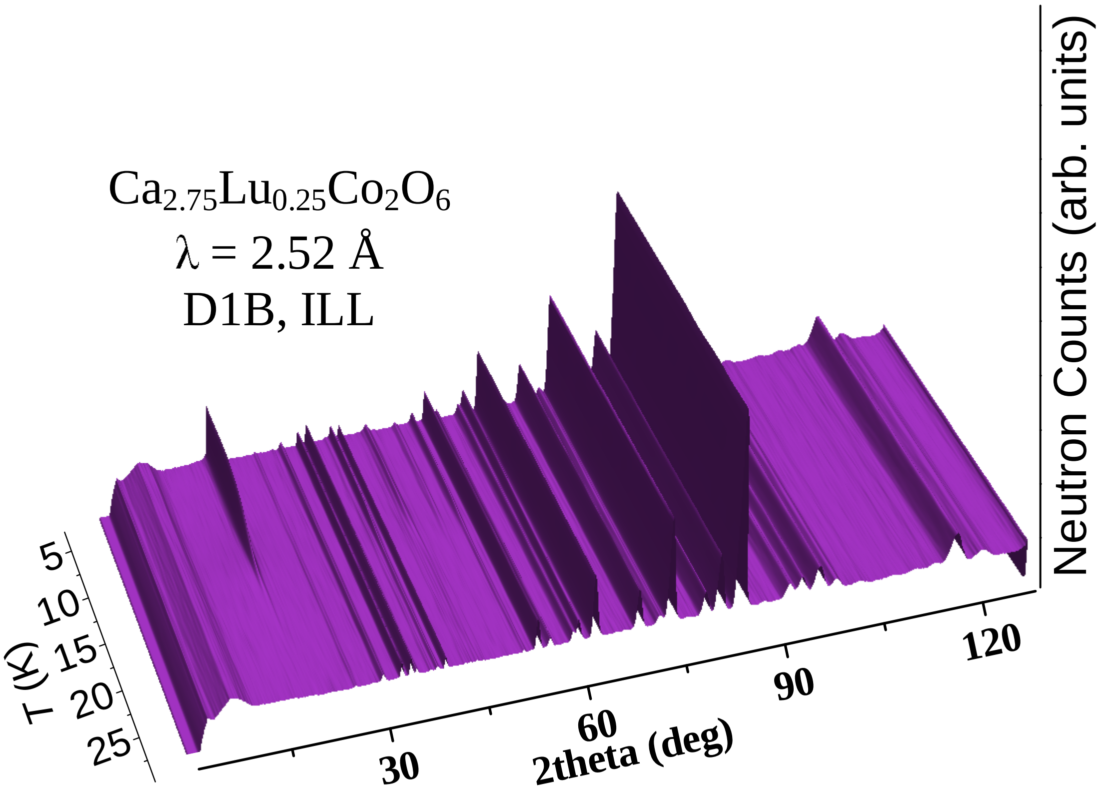

Figure 6.4: Temperature evolution of the neutron powder diffraction patterns of $Ca_{2.75}Lu_{0.25}Co_2O_6$. Additional peaks appear below $\sim$ 16 K due to the onset of an antiferromagnetic ordering.

representational theory as described by Bertaut [75, 76]. The analysis shows that magnetic reducible representation Γ for the $6a$ and $6b$ sites can be written as

$$\Gamma(6a) = 1\Gamma_1^{(1)} + 1\Gamma_2^{(1)} + 2\Gamma_3^{(2)}$$

and

$$\Gamma(6b) = 1\Gamma_1^{(1)} + 1\Gamma_2^{(1)} + 2\Gamma_3^{(2)} \ .$$

Here, the representation Γ_1 and Γ_2 are one dimensional, however, the representation Γ_3 is two dimensional. The observed neutron powder diffraction patterns for both compounds (Fig. 6.6) have been fitted with the magnetic structures corresponding to the representation Γ_2. The resulting magnetic structure with the representation Γ_2 is shown in Fig. 6.7. The magnetic structure corresponds to an incommensurate spin-

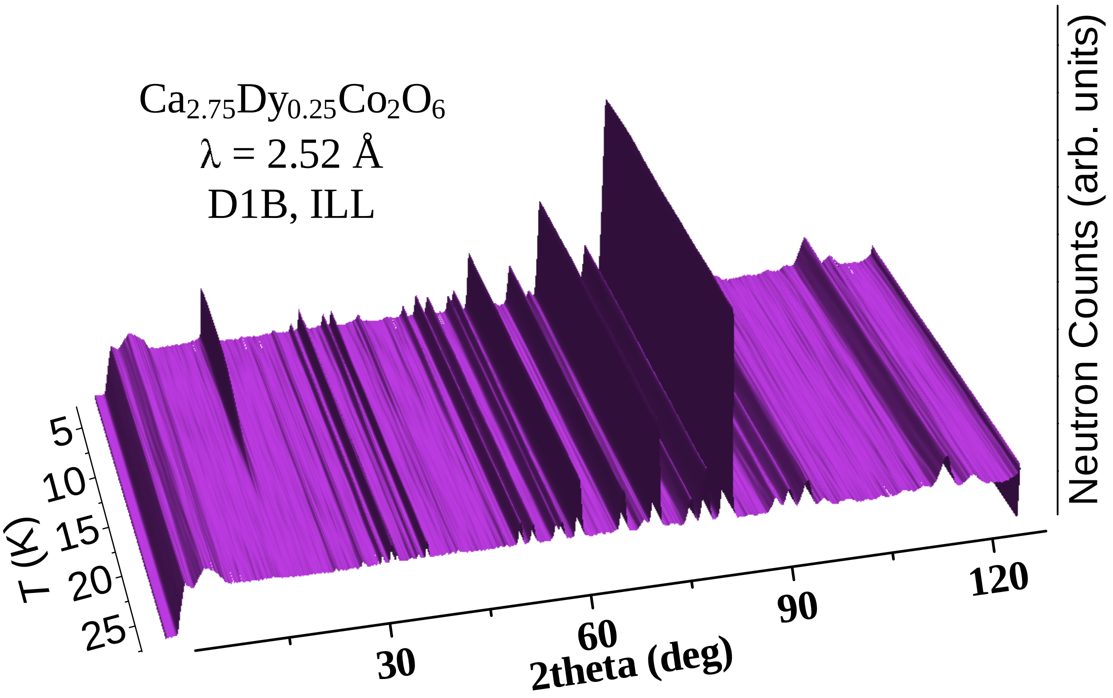

Figure 6.5: Temperature evolution of the neutron powder diffraction patterns of $Ca_{2.75}Dy_{0.25}Co_2O_6$. Additional peaks appear below ~ 16 K due to the onset of an antiferromagnetic ordering.

density wave structure, having c axis as directions of both moment and modulation. In the resulting magnetic structure, the magnetic moments at the $6a$ (0, 0, 1/4) and $6b$ (0, 0, 0) sites are given by

$$\begin{aligned}\mathbf{m}_{L,j(j=6a,6b)} &= \sum_{(-k,+k)} \frac{1}{2}\boldsymbol{S}_j^k exp(-2\pi i\boldsymbol{k}.\boldsymbol{R}_L) \\ &= \frac{1}{2}[\boldsymbol{S}_j^k exp(-2\pi i\boldsymbol{k}.\boldsymbol{R}_L) + \mathrm{S}_j^{-k} exp(-2\pi i\boldsymbol{k}.\boldsymbol{R}_L)] \\ &= \boldsymbol{S}_j^k \cos(2\pi\boldsymbol{k}.\boldsymbol{R}_L) \qquad (6.1)\end{aligned}$$

Here ${\boldsymbol{S}_{6a}}^k$ and ${\boldsymbol{S}_{6a}}^k$, the Fourier coefficients, are the maximum magnetic moments at the $6a$ and $6b$ sites, respectively, and $\boldsymbol{R}_L$ is the translation vector with respect to the zeroth cell including the non-integer translations $t1 = (2/3,\ 1/3,\ 1/3)$ and $t2 = (1/3,\ 2/3,\ 2/3)$. For both compounds, the refined values of the maximum moment at the $6b$ site, $\boldsymbol{m}_{6b}$, are zero. The values of the maximum moment at the $6a$ site

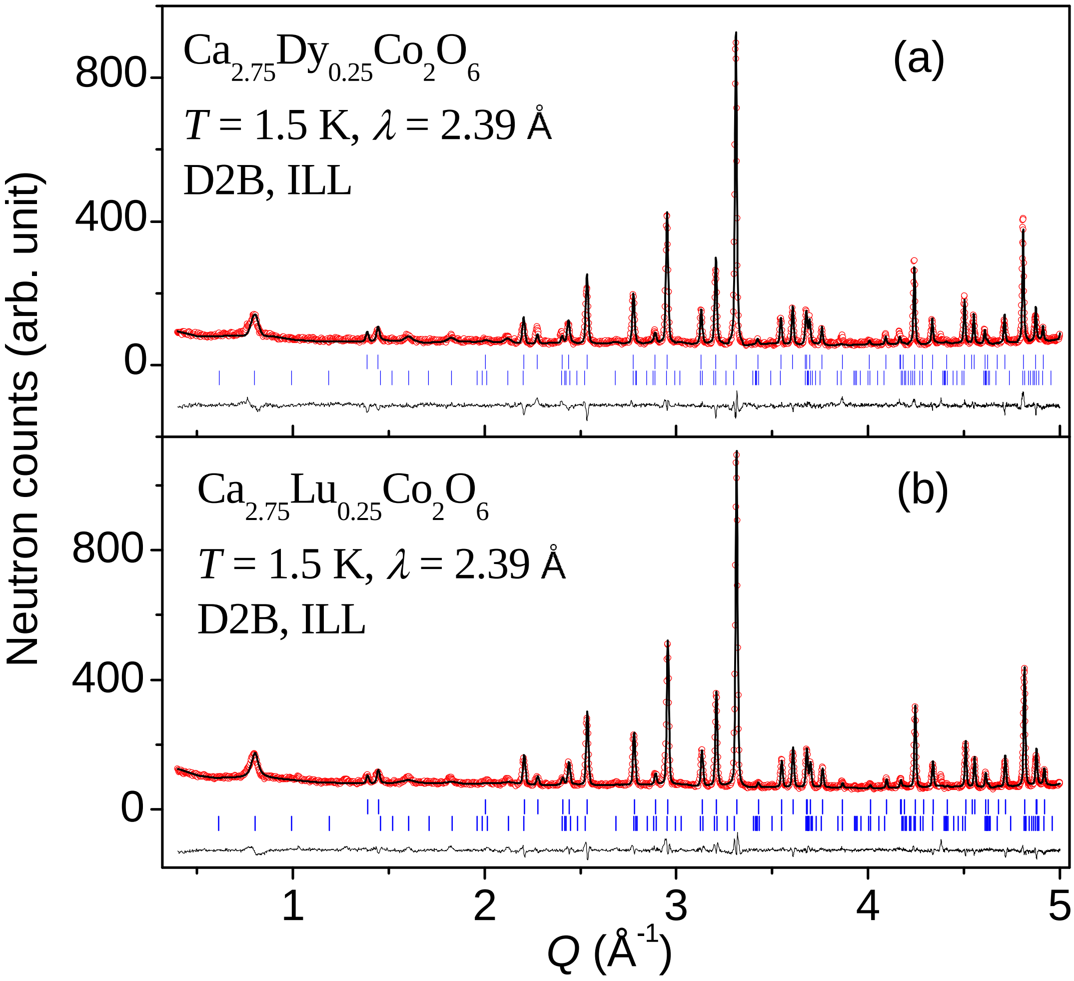

Figure 6.6: The Rietveld refined neutron powder diffraction patterns at 1.5 K for (a) $Ca_{2.75}Dy_{0.25}Co_2O_6$ and (b) $Ca_{2.75}Lu_{0.25}Co_2O_6$ using the SDW structure with propagation vector $\{\boldsymbol{k} = 0, 0, 1.02\}$: experimental data (open circle), calculated curve (solid line), and difference (solid line at the bottom). Vertical marks correspond to the position of all allowed Bragg reflections for the crystal (top row) and magnetic (bottom row) reflections.

are 4.2 (2) and 4.2 (3) for R = Dy and Lu, respectively. For both compounds, the refinement yielded a zero ordered moment for the rare earth ions located at $18e$ site. In the literature, for the parent compound $Ca_3Co_2O_6$, it has been well established [86] that the Co^{3+} ions at the OCT site are in low spin state ($S = 0$) and the Co^{3+} ions at the TP site carry an ordered moment of 5.1 μ_B (including a sizable contribution from the orbital angular momentum). For the present compounds $Ca_{2.75}R_{0.25}C_2O_6$, the refined value (zero) of the ordered moment at the OCT site confirms that cobalt ions at the OCT sites remain in the 3+ oxidation state (d^6,

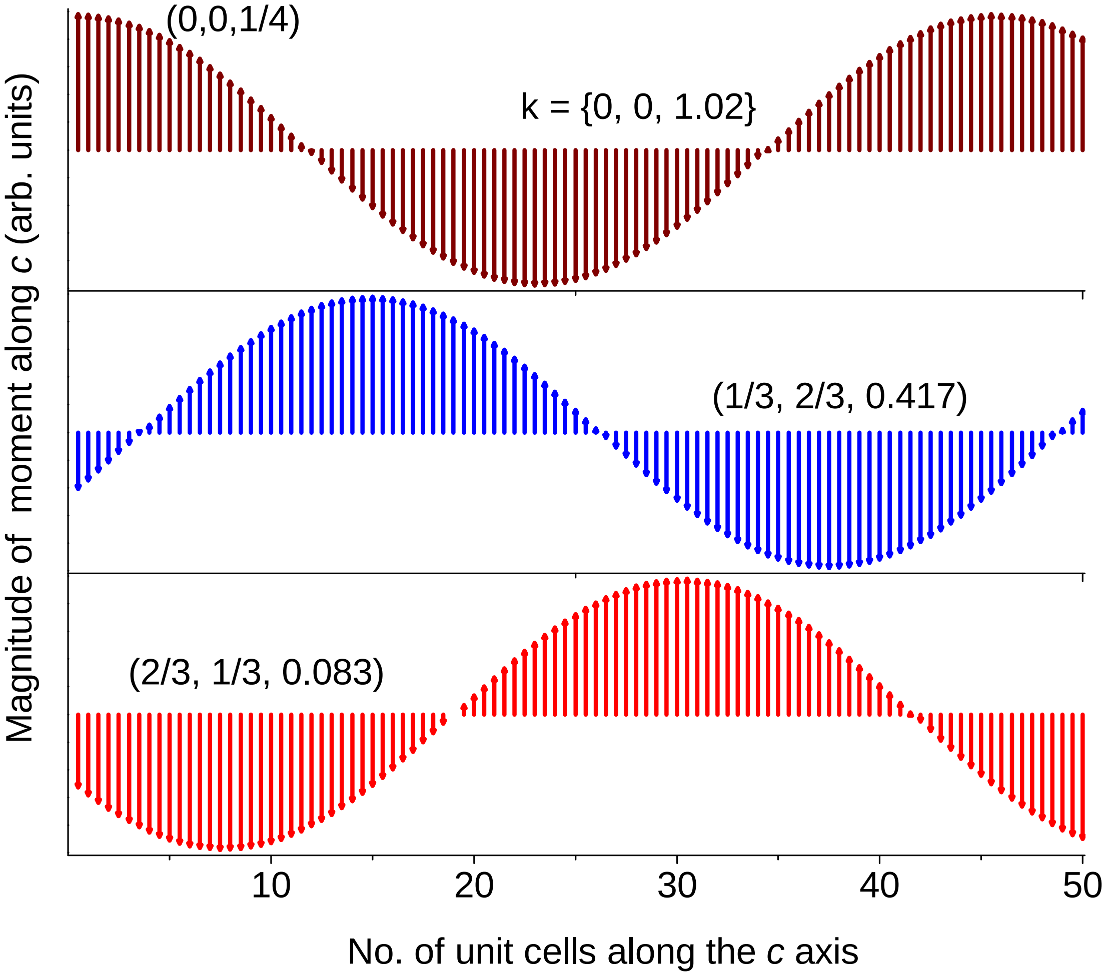

Figure 6.7: Schematic of the proposed incommensurate spin-density wave structure [$\boldsymbol{k} = \{0, 0, 1.02)\}$] for 50 unit cells, with a modulation and alignment of the moments along the crystallographic c axis, corresponding to the model used to calculate the diffraction patterns shown in Figs. 6.6 (a) and (b) for R = Dy and Lu samples, respectively. The magnitude and direction of spins in the three adjacent spin chains with the (x, y) coordinate as (0, 0), (1/3, 2/3), and (2/3, 1/3) are shown.

$S = 0$). The observed reduction in the value of the maximum moment at the TP site (compared to $Ca_3Co_2O_6$) confirms that the extra electrons are transferred to the cobalt ions at the TP site. By considering that 25 percent of the cobalt ions at the TP site change their spin state from $S = 2$ ($3d^6$) to $S = 3/2$ ($3d^7$) due to the transfer of electrons, the theoretically expected spin only value of the maximum ordered moment at the 6a site is given by $\boldsymbol{m}_{6a} = [0.75\ \boldsymbol{m}(\mathrm{Co}^{3+}) + 0.25\ \mathrm{m}(\mathrm{Co}^{2+})]$. Here $\boldsymbol{m}(\mathrm{Co}^{3+})$ and $\boldsymbol{m}(\mathrm{Co}^{2+})$ are the spin only ordered moment for the Co^{3+} and Co^{2+} ions, with values 4 and 3 μ_B, respectively. For both compounds, the theoretically calculated spin only value is 3.75 μ_B per f.u. The observed high value of the maximum moment at the $6a$ site indicates a sizable contribution from the orbital angular momentum of cobalt ions. These results are consistent with the derived values of μ_{eff} from the dc magnetization study.

Now we discuss that the true ground state magnetic structure of the present rare-earth substituted compounds is an incommensurate SDW magnetic structure, not a ferrimagnetic structure, reported by Hervoches *et al.* [108]. The temperature dependence of the integrated intensity of the (110) nuclear Bragg peak plays a very important role in determining the ground state magnetic structure of these compounds. A simple calculation using the program Fullprof [40] shows that the magnetic contribution in the intensity of the (110) peak is zero in the case of SDW structure, however, the contribution is finite in the case of **a** ferrimagnetic structure. Temperature variation of the integrated intensity of the (110) peak is shown in Fig. 6.8 for both compounds. No change in the intestines of the fundamental (nuclear) Bragg peak (110) peak, below T_N, rules out the possibility of the ferrimagnetic structure.

Now we compare the nature of the observed incommensurate SDW magnetic structure for the present rare-earth substituted compounds with the reported incommensurate SDW structure for the parent compound $Ca_3Co_2O_6$ (discussed in Chapter 4). Figure 6.9 shows the temperature dependence of the integrated intensity of the prominent antiferromagnetic Bragg peak (100) for the present rare-earth substituted compounds. For both compounds, the intensity of the (100) AFM peak increases with decreasing the temperature (below T_N) and then saturates at lower temperature. Whereas, for the parent compound $Ca_3Co_2O_6$ ($T_N \sim 25$ K), below $\sim$ 15 K, a decrease in the intensity of AFM peak (100) was reported in the powder [86] as well as single crystal neutron diffraction study [62]. The anomalous reduction

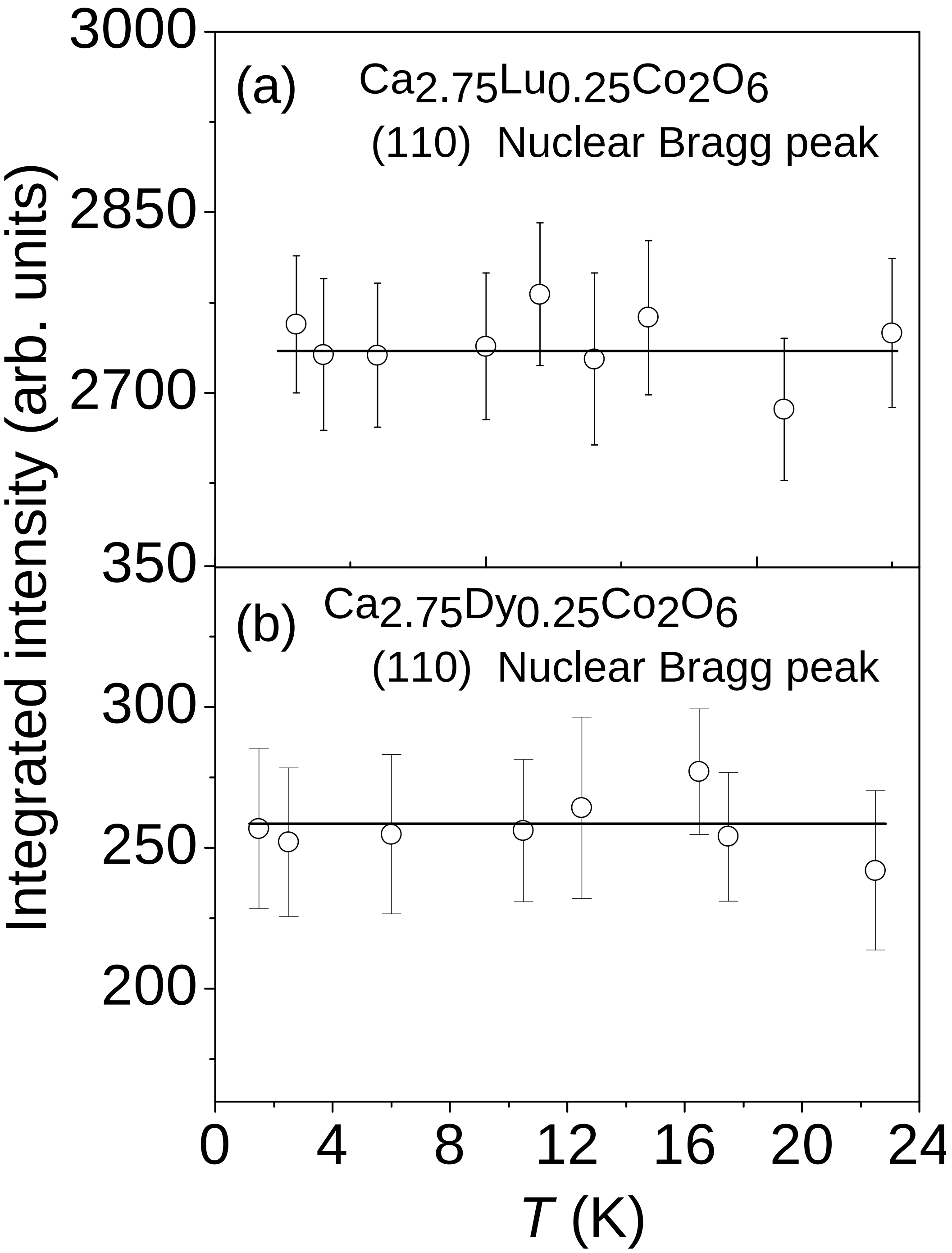

Figure 6.8: Temperature dependence of the integrated intensity of the nuclear Bragg peak (110) for (a) $Ca_{2.75}Lu_{0.25}Co_2O_6$ and (b) $Ca_{2.75}Dy_{0.25}Co_2O_6$.

in the intensity was ascribed to the presence of a magnetic phase with short-range order [86]. The onset of the magnetic short-range order was reported to be originated from the defects in the propagation of the long-range magnetic structure. At low temperatures, the SDW structure was reported to be unstable and a increase

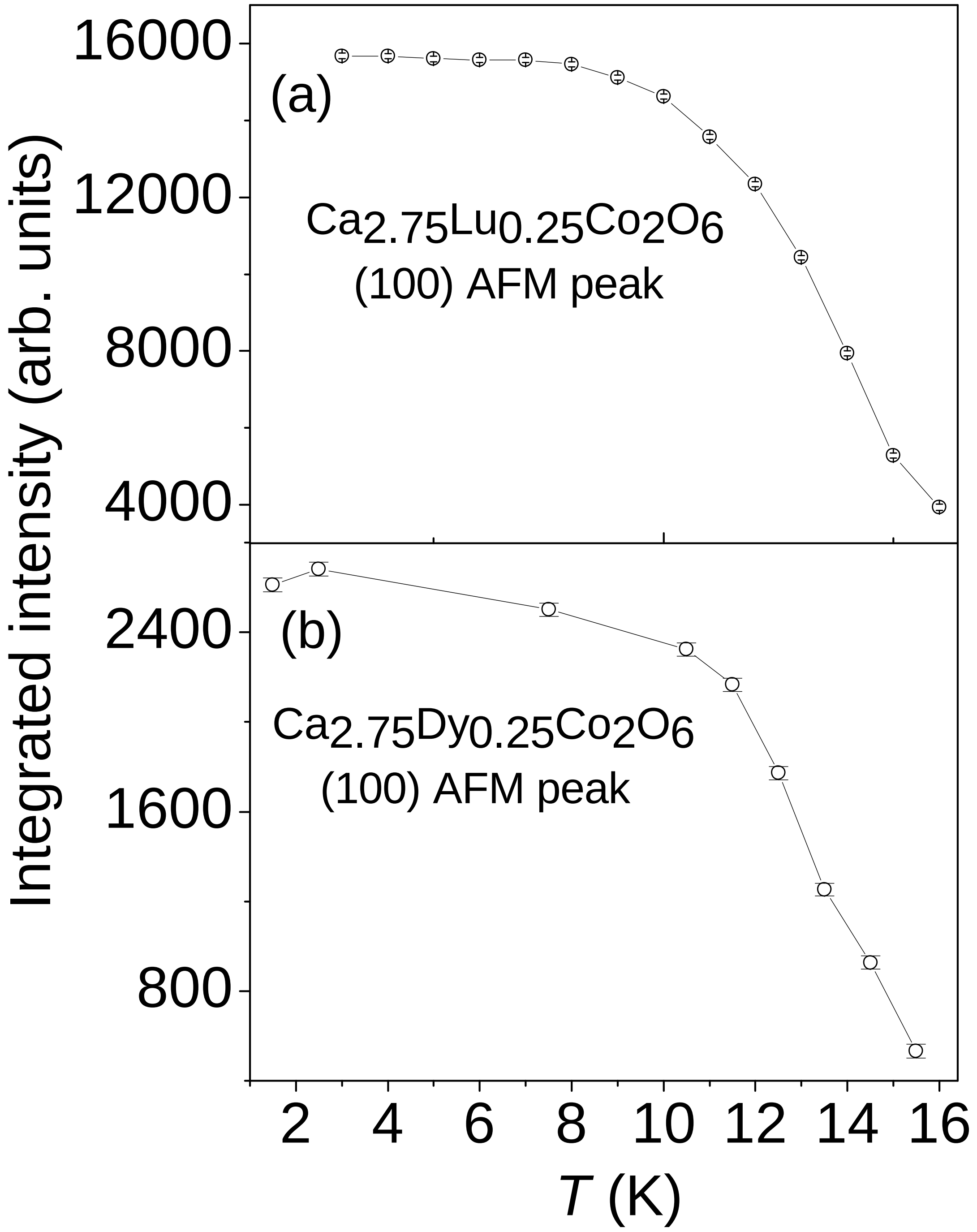

Figure 6.9: Temperature dependence of the integrated intensity of the AFM reflection (100) for (a) $Ca_{2.75}Lu_{0.25}Co_2O_6$ and (b) $Ca_{2.75}Dy_{0.25}Co_2O_6$.

in the volume fraction of short-range ordering (SRO) was reported [86]. For the present rare-substituted compounds, no reduction in the intensity of the (100) peak indicates that the SDW structure for these compounds is stable down to 1.5 K. In addition, for the parent compound $Ca_3Co_2O_6$, below $\sim$ 13 K, a long-time variation of the magnetic structure, in which the magnetic Bragg peaks at (1, 0, $\pm\ \delta$) move toward (1, 0, 0) with real time, was reported in the single crystal neutron diffraction study [89]. Moreover, a second set of magnetic peaks corresponding to the commensurate antiferromagnetic structure with the propagation vector $\boldsymbol{k}_2 = \{0.5, 0.5, 0\}$ was reported to appear in the powder neutron diffraction patterns at low temperatures, if the sample was held at 10 K for some time while cooling [88]. A time dependence of the strongest magnetic Bragg peaks of the SDW and commensurate antiferromagnetic (CAFM) structures was also observed [88]. To examine the presence of a possible time variation of the magnetic structure for the present rare-earth substituted compounds, we have recorded neutron diffraction patterns at 7 and 13 K. Figures 6.10 and 6.11 show the neutron diffraction patterns for the strongest magnetic reflections, collected in 10 minutes (on D1B diffractometer) for R = Dy and Lu compounds, respectively, at 7 and 13 K. For the measurement at 7 and 13 K, the sample was rapidly cooled from 30 K (cooling rate 3 K/min), and then data collection was started. We have binned the data for every 10 minutes. In Figs. 6.10 and 6.11, we show data for three representative binning modules corresponding to an effective time gap of 10, 20, and 30 minutes, after the measurements were started at the respective temperatures. It is evident that the magnetic Bragg peak does not exhibit a time dependence. No observed reduction as well as no time dependence in the intensity of the strongest magnetic Bragg peak (100) suggests that the SDW structure is stable for the present rare earth substituted compounds.

The qualitative nature of the observed SDW structure for the present rare-earth substituted compounds is same as that observed for the Fe-substituted compounds $Ca_3Co_{2-x}Fe_xO_6$ ($x = 0.2$ and 0.4), discussed in Chapter 4. However, the characteristics of the observed SDW structure is very much different from the reported PDA structure for the compounds Ca_3CoRhO_6 and Sr_3HoCrO_6. In the PDA structure

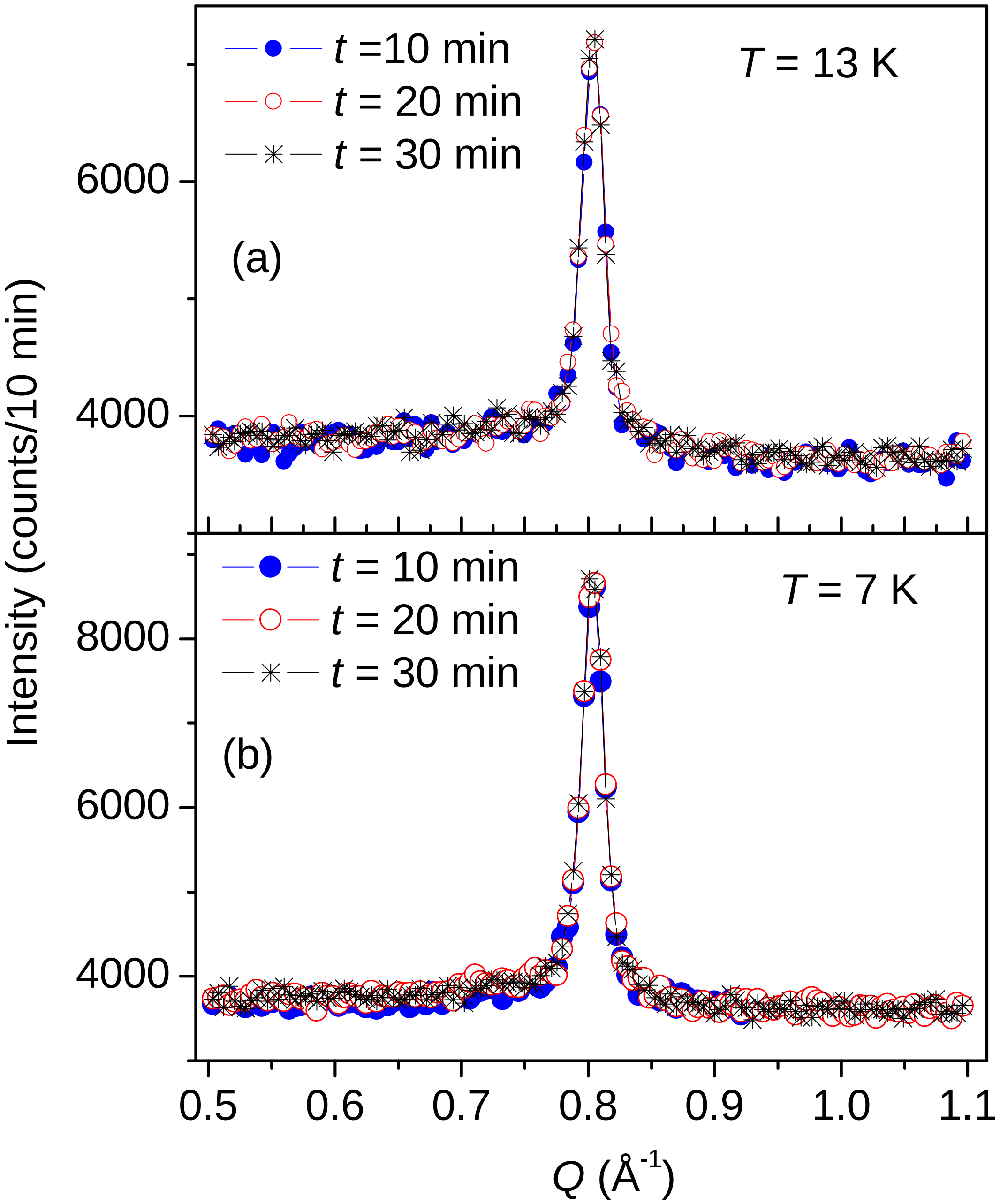

Figure 6.10: Neutron diffraction patterns collected in 10 minutes for the compound $Ca_{2.75}Dy_{0.25}Co_2O_6$ after an effective time gap of 10 (solid circle), 20 (open circle), and 30 (star) minutes, after the measurement was started at (a) 13 K and (b) 7 K. Only the strongest antiferromagnetic peak at $Q \sim 0.79$ Å^{-1} is shown. The solid lines are guides to the eye.

1/3 ferromagnetic spin chains (on a triangle) have spin up ($+M$), 1/3 ferromagnetic spin chains have spin down (-M), and the remaining 1/3 are incoherent (disordered). The resulting magnetic configuration of the neighboring spin chains on a triangle is ($+M$, -M, 0). Whereas, in the incommensurate SDW structure, the magnetic

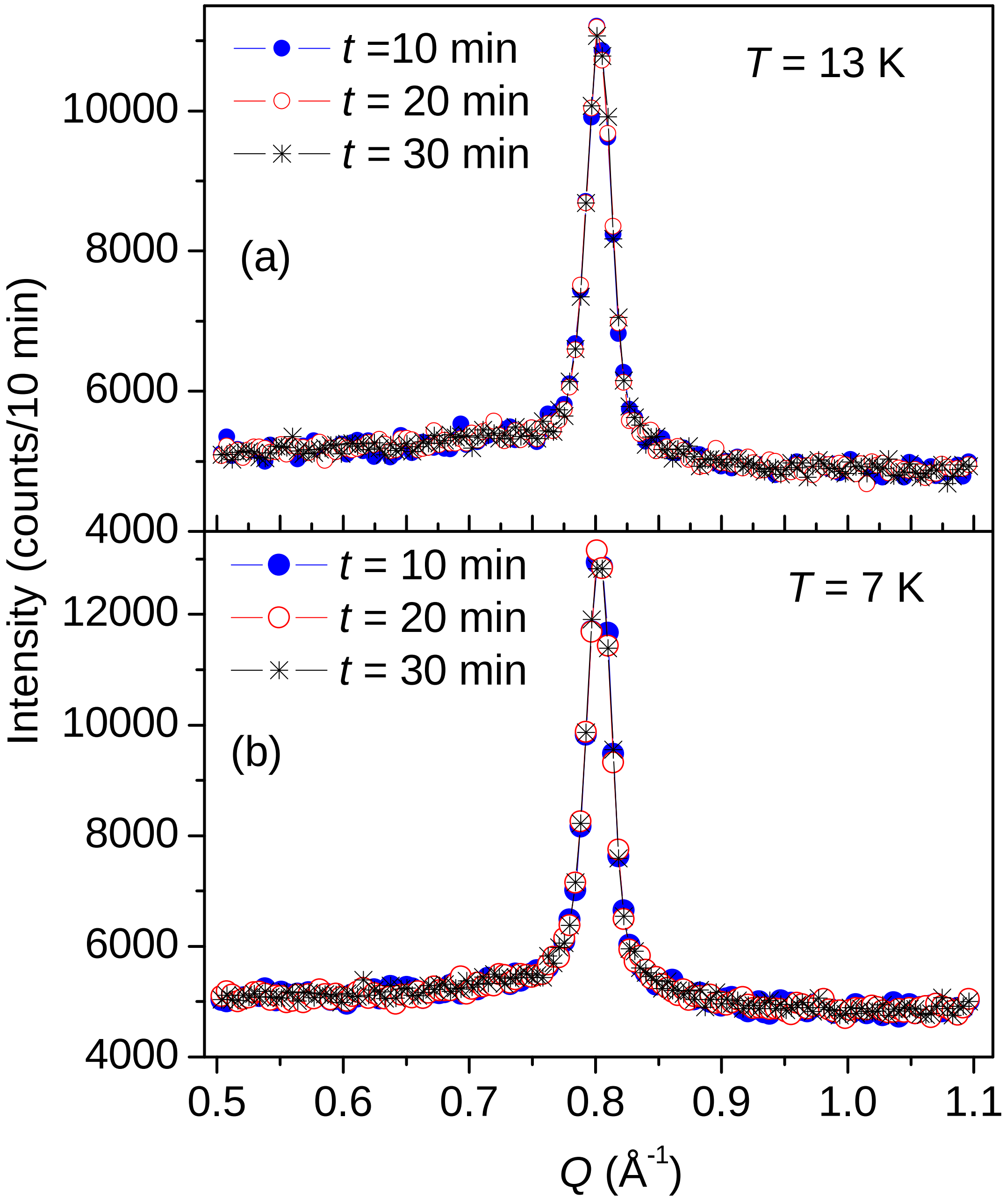

Figure 6.11: Neutron diffraction patterns collected in 10 minutes for the compound $Ca_{2.75}Lu_{0.25}Co_2O_6$ after an effective time gap of 10 (solid circle), 20 (open circle), and 30 (star) minutes, after the measurement was started at (a) 13 K and (b) 7 K. Only the strongest antiferromagnetic peak at $Q \sim 0.79$ Å^{-1} is shown. The solid lines are guides to the eye.

configuration of the neighboring spin chains (arranged on a triangle) is ($+M$, -M, 0) at specific lattice points only (Fig. 6.7).

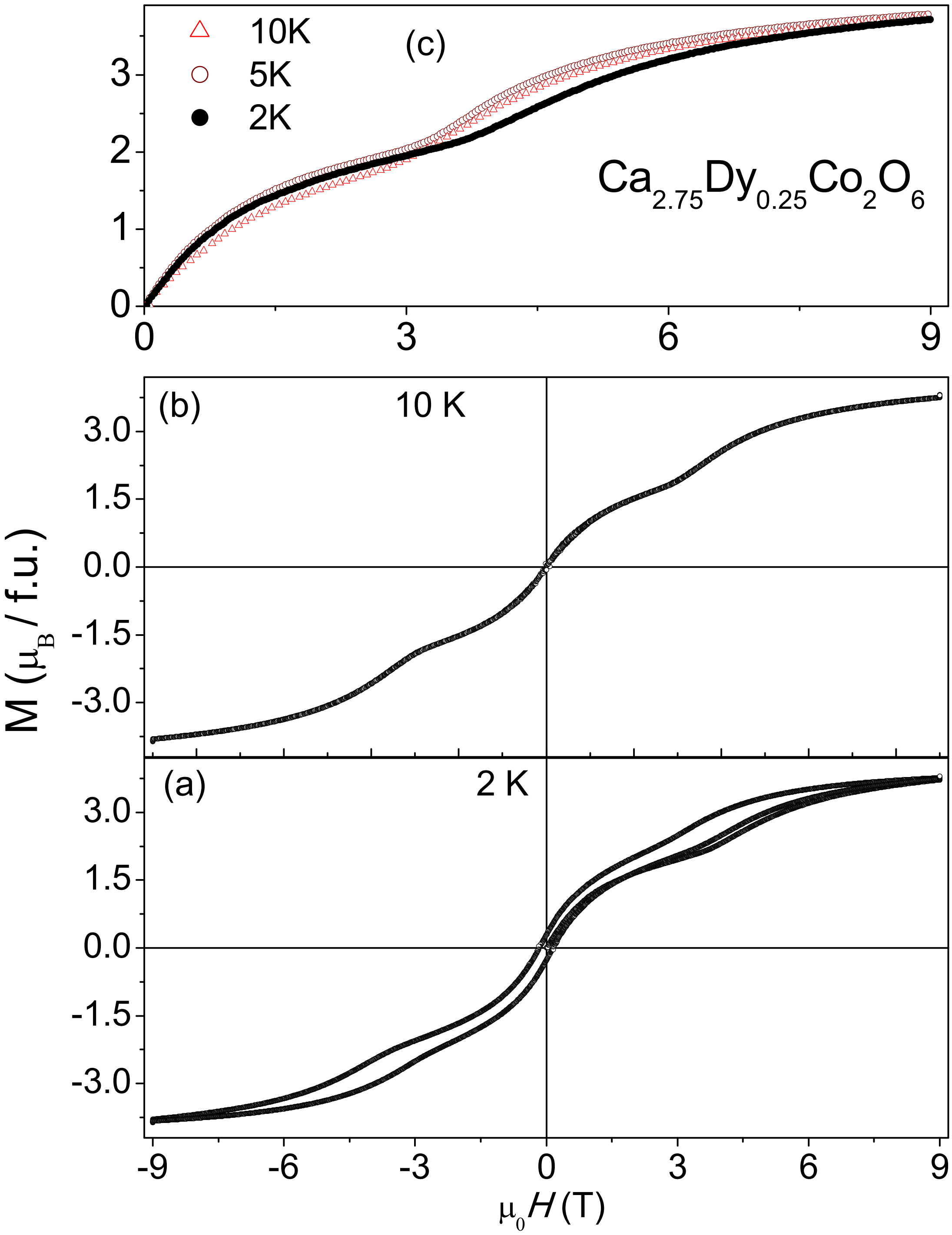

Figure 6.12: Hysteresis loops for the compound $Ca_{2.75}Dy_{0.25}Co_2O_6$ recorded at (a) 2 K and (b) 10 K. (c) The virgin magnetization curves recorded at 2 K(solid circles), 5 K (solid circles), and 10 K (open triangles).

6.3.3 Field Dependence of the Magnetization

Figures 6.12 and 6.13 show the $M(H)$ curves, with the field up to 9 T, measured at various temperatures below T_N, for the compounds $Ca_{2.75}Dy_{0.25}Co_2O_6$ and

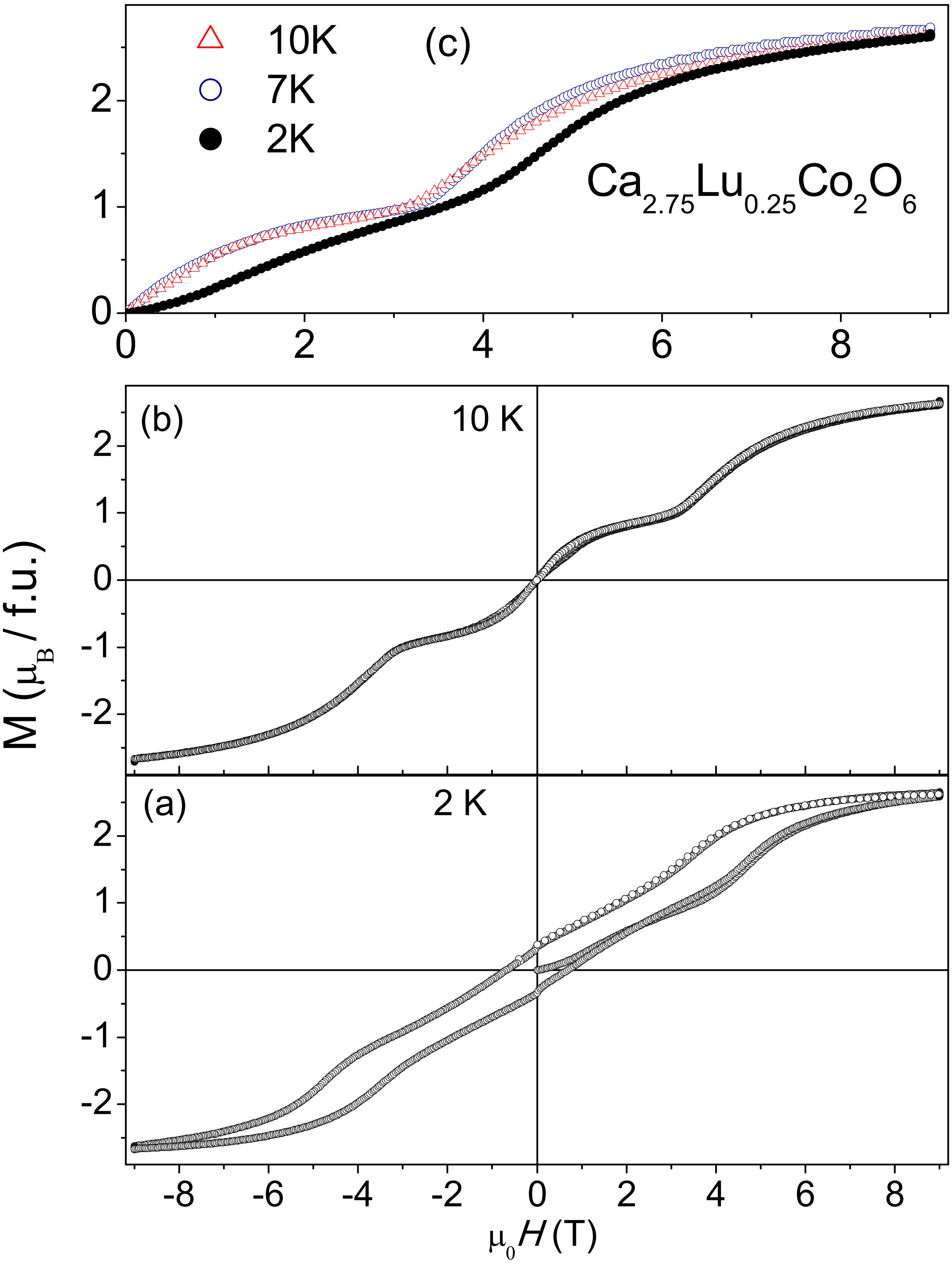

Figure 6.13: Hysteresis loops for the compound $Ca_{2.75}Lu_{0.25}Co_2O_6$ recorded at (a) 2 K and (b) 10 K. (c) The virgin magnetization curves recorded at 2 K(solid circles), 7 K (open circles), and 10 K (open triangles).

$Ca_{2.75}Lu_{0.25}Co_2O_6$, respectively. The virgin magnetization curves at various temperatures are shown in Figs. 6.12 (c) and 6.13 (c). $M(H)$ curves were recorded after cooling the sample from 300 K to measurement-temperature in the absence of a magnetic field. At 2 K, the virgin magnetization (M) varies linearly with field in small field region for both compounds. A change in the slope of the magnetization has been observed at $\sim$ 1 T. At higher fields, the magnetization reaches a distorted plateau. A further increase in magnetic field results in a rounded shape of the magnetization curves. For both compounds, the magnetization curves show a clear hysteresis at 2 K. The saturation in the magnetization could not be observed even under the magnetic fields as high as 9 T. At 10 K, $M(H)$ curves show the distorted plateau in the low field region (*i.e.* below $\sim$ 3 T) for both compounds. At a higher field, the rounded magnetization curves, are obtained. In the literature, similar behavior of the field dependent magnetization [$M(H)$] has been reported for the parent compound $Ca_3Co_2O_6$ [52, 55, 60], and by the author on the iron substituted compounds $Ca_3Co_{2-x}Fe_xO_6$ [77]. Based on these previous studies, the observed magnetization behavior can be related to different field-induced metamagnetic phase transitions in the present rare-earth substituted compounds. In the zero field neutron powder diffraction study (Sec 6.3.2), we have seen that the present rare-earth substituted compounds order magnetically in an incommensurate SDW structure with a propagation vector $\{0, 0, 1.02\}$. The observed change in the slope of the magnetization at $\sim$ 1 T [Figs. 6.12(b) and 6.13(c)] indicates the presence of a metamagnetic like phase transition, which can be ascribed to a transition from the zero field incommensurate spin density wave (SDW) structure to a commensurate amplitude modulated structure (based on the results of the neutron diffraction study for the compound $Ca_3Co_{1.8}Fe_{0.2}O_6$ discussed in Chapter 5). The observed distorted magnetization plateau (below $\sim$ 3 T) can be ascribed to the formation of a ferrimagnetic state (containing ferromagnetic Ising spin-chain with 2/3 chains having spin up and the remaining 1/3 having spin down). The observed rounded magnetization curves at higher fields (above $\sim$ 3.5 T) can be ascribed to a ferri-to-ferromagnetic transition.

Now we discuss the observed magnetization plateau for the present rare-earth substituted compounds and compare it with that for the parent compound $Ca_3Co_2O_6$. An important point to be noted here is that all $M(H)$ curves for the present rare earth substituted compounds were measured on the polycrystalline samples. For the parent compound $Ca_3Co_2O_6$, the $M(H)$ curves have been reported in the literature for the polycrystalline [55, 77] as well as single crystals [57, 99]. In the single crystals dc magnetization study (with $H\|c$) at 10 K, a saturation of magnetization (M_{sat}) has been reported above $\sim$ 4.5 T [57]. However, for the polycrystalline sample, the value of the magnetization at 10 K under an applied field of 4.5 T is $\sim$ 1.9 μ_B/f.u., and it increases slowly with increasing the magnetic field [77]. The magnetization does not saturate even under an applied field of 11 T [77]. The reported remarkable difference in the behavior of the $M(H)$ curves for the polycrystalline and single crystal samples, indicates the presence of a very strong magnetic anisotropy for the parent compound $Ca_3Co_2O_6$. For the present rare earth substituted compounds, the observed non-saturation of the magnetization at 2 K (even under 9 T field) and the distorted plateau could be due to the angular averaging in a powder sample (for a single crystal sample, one could have observed magnetization plateau at $M = M_{sat}/3$, and then a jump to the saturation magnetization M_{sat} at higher fields).

6.4 Summary and Conclusion

We have prepared single phasic polycrystalline samples of the spin-chain compounds $Ca_{2.75}R_{0.25}Co_2O_6 (R = \text{Lu and Dy})$. Rietveld refinement of x-ray and neutron diffraction patterns confirms that both compounds crystallize in the rhombohedral structure (space group $R\bar{3}c$) and the crystal structure contains one-dimensional chains of alternating face-sharing CoO_6 octahedra (with Co1) and $(Co)O_6$ trigonal prisms (with Co2), running along the crystallographic c axis. For both compounds, high temperature (in the paramagnetic region) magnetic susceptibility obeys the Curie-Weiss law. The derived values of the paramagnetic Curie temperature (θ_p) are 28.4 and 16.6 K for R = Lu and Dy, respectively. The positive value of θ_p indicates a ferromagnetic nature of dominant exchange interaction. The observed decrease in the value of the θ_p with rare-earth substitution ($\theta_p \sim 30$ K for $Ca_3Co_2O_6$) indicates a reduction in the dominant intrachain ferromagnetic interaction.

In the neutron diffraction patterns, additional Bragg peaks appear for both compounds below $\sim$ 16 K (T_N), indicating the onset of an antiferromagnetic ordering of cobalt spin chains on the triangular lattice. The magnetic Bragg peaks (below T_N) can be indexed using the incommensurate propagation vector $\boldsymbol{k} = \{0, 0, 1.02\}$. For both compounds, the refinement yielded a zero ordered moment for the 18e site (where rare earth ions are located) indicating that the nature of magnetic ordering is not affected by the presence of magnetic ions between the chains for the compounds $Ca_{2.75}R_{0.25}Co_2O_6$. The magnetic structure corresponds to the SDW structure, having c axis as direction of the moment and the modulation. For the rare earth doped compounds, the refined zero value of the ordered moment at the OCT (6b) site confirms that cobalt ions at the OCT sites remain in the 3+ oxidation state. The refined values of the maximum moment at the 6a site are same ($\sim$ 4.2 μ_B) for both compounds. For the parent compound $Ca_3Co_2O_6$, the reported value of the maximum moment at the 6a site is $\sim$ 5.1 μ_B. The observed reduction in the value of the maximum moment at the TP site for the rare-earth substituted compounds, confirms that the oxidation state of a fraction of the cobalt ions at the TP site is reduced from Co^{3+} to Co^{2+}. The observed decrease in the value of T_N with rare-earth substitution ($T_N \sim 25$ K for $Ca_3Co_2O_6$) indicates a reduction in the value of positive ferromagnetic intrachain exchange interaction J, which is consistent from the structure studies, where a increase in the lattice constants, with the substitution of the rare-earth ions, has been observed. No observed reduction as well as no time dependence in the intensity of the strongest magnetic Bragg peak (100) confirms that the SDW structure is stabilized with the substituted of rare-earth ions. The qualitative nature of the observed magnetic ground states for the rare-earth substituted compounds is same as that observed for the Fe-substituted compounds $Ca_3Co_{2-x}Fe_xO_6$ ($x = 0.2$ and 0.4), however, different from that observed for the parent compound $Ca_3Co_2O_6$.

In the field dependent magnetization study, a distorted plateau (below ~ 3 T) in the $M(H)$ curves has been observed for both compounds, which has been ascribed to the formation of a ferrimagnetic state. The observed rounded shape of the magnetization curves at higher fields has been ascribed to a ferri-to-ferromagnetic transition.

The derived results in the present study are useful to understand the effect of electron doping on the magnetic properties of these spin-chain compounds. The results would encourage the scientific community to extend the investigations for the other compounds of A_3MXO_6 family. Here it should be noted that these compounds are highly anisotropic. The magnetization and neutron diffraction studies using single crystal would be required to get more direct insight into the microscopic nature of the magnetization curves at low temperatures.

Chapter 7

Summary and Conclusion

In this thesis, the structural and magnetic properties of the compounds $Ca_3Co_2O_6$, $Ca_3Co_{2-x}Fe_xO_6$ (x = 0.1, 0.2, 0.4, and 1.0), and $Ca_{2.75}R_{0.25}Co_2O_6$ (R = Lu and Dy) have been studied as a function of temperature and applied magnetic field. In the compound $Ca_3Co_2O_6$, spin-chains are made up of alternating face sharing CoO_6 octahedra (OCT) and CoO_6 trigonal prisms (TP). These chains are arranged on a triangular lattice in the ab plane and are separated by the Ca^{2+} ions. Due to the crystalline electric fields, cobalt ions at the OCT ($6b$) site are in low-spin (S = 0) state. The Co^{3+} spins at the TP sites have an Ising-like magnetic anisotropy and are aligned along the crystallographic c axis. In the compounds $Ca_3Co_{2-x}Fe_xO_6$ (x = 0.1, 0.2, and 0.4), the Fe^{3+} spins have "Heisenberg" character in comparison to the "Ising" character of the Co^{3+} spins. Therefore, spin chains in these Fe-substituted compounds are made up of mixed Ising (Co^{3+}) and Heisenberg (Fe^{3+}) spins. In the compounds $Ca_{2.75}R_{0.25}Co_2O_6$ (R = Lu and Dy), the substitution of rare earth-earth (R^{3+}) ions at the Ca^{2+} site is expected to change the spin state of cobalt ions as well the distance between the magnetic ions. In all these compounds, the ferromagnetic (FM) intrachain and antiferromagnetic (AFM) interchain interactions, combined with a triangular lattice arrangement of the spin chains give rise to a geometrical frustration. Due to the presence of a geometrical frustration, a complex ground state magnetic structure is expected in these compounds.

The polycrystalline samples of spin-chain oxides studied in the present thesis were prepared by the author using the solid state reaction method. Several experimental techniques were employed to investigate the structural and magnetic properties of these compounds. The technique used in the present thesis are x-ray and neutron diffraction, dc magnetization, and Mössbauer spectroscopy. The author has used the Rietveld refinement technique [38] to refine the crystal structures, and to determine the magnetic structures. Bertaut's representation theory [75] has been applied to identify the possible models of magnetic structures.

Prior to the present thesis work, only a few reports existed in the literature on the magnetic properties of the compounds $Ca_3Co_{2-x}Fe_xO_6$ ($x \leq 0.1$) based on the results of the dc magnetization and Mössbauer spectroscopy studies [50, 64]. This led us to make a systematic study on the the effect of iron substitution on the structural and magnetic properties of the compounds $Ca_3Co_{2-x}Fe_xO_6$ ($0 \leq x \leq 1$). The Rietveld refinement of x-ray and neutron diffraction patterns has confirmed that the compounds $Ca_3Co_{2-x}Fe_xO_6$ ($x = 0$, 0.1, 0.2, and 0.4) crystallize in the rhombohedral structure (space group $R\bar{3}c$). The Rietveld refinement of neutron diffraction patterns and Mössbauer study have confirmed that the Fe^{3+} ions are located only at the TP site. For the compound Ca_3CoFeO_6, the profile matching refinement of the x-ray diffraction pattern has confirmed a triclinic crystal structure (space group $P\bar{1}$). The iron resides almost equally in two different crystallographic sites and exhibits a very high magnetic ordering temperature $T_N \sim 500$ K as evident from our Mössbauer spectroscopy study. Both iron sites exhibit quadrupole interactions of almost equal size; however, with opposite sign. The net magnetic interaction is antiferromagnetic.

Neutron powder diffraction technique has been used to study the nature of magnetic ordering in the compounds $Ca_3Co_{2-x}Fe_xO_6$ ($x = 0$, 0.2, and 0.4). In the first approximation, in zero magnetic field, two different commensurate magnetic structures, (i) amplitude-modulated structure with a propagation vector $\boldsymbol{k} = \{0, 0, 1\}$

and (ii) partially disordered antiferromagnetic (PDA) structure, have been proposed for these compounds below their respective Néel temperatures ($T_N \sim 25$, 20, and 17 K, for $x = 0$, 0.2, and 0.4 compounds, respectively). The common point is that magnetization in the unit cell is zero for both magnetic structures. The two magnetic structures are able to fit the same neutron diffraction patterns because the Fourier coefficients for each solution only differ in a global phase factor that cannot be determined by the powder diffraction experiment. However, a detailed analysis reveals that these compounds order magnetically (below T_N) in an incommensurate spin density wave (SDW) structure, having a modulation and an alignment of the spins along the crystallographic c axis.

For the parent compound $Ca_3Co_2O_6$, in addition to the magnetic Bragg peaks corresponding to the SDW structure (below $T_N \sim 25$ K), a second set of magnetic peaks corresponding to the commensurate antiferromagnetic (CAFM) structure has been observed in the neutron diffraction patterns below $\sim$ 15 K. Moreover, the magnetic Bragg peaks corresponding to the CAFM and SDW structures exhibit a time dependence at some fixed temperature below $\sim$ 14 K. For both magnetic structures (the SDW and CAFM), a short-range ordering (SRO) coexists with a long-range ordering (LRO). The ratio of the intensities contribution (in both SDW and CAFM structures) of the LRO and SRO is 3:7 over 5 - 7 K and the ratio decreases to 1: 9 at 1.5 K. The magnetic ground state is a coherent superposition of the magnetic structures belonging to the propagation vectors $\boldsymbol{k}_1 = \{0, 0, 1.009(3)\}$ and $\boldsymbol{k}_2 = \{0.5, 0.5, 0\}$.

The magnetic ground state for the Fe- substituted compounds ($x = 0.2$ and 0.4) is an incommensurate spin density wave, with the propagation vector $\boldsymbol{k} = \{0, 0, 1.0182(9)\}$. Further, a coexistence of short-range and long-range incommensurate magnetic structures, below T_N, has been observed. The relative contributions of the LRO and SRO in the magnetic Bragg peaks are in the ratio of 13:7 and 3:2 for $x = 0.2$ and $x = 0.4$, respectively. This ratio remains unchanged down to 1.5 K for both compounds, indicating that the volume fractions of the compound exhibiting the short-range order and long-range order remain constant. The observed behavior for the Fe- substituted compounds is very much different from that observed in the compound $\mathrm{Ca_3Co_2O_6}$, where an increase in the volume fraction of the SRO has been observed at low temperatures.

The effect of an external magnetic field on the nature of magnetic ordering in the compounds $\mathrm{Ca_3Co_{2-\mathit{x}}Fe_{\mathit{x}}O_6}$ (x = 0, 0.1, 0.2, and 0.4) has also been investigated. The values of intrachain and interchain exchange interactions for the compounds $\mathrm{Ca_3Co_{2-\mathit{x}}Fe_{\mathit{x}}O_6}$ (x = 0.0, 0.1, 0.2, and 0.4) have been derived from the dc-magnetization study. A decrease in the intrachain positive exchange constant J and an increase in the interchain negative exchange constant J' have been observed with the substitution of iron, which result in a deviation from "1D character". An indication of the presence of a field induced transition from a ferri-to-ferromagnetic state has been observed in the dc magnetization study. Neutron diffraction study has been employed to measure the magnetic order in the compound $\mathrm{Ca_3Co_{1.8}Fe_{0.2}O_6}$, as a function of applied magnetic field and temperature. We have observed field induced transitions, form the zero field SDW structure to an amplitude modulated (AM) structure, and then to a ferrimagnetic structure. Besides, the application of a magnetic field affects the short-range magnetic ordering. In the applied magnetic fields of 2 and 4 T, the SRO is converted into the LRO only over the temperature range 12 - 20 K, however, below $\sim$ 12 K, an increase in the volume fraction of the SRO has been observed. The correlation length for the SRO (below $\sim$ 12 K) also gets affected by the application of field.

Electron doping effects on the structural and magnetic properties of the compounds $Ca_3Co_2O_6$ have been studied in the present thesis. Here the electron doping has been performed with the substitution of rare earth (R^{3+}) ions at the Ca^{2+} site in the compounds $Ca_{2.75}R_{0.25}Co_2O_6$ (R = Lu and Dy). The Rietveld refinement of x-ray and neutron diffraction patterns has confirmed a single phase formation of both compounds in the rhombohedral structure (space group $R\bar{3}c$). With the rare-earth substitution, a decrease in the value of T_N has been observed. This indicates a reduction in the value of positive ferromagnetic intrachain exchange interaction J, which is consistent with the structural studies, where an increase in the lattice constants with the substitution of the rare-earth ions, has been observed. The results of the dc magnetic susceptibility and neutron diffraction studies have confirmed that extra electrons in these compounds are transferred to the cobalt ions at the TP site. No time dependence in the intensity of the strongest magnetic Bragg peak (100) has been observed. This confirms that the SDW structure is stabilized with the substitution of rare-earth ions. The qualitative nature of the observed magnetic ground states for the rare-earth substituted compounds $Ca_{2.75}R_{0.75}Co_2O_6$ is same as that observed for the Fe-substituted compounds $Ca_3Co_{2-x}Fe_xO_6$ ($x = 0.2$ and 0.4), however, different from that observed for the parent compound $Ca_3Co_2O_6$. In the field dependent magnetization study, signatures of the field induced metamagnetic-like phase transitions have been observed.

The magnetic properties of the spin-chain oxides studied in the present thesis work, have been compared with that of the similar systems. In literature, there are a few examples where the 1D Ising spin chains are arranged on a triangular lattice. The most of the compounds belong to the either A_3MXO_6 family (considered in the present thesis work) or $A'BX_3$ (where A' is an alkali ion, B is a transition metal ion, and X is a halide ion) [31–33] family. The compound $CsCoCl_3$ [31, 32] is one of the well studied compounds in the $A'BX_3$ family. Unlike the compounds studied in the present thesis (where the intrachain interaction is ferromagnetic and the interchain interaction is antiferromagnetic), both the intrachain and interchain interactions in the compound $CsCoCl_3$ are antiferromagnetic. This compound undergoes two successive magnetic phase transitions; one at 21 K and other at 9 K. In the temperature range between 9 K and 21 K, the PDA state and, below 9 K, a ferrimagnetic state have been reported [32]. In the literature, it was suggested that magnetic phase diagram of the compound $Ca_3Co_2O_6$ is similar to that reported for the compound $CsCoCl_3$. In the present thesis work, PDA state has been observed (in the first approximation) for the parent compound $Ca_3Co_2O_6$ and Fe-substituted compounds $Ca_3Co_{2-x}Fe_xO_6$ ($x = 0.2$ and 0.4) below their respective Nèel temperatures [72]. However, a detailed analysis of the neutron diffraction pattern has shown that the ground state magnetic structure of the compounds $Ca_3Co_{2-x}Fe_xO_6$ ($x =$ 0.2 and 0.4) is SDW structure. Unlike $CsCoCl_3$, the transition to a ferrimagnetic state has not been observed for the compounds $Ca_3Co_{2-x}Fe_xO_6$ ($x = 0.2$ and 0.4) at low temperatures. For the parent compound $Ca_3Co_2O_6$, the magnetic ground state is a coherent superposition of the magnetic structures belonging to the propagation vectors $\boldsymbol{k}_1 = \{0, 0, 1.009(3)\}$ and $\boldsymbol{k}_2 = \{0.5, 0.5, 0\}$.

To conclude, the present thesis work emphasizes the role of intrachain and interchain interactions in tuning the magnetic properties of the quasi-one-dimensional spin-chain oxides. The importance of magnetic geometrical frustration and local anisotropy (Ising or Heisenberg) in the determining the magnetic ordering on the triangular lattice Ising antiferromagnets has been brought out. The role of external magnetic field in tuning the magnetic properties of these spin-chain compound has been highlighted. The derived results in the present thesis work are very helpful in gaining a broader understanding of the physics of the observed magnetic behavior in these spin-chain oxides and will help in designing the materials with predictable magnetic properties.

Scope of Future Study:

The work presented in this thesis provides a basis for many future research projects. First of all, the time dependence of the magnetic Bragg peaks in the compound $Ca_3Co_2O_6$ has been observed for polycrystalline samples, the single crystal neutron diffraction study will be useful to gain more insight about the nature of magnetic ground state of this compound. Moreover, the effect of an external magnetic field on the ground state as well as on the time dependencies of the magnetic Bragg peaks can be investigated.

The effect of pressure on the magnetic properties of polycrystalline $Ca_3Co_2O_6$ has been reported from the dc magnetization measurements [55, 111]. With an applied pressure (up to 1.4 GPa) a linear increase in the T_N, in all fields up to 5.0 T, has been reported [111]. A ferrimagnetic phase is reported to be stabilized under pressure at low temperatures. The results have been ascribed to interchain bond-length compression, which enhances the strength of antiferromagnetic interchain interactions. There is no report in the literature on the x-ray scattering (resonant/non-resonant) and neutron diffraction studies under pressure on polycrystalline as well as single crystal of $Ca_3Co_2O_6$. These microscopic studies will be useful to quantify the changes in the bond-lengths and bond-angles, which can modify the strength of antiferromagnetic interchain interaction, with applied pressure. Moreover, the effect of an applied pressure on the magnetic ground state and the time dependence of the magnetic structures can be investigated. Finally, a temperature-magnetic field-pressure phase diagram can be constructed by combing the results of these studies.

It would be interesting to grow the single crystals of the compounds $Ca_3Co_{2-x}Fe_xO_6$ and $Ca_{2.75}R_{0.25}Co_2O_6$ (R = Dy and Lu), and carry out a single crystal neutron diffraction study under applied fields to gain more insight into the observed field-induced phase transitions: (i) from the zero field SDW to an AM structure , (ii) from the AM to a ferromagnetic structure at higher field, and (ii) then from the ferrimagnetic to a ferromagnetic state at further higher fields. This study would be useful to determine a refined magnetic phase diagram of these iron and rare-earth substituted compounds in the field-temperature plane.

Recently Wang *et al.* [112] have synthesized the compound $Sr_3Co_2O_6$, isostructural to $Ca_3Co_2O_6$, crystallizing in the rhombohedral structure (space group $R\bar{3}c$). This compound also shows complex magnetic behavior, including 1/3 magnetization plateau. Low temperature neutron diffraction and other microscopic measurements are required to throw more light on the microscopic nature of spin-spin correlation in the compound $Sr_3Co_2O_6$.

The $M(H)$ curves for the compound $Ca_3Co_2O_6$, at low temperatures (below $\sim$ 7 K), exhibit several steps whose origins are still a matter of debate. Several models have been proposed to explain these steps : (i) the existence of metastable states [113, 114], (ii) quantum tunneling of the magnetization [60, 99], and (iii) field-induced spin state transitions [93]. Recently Mohapatra *et al.* [115] have synthesized the nanoparticles of $Ca_3Co_2O_6$. The nanoparticles do not show multiple-step isothermal magnetization behavior as observed for the bulk compound. The other features of the magnetization behavior (ordering temperature) remain same as that observed for the bulk samples. Neutron diffraction experiments of these nanoparticles in zero field and under applied magnetic field are required to understand the origin of the magnetization steps observed in the bulk samples. Moubah *et al.* [116] have studied the effect of the film thickness on the magnetization steps in $Ca_3Co_2O_6$ films. For the films with thickness below a critical value of about 60 nm, no magnetization plateau was observed at 2 K. Polarized neutron reflectivity study of the magnetic structure of $Ca_3Co_2O_6$ films are required to find out the origin of magnetization steps in thicker films. These studies will be helpful in developing the theoretical models to describe the magnetization behavior in the bulk samples of $Ca_3Co_2O_6$.

Bibliography

[1] R. Moessner, Tutorial on frustrated magnetism, available at *http://online.itp.ucsb.edu/online/motterials07/moessner.*

[2] A. P. Ramirez, Annu. Rev. Mater. Sci. **24**, 453 (1994).

[3] S. K. Sinha, Introduction to neutron and x-ray scattering, available at *http://www.dep.anl.gov/nx/lectrnotes.pdf.*

[4] *Booklet on 'National Facility for Neutron Beam Research'*, available at *http://www.barc.ernet.in/publications/tb/nfnbr-book-R.pdf.* Published by Bhabha Atomic Research Centre, Mumbai.

[5] DMC: Cold Neutron Powder Diffractometer, available at *http://www.psi.ch/sinq/dmc/DescriptionEN/poster_dmc.pdf* .

[6] *CRG - two-axis diffractometer D1B*, available at *http://www.ill.eu/instruments-support/instruments-groups/instruments/d1b.*

[7] High-resolution two-axis diffractometer D2B, available at *http://www.ill.eu/instruments-support/instruments-groups/instruments/d2b.*

[8] *User Manual for VSM & AC Susceptibility Measurement Option*, Cryogenics Limited, available at *http://www.cryogenic.co.uk/downloads/default.asp.*

[9] P. Gütlich, Mössbauer spectroscopy-principles and applications, available at *http://obelix.physik.uni-bielefeld.de/∼schnack/molmag/material/Guetlich-Moessbauer_Lectures_web.pdf.*

[10] M. D. Dyar, Geochemical instrumentation and analysis: Mössbauer spectroscopy, retrieved march 20, 2012, from *http://serc.carleton.edu/research_education/geochemsheets/techniques/mossbauer.html.*

[11] H. Sirringhaus, N. Tessler, and R. H. Friend, Science **280**, 1741 (1998).

[12] M. Granström, K. Petritsch, A. C. Arias, A. Lux, M. R. Andersson, and R. H. Friend, Nature **395**, 257 (1998).

[13] D. C. Mattis, *The theory of magnetism* (Springer-Verlag, Heidelberg, 1981).

[14] D. C. Mattis, *The Theory of Magnetism Made Simple* (World Scientific, Singapore, 2004).

[15] B. A. Cipra, American Mathematical Monthly **94**, 937 (1987).

[16] S. M. Bhattacharjee and A. Khare, arXiv:con-mat/9511003 v2 (1995).

[17] L. Onsager, Phys. Rev. B **65**, 117 (1944).

[18] N. D. Mermin and H. Wagner, Phys. Rev. Lett. **17**, 1133 (1966).

[19] N. Majlis, *The Quantum Theory of Magnetism* (World Scientific, Singapore, 2001).

[20] A. M. Tsvelik, *Quantum Field Theory in Condensed Matter Physics* (Cambridge University Press, 2007).

[21] J. P. Goff, D.A. Tennant, R. A. Cowley, R. C. C. Ward, S. E. Nagler, and T. G. Perring, J. Mag. Magn. Materials **140-144**, 69 (1991).

[22] J. P. Goff, D. A. Tennant, and S. E. Nagler, Phys. Rev. B **15992**, 52 (1995).

[23] B. Lake, D. A. Tennant, C. D. Frost, and S. E. Nagler, Nat. Mater **4**, 329 (2004).

[24] F. D. M. Haldane, Phys. Lett. **93A**, 464 (1983).

[25] F. D. M. Haldane, Phys. Rev. Lett. **50**, 1153 (1983).

[26] H. Bethe, Z. Phys. **71**, 205 (1931).

[27] W. J. L. Buyers, R. M. Morra, R. L. Armstrong, M. J. Hogan, P. Gerlach, and K. Hirakawa , Phys. Rev. Lett. **56**, 361 (1986).

[28] R. M. Morra, W. J. L. Buyers, R. L. Armstrong, and K. Hirakawa , Phys. Rev. B **38**, 543 (1988).

[29] G. Xu, J. F. Ditusa, T. Ito, K. Oka, H. Takagi, C. Broholm, and G. Aeppli, Phys. Rev. B **54**, R6827 (1996).

[30] G. H. Wannier, Phys. Rev. **79**, 357 (1950).

[31] M. Mekata, J. Phys. Soc. Jpn. **42**, 76 (1977).

[32] M. Mekata and K. Adachi, J. Phys. Soc. Jpn. **44**, 806 (1978).

[33] M. L. Plumer and A. Caillé, J. Appl. Phys. **70**, 5961 (1991).

[34] J. Als-Nielsen and D. McMorrow, *Elements of Modern X-ray Physics* (John Wiley & Sons, Ltd., 2001).

[35] B. Cullity, *Elements of X-ray Diffraction* (Addison-Wesley, 1978).

[36] R. L. Mössbauer, Z Physik. **151**, 124 (1958).

[37] R. L. Mössbauer, Recoilless Nuclear Resonance Absorption of Gamma Radiation, Nobel Lecture (1961), available at *http://nobelprize.org.*

[38] H. M. Rietveld, J. Appl. Cryst. **2**, 65 (1969).

[39] J. Rodriguez-Carvajal, Recent developments of the program fullprof, in commission on powder diffraction (iucr) newsletter, **26**, 12 (2001), available at *http://www.ill.eu/sites/fullprof/index.html*.

[40] J. Rodríguez-Carvajal, Physica B **192**, 55 (1993).

[41] A. S. Wills, Physica B **276-278**, 680 (2000).

[42] S. Majumdar, V. Hardy, M. R. Lees, D. M. Paul, H. Rousseliére, and D. Grebille, Phys. Rev. B **69**, 024405 (2004).

[43] K. Sengupta, S. Rayaprol, K. K. Iyer, and E. V. Sampathkumaran, Phys Rev. B **68**, 012411 (2003).

[44] V. G. Zubkov, G. V. Bazuev, A. P. Tyutyunnik, and I. F. Berger, J. Solid State Chem **160**, 193 (2001).

[45] K. E. Stitzer, J. Darriet, and H.-C. zur Loye, Curr. Opin. Solid State Mater. Sci. **5**, 535 (2001).

[46] H. Fjellvåg, E. Gulbrandsen, S. Aasland, A. Olsen, and B. C. Hauback, J. Solid State Chem. **124**, 190 (1996).

[47] H. Shigemura, H. Sakaebe, H. Kageyama, H. Kobayashi, A. R. West, R. Kanno, S. Morimoto, S. Nasu, and M. Tabuchi, J. Electrochem. Soc. **148(7)**, A730 (2001).

[48] M. Tabuchi, K. Ado, H. kobayashi, I. Matsubara, H. Kageyama, M. Wakita, S. Tsutsui, S. Nasu, Y. Takeda, C. Masquelier, A. Hirano, and R. Kanno, J. Solid State Chem. **141**, 554 (1998).

[49] S. Niitaka, K. Yoshimura, K. Kosuge, K. Mibu, H. Mitamura, and T. Goto, J. Mag. Magn. Mater. **260**, 48 (2003).

[50] H. Kageyama, S. Kawasaki, K. Mibu, M. Takano, K. Yoshimura, and K. Kosuge, Phys. Rev. Lett. **79**, 3258 (1997).

[51] M. Tabuchi, S. Tsutsui, C. Masquelier, R. Kanno, K. Ado, I. Matsubara, S.Nasu, and H. Kageyama, J. Solid State Chem. **140**, 159 (1998).

[52] S. Aasland, H. Fjellvåg, and B. Hauback, Solid State Commun. **101**, 187 (1997).

[53] H. Kageyama, K. Yoshimura, K. Kosuge, M. Azuma, M.Takano, H. Mitamura, and T. Goto, J. Phys. Soc. Jpn. **66**, 3996 (1997).

[54] V. Hardy, S. Lambert, M. R. Lees, and D. M. Paul, Phys. Rev. B **68**, 014424 (2003).

[55] B. Martínez, V. Laukhin, M. Hernando, J. Fontcuberta, M. Parras, and J. M. González-Calbet, Phys. Rev. B **64**, 012417 (2001).

[56] B. Raquet, M. N. Baibich, J. M. Broto, H. Rakoto, S. Lambert, and A. Maignan, Phys. Rev. B **65**, 104442 (2002).

[57] V. Hardy, M. R. Lees, O. A. Petrenko, D. M. Paul, D. Flahaut, S. Hébert, and A. Maignan, Phys. Rev. B **70**, 064424 (2004).

[58] E. V. Sampathkumaran, N. Fujiwara, S. Rayaprol, P. K. Madhu, and Y. Uwatoko, Phys. Rev. B **70**, 014437 (2004).

[59] R. Frésard, C. Laschinger, T. Kopp, and V. Eyert, Phys. Rev. B **69**, 140405(R) (2004).

[60] V. Hardy, D. Flahaut, M. R. Lees, and O. A. Petrenko, Phys. Rev. B **70**, 214439 (2004).

[61] J. Sugiyama, H. Nozaki, J. H. Brewer, E. J. Ansaldo, T. Takami, H. Ikuta, and U. Mizutani, Phys. Rev. B **72**, 064418 (2005).

[62] O. A. Petrenko, J. Wooldridge, M. R. Lees, P. Manuel, and V. Hardy, Eur. Phys. J. B **47**, 79 (2005).

[63] H. Kageyama, K. Yoshimura, K. Kosuge, X. Xu, and S. Kawano, J. Phys. Soc. Jpn. **67**, 357 (1998).

[64] J. Arai, H. Shinmen, S. Takeshita, and T. Goko, J. Magn. Magn. Mater. **272-276**, 809 (2004).

[65] M. Loewenhaupt, W. Schofer, A. Niazi, and E. V. Sampathkumaran, Europhys. Lett. **63**, 374 (2003).

[66] S. Niitaka, K. Yoshimura, K. Kosuge, M. Nishi, K. Kakurai, A. Mitsuda, H. Mitamura, and T. Goto, Phys. Rev. Lett. **87**, 177202 (2001).

[67] S. Niitaka, H. Kageyama, M. Kato, K. Yoshimura, and K. Kosuge, J. Phys. Soc. Jpn. **70**, 1222 (2001).

[68] H. Kageyama, K. Yoshimura, K. Kosuge, H. Mitamura, and T. Goto, J. Phys. Soc. Jpn. **66**, 1607 (1997).

[69] T. Burnus, Z. Hu, M. W. Haverkort, J. C. Cezar, D. Flahaut, V. Hardy, A. Maignan, N. B. Brookes, A. Tanaka, H. H. Hsieh, H.-J. Lin, C. T. Chen, and L. H. Tjeng, Phys. Rev. B **74**, 245111 (2006).

[70] H. Kageyama, K. Yoshimura, K. Kosuge, H. Nojiri, K. Owari, and M. Motokawa, Phys. Rev. B **58**, 11150 (1998).

[71] I. Nowik, A. Jain, S. M. Yusuf, and J. V. Yakhmi, Phys. Rev. B **77**, 054403 (2008).

[72] A. Jain, S. M. Yusuf, J. Campo, and L. Keller, Phys. Rev. B **79**, 184428 (2009).

[73] A. Jain and S. M. Yusuf, Phys. Rev. B **83**, 184425 (2011).

[74] I. Nowik and H. H. Wickman, Phys. Rev. Lett. **17**, 949 (1966).

[75] E. F. Bertaut,*Spin Configurations in Ionic Structures: Theory and Practice in Magnetism, edited by G.T. Rado and H. Suhl* Vol. 3 (Academic Press, NY, 1963).

[76] E. F. Bertaut, Acta Crystallogr., Sect. A: Cryst. Phys., Diffr., Theor. Gen. Crystallogr. **24**, 217 (1968).

[77] A. Jain, S. Singh, and S. M. Yusuf, Phys. Rev. B **74**, 174419 (2006).

[78] S. Takeshita, J. Arai, T. Goko, K. Nishiyama, and K. Nagamine, J. Phys. Soc. Jpn. **75**, 034712 (2006).

[79] M. Cwik, T. Lorenz, J. Baier, R. Muller, G. Andre, F. Bouree, F. Lichtenberg, A. Freimuth, R. Schmitz, E. Muller-Hartmann, and M. Braden, Phys. Rev.B **68**, 060401(R) (2003).

[80] H. A. Alperin, Phys. Rev. Lett. **6**, 55 (1961).

[81] J. Campo, J. Luzón, F. Palacio, A. Millán, and G. J. McIntyre, Polyhedrom **22**, 2297 (2003).

[82] J. Campo, J. Luzón, F. Palacio, G. J. McIntyre, and E. Ressouche, Physica B **335**, 15 (2003).

[83] J. Luzón, J. Campo, F. Palacio, G. J. M. Intyre, and A. Millán, Phys Rev B. **78**, 054414 (2008).

[84] I. Mirebeau, H. Mutka, P. Bonville, A. Apetrei, and A. Forget, Phys. Rev. B **78**, 174416 (2008).

[85] J. E. Greedan, C. R. Wiebe, A. S. Wills, and J. R. Stewart, Phys. Rev. B **65**, 184424 (2002).

[86] S. Agrestini, L. C. Chapon, A. Daoud-Aladine, A. Gukasov, J. Schefer, C. Mazzoli, M. R. Lees, and O. A. Petrenko, Phys. Rev. Lett. **101**, 097207 (2008).

[87] V. Hardy, C. Martin, G. Martinet, and G. André, Phys. Rev. B **74**, 064413 (2006).

[88] S. Agrestini, C. L. Fleck, L. C. Chapon, C. Mazzoli, A. Bombardi, M. R. Lees, and O. A. Petrenko, Phys. Rev. Lett. **106**, 197204 (2011).

[89] T. Moyoshi and K. Motoya, J. Phys. Soc. Jpn. **80**, 034701 (2011).

[90] V. Eyart, U. Schwingenschlögl, R. Fresard, A. Maignan, C. Martin, N. Nguyen, C. Hackenberger, and T. Kopp, Phys. Rev. B **75**, 115105 (2007).

[91] T. Kyomen, Y. Asaka, and M. Itoh, Phys. Rev. B **67**, 144424 (2003).

[92] L. Pauling, *The Nature of the Chemical Bond* (Cornell University and Ithaca, NY, 1960).

[93] A. Maignan, C. Michel, A. C. Masset, C. Martin, and B. Raveau, Eur. Phys. J. B **15**, 657 (2000).

[94] V. Hardy, M. R. Lees, A. Maignan, S. Hébert, D. Flahaut, C. Martin, and D. M. Paul, J. Phys.: Condens. Matter **15**, 5737 (2003).

[95] R. Vidya, P. Ravindran, H. Fjellvåg, A. Kjekshus, and O. Eriksson, Phys. Rev. Lett. **91**, 186404 (2003).

[96] S. Rayaprol, K. Sengupta, and E. Sampathkumaran, Solid State Commun. **128**, 79 (2003).

[97] D. Flahaut, A. Maignan, S. Hébert, C. Martin, R. Retoux, and V. Hardy, Phys. Rev. B **70**, 094418 (2004).

[98] S. Ohkoshi and K. Hashimoto, Phys. Rev. B **60**, 12820 (1999).

[99] A. Maignan, V. Hardy, S. Hébert, M. Drillon, M. R. Lees, O. Petrenko, D. M. Paul, and D. Khomskii, J. Mater. Chem. **14**, 1231 (2004).

[100] H. J. M. de Groot, L. J. D. Jongh, R. Thiel, and J. Reedijk, Phys. Rev. B **30**, 4041 (1984).

[101] M. F. Thorpe and M. Thomsen, J. Phys. C: Solid State Phys. **16**, L237 (1983).

[102] J. B. Claridge, R. C. Layland, W. H. Henley, and H.-C. zur Loye, Chem. Mater. **11**, 1376 (1999).

[103] S. Karmakar, S. M. Sharma, M. D. Mukadam, S. M. Yusuf, and A. K. Sood, J. Appl. Phys. **97**, 054306 (2005).

[104] R. S. Iskhakov, S. V. Komogortsev, A. Balaev, and L. A. Chekanova, JETP Lett. **72**, 304 (2000).

[105] H. T. Diep, editor, *Frustrated Spin Systems* (World Scientific, Singapore, 2004).

[106] C. L. Fleck, M. R. Lees, S. Agrestini, G. J. McIntyre, and O. A. Petrenko, Eur. Phys. Lett. **90**, 67006 (2010).

[107] T. Sekimoto, S. Noguchi, and T. Ishida, J. Phys. Soc. Jpn. **73**, 3217 (2004).

[108] C. H. Hervoches, H. Fjellvåg, A. Kjekshus,V. M. Fredenborg, and B. C. Hauback, J. Solid State Inorg. Chem. **180**, 628 (2007).

[109] R. D. Shannon, Acta Crysttalogr. **32**, 751 (1976).

[110] N. Mohapatra, K. K. Iyer, S. Rayaprol, and E. V. Sampathkumaran, Phys. Rev. B **75**, 214422 (2007).

[111] T. Goko, N. Nomura, S. Takeshita, and J. Arai, J. Magn. Magn. Mater. **272-276**, E633 (2004).

[112] X. X. Wang, J. J. Li, Y. G. Shi Y. Tsujimoto, Y. F. Guo, S. B. Zhang, Y. Matsushita, M. Tanaka, Y. Katsuya, K. Kobayashi, K. Yamaura, and E. Takayama-Muromachi, Phys. Rev. B **83**, 100410(R) (2011).

[113] Y. B. Kudasov, Phys. Rev. Lett. **96**, 027212 (2006).

[114] R. Soto, G. Martìnez, M. N. Baibich, J. M. Florez, and P. Vargas, Phys. Rev. B **79**, 184422 (2009).

[115] N. Mohapatra, K. K. Iyer, S. D. Das, B. A. Chalke, S. C. Purandare, and E. V. Sampathkumaran, Phys. Rev. B **79**, 140409 (2009).

[116] R. Moubah, S. Colis, C. Ulhaq-Bouillet, M. Drillon, and A. Dinia, J. Phys.: Condens. Matter **23**, 276002 (2011).